

**ALMA MATER STUDIORUM  
UNIVERSITÀ DEGLI STUDI DI BOLOGNA**

---

---

**Dottorato di Ricerca in Ingegneria Energetica, Nucleare e del  
Controllo Ambientale**

*Ciclo XXVII*

Settore Concorsuale:

**09/C2 – Fisica Tecnica e Ingegneria Nucleare**  
02/B3 – Fisica Applicata

Settore Scientifico-Disciplinare:

**ING-IND/18 - Fisica dei Reattori Nucleari**  
ING-IND/20 – Misure e Strumentazione Nucleari  
FIS/07 – Fisica Applicata (a beni culturali,  
ambientali, biologia e medicina)

***Advanced aspects of radiation protection in  
the use of particle accelerators in the  
medical field***

Presentata da:

***Ing. Angelo Infantino***

Coordinatore Dottorato:

*Prof. Vincenzo Parenti Castelli*

Relatore:

*Prof. Ing. Domiziano Mostacci*

Correlatore:

*Dr. Mario Marengo*



# Contents

LIST OF TABLES.....	III
LIST OF FIGURES.....	V
SOMMARIO .....	XI
ABSTRACT.....	XIII
INTRODUCTION .....	1
<b>CHAPTER 1 RADIATION PROTECTION PROBLEMS IN THE USE OF BIOMEDICAL ACCELERATORS</b>	<b>9</b>
1.1 BIOMEDICAL CYCLOTRONS .....	9
1.2 RADIATION PROTECTION PROBLEMS .....	16
1.2.1 <i>International and National Regulations</i> .....	17
1.2.2 <i>Design of Shielding</i> .....	21
1.2.3 <i>Activation of Accelerators and Production of Radionuclides</i> .....	29
1.2.4 <i>Decommissioning of Accelerators</i> .....	32
<b>CHAPTER 2 THE MONTE CARLO FLUKA CODE.....</b>	<b>35</b>
2.1 THE MONTE CARLO METHOD.....	36
2.2 THE FLUKA CODE .....	44
2.2.1 <i>FLUKA</i> .....	44
2.2.2 <i>Flair</i> .....	46
2.2.3 <i>SimpleGeo</i> .....	47
<b>CHAPTER 3 MONTE CARLO MODEL OF THE GE PETTRACE CYCLOTRON .....</b>	<b>49</b>
3.1 THE GE PETTRACE CYCLOTRON .....	49
3.2 MONTE CARLO MODEL OF THE GE PETTRACE CYCLOTRON .....	55
3.3 VALIDATION OF THE MODEL .....	62
3.3.1 <i>Production of <sup>18</sup>F</i> .....	62
3.3.2 <i>Assessment of the Neutron Ambient Dose Equivalent</i> .....	64
3.3.3 <i>Comparison with Tesch's Data</i> .....	70
3.4 EXPERIMENTAL MEASUREMENTS OF <sup>41</sup> AR .....	72
3.5 CYCLOTRON PRODUCTION OF <sup>99m</sup> Tc.....	81
<b>CHAPTER 4 MODELING OF TRIUMF TR13 LIQUID AND SOLID TARGET ASSEMBLY .....</b>	<b>93</b>
4.1 MONTE CARLO MODEL OF THE TR13 LIQUID AND SOLID TARGET ASSEMBLY .....	94
4.1.1 <i>Geometrical model of the targets</i> .....	94
4.1.2 <i>Composition of the Targets</i> .....	98
4.1.2.1 <i>O-18</i> .....	98
4.1.2.2 <i>O-nat</i> .....	98

4.1.2.3	<i>Mo-nat</i> .....	99
4.1.2.4	<i>Ca-nat</i> .....	99
4.1.2.5	<i>Zn-nat</i> .....	100
4.1.2.6	<i>Sr-nat</i> .....	100
4.1.2.7	<i>Y-nat</i> .....	100
4.1.2.8	<i>Fe-nat</i> .....	101
4.1.2.9	<i>Cr-nat</i> .....	101
4.1.2.10	<i>Ni-nat</i> .....	101
4.1.3	<i>Beam Analysis and Modelling</i> .....	102
4.1.4	<i>Physical Parameters and Scores</i> .....	104
4.2	RESULTS OF THE SIMULATIONS.....	105
4.2.1	<i>Reference Values</i> .....	105
4.2.2	<i>Direct Assessment</i> .....	106
4.2.3	<i>External Cross Sections Method (ECSM)</i> .....	109
<b>CHAPTER 5</b>	<b>APPLICATION OF THE DEVELOPED MODEL</b> .....	<b>113</b>
5.1	PLANNING OF A NEW PET FACILITY.....	113
5.1.1	<i>Description of the New PET Facility</i> .....	113
5.1.1.1	<i>Layout of the New PET Facility</i> .....	113
5.1.1.2	<i>The TR19 Cyclotron</i> .....	115
5.1.2	<i>Monte Carlo Model of the TR19 Cyclotron</i> .....	121
5.1.3	<i>Design of shielding and ducts</i> .....	123
5.1.4	<i>Release of <sup>41</sup>Ar</i> .....	134
5.1.5	<i>Activation of Walls and Local Shield</i> .....	136
5.2	ASSESSMENT OF THE DOSE TRANSMISSION THROUGH SEVERAL TYPES OF PLUG-DOORS.....	139
5.2.1	<i>Bunker BC</i> .....	141
5.2.2	<i>Bunker B2</i> .....	144
5.3	REPLACEMENT OF SCANDITRONIX MC17 WITH A TR19 CYCLOTRON.....	147
5.4	AMBIENT DOSE ASSESSMENT AROUND AN ENERGY DEGRADER FOR PROTON THERAPY.....	152
<b>CHAPTER 6</b>	<b>CONCLUSIONS</b> .....	<b>159</b>
<b>REFERENCES</b>	.....	<b>165</b>
<b>ACKNOWLEDGES</b>	.....	<b>177</b>

# ***List of Tables***

Table 1-1 – Main available commercial cyclotrons for the production of medical radionuclides and comparison of some key specifications. ....	13
Table 1-2 – Main manufacturers of hadron therapy systems. ....	14
Table 3-1 - Main features of the radionuclides produced routinely and for research purpose at “S. Orsola-Malpighi” Hospital.....	54
Table 3-2 - Composition of "Air, Dry (near sea level)" as reported from NIST database.....	59
Table 3-3 - Validation of the physics and transport parameters in the energy range of medical applications: assessment of the saturation yield of <sup>18</sup> F.....	63
Table 3-4 - Main features of the detectors used in the measurement of the neutron ambient dose equivalent. ....	65
Table 3-5 - Comparison of neutron ambient dose equivalent obtained with simulation and experimental measurements.....	68
Table 3-6 - Ratio between FLUKA (XYZ) values and experimental measurements. ....	69
Table 3-7 - FLUKA neutron yields obtained for several target materials. ....	70
Table 3-8 - Results of the experimental measurements of <sup>41</sup> Ar in the different positions. For each beaker the weighted average, over 17 samples, and standard deviation of the mean were calculated.....	78
Table 3-9 - Activity concentration, at EOB, of the radionuclides produced in air during irradiation. ....	79
Table 3-10 - FLUKA assessment of the <sup>41</sup> Ar concentration: total air volume.....	80
Table 3-11 - FLUKA assessment of the <sup>41</sup> Ar concentration: ratio of the simulated concentrations for Marinelli beakers and 1m <sup>3</sup> -volumes over experimental measurements.....	80
Table 3-12 - Data of the different targets simulated. For the <sup>100</sup> MoO <sub>3</sub> pellet target impurities reported in the batch certificate were modeled.....	83
Table 3-13 - Natural isotopic abundance for natural and enriched Molybdenum used in the simulations.....	84
Table 3-14 - Results of FLUKA simulation of a 100 μm thick <sup>nat</sup> Mo foil and comparison with experimental measurements. ....	88
Table 3-15 - Results of FLUKA simulation of a 100 μm thick <sup>100</sup> Mo foil and comparison with experimental measurements. ....	89

Table 3-16 - Results of FLUKA simulation of a 1 mm thick $^{nat}\text{MoO}_3$ pellet and comparison with experimental measurements. ....	90
Table 3-17 - Results of FLUKA simulation of a 1 mm thick $^{100}\text{MoO}_3$ pellet and comparison with experimental measurements. ....	90
Table 4-1 - Natural isotopic abundance of natural Oxygen.....	99
Table 4-2 - Natural isotopic abundance of natural Molybdenum. ....	99
Table 4-3 - Natural isotopic abundance of natural Calcium.....	99
Table 4-4 - Natural isotopic abundance of natural Zinc. ....	100
Table 4-5 - Natural isotopic abundance of natural Strontium. ....	100
Table 4-6 - Natural isotopic abundance of natural Yttrium. ....	101
Table 4-7 - Natural isotopic abundance of natural Iron. ....	101
Table 4-8 - Natural isotopic abundance of natural Chromium.....	101
Table 4-9 - Natural isotopic abundance of natural Nickel.....	102
Table 4-10 - Comparison of extracted beam currents on several extraction elements between FLUKA and the averaged experiment (at 2-sigma level). The beam currents on the different elements are normalized to the sum of the total extracted current (Infantino, et al., 2015b).....	103
Table 4-11 - Experimental (and literature) values of the saturation yield for the radioisotopes of interest.....	106
Table 4-12 - Comparison of the saturation yields obtained with FLUKA with the pencil beam ( $Y_P$ ) and the spread out beam in direction and energy ( $Y_{SE}$ ) to the experimental values ( $Y_{exp}$ ). The saturation yields are both normalized to the current on the target material.....	107
Table 4-13 - Average values of the ratio of the $Y_{exp}$ to $Y_P$ and $Y_{SE}$ for both liquid and solid targets and total average for all the radionuclides studied.....	107
Table 4-14 - Comparison of the saturation activities obtained with FLUKA with the pencil beam ( $A_{satP}$ ) and the spread out beam in direction and energy ( $A_{satSE}$ ). The saturation activities take into account the current on the target material. ....	108
Table 4-15 - Saturation yields obtained with the external cross section method ( $Y_{CS}$ ) and comparison to the direct assessment with FLUKA $Y_P$ and the experimental values $Y_{exp}$ where cross section data is available.....	111
Table 5-1 - Overview of the main features of the TR19 cyclotron (ACSI, 2014). ....	115
Table 5-2 - Assessment of the attenuation factor of the local shield. ....	124
Table 5-3 – Data used to compute the expected dose equivalent $H_{exp}(\theta,d)$ .....	128
Table 5-4 - Thickness of the degrader wedges for different out-coming proton energies.....	153
Table 5-5 – Assessment of the neutron and gamma dose equivalent at the reference distance of 100 cm.....	156

# List of Figures

Figure 1-1 - The Lawrence brothers at the console of the first cyclotron used for isotope production and radiation treatments with neutron beams.....	9
Figure 1-2 – The IBA Cyclone 18/9 cyclotron used in the production of medical radionuclides.....	12
Figure 1-3 - The IBA C235 resistive cyclotron for proton therapy.....	15
Figure 1-4 - Radiation protection problems in the use of accelerators in the medical field. ....	16
Figure 1-5 - Hierarchy of the international regulations on radiation protection.....	18
Figure 1-6 - Total neutron yield per proton for different target materials (Tesch, 1985). ....	24
Figure 1-7 - Neutron fluence-to dose equivalent conversion factor (IAEA, 2001b)....	25
Figure 1-8 - The variation of the attenuation length ( $\rho\lambda$ ) for mono-energetic neutrons in concrete as a function of neutron energy. Solid circles indicate the data of (Alsmiller, et al., 1969) and open circles those of (Wyckoff & Chilton, 1973). The solid line shows recommended values of RL and the dashed line shows the high-energy limiting value of 1,170 kg m <sup>-2</sup> (NCRP, 2003).....	27
Figure 2-1 - The PDF and CDF for the normal or Gaussian distribution with $\mu=20$ and $\sigma=5$ . ....	39
Figure 2-2 - The FLUKA graphical interface Flair (v 2.0-8). ....	47
Figure 2-3 - Interface of the 3D solid modeler SimpleGeo (v 4.3.3).....	48
Figure 3-1 - The GE PETtrace cyclotron installed at "S. Orsola-Malpighi" Hospital. ...	50
Figure 3-2 - Overview of the vacuum chamber and the main components of the GE PETtrace cyclotron. ....	50
Figure 3-3 - Targets currently mounted on the GE PETtrace cyclotron. ....	53
Figure 3-4 – Comparison of the FLUKA MC model of the GE PETtrace cyclotron and the cyclotron vault (a) of "S. Orsola-Malpighi" Hospital with an original technical drawing (b). ....	56
Figure 3-5 – FLUKA Monte Carlo model of the cyclotron bunker of "S. Orsola - Malpighi" Hospital. ....	57
Figure 3-6 – FLUKA Monte Carlo model of the cyclotron bunker of "S. Orsola - Malpighi" Hospital: detail of the cyclotron and the ducts through the vault walls. ....	57

Figure 3-7 – Comparison between the real (a) and modeled (b) $^{18}\text{F}$ target assembly of the GE PETtrace cyclotron. ....	58
Figure 3-8 – FLUKA MC model of the PETtrace collimator. ....	58
Figure 3-9 - Definition of the [ $^{18}\text{O}$ ]-water material in Flair. ....	58
Figure 3-10 - Definition of Havar and Portland materials. Composition is reported in mass fraction. ....	59
Figure 3-11 - Definition of the proton beam. ....	60
Figure 3-12 - USRBDX cards used in the modelling of the PETtrace beam spot: proton current was measured both on the collimator and on the target material. ....	60
Figure 3-13 - Cards RADDECAY, IRRPROFI and DCYTIMES used in the simulations. ...	61
Figure 3-14 - Cards START, RANDOMIZE and STOP. ....	62
Figure 3-15 - DEFAULT card ....	62
Figure 3-16 - RESNUCLE and DCYSCORE cards. ....	63
Figure 3-17 - PHYSICS and PART-THR cards. ....	63
Figure 3-18 - Cross section of the $^{18}\text{O}(p,n)^{18}\text{F}$ reaction (IAEA, 2011a). ....	64
Figure 3-19 - Experimental setup used in the measurement campaign: numbers indicate the position of the dosimeters (Gallerani, et al., 2008). ....	65
Figure 3-20 - USRBIN cards used for the assessment of the neutron ambient dose equivalent $H^*(10)$ . ....	66
Figure 3-21 – FLUKA assessment of the neutron ambient dose equivalent $H^*(10)$ over the whole cyclotron vault (Cartesian mesh). ....	67
Figure 3-22 - FLUKA assessment of the neutron ambient dose equivalent $H^*(10)$ in an area close to the cyclotron (cylindrical mesh). ....	67
Figure 3-23 – FLUKA total neutron yield per incident proton for different target materials. ....	71
Figure 3-24 - Sampling positions adopted during the measurement campaign of $^{41}\text{Ar}$ within the bunker. ....	73
Figure 3-25 - RESNUCLE and USRTRACK scores used in the assessment of $^{41}\text{Ar}$ concentration. ....	74
Figure 3-26 - Section of the FLUKA Monte Carlo model used in the simulations: The model reproduces one of the experimental setup adopted. ....	74
Figure 3-27 - Neutron spectra in the whole air volume within the cyclotron vault. ....	75
Figure 3-28 - Example of a generic spectrum obtained with the USRTRACK score of FLUKA. ....	76
Figure 3-29 - Differential neutron fluence distribution as a function of energy and fit of the $^{40}\text{Ar}(n,\gamma)^{41}\text{Ar}$ cross section to the low energy neutrons structure. The figure gives an idea of the convolution process. ....	77
Figure 3-30 - Bi-dimensional map of the radionuclides produced during irradiation in the air volume within the cyclotron vault: Concentrations were normalized for the charge accumulated on the target, expressed in $\mu\text{Ah}$ . ....	79

Figure 3-31 - FLUKA MC model of the solid target assembly mounted on the GE PETtrace cyclotron. ....	82
Figure 3-32 - Target setups used in the simulation: $^{nat/100}\text{Mo}$ foil (a) and $^{nat/100}\text{MoO}_3$ pellet (b). ....	83
Figure 3-33 - Example of the definition of the target material ( $^{100}\text{MoO}_3$ ) using the MATERIAL and COMPOUND cards. ....	83
Figure 3-34 - Scores used in the assessment of the production of $^{99m}\text{Tc}$ . ....	84
Figure 3-35 - Cross section data obtained from TALYS simulation for the irradiation with 16.5 MeV protons of a 99.01% $^{100}\text{Mo}$ -enriched target. ....	85
Figure 3-36 - Differential proton fluence distribution in energy within a 100 $\mu\text{m}$ thick $^{nat}\text{Mo}$ foil target (bin each 0.25 MeV). A similar proton spectrum, within the random uncertainty, was obtained for the enriched target. ....	87
Figure 3-37 - Differential proton fluence distribution in energy within a 1 mm thick $^{nat}\text{MoO}_3$ pellet (bin each 0.25 MeV). A similar proton spectrum, within the random uncertainty, was obtained for the enriched target. ....	87
Figure 4-1 - The TRIUMF TR13 cyclotron. ....	94
Figure 4-2 - Section of the of the target plate: in the figure it is possible to recognize the baffle, two collimator rings (two for each target), the conical collimator (one for each target) composed from four pieces, the liquid and the gas target. ....	95
Figure 4-3 - Detail of the TR13 baffle (a) and four pieces-conical collimator (b). ....	95
Figure 4-4 - Section of the original technical drawings of the TR13 liquid (a) and solid (b) target assembly (Buckley, 2006). ....	96
Figure 4-5 - Section of the FLUKA MC model of the liquid (a) and solid (b) target assembly (plane ZX). ....	97
Figure 4-6 - 3D of the FLUKA MC model of the TR13 liquid target with (a) and without (b) the baffle plate. ....	97
Figure 4-7 - 3D of the FLUKA MC model of the TR13 solid target with (a) and without (b) the baffle plate. ....	97
Figure 4-8 - Example of the definition of a complex target material: a solution of water+ $\text{HNO}_3$ was created using several MATERIAL and COMPOUND cards. ....	98
Figure 4-9 - Proton beam intensity impinging onto the collimator and target in the xz plane ( $y=0$ ). ....	103
Figure 4-10 - Proton beam intensity impinging onto the collimator and target in the xy plane ( $z=0$ ). ....	104
Figure 4-11 - Definition of the proton beam used in the simulation of the TR13 liquid target assembly. ....	104
Figure 4-12 - MCSTHRES and FLUKAFIX cards used in the simulation of the TR13 target assembly. ....	105
Figure 4-13 - USRTRACK score used in the assessment of proton fluence distribution in energy within the target material. ....	110
Figure 4-14 - Proton flux distribution in energy in a liquid target of $\text{H}_2^{18}\text{O}$ . ....	110

Figure 4-15 - Proton flux distribution in energy in a solid target of $^{nat}\text{Fe}$ .....	111
Figure 5-1 - Layout of the ground floor new PET facility of "Sacro Cuore-Don Calabria" Hospital. ....	114
Figure 5-2 - Layout of first floor of the new PET facility of "Sacro Cuore-Don Calabria" Hospital. ....	114
Figure 5-3 - The ACSI TR19 cyclotron.....	115
Figure 5-4 - The external ion source of the TR19 cyclotron. ....	118
Figure 5-5 – TR19 target selector with two targets mounted. In the top of the picture it is possible to see also one of the extraction probes. ....	119
Figure 5-6 - TR19 local-shielding: when closed, the local-shield encloses the target selector completely. ....	120
Figure 5-7 - 3D of the FLUKA MC model of the TR19 cyclotron. ....	121
Figure 5-8 - 3D of the FLUKA MC model of the TR19 cyclotron, the cyclotron vault and the ducts through the vault walls. ....	122
Figure 5-9 - Comparison between the original technical drawing (a) and modeled (b) $^{18}\text{F}$ target assembly of the TR19 cyclotron.....	122
Figure 5-10 - Assessment of the attenuation factor of the local shield. In the picture, local shields are made of air, simulating their absence. Point A ( $0^\circ$ ) and point B ( $90^\circ$ ) are both at 1m from the target. ....	123
Figure 5-11 - USRTRACK score used in the assessment of the neutron fluence distribution in air. ....	124
Figure 5-12 - Differential neutron fluence distribution in energy, in air, without local shielding.....	125
Figure 5-13 - Differential neutron fluence distribution in energy, in air, with local shielding.....	125
Figure 5-14 - Design of shielding: the expected dose equivalent $H_{\text{exp}}(\theta,r)$ was assessed in several points, along different direction, to assess the required thickness of the walls.....	126
Figure 5-15 - Assessment of the neutron ambient dose equivalent $H^*(10)$ around the target selector "NORTH" using a USBIN score with a fine cylindrical mesh.....	127
Figure 5-16 - Assessment of the neutron ambient dose equivalent $H^*(10)$ around the target selector "SOUTH" using a USBIN score with a fine cylindrical mesh.....	127
Figure 5-17 – Differential neutron fluence distribution in energy, in air within the cyclotron vault, during a dual beam irradiation with closed local shield. ....	128
Figure 5-18 – First version of the planning of the cyclotron vault: transmission of the dose through the pipe of the out-coming ventilation was identified. .	129
Figure 5-19 – Optimization of the position and the orientation of the pipe through the wall allows avoiding any significant transmission of dose. ....	130
Figure 5-20 - Ducts through the cyclotron vault walls for the RF and power supply (original technical drawing). ....	131

---

Figure 5-21 - Assessment of the dose transmission through the ducts: detail of the RF and power supply ducts. ....	131
Figure 5-22 – Detail of the pipe for the loading of the enriched-water target (original technical drawing). ....	132
Figure 5-23 – Assessment of the dose transmission through the pipe for the loading of the $^{18}\text{O}$ -water target. ....	132
Figure 5-24 – Overlap of the neutron ambient dose equivalent $H^*(10)$ over a 3D geometry: dose field around the TR19 cyclotron. ....	133
Figure 5-25 – Overlap of the neutron ambient dose equivalent $H^*(10)$ over a 3D geometry: dose field through the RF and power supply ducts. ....	133
Figure 5-26 – Overlap of the neutron ambient dose equivalent $H^*(10)$ over a 3D geometry: dose field through the pipe for the loading of the $^{18}\text{O}$ -water target. ....	134
Figure 5-27 - Assessment of $^{41}\text{Ar}$ within the cyclotron vault without ventilation. ....	134
Figure 5-28 - Radiological impact assessment, for the representative person of the population, of the release of $^{41}\text{Ar}$ in the external atmosphere. ....	135
Figure 5-29 - Irradiation profile used in the assessment of the long-term activation of local shields and cyclotron vault walls. ....	136
Figure 5-30 – Long-term activation of local shields: the radionuclidic inventory was assessed at EOB and 4 weeks after EOB. ....	137
Figure 5-31 - Long-term activation of cyclotron vault walls: the radionuclidic inventory was assessed at EOB. ....	138
Figure 5-32 - Long-term activation of cyclotron vault walls: the radionuclidic inventory was assessed 4 weeks after EOB. ....	139
Figure 5-33 - Layout of the new cyclotron facility. ....	140
Figure 5-34 - FLUKA MC model of plug-door studied: the figure shows the solution with a borated-PE block in front of the door. ....	140
Figure 5-35 – Comparison of the different solutions of plug-doors studied: assessment of the neutron ambient dose equivalent over the whole BC (coarse mesh) and detail of the plug-door (fine mesh). ....	142
Figure 5-36 – Comparison of the different solutions of plug-doors studied: assessment of the neutron ambient dose equivalent over the BC plug-door in the transverse direction (fine mesh). ....	143
Figure 5-37 – Comparison of the different solutions of plug-doors studied: assessment of the neutron ambient dose equivalent over the whole bunker B2 (coarse mesh) ....	144
Figure 5-38 – Comparison of the different solutions of plug-doors studied: detail of the assessment of the neutron ambient dose equivalent over the B2 plug-door (fine mesh). ....	145
Figure 5-39 - Comparison of the different solutions of plug-doors studied: assessment of the neutron ambient dose equivalent over the B2 plug-door in the transverse direction (fine mesh). ....	146
Figure 5-40 - The Scanditronix MC17 cyclotron. ....	147

---

Figure 5-41 - FLUKA MC model of the Scanditronix MC17 cyclotron.....	148
Figure 5-42 - FLUKA MC model of a Scanditronix MC17 cyclotron and the cyclotron vault. ....	148
Figure 5-43 - Assessment of the neutron ambient dose equivalent $H^*(10)$ produced by the MC17 cyclotron over the whole cyclotron vault. ....	149
Figure 5-44 - Long-term activation of the part of wall NORTH in front of the target assembly. ....	150
Figure 5-45 – Replacement of a MC17 cyclotron with a TR19: Assessment of the neutron ambient dose equivalent $H^*(10)$ using the existing layout of the cyclotron vault. ....	151
Figure 5-46 - Section of the 3D FLUKA MC model of a degrader for proton therapy application (45° clipping plane). ....	152
Figure 5-47 - USRBIN score used in the simulation of the energy degrader.....	153
Figure 5-48 - Assessment of the neutron ambient dose equivalent $H^*(10)$ for the different out-coming proton energies in the longitudinal plane. ....	154
Figure 5-49 - Assessment of the neutron ambient dose equivalent $H^*(10)$ for the different out-coming proton energies in the transverse plane.....	155
Figure 5-50 – Average neutron dose equivalent, as a function of the radial distance from the beam spot, for the different out-coming proton energies....	156
Figure 5-51 – Average gamma dose equivalent, as a function of the radial distance from the beam spot, for the different out-coming proton energies....	157
Figure 5-52 – Overlap of the particles produced during the irradiation on the section of the degrader: tracks in the picture represent protons (red), electrons (green), photons, (yellow) and neutrons (blue). The plot was obtained using the SimpleGeo PipsiCAD 3D plugin. ....	158

# ***Sommario***

L'utilizzo dei ciclotroni in industria, ospedali e centri di ricerca è oggi ampiamente diffuso. In campo medico i ciclotroni sono usati in diagnostica e in terapia: in diagnostica per la produzione di isotopi radioattivi usati, in particolare, nei traccianti per Tomografia ad Emissione di Positroni (PET); in terapia oncologica per il trattamento di tessuti con fasci di protoni o ioni pesanti, quali ad esempio carbonio. La radioprotezione nell'utilizzo di questi acceleratori coinvolge una serie di aspetti complessi nella fase progettuale, nell'utilizzo giornaliero e nella fase di decommissioning del sito. In letteratura esistono una serie di guide tecniche, raccomandazioni internazionali e norme riguardo la progettazione e l'installazione di questi acceleratori. Tuttavia, queste guide si basano su metodi di calcolo analitici fondati su forti approssimazioni riguardo il termine sorgente di radiazioni e applicati in condizioni geometriche idealizzate. Tali guide studiano inoltre un solo problema per volta non considerando le interconnessioni che questi hanno tra loro: ad esempio, una scelta accurata dei materiali da usare nella costruzione delle schermature è indispensabile sia nella fase progettuale, per raggiungere gli obiettivi di dose prefissati, sia nella fase di decommissioning dato che queste strutture andranno inevitabilmente col tempo incontro a fenomeni di attivazione divenendo un rifiuto radioattivo da gestire e smaltire. Inoltre, ad oggi, non esiste un vero e proprio riferimento, universalmente approvato dalla comunità scientifica, sul decommissioning di tali apparecchiature. Data la complessità dei fenomeni fisici coinvolti nel trasporto di radiazione e particelle, l'attuale disponibilità di codici Monte Carlo con librerie aggiornate per il trasporto di particelle cariche e neutroni con energia inferiore ai 250 MeV, e il continuo incremento della potenza di calcolo dei computer moderni, rende l'utilizzo sistematico in radioprotezione di tali codici un valido strumento per la progettazione di schermature e la valutazione accurata, allo stesso tempo, del termine sorgente di radiazioni e di tutte le grandezze dosimetriche di interesse.

In questo lavoro, il codice Monte Carlo (MC) FLUKA è stato utilizzato per simulare il ciclotrone GE PETtrace (16.5 MeV) installato presso l'azienda ospedaliera "S. Orsola-Malpighi" (Bologna, IT), quotidianamente utilizzato per la produzione di radiofarmaci PET. Le simulazioni sono state effettuate per valutare diversi fenomeni e quantità d'interesse radiologico tra cui l'equivalente di dose ambientale

nell'intorno dell'acceleratore, il numero di neutroni emessi per protone incidente e la loro distribuzione spettrale, l'attivazione dei componenti del ciclotrone e delle pareti del bunker, l'attivazione dell'aria interna al bunker ed in particolare la produzione di  $^{41}\text{Ar}$ , la resa a saturazione di radionuclidi d'interesse in medicina nucleare. Le simulazioni sono state validate, in termini di parametri fisici e di trasporto da utilizzare nel range energetico caratteristico delle applicazioni mediche, con una serie di misure sperimentali. In particolare, un'accurata campagna di misura dell'equivalente di dose ambientale da neutroni è stata condotta utilizzando diversi strumenti di misura (rem-counter e dosimetri TLD) e i risultati confrontati con le simulazioni MC. La misura di  $^{41}\text{Ar}$  è stata condotta campionando l'aria interna al bunker e misurando l'attività prodotta tramite spettrometria gamma ad alta risoluzione. Infine, la produzione di radionuclidi PET, come il  $^{18}\text{F}$  e  $^{89}\text{Zr}$ , è stata confrontata con le produzioni quotidiane. In tutti i casi le simulazioni hanno fornito un risultato in ottimo accordo con le misure sperimentali confermando i setup fisici utilizzati.

Il modello MC validato è stato quindi applicato ad altri casi pratici. Uno studio di fattibilità della produzione diretta in ciclotrone di  $^{99\text{m}}\text{Tc}$ , attraverso la reazione  $^{100}\text{Mo}(p,2n)^{99\text{m}}\text{Tc}$ , è stato condotto al fine di sviluppare e ottimizzare un target a basso costo. La produzione di radionuclidi ad uso medico è stata studiata simulando il ciclotrone TR13 (13 MeV) installato presso il centro di ricerca TRIUMF (Vancouver, CA) attraverso la valutazione dell'attività a saturazione e il confronto con misure sperimentali condotte in loco. Il nuovo centro PET dell'ospedale "Sacro Cuore-Don Calabria" di Negrar (Verona, IT) è stato completamente progettato utilizzando il modello sopra citato. Per il calcolo delle schermature e lo studio della trasmissione di dose attraverso le penetrazioni del bunker è stato creato un modello dettagliato del ciclotrone ACSI TR19 (19 MeV), installato presso il centro. Il campo di dose nell'intorno di un sistema di selezione dell'energia (degrader) di un ciclotrone per terapia è stato studiato al fine di determinare, per diverse energie dei protoni in uscita, un set di valori di dose di riferimento da utilizzare nella prima fase progettuale di una nuova installazione. Infine il modello è stato applicato alla progettazione di specifiche "porte a tappo" per un sito di produzione di radionuclidi ad uso medico, in cui verrà installato un ciclotrone da 70 MeV e sei diverse beam line, e per il parziale decommissioning di un centro PET e la sostituzione di un ciclotrone Scanditronix MC17 (17 MeV), attualmente installato, con una nuova unità TR19.

# ***Abstract***

Cyclotrons are widely diffused and established in industrial facilities, hospitals and research sites. In the medical field cyclotron are used both in diagnostic and therapy: in diagnostic they are used in the production of radioactive isotopes used, in particular, in the tracers for Positron Emission Tomography (PET); in oncology therapy for the treatment of tissues with proton or heavy ions beams, such as carbon. Radiation protection in the use of these accelerators involves many aspects both in the routine use and for the decommissioning of a site: knowledge of the radiation field around these devices is necessary for the design of shielding, the classification of areas and the protection of workers and patients; knowledge about the activation of the bunker and of the components of the accelerator is important in planning the decommissioning of a site. Guidelines for site planning and installation, as well as for radiation protection assessment, are given in a number of international documents: however, these well-established guides typically offer analytic methods of calculation of both shielding and materials activation, but in approximate or idealized geometry set ups; no specific guidelines for the decommissioning of these types of accelerators have been published. Furthermore, these guidelines study single problems without considering the interconnection between them: for example, an accurate choice of the materials to be used in the shielding is necessary in the planning, to achieve the dose limits, as well as in the decommissioning since these materials will become, in time, a radioactive waste to be managed. Since the complexity of the physical phenomena involved in the transport of radiations, the availability of Monte Carlo (MC) codes with accurate up-to-date libraries for transport and interactions of neutrons and charged particles at energies below 250 MeV, together with the continuously increasing power of nowadays computers, makes systematic use of simulations with realistic geometries possible, yielding equipment and site specific evaluation of the source terms, shielding requirements and all quantities relevant to radiation protection at the same time.

In this work, the well-known MC code FLUKA was used to simulate the GE PETrace cyclotron (16.5 MeV) installed at “S. Orsola-Malpighi” University Hospital (Bologna, IT) and routinely used in the production of positron emitting radionuclides. Simulations yielded estimates of various quantities of interest,

including: the effective dose distribution around the equipment; the effective number of neutron produced per incident proton and their spectral distribution; the activation of the structure of the cyclotron and the vault walls; the activation of the ambient air, in particular the production of  $^{41}\text{Ar}$ , the assessment of the saturation yield of radionuclides used in nuclear medicine. The simulations were validated against experimental measurements in terms of physical and transport parameters to be used at the energy range of interest in the medical field. A careful validation of the dose field around the cyclotron yielded by the simulations, was obtained from an extensive measurement campaign of the neutron environmental dose equivalent. Measurements were conducted with different instruments (rem-counter and TLD dosimeters) and results were found in excellent agreement, allowance made for statistical fluctuations. The estimates of  $^{41}\text{Ar}$  in air were validated against experimental sampling and analysis by high resolution gamma-ray spectrometry. Target activation studies for  $^{18}\text{F}$  and  $^{89}\text{Zr}$  gave results in agreement with experimental measurements and theoretical yields.

The validated model was also extensively used in several practical applications. The feasibility of the direct cyclotron production of non-standard radionuclides such as  $^{99\text{m}}\text{Tc}$ , through the  $^{100}\text{Mo}(p,2n)^{99\text{m}}\text{Tc}$  reaction, was studied. Production of medical radionuclides at TRIUMF (Vancouver, CA) TR13 cyclotron (13 MeV) was studied by the assessment of saturation yields and the comparison with in-house experimental productions. The new PET facility of "Sacro Cuore – Don Calabria" Hospital (Negrar, IT), including the ACSI TR19 (19 MeV) cyclotron, was completely designed using the MC model developed: investigation of dose distribution around the cyclotron was fundamental in the planning, in particular insofar as "bad geometry" items are concerned, like ducts and wall penetrations. Dose field around the energy selection system (degrader) of a proton therapy cyclotron, was assessed to find a set of neutron and gamma dose equivalent references to use in the very first design of a new installation. Finally, the model was applied to the design of plug-doors for a new cyclotron facility, in which a 70 MeV cyclotron will be installed, and the partial decommissioning of a PET facility, including the replacement of a Scanditronix MC17 cyclotron with a new TR19 cyclotron.

# ***Introduction***

When discussing the application of particle accelerators, one should also mention the technical and industrial evolution induced by these applications. Whereas the front line machines are usually general purpose facilities designed for fundamental physics research such as particle or nuclear physics, these machines may later find a new life in more applied research fields such as solid state or material science. They are then followed by dedicated facilities for a more specialised type of research or process (synchrotron radiation, pulsed neutron generation, isotope production) and finally by single purpose optimized devices such as soft X-ray generators for microlithography, compact cyclotrons for positron emitting isotope production, ion implanters or radiotherapy electron accelerators. They are then produced on an industrial basis rather than designed and built by or for a research laboratory (Barbalat, 1994).

Nowadays the use of particle accelerators in the medical field is something considered routine and that people usually take for granted. Knowledge of the historical evolution of these machines is important not only for a cultural purpose but also to understand the actual and the future evolution of these devices. In literature it is possible to find a number of reviews (Friesel & Antaya, 2009; Milton, 1996; Qaim, 2004; Ruth, 2009), part of them more historical and part more technical, on the evolution of particle accelerators and in particular of cyclotrons from the first prototype developed by Ernest Orlando Lawrence in the 1930's. In the following a brief historical summary, mostly based on the review published by Friesel & Antaya, of the evolution of particle accelerators and their application in medical field is reported.

Particle accelerators were initially developed to address specific scientific research goals, yet they were used for practical applications, particularly medical applications, within a few years of their invention. The cyclotron's potential for producing beams for cancer therapy and medical radioisotope production was realized with the early Lawrence cyclotrons and has continued to grow with more technically advanced successors - synchrocyclotrons, sector-focused cyclotrons and superconducting cyclotrons. While a variety of other accelerator technologies was developed to achieve today's high energy particles, this contribution will chronicle

the development of one type of accelerator, the cyclotron and its medical applications. These medical and industrial applications eventually led to the commercial manufacture of both small and large cyclotrons and facilities specifically designed for applications other than scientific research. This development, which started with simple electrostatic linear accelerators in 1924 and the Lawrence cyclotron in the 1930's, continues today with the commissioning of the LHC at CERN. Particle energies have increased over the last 80 years to nearly  $10^7$  times that available from naturally decaying elements, and have allowed a rich, if not yet complete, understanding of the makeup of matter and the Universe.

From its inception in 1930 by Ernest Orlando Lawrence through its many design variations to increased particle energy and intensity for research, the cyclotron has been used for a variety of biological, medical and industrial applications. Soon after the first experimental demonstration of the cyclotron resonance principle by Ernest Lawrence and Stanley Livingston, new radioisotopes produced by high energy particles were discovered and used for the study of both biological processes and chemical reactions. Lawrence developed the cyclotron for nuclear physics research, yet he was very much aware of its possible applications in medicine. The earliest medical applications of cyclotron beams began at the University of California, Berkeley when Lawrence brought his brother John to join Lawrence's group in 1935. John Hundale Lawrence, a physicist with an M.D. from the Harvard Medical School (1930), quickly demonstrated the worth of cyclotron produced radioisotopes in disease research. He became the Director of the Division of Medical Physics at the University of California at Berkeley. In 1936 he opened the Donner Laboratory to treat leukemia and polycythemia patients with radioactive phosphorus ( $^{32}\text{P}$ ). These were the first therapeutic applications of artificially produced radioisotopes on human patients. By 1938, the Berkeley 27-inch (later upgraded to 37-inch) cyclotron had produced  $^{14}\text{C}$ ,  $^{24}\text{Na}$ ,  $^{32}\text{P}$ ,  $^{59}\text{Fe}$  and  $^{131}\text{I}$  radioisotopes, among many others that were used for medical research. John Lawrence and Cornelius Tobias, another student of Ernest Lawrence, used this cyclotron to research one of the earliest biomedical uses of radioactive isotopes. They used radioactive nitrogen, argon, krypton, and xenon gases to provide diagnostic information about the functioning of specific human organs. In other activities, Dr. John Lawrence and Dr. Robert Stone were the first to use hadron therapy to treat cancer using the Crocker 60" cyclotron. They began clinical trials treating cancer with neutrons in 1938, just six years after the discovery of the neutron by Chadwick in 1932. After the World War II, a renewed interest in neutron therapy precipitated clinical trials at several facilities around the world in the 1970's. Except for the early trials at Berkeley, most of the later trials were conducted using accelerators other than cyclotrons. By the 1980's, neutron therapy was no longer used for routine cancer treatment. Robert Wilson, yet another graduate student of Lawrence, realizing the advantages of the hadron Bragg peak, proposed the use of high-energy protons and other charged ions to treat deep-seated tumors in the human body. The basic physics that makes hadron

therapy so attractive is the manner in which high energy ions lose energy while passing through matter. Energetic ionizing (charged) particles lose energy slowly through atomic interactions as they penetrate matter until near the end of their range, where they give up the last 85% of their energy. Wilson's proposal led to the routine use of high energy ion beams for the direct treatment of localized (cancerous) tumors within the human body. Today there are over 30 operating Ion Beam Therapy (IBT) facilities around the world, many of them designed and built by commercial vendors, with several more planned or under construction. Over 60% of these facilities use one commercial cyclotron design as the source of energetic ions required for the treatment.

Through these and other pioneering works, John Lawrence became known as the "Father of Nuclear Medicine and the Donner laboratory is recognized as its birthplace". The cyclotron development activities at the Berkeley Radiation Laboratory became the crucible for the growth of nuclear medicine and hadron therapy as an indispensable part of modern health care. Accelerator produced radioisotopes are now routinely used for imaging diagnostics or to treat diseases.

An interesting and complete review on the technical evolution of cyclotron can be found again in (Friesel & Antaya, 2009) from where most of the information in the summary reported below were taken. The classical cyclotron (also called "conventional" or "Lawrence" cyclotron) invented by Lawrence in 1930 was quite simple in concept and construction. The underlying physics principles are that charged ions (protons, electrons, etc.) are accelerated with electric fields and contained or focused by magnetic fields. Lawrence's brilliant insight was that the orbit period of a particle of charge  $q$ , mass  $m$  and velocity  $v$  traveling in a circle in a uniform magnetic field  $B$  normal to the particle velocity is constant; only the radius  $R$  of the orbit increases with the particle momentum ( $mv$ ). Hence, a constant frequency sinusoidal oscillating voltage on the accelerating cavities, called dees because of their shape, matching the cyclotron resonance condition ( $\omega = qB/m$ ) accelerates the particles twice per revolution, causing them to increase their orbit radius as they gain energy. The repetitive dee gap crossing of the recirculating beam allows it to be accelerated to high energies with relatively low dee voltages, thus eliminating the need for the high voltages used on the competing technologies of the time, the Van de Graaff and Cockcroft-Walton linear accelerators. The ideal kinetic energy gain per revolution in a cyclotron for a synchronous particle of charge  $q$  and a peak dee voltage  $V_0$  is given by  $T = 4qV_0$ . A critical design issue for all particle accelerators is the orbital stability of the circulating beam during acceleration. The particles must remain focused into small bunches in all three spatial dimensions and orbit oscillations about the magnet mid-plane and equilibrium orbit must be small enough to keep beams from getting lost on the magnet poles or dee structures. Electric and magnetic restoring forces must be built into the accelerator to keep the beam centered in the orbit. Also, the magnetic field must be constant to a high

precision to maintain a constant orbit frequency that matches the constant RF electric field frequency throughout the many revolutions of the acceleration cycle. This later condition, called “*isochronism*”, ensures that the particles arrive at the acceleration gap when the RF voltage is near its peak value  $V_0$ . The two requirements of beam focusing and isochronism compete with one another in the classical cyclotron and ultimately limit the maximum energy of this initial design. Beam focusing and orbit stability in a cyclotron requires a small restoring force to push a divergent circulating beam back into the mid-plane equilibrium orbit. The magnetic field of a classical cyclotron tends to bulge out and decrease slightly with radius because of leakage near the pole outer edges. The resulting magnetic field thus has a small radial component ( $B_r$ ) that applies weak axial and radial forces to the circulating beam. The slight field decrease with radius is too small to provide the necessary focusing forces to keep the beam in the machine throughout the acceleration cycle. Lawrence’s team added iron “shims” to the magnet pole tips to produce a more rapid field fall-off with radius to provide the required focusing forces. The shims increase the pole gap from the center outward with radius to reduce the field in a controlled way. For a constant sinusoidal RF accelerating voltage  $\pm V_0$ , a synchronous particle arriving at the dee gap at the maximum voltage receives a kinetic energy gain per revolution. The only force maintaining the particle in synchronism with the accelerating voltage is the magnetic field, which must be maintained to a very high precision ( $\sim 0.1\%$ ) for particles making hundreds of turns. Variation in the magnet gap or the magnet excitation current will cause the particle orbit period to deviate from the synchronous value. For a field constrained to decrease with radius as required for focusing, the particle orbit periods will be longer than the synchronous orbit, and will hence arrive at the dee gap at increasingly later times relative to the RF period, causing the particles to become increasingly out of phase with the RF electric field. This is referred to as “*Phase Slip*”, i.e. the particles slowly slip out of phase with the RF accelerating voltage with each passing turn. Two things happen when this occurs. First, the accelerating voltage experienced by the particle is less than  $V_0$  by a factor depending on the RF phase angle  $\theta$  as well as the resulting kinetic energy gain per turn. The lower energy gain per turn causes the particles to make a larger number of orbits in the cyclotron to reach the maximum design energy. In the worst-case scenario, the particles will eventually arrive late enough after many turns to receive no acceleration or even deceleration. Second, an increase in the particle bunch spatial size and time width during acceleration. Both effects cause beam intensity loss during the acceleration process. Yet a third effect of acceleration in any cyclotron that causes the particles to lose synchronism with the fixed frequency RF electric field is that the particle mass  $m(t)$  increases with velocity according to Einstein’s theory of relativity. A 20 MeV proton’s mass is 2% higher than one at rest. This mass increase further increases the orbit period adding to the loss of synchronism. To compensate for the relativistic mass increase with energy, the field must increase with radius in proportion to the particle mass increase, exactly the opposite of what is required for

focusing. Using high dee voltages to reduce the number of turns required to achieve maximum energy can mitigate the competing requirements of relativity, focusing and isochronism. Even with this, the maximum proton energy capability of the classical cyclotron originally invented by Lawrence can be shown to be approximately 20 MeV. This situation lasted until about 1958 for the classical cyclotron design. One obvious solution to the classical cyclotron energy limit is to reduce the frequency of the RF accelerating voltage with time in synchronism with the increase in the particle orbit period caused by the effects, primarily relativity, described above. This “frequency modulated” (fm) operation requires a single beam bunch to be accelerated with the phase of the accelerating particles shifted to between  $40^\circ$  and  $60^\circ$  after the voltage peak. One drawback of the synchrocyclotron is that once a beam bunch is captured and accelerating, the next bunch cannot be accelerated until the first is accelerated to full energy and the RF frequency reset to the injection value. The resulting extracted beam has a pulse period several thousand times the RF accelerating frequency, compared to the classical cyclotron pulse period of twice the accelerating RF frequency, significantly reducing the average extracted beam intensity. The major disadvantage of the synchrocyclotron, low average intensity pulsed beams, was overcome by the development a third type of cyclotron known as the isochronous cyclotron which is capable of accelerating a continuous stream of particle bunches at a constant orbit frequency to high energies. The approach to addressing the relativistic mass increase is to allow the field to increase radially at the same rate as the relativistic mass increases during acceleration. The high energy isochronous cyclotron was not considered in the early days of cyclotrons because the increasing field violated the conditions necessary for axial stability of the classical and synchrocyclotrons. A method to overcome the weak focusing properties of the required radially increasing field was proposed in 1938 by Llewellyn Thomas. Thomas proposed to use an azimuthally varying magnetic field to provide edge focusing for particles entering and exiting the high and low field regions of the magnet. This was accomplished by dividing the cyclotron magnet pole faces into regions of high fields, called “Hills” (H), and low fields, called “Valleys” (V), such that the average radial field of the cyclotron increases with the energy to maintain a constant orbit period. The azimuthally varying magnetic field makes the protons travel in non-circular orbits causing them to pass through the interface between the high and low fields at an angle  $k$ , referred to as the ‘Thomas’ angle. The radial components of the fields at the interface can be made strong enough to produce adequate radial and axial focusing forces to maintain beam stability throughout the acceleration cycle. These forces are proportional to the Thomas angle  $k$  and the ratio of the high and low field values, which must be calculated during the design of the accelerator. An ion traversing a pole gap with an axial variation in pole height sees a net axial focusing force back towards the cyclotron median plane. The pole field variation required to provide the Thomas focusing may be done with a sine wave or square wave pole gap variation, and with radial or spiral ridge pole shapes. The energy capability of the radial ridge design is

limited to about 45 MeV by the small Thomas angle that can be achieved, which limits the strength of the axial focusing forces that can be obtained. This constraint was removed by the introduction of spiral, rather than radial ridge pole tip sectors. The spiral angle magnet pole sectors caused the circulating particles to cross the pole edges at an angle greater than the Thomas angle, producing a stronger axial focusing force. The spiral pole tip shape can be adjusted during the design process to select the strength of the focusing required for orbit stability. This process could not be done empirically, but required the use of digital computers, which became available to scientists in the late 1950s. The radial and spiral ridge cyclotrons belong to a cyclotron group referred to as isochronous, azimuthally varying field, and sector-focused cyclotrons. One of the largest spiral ridge cyclotrons, TRIUMF, was built in Vancouver, B.C. This accelerator, a 6 sector cyclotron, accelerated  $H^+$  ions to 520 MeV and is physically the largest cyclotron ever built (pole diameter of 17.17 m) because the maximum field was limited to 6 kG to prevent magnetic stripping of the  $H^+$  ions during the acceleration process. The development of the sector-focused cyclotron required sophisticated machining and fabrication techniques, and was initially available only for scientific research. However, the efficiency and compactness of the design made these cyclotrons ideal for the production of medical isotopes for SPECT and PET. Today, with the omnipresence of accelerator design computer codes, the sector-focused cyclotron has become an immensely practical high energy, efficient and relatively low cost machine that has made the applications of high energy particle beams a common commercial commodity used for the production of a large number of medical imaging, diagnostic and therapeutic applications.

Nowadays, cyclotrons are widely diffused and established in industrial facilities, hospitals and research sites. In the medical field cyclotron are used both in diagnostic and therapy: in diagnostic they are used in the production of radioactive isotopes used, in particular, in the tracers for Positron Emission Tomography (PET); in oncology therapy for the treatment of tissues with proton or heavy ions beams, such as carbon. Radiation protection in the use of these accelerators involves many aspects both in the routine use and for the decommissioning of a site: knowledge of the radiation field around these devices is necessary for the design of shielding, the classification of areas and the protection of workers and patients; knowledge about the activation of the bunker and of the components of the accelerator is important in planning the decommissioning of a site. Guidelines for site planning and installation, as well as for radiation protection assessment, are given in a number of international documents: however, these well-established guides typically offer analytic methods of calculation of both shielding and materials activation, but in approximate or idealized geometry set ups; no specific guidelines for the decommissioning of these types of accelerators have been published. Furthermore, these guidelines study single problems without considering the interconnection between them: for example, an accurate choice of the materials to be used in the

shielding is necessary in the planning, to meet the dose limits, as well as in the decommissioning since these material will became, in time, a radioactive waste to be managed.

In this work the radiation protection (RP) in the use of particle accelerators in the medical field will be studied. The application of Monte Carlo simulation in the energy range of particle accelerators of medical interest will be discussed: special attention will be given to biomedical cyclotrons used in the production of medical radionuclides and hadron therapy applications. The well-known Monte Carlo code FLUKA, a general purpose tool for calculations of particle transport and interactions with matter, covering an extended range of applications spanning from proton and electron accelerator shielding to target design, calorimetry, activation, dosimetry, detector design, Accelerator Driven Systems, cosmic rays, neutrino physics, radiotherapy, radiobiology, will be used to study RP problems with a unified approach.

By nature, the work presented in this thesis is divided in different parts, each whit its material & methods and results, but running on a common thread.

In Chapter 1 the main radiation protection problems in the use of biomedical cyclotron will be discussed. An overview of the national and international regulations in RP is extremely important since each calculation has to fit, at the end, the reference or limit values recommended in these publications; general knowledge on design of shielding and cyclotron production of radionuclides will be given to better understand the results obtained in the following of the thesis; decommissioning of particle accelerators will be discussed at the end of this chapter.

In Chapter 2 a brief introduction on the mathematical basis of the Monte Carlo Method will be provided. The Monte Carlo FLUKA code will be presented as well as its graphical interface Flair and the 3D modeler SimpleGeo.

In Chapter 3 the creation and the validation, in terms of physical and transport parameters to be used in the energy range of biomedical cyclotron, of the MC model of the GE PETtrace cyclotron, installed at "S. Orsola-Malpighi" Hospital (Bologna, IT) will be discussed. In particular, the production of  $^{18}\text{F}$  by the well-known reaction  $^{18}\text{O}(p,n)^{18}\text{F}$  will be studied to find the set of physical and transport parameters that gives the best result with the least cpu-time usage; results will be compared with the recommended saturation activity for 1  $\mu\text{A}$  ( $A_2$ ) provided in the IAEA database for medical radioisotopes production. Neutron ambient dose equivalent  $H^*(10)$  assessment around the PETtrace will be performed with experimental measurements using a neutron rem-counter, fitted with a  $\text{BF}_3$  proportional-counter and a PE-moderator, and a set of 12 TLD dosimeters, type CR39; measurements will be compared with MC simulations. To further validate the model, the number of neutrons produced per primary incident proton in the irradiation of a cylindrical

thick target of copper, iron, graphite, tantalum and aluminium will be compared with data obtained by Tesch in 1980's in the 50-250 MeV energy range and at extended energies characteristic of PET cyclotrons. The activity concentration of  $^{41}\text{Ar}$  within the cyclotron vault will be assessed from both Monte Carlo simulation and an extensive measurement campaign of air samples. Finally, the development of a low-cost target for the direct cyclotron-production of  $^{99\text{m}}\text{Tc}$  via the  $^{100}\text{Mo}(p,2n)^{99\text{m}}\text{Tc}$  reaction will be studied using MC simulation.

In Chapter 4 the Monte Carlo simulation will be applied to the production of a number of established and emerging positron emitting radionuclides such as  $^{18}\text{F}$ ,  $^{13}\text{N}$ ,  $^{94}\text{Tc}$ ,  $^{44}\text{Sc}$ ,  $^{68}\text{Ga}$ ,  $^{86}\text{Y}$ ,  $^{89}\text{Zr}$ ,  $^{56}\text{Co}$ ,  $^{52}\text{Mn}$ ,  $^{61}\text{Cu}$  and  $^{55}\text{Co}$ , at TRIUMF (Vancouver, CA) TR13 cyclotron from liquid and solid targets. Saturation yield will be assessed for each of the radionuclides of interest and results will be compared with TR13 experimental productions and IAEA recommended value.

Chapter 5 will be dedicated to the practical applications of the validated MC model in the planning and the decommissioning of cyclotron facilities. The design of the new PET facility of "Sacro Cuore-Don Calabria" Hospital (Negrar, IT) will be presented. The design of the required thickness of the cyclotron vault will be conducted by the assessment of the ambient neutron dose equivalent  $\text{H}^*(10)$  around the accelerator in a dual beam irradiation; in a second step penetrations through the vault walls will be optimized. Activation of air inside the bunker will be studied to assess the production of  $^{41}\text{Ar}$  due the secondary neutrons as well as the activation of shielding and cyclotron components to plan decommission strategies as requested from the Italian national regulations on radiation protection. The assessment of dose transmission through several types of plug-doors in planning a new cyclotron facility will be studied to identify critical points and to find possible solutions. The partial decommissioning of a PET facility and the replacement of a Scanditronix MC17 cyclotron with a new TR19 unit will be evaluated using the validate MC model; assessment of the long-term activation of the vault walls and use of the existing layout of the cyclotron vault with the new cyclotron will be evaluated. Finally, a general and simplified model of the energy selection system (degrader) of a hadron therapy cyclotron will be created to obtain an assessment of reference dose equivalents, for neutron and gamma radiation and for several out-coming proton energies, to use in the very first design of a new installation.

In Chapter 6 the conclusions of the work presented in this thesis will be discussed.

# **Chapter 1**

## ***Radiation Protection Problems in the Use of Biomedical Accelerators***

### ***1.1 Biomedical Cyclotrons***

The original cyclotron concept, invented by Ernest Orlando Lawrence in 1931 (Lawrence & Livingston, 1932), has been developed over the last 8 decades into machines that can provide any ion and energy desired for research or applications given the practical limit of cost (Chu, 2005). The applications of cyclotron beams in medicine and industry have grown from the first investigations of Lawrence's brothers in the 1930s to the point where commercial cyclotrons are designed and built to specifications to meet a large array of user applications, including industry, national security and medicine (Friesel & Antaya, 2009).



***Figure 1-1 - The Lawrence brothers at the console of the first cyclotron used for isotope production and radiation treatments with neutron beams.***

In the field of medicine their use is both in diagnosis and therapy. In vivo diagnostic studies are performed using suitable radionuclides, i.e. pure gamma

emitters or positron emitters. Whereas the former are produced using both nuclear reactors and cyclotrons, the latter, being neutron deficient, can be produced only at a cyclotron via charged-particle-induced reactions. Therapy, especially with protons and other hadrons, on the other hand, is generally carried out either directly by accelerated ions themselves or by neutrons generated as secondary products. The major emphasis is on the production of radionuclides at cyclotrons for utilization in nuclear medicine, both for diagnosis and therapy (Qaim, 2004).

Cyclotrons have become the tool of choice for producing the short-lived, proton-rich radioisotopes used in biomedical applications (Milton, 1996; Strijckmans, 2001; IAEA, 2006). Cyclotron produced medical isotopes are used in planar (2D) imaging studies with the gamma cameras, and tomographic studies (3D) such as Single Photon Emission Computed Tomography (SPECT) and Positron Emission Tomography (PET). Generally a compound labeled with a radioactive tracer, prepared in a modular chemistry unit from an irradiated target material, is introduced in vivo. The tracer element, a gamma emitter or positron emitter, travels through the body and accumulates in specific parts or tissues of the body depending upon the chemistry of the compound, which can then be imaged for clinical diagnostic purposes or treatment. The use and need of radioactive isotopes for biomedical applications continues to increase worldwide (Birattari, et al., 1987a). The primary SPECT isotopes for medical imaging produced by cyclotrons are:  $^{99m}\text{Tc}$  for bone, myocardial and brain scans;  $^{123}\text{I}$  for tumor scans and  $^{111}\text{In}$  for white blood cells. PET differs from SPECT not only in the tracer elements used, short lived positron emitters like  $^{11}\text{C}$ ,  $^{13}\text{N}$ ,  $^{15}\text{O}$ , and  $^{18}\text{F}$ , but also in the way images are generated. Positrons readily annihilate with any free electron in the body yielding a pair of 511 keV photons. The two 511 keV photons are emitted at nearly 180 degrees from each other. Timing can be used to determine the location of the positron annihilation event (Time of Flight techniques) and thus 3D images can be constructed with computer analysis. The timing also improves the signal-to-noise ratio and fewer events are needed to construct the image (Friesel & Antaya, 2009).

Industry has responded with a variety of cyclotrons to address the particular needs of different users groups. Most of these machines have been installed in hospitals, research institutes, and commercial facilities specializing in producing and selling radioisotopes. Cyclotrons for biomedical radionuclide production are generally compact, accelerate light ions (proton, deuteron or helium) and are primarily used to produce short-lived, proton-rich radionuclides. The principle advantage of accelerator produced radionuclides is the high specific activity<sup>1</sup> (SA) that can be obtained via the nuclear reactions that produce a nuclide that is chemically different from the target element. Another significant advantage is the

---

<sup>1</sup> Specific Activity is a measure of the number of radioactive atoms or molecules as compared to the total number of those atoms or molecules present in the sample (Ruth, 2009).

smaller amount of radioactive waste generated in particle reactions compared to reactor produced radioactive isotopes. Most of the reactions used are of the form  $(p,n)$ ,  $(p,2n)$ ,  $(p,xn)$ ,  $(p,\alpha)$  and to a lesser extent reactions involving D,  $^3\text{He}$  and  $^4\text{He}$  as the projectile. Measured cross sections (CS) for many of these reactions along with references for the measurements can be found in IAEA reports (IAEA, 2001a; IAEA, 2009). In 2006, an IAEA report estimated that there were about 350 cyclotrons worldwide primarily used for the production of radionuclides (IAEA, 2006). Nearly 50% of these were in the 10-20 MeV energy range and about 75% of the cyclotrons were being used to produce  $^{18}\text{F}$  for FDG. It is convenient to categorize the cyclotrons into three broad (proton) energy ranges based on their primary function (IAEA, 2008) (for reasons based on efficiency and cost considerations, some facilities/manufacturers have chosen accelerators and reactions that also use deuterons and helium as a projectile) (Schmor, 2010). These proton energy ranges are (Schmor, 2010):

- Cyclotrons with proton energy **less than 20 MeV** are primarily used for producing positron emitting radionuclides. These PET isotopes tend to have short half-lives and the cyclotrons are located in regional centres/hospitals determined by the yield loss due to the delivery time from cyclotron to patient. Many of the cyclotrons have the capability of being shielded with close-packed steel and thereby reduce the need for the user to provide a heavily shielded bunker. The delivery time of the radionuclide, the patient dose requirement and the activity required per day lead to a cyclotron providing up to (nowadays it better to say “at least”) 50  $\mu\text{A}$  per target. Many of the current cyclotrons have the capability of using multiple targets on each of two or more extracted beams.
- Cyclotrons with proton energies **between 20 and 35 MeV** are primarily used to produce many of the gamma-emitting radioisotopes (commonly used as imaging radioisotopes for SPECT) as well as the production of several PET isotopes. The much longer half-life of SPECT radioisotopes permits the delivery to more distant users and this leads to dedicated production facilities with high power targets and larger throughput.
- Cyclotrons providing protons with energies **between 35 and 70 MeV** are used in the production of a number of radioisotopes, including the ones used in radiotherapy. The primary need is for high current cyclotrons with currents in the 1mA range.
- Cyclotrons providing proton energies **greater than 70 MeV and up to 250 MeV** are dedicated to hadron therapy. Typical beam current incident on a target tissue are in the range of 5–10 nA. Further details of this class of accelerators will be given in the following.



*Figure 1-2 – The IBA Cyclone 18/9 cyclotron used in the production of medical radionuclides.*

In general, most of the commercially available isotope production machines are room temperature sector-focused cyclotrons employing either radial ( $< 30$  MeV) or spiral ridge sector magnets. As in all circular accelerators, one of the most challenging aspects is extracting the beam once it has reached the desired energy. For positive ion cyclotrons only in a few exceptional cases extraction efficiencies as high as 98% have been met, and efficiencies in the 75% region are not uncommon. Isotope production machines need to be reliable yet operate at high current with moderate spills. It is very hard to meet these requirements with a positive ion machine with extracted beams. Internal targets are limited to metallic compounds. Besides they provide very little flexibility to the shape and distribution of the beam on target, beam diagnostics are very difficult. Finally and perhaps most important the neutrons created in the target produce induced radioactivity in the cyclotron components. By contrast if  $H^-$  particles are accelerated, they can be extracted simply by stripping, using a thin foil to intercept the beam (Milton, 1996). Actually the majority of medical isotope production cyclotrons accelerate  $H^-$  ions. Some of the  $H^-$  ions imping on a thin internal target, called “stripper foil,” set at an internal radius and have their two electrons removed (“stripped” away); the resulting  $H^+$  ions follow a reverse curvature orbit (with respect to the  $H^-$  ions) directed out of the cyclotron. The remaining unstripped ions continue to accelerate to a larger radius where they can be stripped at a higher energy. Multiple thin stripper foils can be inserted at several radii within the cyclotron, making it possible to extract simultaneously several  $H^+$  beams of different energies from a single cyclotron (Friesel & Antaya, 2009). However everything has its counter-balancing problems. The second  $H^-$  electron is fairly weakly bound (0.755 eV) and may thus be lost due to interaction with the background gas (*vacuum stripping*), or by electro-magnetic disassociation. This lost beam causes heating and induces significant radioactivity in the cyclotron components. To reduce vacuum stripping,  $H^-$  cyclotrons need to operate in high vacuum (Milton, 1996). A partial list of the main available commercial cyclotrons for

the production of medical radionuclides is reported in Table 1-1 (Friesel & Antaya, 2009; Schmor, 2010; Vallabhajosula, 2009).

The 1946 suggestion of Robert Wilson to use high energy protons to kill deep seated tumors in the human body, became a reality beginning in the late 50s, and has grown into a well establish protocol for curing a host of otherwise untreatable cancers, as well as a preferred method of curing other cancers while reducing radiation damage side-effects. This cancer-fighting technique is referred to as “hadron therapy” or “ion beam therapy” (IBT) and is most effective in eliminating well localized cancerous tumors located within the human body, particularly in the head and neck areas (Friesel & Antaya, 2009). Two important considerations in radiation therapy are linear energy transfer (LET) and relative biological efficiency (RBE). Use of hadrons in comparison to conventional therapy can have the advantage of a better physical selectivity, i.e. an improved dose profile and a higher biological efficiency, corresponding to greater killing in the tumour. However, the various types of hadrons differ in their properties (Qaim, 2004). The basic physics that makes hadron therapy so attractive is the manner in which high-energy particles (protons, deuterons, pions, and heavier ions) lose energy while passing through matter. While MV photons used in conventional radiotherapy have an exponentially decreasing depth-dose profile, almost the entire proton beam is

**Table 1-1 – Main available commercial cyclotrons for the production of medical radionuclides and comparison of some key specifications.**

Manufacturer	Model	Particle Beam			Ion Source Type	Peak Field [T]	RF Freq. [MHz]	Plane Of Accel.	Power [W]
		Type	Energy [MeV]	Current [ $\mu$ A]					
ACSI	TR13	H <sup>-</sup>	13	100	CUSP	2.1	74	V	60
ACSI	TR19/(9)	H <sup>-</sup> /(D <sup>-</sup> )	19/(9)	300/100	CUSP	2.1	74/37	V	65
ACSI	TR24	H <sup>-</sup>	24	300	CUSP	2.1	83.5	H/V	80
ACSI	TR30/(15)	H <sup>-</sup> /(D <sup>-</sup> )	30/15	1500/400	CUSP	1.9		H	150
GE	MINItrace	H <sup>-</sup>	9.6	50	PIG	2.2	101	V	35
GE	PETtrace	H <sup>-</sup> /D <sup>-</sup>	16.5/8.4	100/65	PIG	1.9	27.2	V	70
IBA	Cyclone 3	D <sup>+</sup>	3.8	60	PIG	1.8	14	H	14
IBA	Cyclone 10/5	H <sup>-</sup> /D <sup>-</sup>	10/5	100/35	PIG	1.9	42	H	35
IBA	Cyclone 11	H <sup>+</sup>	11	120	PIG	1.9	42	H	35
IBA	Cyclone 18/9	H <sup>-</sup> /D <sup>-</sup>	18/9	150/40	PIG	1.9	42	H	50
IBA	Cyclone 18 <sup>+</sup>	H <sup>+</sup>	18	2000	PIG	1.9	42	H	50
IBA	Cyclone 30	H <sup>-</sup> /(D <sup>-</sup> )	30/(15)	1500/?	CUSP	1.7		H	180
IBA	Cyclone 70 (Arronax)	H <sup>-</sup> /D <sup>-</sup> /H <sub>2</sub> <sup>+</sup> / $\alpha$	30-70/15-35/17.5/70	2x350/50/50/35		1.7	66/30	H	350
SIEMENS (CTI)	RDS Eclipse	H <sup>-</sup>	11	100	PIG	1.9	72	H	35
SIEMENS (CTI)	RDS-111	H <sup>-</sup>	11	100	PIG	1.9			
SIEMENS (CTI)	RDS-112	H <sup>-</sup>	11	100	PIG	1.9			

stopped at the same depth, called the *Bragg Peak*. The depth of penetration of the ion beam into the body depends precisely upon the particle type and energy used for the IBT treatment, as well as the density of the area to be penetrated. This energy loss property allows the physician to target precisely a tumor located within the human body while sparing radiation damage to the healthy tissue around it (Friesel & Antaya, 2009).

The majority of the existing hadron therapy facilities today use protons, but a few use heavier ion beams such as helium, carbon and neon. IBT using pion beams has also been conducted. There are currently about 30 operating IBT facilities in the world, of which only a few have a heavy ion capability (Friesel & Antaya, 2009). The energies involved in proton therapy (PT) range between about 60 and 250 MeV: actually a 230 MeV proton beam will penetrate 32 cm into the human body, a depth large enough for most human applications; hence, this has become the canonical energy for all proton therapy accelerators (Friesel & Antaya, 2009). In general a very well collimated or sharp pencil beam is required. It has to be of much higher quality than in the production of neutrons or radioactive tracers. The beam intensities needed are, however, low. A typical beam incident on an organ target may lie in the range of 5–10 nA. The incident beam on the collimator/homogenizer, however, may reach values up to 1  $\mu$ A (Qaim, 2004). There are only a few vendors of completely designed and operational hadron therapy facilities and they are listed in Table 1-2 (Friesel & Antaya, 2009).

About 50 % (Friesel & Antaya, 2009) of worldwide hadron therapy facilities are provided with an IBA system. The *IBA Proteus 235 Proton Therapy System* consists in fully integrated treatment site comprised of a 230 MeV cyclotron (Figure 1-3), an energy selector, a beam transportation line and one or more gantries. The cyclotron uses a fixed field resistive magnet, a fixed frequency RF system, and accelerates protons to a fixed energy of 230 MeV. The cyclotron magnet is 4.34 meters in diameter, 2.1 meters high, weighs 220 tons, and the coils power is 175 kW. The RF system uses two 30° dees located in opposite valleys and connected at the center. The dees operate at 106 MHz, on the 4<sup>th</sup> harmonic of the proton orbital frequency.

**Table 1-2 – Main manufacturers of hadron therapy systems.**

<b>Manufacturer</b>	<b>Accelerator Type</b>	<b>Maximum Energy/Particle</b>
Ion Beam Application (Belgium)	S.C. Cyclotron	235 MeV/p
Varian Inc. (USA)	S.C. Cyclotron	250 MeV/p
Still Rivers Inc. (USA)	S.C. Sinchrocyclotron	235 MeV/p
Optivus Proton Therapy (USA)	Synchrotron	370 MeV/p
Mitsubishi Heavy Industries (Japan)	Synchrotron	370 MeV/p
Hitachi (Japan)	Synchrotron	250 MeV/p
Sumitomo Heavy Industries (Japan)	S.C. Cyclotron	235 MeV/p

The beam extraction is effected by an electrostatic deflector (ESD) located in one of the valleys without RF cavities. The beam extracted at 230 MeV is then adjusted to the energy required for the treatment by the use of a variable energy degrader made of graphite, followed by a magnetic analyzer to select the required energy width. The system formed by the degrader and the magnetic analyzer is named the Energy Selection System (ESS). This energy selection system allows precise tuning of the continuous proton beam, from 60 MeV to 230 MeV, in under a second. Most often, proton therapy is delivered in rooms equipped with isocentric gantries. The IBA isocentric gantry has 360 degrees of rotation with 0.4 mm radius precision, and a gantry rolling floor. Each gantry room includes a patient positioning system featuring a robot controlled patient couch with 6 degrees of freedom (horizontal, lateral, vertical, rotation, pitch and roll movement are possible) (Jongen, 2010).

Another fully integrated PT system is the *Varian Proscan* based on an isochronous superconducting cyclotron, providing 250 MeV beam up to 800 nA. The use of superconduction technology with its closed cycle, zero boil-off liquid helium cryosystem allows a high induction that saturates completely the iron yoke of the compact machine (Röcken, et al., 2010). Unlike the IBA and Sumitomo Heavy Industries (SHI) isochronous cyclotrons, the ACCEL-Varian cyclotron is equipped with four RF cavities to maximize the energy gain per turn and the extraction efficiency. Here again, a graphite variable energy degrader is used to adjust the proton energy between 70 and 250 MeV. The 3 meter diameter, 1.6 meter-high cyclotron weighs 90 Tons (Jongen, 2010).



**Figure 1-3 - The IBA C235 resistive cyclotron for proton therapy.**

These are relatively large and complex facilities compared to the commercial proton IBT centers. IBA has designed a high-field (4.5 T) superconducting cyclotron to accelerate ions with a charge to mass ratio  $q/a=1/2$  ( $H_2^+$ , He, Li, B, C, Ni, O, and Ar) to 400 MeV/amu. This cyclotron, called the C400, is based on the IBT C235 design

but with higher magnetic fields and a larger diameter (6.4 m vs. 4.7 m). The machine will be capable to provide 265 MeV protons as well as 400 MeV/amu heavy ions, making it an all-purpose accelerator for IBT applications within a very small footprint and a serious competitor to the synchrotron as a practical and affordable source of ions for hadron therapy (Friesel & Antaya, 2009).

## 1.2 Radiation Protection Problems

Radiation Protection (RP) problems in the use of particle accelerators in the medical field can be divided in three categories considering the working life of the accelerator itself (Figure 1-4):

- Problems related to the *site planning*;
- Problems related to the *routine use* of the accelerator;
- Problems related to the *decommissioning* of the accelerator/site.

Guidelines for site planning and installation, as well as for radiation protection assessment, are given in a number of international documents (some of them will be analyzed in detail in the next sections); however these well-established guidelines

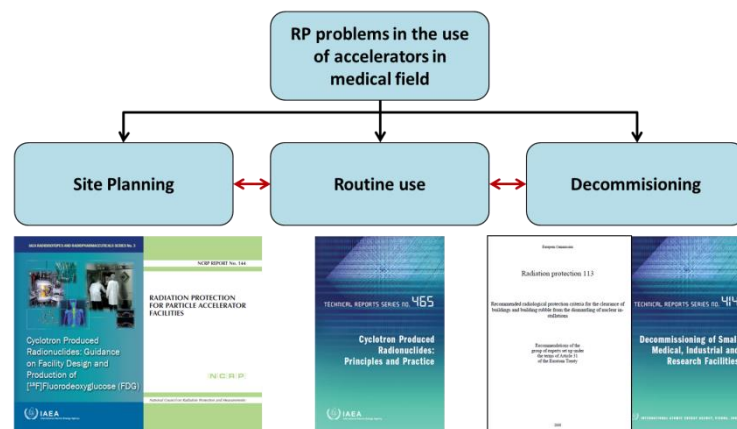


**Figure 1-4 - Radiation protection problems in the use of accelerators in the medical field.**

typically discuss analytic methods of calculation of both shielding and materials activation in approximate or idealized geometry setups. Moreover these guidelines refer to one problem at a time without any connection to the other problems. For example the design of the shielding during the site planning is a problem strongly correlated to the decommissioning of the site: shielding thickness should be calculated taking into account the ability of the different shielding materials to minimize the volume of radioactive waste at the end of the working life of the site

and the cost of the decommissioning. In other cases, works in the scientific literature try to generalize results obtained from meta-analysis on facilities already built, as reported by Tesch (Tesch, 1985), or are based on general hypothesis about the source term (Birattari, et al., 1985; Birattari, et al., 1987b). Experimental measurements of the neutron dose field around PET cyclotrons (Gallerani, et al., 2008; Silari, et al., 2009; Guimaraes, et al., 2012) can be valuable references, but inevitable differences (in equipment, configuration, layout) should be carefully considered when planning new facilities as generalization of experimental results is not straightforward.

### ***1.2.1 International and National Regulations***

Ionizing radiation is a potentially dangerous agent, but at the same time it is very useful in several fields of human activities. From the early years after its discovery and initial use, it has been clear that ionizing radiation can be used only following safety and protection rules. It should be understood that the concept of “safety” changes with time, not only due to increased scientific knowledge, but also taking into account health standards, social, economic issues and political factors. International and National regulation are on the basis of every radiation protection evaluation. Beyond the calculation, the methodology applied and the final result obtained every evaluation has to be performed according to the prescriptions of these regulations. It is important to remember that regulating safety is a national responsibility. However, radiation risks may transcend national borders, and international cooperation serves to promote and enhance safety globally by exchanging experience and by improving capabilities to control hazards, to prevent accidents, to respond to emergencies and to mitigate any harmful consequence. States have an obligation of diligence and duty of care, and are expected to fulfil their national and international undertakings and obligations. International safety standards provide support for States in meeting their obligations under general principles of international law, such as those relating to environmental protection. International safety standards also promote and assure confidence in safety and facilitate international commerce and trade.

There is a well-established hierarchy in the available international regulations (Figure 1-5).

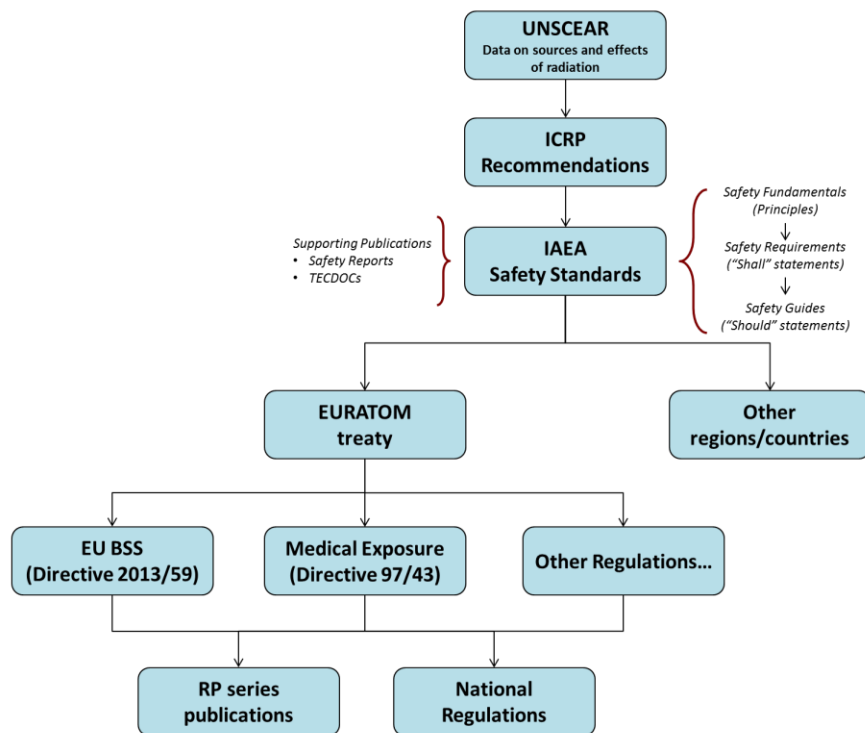


Figure 1-5 - Hierarchy of the international regulations on radiation protection.

The scientific community has then developed a “philosophical” approach for risk factors; in view of avoiding political and economic influences, this delicate task has been entrusted to an international commission of highly reputed experts in the field, the *International Commission on Radiological Protection* (ICRP). The ICRP is an independent body: members of the Commission are not indicated by governments, the ONU or other political or economic entities, but are expressed by the scientific community. The ICRP publishes periodical Reports that, thanks to their balance, scientific level and value, are considered as the basis for any international and national regulation. The ICRP finances its activities with the revenues coming from selling publications and reports. In the 1990 Recommendations, the Commission gave the principles of protection for practices separately from intervention situations. The Commission continues to regard these principles as fundamental for the system of protection, and has now formulated a single set of principles that apply to planned, emergency, and existing exposure situations. In these Recommendations, the Commission also clarifies how the fundamental principles apply to radiation sources and to the individual, as well as how the source-related principles apply to all controllable situations. These principles are (ICRP, 2007):

- **The principle of justification.** “Any decision that alters the radiation exposure situation should do more good than harm”. This means that, by introducing a new radiation source, by reducing existing exposure, or by

reducing the risk of potential exposure, one should achieve sufficient individual or societal benefit to offset the detriment it causes.

- **The principle of optimisation of protection.** *“The likelihood of incurring exposures, the number of people exposed, and the magnitude of their individual doses should all be kept as low as reasonably achievable, taking into account economic and societal factors”*. This means that the level of protection should be the best under the prevailing circumstances, maximising the margin of benefit over harm. To avoid severely inequitable outcomes of this optimisation procedure, there should be restrictions on the doses or risks to individuals from a particular source (dose or risk constraints and reference levels).
- **The principle of application of dose limits.** *“The total dose to any individual from regulated sources in planned exposure situations other than medical exposure of patients should not exceed the appropriate limits recommended by the Commission”*. Regulatory dose limits are determined by the regulatory authority, taking account of international recommendations, and apply to workers and to members of the public in planned exposure situations.

Two principles are source-related and apply to all exposure situations (justification and optimization) while one principle is individual-related and applies to planned exposure situations (application of dose limits).

The findings of the *United Nations Scientific Committee on the Effects of Atomic Radiation* (UNSCEAR) and the recommendations of ICRP, are taken into account in developing the *Safety Standards of the International Atomic Energy Agency* (IAEA). Safety standards are developed in cooperation with other bodies in the *United Nations* (UN) system or other specialized agencies, including the Food and Agriculture Organization of the United Nations, the United Nations Environment Programme, the International Labour Organization, the OECD Nuclear Energy Agency, the Pan American Health Organization and the World Health Organization. A global nuclear safety regime is in place and is being continuously improved. IAEA safety standards, which support the implementation of binding international instruments and national safety infrastructures, are a cornerstone of this global regime. The IAEA safety standards constitute a useful tool for contracting parties to assess their performance under these international conventions. The status of the IAEA safety standards derives from the IAEA Statute, which authorizes the IAEA to establish or adopt, in consultation and, where appropriate, in collaboration with the competent organs of the United Nations and with the specialized agencies concerned, standards of safety for protection of health and minimization of danger to life and property, and to provide for their application. With a view to ensuring the protection of people and the environment from harmful effects of ionizing radiation, the IAEA safety standards establish fundamental safety principles, requirements and

measures to control the radiation exposure of people and the release of radioactive material to the environment, to restrict the likelihood of events that might lead to a loss of control over a nuclear reactor core, nuclear chain reaction, radioactive source or any other source of radiation, and to mitigate the consequences of such events if they were to occur. The standards apply to facilities and activities that give rise to radiation risks, including nuclear installations, the use of radiation and radioactive sources, the transport of radioactive material and the management of radioactive waste. Safety measures and security measures have in common the aim of protecting human life and health and the environment. Safety measures and security measures must be designed and implemented in an integrated manner so that security measures do not compromise safety and safety measures do not compromise security. The IAEA safety standards reflect an international consensus on what constitutes a high level of safety for protecting people and the environment from harmful effects of ionizing radiation. They are issued in the IAEA Safety Standards Series, which are divided in three categories (IAEA, 2014):

- **Safety Fundamentals.** Safety Fundamentals present the fundamental safety objective and principles of protection and safety, and provide the basis for the safety requirements;
- **Safety Requirements.** An integrated and consistent set of Safety Requirements establishes the requirements that must be met to ensure the protection of people and the environment, both now and in the future. The requirements are governed by the objective and principles of the Safety Fundamentals. If the requirements are not met, measures must be taken to reach or restore the required level of safety. The format and style of the requirements facilitate their use for the establishment, in a harmonized manner, of a national regulatory framework. Requirements, including numbered “overarching” requirements, are expressed as “shall” statements. Many requirements are not addressed to a specific party, the implication being that the appropriate parties are responsible for fulfilling them;
- **Safety Guides.** Safety Guides provide recommendations and guidance on how to comply with the safety requirements, indicating an international consensus that it is necessary to take the measures recommended (or equivalent alternative measures). The Safety Guides present international good practices, and increasingly they reflect best practices, to help users striving to achieve high levels of safety. The recommendations provided in Safety Guides are expressed as “should” statements.

The principal users of safety standards in IAEA Member States are regulatory bodies and other relevant national authorities. The IAEA safety standards are also used by co-sponsoring organizations and by many organizations that design, construct and operate nuclear facilities, as well as organizations involved in the use

of radiation and radioactive sources. The IAEA safety standards are applicable, as relevant, throughout the entire lifetime of all facilities and activities, existing and new, utilized for peaceful purposes and to protective actions to reduce existing radiation risks. They can be used by States as a reference for their national regulations in respect of facilities and activities (IAEA, 2014).

Regarding the Italian national regulation about radiation protection, the most important document, to which this thesis refers, is the *Decreto Legislativo 230 of 17 March 1995* (D.Lgs 230/95). The D.Lgs 230/95 (updated in 2000 and 2001) is the Italian implementation of the *Council Directive 96/29EURATOM of 13 May 1996*. Even if at the time of writing of this thesis a new European directive has been published (*2013/59EURATOM of 5 December 2013*) Italy has not yet implemented an updated regulation. To make this document more readable, specific aspects of the D.Lgs 230/95 (dose limits for the workers and the populations, the exemption limit for the release of radioactive materials in the environment, authorization procedures, etc.) will be presented contextually to related argument in the next chapters.

An important issue to remember is that even if the above regulations provide the limitations to respect for a correct radiation safety practice (from a practical point of view the principle of application of dose limits) no information are provided on how to achieve this goal. In other words a regulation providing the *Radiation Protection Officer* (RPO) or the *Qualified Expert* (QE or RPE) with the methodology to do the calculation and satisfy the limits mentioned has not been published yet at any level, national or international. Generally, these methodologies are reported in “good practice technical guides” published by accredited organizations such as the *National Council on Radiation Protection and Measurements* (NCRP).

### 1.2.2 Design of Shielding

A number of references regarding the design of shielding of accelerators are available in literature. NCRP published several dedicated reports in which calculation methodologies for design of shielding are proposed:

- **NCRP Report No. 144.** “*Radiation Protection for Particle Accelerator Facilities*” (NCRP, 2003);
- **NCRP Report No. 147.** “*Structural Shielding Design for Medical X-Ray Imaging Facilities*” (NCRP, 2004);
- **NCRP Report No. 151.** “*Structural Shielding Design and Evaluation for Megavoltage X- and Gamma-Ray Radiotherapy Facilities*” (NCRP, 2005).

While NCRP 147 and 151 reports are dedicated to a class of accelerators used in the medical field (X-ray tubes and CT in the 144 and linear accelerators in the 151), NCRP

144 is a more general report about shielding of accelerators. Actually, even if the NCRP 144 is an all-inclusive report in which many aspects, from physics to practical issues, related to accelerators are reported, it covers a wide range of energies from 5 MeV to the multi-giga-electron Volt energy region. Moreover, a dedicated calculation methodology for cyclotrons used in the medical field (especially for PET cyclotron <30 MeV) is not provided even if these accelerators are the most widely installed in the world: for example no information about the *Use Factor (U)* or the *Occupancy Factor (T)* are provided since this publication is mostly focused on the large accelerators used in the research field in which the occupancy near the device is moderate. The application of NCRP 144 for this class of accelerators is in the end quite dispersive and time consuming.

A dedicated calculation methodology for PET cyclotrons is reported in two standards published by the *Deutsches Institut für Normung (DIN)*, the German Institute for standardization:

- **DIN 6871-1.** “Cyclotron systems for positron emission tomography - Part 1: Requirements for constructional radiation protection” (DIN, 2003);
- **DIN 6871-2.** “Cyclotron systems for positron emission tomography - Part 2: Radiation protection labyrinths and wall entrances” (DIN, 2005).

Both NCRP reports and DIN standards are based on analytical methods in which general hypothesis, especially regarding the source term, are made and applied to an idealized or generic geometry that usually does not fit the real layout that we want to use. Even if for a simple estimation of the primary barrier these methods give with a good approximation a satisfactory result, for other critical points, such as ducts and mazes, not only these analytical methods do not guarantee satisfactory results but in some situations they cannot be applied (NCRP, 2005).

Finally, scientific literature provides a number of data derived from meta-analysis (Tesch, 1985) and experimental measurements, in existing facilities, of several quantities of interest in the design of accelerator shielding such as the neutron dose field (Gallerani, et al., 2008) or the neutron spectra (Guimaraes, et al., 2012; Wiegel, et al., 2009; Silari, et al., 2009); simplified calculation methodology based on general hypothesis (Birattari, et al., 1985; Birattari, et al., 1987b). These data should be carefully considered when planning new facilities as generalization of experimental results is not straightforward given the inevitable differences in equipment, configuration and layout.

An approach based on NCRP 151 can be applied to biomedical cyclotrons. Actually the *Transmission Factor*<sup>2</sup>  $B(t_b)$  of the primary barrier, of thickness  $t_b$ , can be calculated as

$$B(t_b) = \frac{H_{lim}(\vartheta, d)}{H_{exp}(\vartheta, d)} \quad \text{Equation 1-1}$$

where  $H_{lim}(\theta, d)$  is the limit dose equivalent required in the direction  $\theta$  at the distance  $d$  from the source (usually reported as *Shielding Design Goal P* in the NCRP reports) while  $H_{exp}(\theta, d)$  is the expected dose equivalent in the direction  $\theta$  at the distance  $d$  from the source without any barrier. From Equation 1-1 it is clear how the problem is the correct assessment of the term in the denominator. In the following chapters it will be shown how Monte Carlo simulation allows to assess this term more accurately than to analytical methods. The expected dose equivalent can be evaluated analytically with a simple point kernel (NCRP, 2003).

$$H_{exp}(\vartheta, d) = H_{ref}(\vartheta, r) \cdot \frac{UTr^2}{d^2} \quad \text{Equation 1-2}$$

where  $H_{ref}(\theta, r)$  is the dose equivalent in the direction  $\theta$  at the reference distance  $r$  from the source (typically 100 cm);  $U$  is the use factor defined as the fraction of the primary beam workload that is directed toward a given primary barrier;  $T$  is the occupancy factor for an area defined as the average fraction of time that the maximally exposed individual is present while the beam is on;  $d$  is the distance to the occupied area of interest and should be taken from the source to the nearest likely approach of the sensitive organs of a person to the barrier. For a wall this may be assumed to be not less than 0.3 m. For a source located above potentially occupied spaces, the sensitive organs of the person below can be assumed to be not more than 1.7 m above the lower floor, while for ceiling transmission the distance of at least 0.5 m above the floor of the upper room is generally reasonable (NCRP, 2004). The order of magnitude of the term  $H_{ref}(\theta, r)$  can be assessed using a simple calculation method based on the knowledge of the neutron yield, expressed in neutrons emitted per incident proton. Actually, the shielding thickness for proton accelerators of moderately high energy, up to 400 MeV, is determined by the neutron-attenuation characteristics of the shielding material (NCRP, 2003). If the material used in the barrier is concrete, then experience has shown that the barrier will adequately absorb all photoneutrons and neutron capture gamma rays and no additional barrier is required. This is due to the relatively high hydrogen content of

---

<sup>2</sup> The terms attenuation and transmission are often confused in literature. In proper use, almost always, an attenuation factor is greater than one, and a transmission factor is less than one. Thus, e.g., when a shield reduces the radiation intensity by a factor of 10, the attenuation factor is 10 and the transmission factor is  $10^{-1}$ .

concrete and its resultant high neutron absorption cross section (NCRP, 2005). Data on the neutron yield for different materials, available also in the NCRP 144 report, were published by Tesch in 1985 (Tesch, 1985) from a meta-analysis conducted in existing facilities in the previous 10 years.

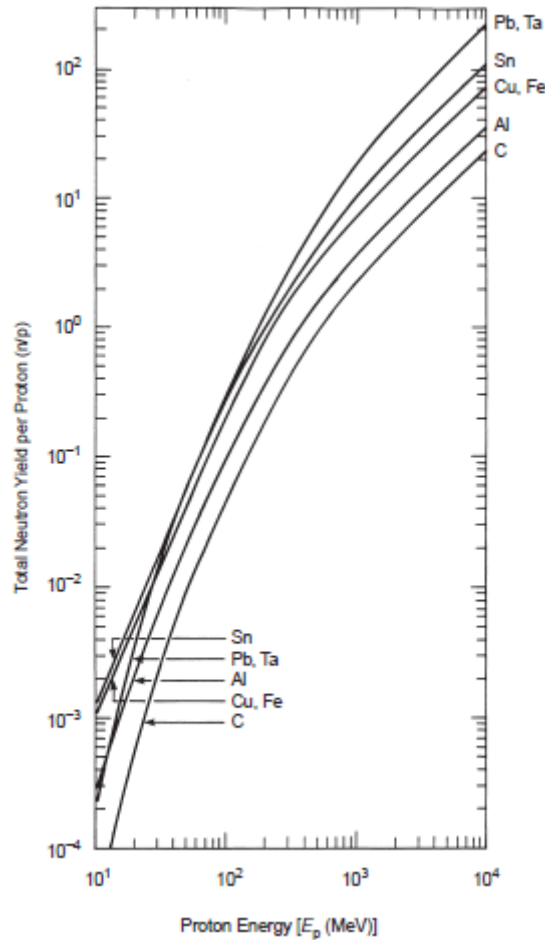


Figure 1-6 - Total neutron yield per proton for different target materials (Tesch, 1985).

The neutron flux can be assessed using the following equation:

$$\dot{\phi} = \frac{Y \cdot I_P \cdot n_Y}{4\pi d^2} \quad \text{Equation 1-3}$$

where  $\dot{\phi}$  is the neutron flux in [ $\text{cm}^{-2} \text{s}^{-1}$ ];  $Y$  is a dimensionless angular distribution factor<sup>3</sup> (NCRP, 1976);  $I_P$  is the proton current in [ $\text{s}^{-1}$ ];  $n_Y$  is the neutron yield per

<sup>3</sup> NCRP 51 reports typical angular distributions in neutron yield ratios,  $\text{Yield}(90^\circ)/Y_{\text{total}}$  and  $\text{Yield}(0^\circ)/Y_{\text{total}}$ , for several neutron-producing reactions, here indicated with using  $Y$ . only  $Y$ . For (p,n) reactions, with a proton energy > 5 MeV,  $Y$  can be assumed equals to 1 to be conservative.

incident proton;  $d$  is the reference distance in [cm]. To convert the flux into dose equivalent it is necessary to take into account the *fluence-to-dose conversion factors* reported in the IRCP 74 (ICRP, 1996), or in the ICRP 116 (ICRP, 2010) and the IAEA TecRep 403 (IAEA, 2001b), and the neutron distribution in energy.

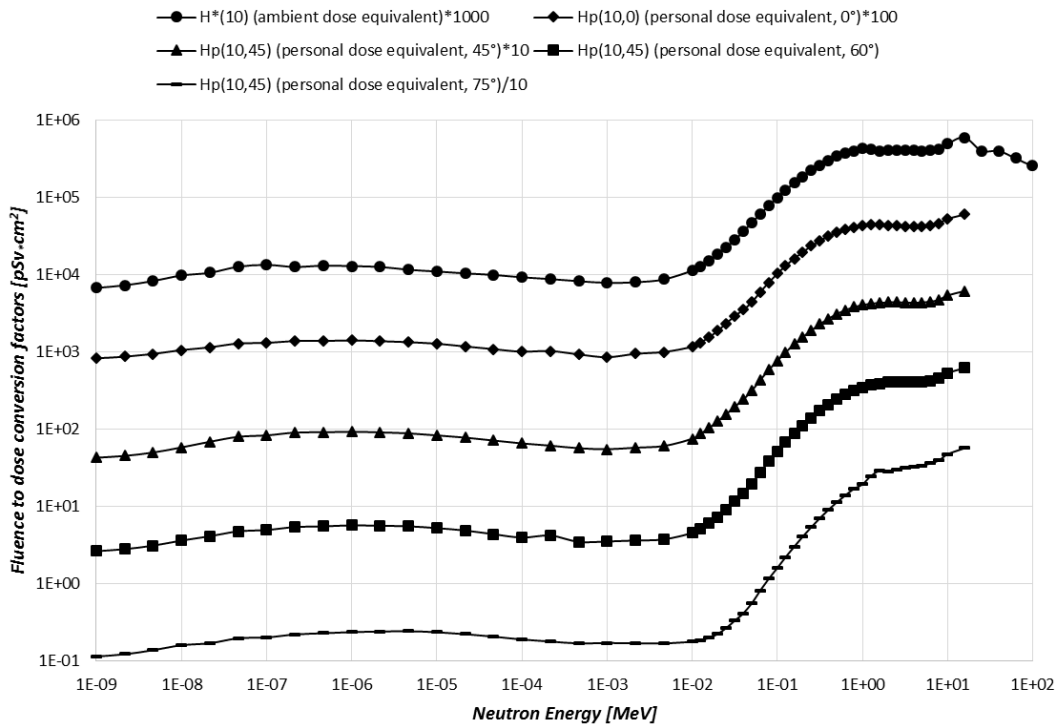


Figure 1-7 - Neutron fluence-to dose equivalent conversion factor (IAEA, 2001b).

Under idealized circumstances, the transmission factor may be expressed in the following equivalent ways:

$$B(t_b) = 10^{-t_b/\lambda_T} = 2^{-t_b/\lambda_H} = e^{-t_b/\lambda} \tag{Equation 1-4}$$

where the *tenth-value layer* ( $\lambda_T$ ) is the thickness which attenuates the radiation in question by a factor of 10; the *half-value layer* ( $\lambda_H$ ) is the thickness which attenuates it by a factor of 2; and the *attenuation length* ( $\lambda$ ) is the thickness which attenuates it by a factor of  $e$ . Equation 1-4 assumes that each additional equal increment of barrier thickness reduces the radiation by a constant factor. When expressed as in Equation 1-4 and plotted on a semi-log graph as a function of  $t_b$ ,  $B(t_b)$  appears as a straight line. Significant deviations from this ideal behaviour may occur in the shielding layers closest to the radiation source. Over a limited range of shield thicknesses, approximating the radiation transmission by an exponential function works well. For shields of thickness less than  $100 \text{ g cm}^{-2}$ , the value of  $\lambda$  changes with

increasing depth in the shield because the more easily absorbed (“softer”) radiations are attenuated more rapidly. This process is often described as “*spectrum-hardening*”. Depending on the material and energy, there may be a transition region (a change in slope in the attenuation curves) which can be taken into account by using a value for the attenuation length over the first tenth-value layer (TVL), designated as  $\lambda_{T1}$  in the shield nearest the radiation source which is different from TVL used for thick shields ( $\lambda_T$ ). Use of a value for  $\lambda_{T1}$  different from  $\lambda_T$  is similar to using a buildup factor for the radiation. For a desired barrier transmission factor  $B$  the total barrier thickness is determined from the number of TVLs ( $n_{\lambda_T}$ ) required (NCRP, 2003):

$$n_{\lambda_T} = \log_{10} \left( \frac{1}{B} \right) \quad \text{Equation 1-5}$$

If  $\lambda_{T1}$  is significantly different from the equilibrium value of the attenuation length ( $\lambda_T$ ), the total thickness  $t_b$  is given by (NCRP, 2003):

$$t_b = \lambda_{T1} + (n_{\lambda_T} - 1)\lambda_T \quad \text{Equation 1-6}$$

To take into account the scattering radiation an additional HVL is added to the thickness of the barrier:

$$t_{b_{eff}} = t_b + HVL \quad \text{Equation 1-7}$$

The nomenclature which is widely used in the literature is repeated here but is nevertheless confusing. The attenuation length ( $\lambda$ ), tenth-value layer ( $\lambda_T$ ), and the half-value layer ( $\lambda_H$ ) are related by the equations (NCRP, 2003):

$$\lambda_T = \lambda \cdot \ln 10 \quad \text{Equation 1-8}$$

$$\lambda_H = \lambda \cdot \ln 2 \quad \text{Equation 1-9}$$

To add further confusion, the value of the tenth-value layer at equilibrium is often denoted as  $\lambda_e$ , where the “e” denotes equilibrium, not to be confused with  $\lambda$ , that reduces the radiation intensity by a factor of  $e$ . If the total shielding barrier consists of more than one material, it is necessary to adjust only the material thicknesses such that the number of  $\lambda_T$  of all the materials combined is equal to  $n_{\lambda_T}$  (similar arguments apply both to half-value layers and attenuation lengths).

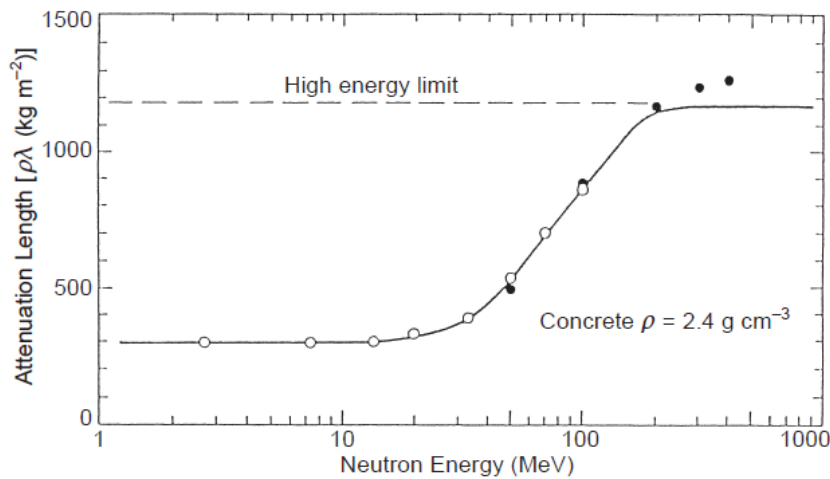


**Figure 1-8 - The variation of the attenuation length ( $\rho\lambda$ ) for mono-energetic neutrons in concrete as a function of neutron energy. Solid circles indicate the data of (Alsmiller, et al., 1969) and open circles those of (Wyckoff & Chilton, 1973). The solid line shows recommended values of RL and the dashed line shows the high-energy limiting value of  $1,170 \text{ kg m}^{-2}$  (NCRP, 2003).**

Data about the TVL for different shielding materials and for both photons and neutrons can be found in the NCRP 144 (NCRP, 2003) and in the IAEA TecRep 283 (IAEA, 1988). Figure 1-8 shows how for neutrons  $<30 \text{ MeV}$  the attenuation length slowly changes when energy increases: in this case it is safe to use only one value of TVL (the maximum) for all the energies in the neutron spectrum. In the other cases, knowledge of the neutron spectrum is fundamental to assess correct values of TVL for different energy range.

It is known that the intensity  $I(x)$  of a mono-energetic photon beam traveling through a thickness  $x$  [cm] of a given material follows the well-known exponential attenuation law

$$I(x) = I_0 \cdot e^{-\mu \cdot x} \quad \text{Equation 1-10}$$

where  $I_0$  is the intensity of the uncollided beam and  $\mu$  is the linear absorption coefficient in  $[\text{cm}^{-1}]$ . The assumption of a simple exponential attenuation law results a valid approximation in situations where photoelectric effect and pair production predominate: if during the attenuation the beam undergoes Compton scattering, the interacting photons are not really removed from the initial beam, as is the case with the other two effects. As a consequence, they can reach the detector degraded in energy but not in intensity. The contribution of the scattered radiation can be taken into account considering the so called *build-up factor*  $B(E_0, \mu x)$  (Sandri, et al., 2008). The build-up factor is defined as the ratio of the actual photon flux to that which would be calculated using a simple exponential attenuation with linear

absorption coefficient (Rockwell, 1956). Taking into account the build-up factor Equation 1-10 becomes

$$I(x) = B(E_0, \mu x) \cdot I_0 \cdot e^{-\mu \cdot x} \quad \text{Equation 1-11}$$

The build-up factor depends on many factors such as geometry, initial energy of the radiation, distance from the source and dimensions of the beam. For a narrow beam the probability that the scattered radiation reaches the detector is negligible and  $B(E_0, \mu x) = 1$ . In this case we talk about “good geometry”. Vice versa, for a broad beam this probability cannot be neglected and  $B(E_0, \mu x) > 1$ ; this case is referred to as “bad geometry” (D'Arenzio, et al., 2014). A “best method” of handling the build-up factor for every situation is not yet agreed upon. In literature, a number of empirical relationships for the computation of the build-up factor are available (Rockwell, 1956; Sandri, et al., 2008) as well as tabulated data. For example, one of the most used relationships, for an isotropic source in an infinite medium, is given by the sum of two simple exponential terms

$$B_{ms}(E_0, \mu x) = A_1(E_0) e^{-\alpha_1(E_0)\mu x} + (1 - A_1(E_0)) e^{-\alpha_2(E_0)\mu x} \quad \text{Equation 1-12}$$

where  $m$  is the attenuating medium,  $s$  is the source geometry and the parameters  $A_1$ ,  $\alpha_1$  and  $\alpha_2$  are functions of energy. A simple approximation is reported in (Knoll, 2000) for gamma radiation: as a rough rule of thumb, the build-up factor for thick slab absorbers tends to be about equal to the thickness of the absorber measured in units of mean free path ( $B \approx \mu x$ ) of the incident gamma rays, provided the detector responds to a broad range of gamma-ray energies. When the shield is made up of several materials, the total relaxation lengths<sup>4</sup> is the sum of the relaxation lengths of the various components (Rockwell, 1956).

Other important phenomena to take into account during the shielding design are the “skyshine” and the “groundshine” effect. The precise definition of “skyshine” (as well as groundshine) is not apparent from the literature and is defined here as that radiation observed at a point on the ground surface which arrives at that point having undergone one or more large-angle scatters in the air (NCRP, 2003). Any accelerator of sufficient energy will produce neutrons in the accelerator enclosure, and the energy of these neutrons will be distributed over a wide range. In passing through the shield, if the shield is sufficiently thick, the primary neutrons, degraded both in energy and intensity, will reach thermal equilibrium with the shielding material media. Neutrons are the principal component of radiation transmitted by a

<sup>4</sup> The attenuation length is often called *relaxation length* to indicate the distance in a material for which  $\mu x = 1$  and thus which attenuates the radiation by a factor of  $e$ , or 2.7 (Rockwell, 1956).

thick-roof shield and will emerge into the surrounding air. In those cases where the roof is thin, particle equilibrium may not be achieved and the emerging neutron spectrum will be intermediate between that of the primary source spectrum and the ultimate equilibrium spectrum. Skyshine results from scattering processes and it is largely due to lower-energy neutrons that are scattered back to ground. High-energy neutrons, which penetrate the roof, undergo inelastic collisions with air atoms to generate more low-energy neutrons in the air augmenting those which have “leaked” from the roof. To quantify skyshine phenomena, it is necessary to know the intensities and both energy and angular distributions of neutrons entering the sky above the accelerator. Details on the calculation method for skyshine and groundshine can be found in (Ladu, et al., 1968) and (Chilton, 1974) and in NCRP Report 51 (NCRP, 1976).

### 1.2.3 Activation of Accelerators and Production of Radionuclides

Activation of cyclotron components and shielding is another important radiation protection problem, especially concerning the decommissioning of a site as will be shown in the next section. In the following, general knowledge and definitions about production of radionuclides will be presented. The terms cross-section and yield, widely used in practical radionuclide production, often differ from basic definitions used in nuclear reactions theory (IAEA, 2001a). Different application oriented groups use these terms in a non-standard way. This fact has created over the years much confusion in scientific literature as far as the terminology used to define saturation activity, the saturation and physical yield and the related quantities: actually it is not uncommon to find different quantities reported with the same name or, vice versa, the same quantity reported with different names. To avoid misinterpretation of the data and the results reported in the present thesis, a brief summary is reported, with the definitions of the most important quantities describing nuclear reactions in the field of practical radionuclide<sup>5</sup> production and activation technology.

The production of a radionuclide can be expressed in terms of the variation, with time, of the number  $N$  of nuclei produced considering the following differential equation

$$\begin{cases} \frac{dN(t)}{dt} = S - \lambda N(t) \\ N(t = 0) = 0 \end{cases} \quad \text{Equation 1-13}$$

where  $S$  is the source term (nuclei produced per unit time) and  $\lambda$  is the decay

---

<sup>5</sup> The terminology “radioisotopes production” is often used instead “radionuclides production”: “radioisotopes” production is strictly correct only considering  $(n, \gamma)$  reactions while “radionuclides” production is always correct, first of all with cyclotrons.

constant in [ $s^{-1}$ ]. Equation 1-13 is a nonhomogeneous linear ordinary differential equation (ODE) that can be solved considering the following integral general solution (Kreyszig, 2006)

$$y'(x) = a(x)y(x) + b(x)$$

$$y(x) = e^{-\int_0^t a(x)dx} \left\{ C + \int_0^t b(x')e^{\int_0^{x'} a(x)dx} dx' \right\} \quad \text{Equation 1-14}$$

where  $C$  is an integration constant. Solving Equation 1-13 is now reduced to evaluating the integral in Equation 1-14, which gives (expressing everything in terms of activity) the well-known equation

$$A(t) = A_{sat} \cdot (1 - e^{-\lambda t}) \quad \text{Equation 1-15}$$

where  $A_{sat}$  is the *Saturation Activity* in [Bq], which represents the source term of Equation 1-13, and  $t$  is the irradiation time.

The Saturation Activity can be expressed in two equivalent ways. The first is often used in Nuclear Engineering, in particular in Neutron Activation Analysis (NAA) where the neutron flux is generally known. Saturation Activity can be written as

$$A_{sat} = \int_{E_{out}}^{E_{in}} n_x \phi(E) \sigma_{xy}(E) dE = \rho V \omega_x \frac{N_A}{A_x} \int_{E_{out}}^{E_{in}} \phi(E) \sigma_{xy}(E) dE \quad \text{Equation 1-16}$$

where  $n_x$  is the number of target nuclei in the target material;  $\phi(E)$  is the particle flux (protons or neutrons in the cases studied in this thesis) in [ $cm^{-2} \cdot s^{-1}$ ];  $\sigma_{xy}$  is the microscopic production cross section of the nuclide  $y$  from the nuclide  $x$  in [ $cm^2$ ];  $\rho V$  is the mass of the target material in [g];  $\omega_x$  is the mass fraction of the nuclide  $x$ ;  $N_A$  is the Avogadro's Number ( $6.022 \cdot 10^{23}$  atoms/mol);  $A_x$  is the mass number of the nuclide  $x$  in [g/mol];  $E_{in}$  and  $E_{out}$  are respectively the incoming and the outgoing particle energies in the target material ( $E_{out}=0$  if completely absorbed). Equation 1-16 is a very intuitive form in which  $A_{sat}$  can be written: actually the product  $n\phi\sigma = \Sigma\phi$ , where  $\Sigma$  is the macroscopic cross section, is nothing else than the *Reaction Rate* that is the number of nuclei produced per unit time.

The other way to write  $A_{sat}$  is generally used in Accelerator Physics: in this field the quantity that is generally known is the irradiation current. First of all, consider the following definitions that can be found in the IAEA TECHDOC-1211 (IAEA, 2001a):

- **$A_1$  or Production Yield or 1h-1 $\mu$ A Yield.** "The activity at the end of a bombardment performed at a constant 1 $\mu$ A beam current on a target

during 1 hour is closely related to the measured activity in every day isotope production by accelerators, the so called 1h–1μA yield,  $A_1$ . In practice, this latter quantity can be used when the bombardment time is significantly shorter than or comparable with the half-life of the produced isotope.”

- **$A_2$  or Saturation Yield.** “When the irradiation time is much longer than the half-life of the produced isotope, a saturation of the number of the radioactive nuclei present in the target is reached, and their activity becomes practically independent of the bombardment time (at a constant beam current, generally considered 1μA). This activity produced by a unit number of incident beam particles is the so-called saturation yield,  $A_2$ .”

These two quantities are related with the so called *Physical Yield*  $Y$  that is defined, for a target having any thickness (IAEA, 2001a), as “the ratio of the number of nuclei formed in the nuclear reaction to the number of particles incident on the target”. It is customary to express the number of radioactive nuclei in terms of the activity, and the number of incident particles in terms of the charge. Thus,  $Y$  can be given as activity per Coulomb, in units of [GBq/C]. The analytical meaning of the Physical Yield is the slope (at the beginning of the irradiation) of the curve of the growing activity of the radionuclide produced versus irradiation time (IAEA, 2001a). Remembering the definition of the *Mass Stopping Power*  $S_P(E)$

$$S_P(E) \left[ \frac{\text{MeV} * \text{cm}^2}{\text{g}} \right] = \frac{1}{\rho} \frac{dE}{dx} \quad \text{Equation 1-17}$$

the Physical Yield for a thick target<sup>6</sup> can be defined as (Bonardi, 1987; McLane, 2004; Otsuka & Takács, 2012)

$$Y = \frac{\lambda N_A}{QM} \int_{E_{out}}^{E_{in}} \frac{\sigma_{xy}(E)}{S_P(E)} dE \quad \text{Equation 1-18}$$

where  $Q=Ze$  is the charge of the incident particle in [C] and  $M$  in the molar mass in [g/mol]. There are close relationships between the above-mentioned yields: using the decay constant of the radionuclide  $\lambda$ , and considering an irradiation time  $t$  of 1 hour, it is possible to obtain (IAEA, 2001a)

---

<sup>6</sup> A thin target has a thickness so small that the reaction cross-section can be considered as constant through the whole target. This is equivalent to the energy loss being negligible when compared to the energy range needed to see significant changes in the reaction cross-section. A thick target has its thickness comparable or larger than the range of the incident particle in the target material.

$$Y = A_1 \cdot \frac{\lambda}{(1 - e^{-\lambda})} = A_2 \lambda \quad \text{Equation 1-19}$$

Equation 1-18 is calculated for a unit current (1 C/s); considering Equation 1-19 and the particle current  $I_P$  in [ $s^{-1}$ ] it is possible to write  $A_{sat}$  as

$$A_{sat} = \frac{N_A}{M} I_P \int_{E_{out}}^{E_{in}} \frac{\sigma(E)}{S_P(E)} dE \quad \text{Equation 1-20}$$

It is important to understand that the two forms of Equation 1-16 and Equation 1-20 are totally equivalent: if the density is explicated in the definition of the mass stopping power it is possible to obtain the following equivalence

$$\int_{E_{out}}^{E_{in}} n_x \phi(E) \sigma_{xy}(E) dE = \frac{N_A m I_P}{M V} \int_{E_{out}}^{E_{in}} \sigma(E) \frac{dx}{dE} dE \quad \text{Equation 1-21}$$

where the term on the right represents the sum (the integral) of the particle track lengths  $dx$  per unit of volume multiplied by the particle current (that means the particle flux) and multiplied by the macroscopic cross section ( $n\sigma$ ). In other words we obtain again the Reaction Rate  $n\phi\sigma$ .

In this thesis, the *Saturation Yield* will be indicated with  $Y_{sat}$  and corresponds to IAEA's  $A_2$  through the following relationship considering the irradiation current  $I$  in [ $\mu A$ ]

$$A_2 = Y_{sat} = \frac{A_{sat}}{I} \quad \text{Equation 1-22}$$

It is usually suitable to express  $Y_{sat}$  in [ $MBq/\mu A$ ] or [ $mCi/\mu A$ ].

#### 1.2.4 Decommissioning of Accelerators

In 2006 IAEA published an update of the document called “*Directory of Cyclotrons Used for Radionuclide Production in Member States*” reporting the complete list of the cyclotrons installed in all the member states, including technical, utilization and administrative information: at that time 262 operating cyclotrons were installed, in the 39 member states, over the ~350 present in the world (IAEA, 2006). Nowadays this number has surely increased not only in developed countries, but even more in the developing ones. Large concentrations of cyclotrons for radionuclide production are located in the United States of America, Japan and Germany. Although the USA are the country with the highest number of cyclotrons, the number of machines installed in the EU for medical radionuclide production is

even higher. The number of institutions that distribute radiopharmaceuticals and [ $^{18}\text{F}$ ]FDG, in particular, is large and still growing. Among them, 75% of the cyclotrons are being used to produce FDG, either for internal use or for distribution. This is certainly an underestimation as the commercial suppliers are under-represented in the IAEA survey. The number of types of cyclotrons available commercially is also quite large and increasing. The energies range from a few MeV for PET isotope production only, to a few hundreds MeV for proton therapy or production of radioisotopes requiring these high energies. The beam currents range upwards from 40  $\mu\text{A}$  to over 1 mA (IAEA, 2006).

The use of isotopes in medical and industrial applications is, as reported above, constantly growing requiring an increasing number of different isotopes to be produced; this lead to the construction of new and improved accelerators but the estimated life expectancy of these accelerators and the reasons for shutting them down are quite different. Accelerators facilities could be shut down due to extreme weather conditions experience, such as tropical storms or tornados, as in the case of the Scanditronix MC40 cyclotron at the Texas Medical Centre operated by the University of Texas in Houston that became a victim of an extreme tropical Storm in June 2001. The changes in finances, politics, market switches, improved technology, changes in institution goals and aging of equipment could initiate the shutdown of an accelerator facility. For biological protection, electrostatic, linear or circular accelerators are housed in thick-walled concrete buildings. During the operation of the accelerators, the concrete walls become slightly radioactive over time due to the activation of traces of rare earths and metals present in the concrete or the reinforcement bars. Other activation mechanisms give rise to a light activation of the metal parts of the accelerators themselves. When considering the dismantling of such accelerators, considerable amounts of low level solid radioactive waste (several thousands of  $\text{m}^3$  of concrete, plus several hundred tons of metal) have to be taken into account. The specific activation levels in these materials may exceed the exemption limits and the proposed limits for unrestricted clearance by a factor of 50 to 100 (European Commission, 1999). The stakeholders want guarantees that all radioactivity and other hazardous materials have been identified and are or will be removed during decommissioning of nuclear facilities. This is in no way less applicable in the case of the decommissioning of accelerator facilities. In many case the site owner of an accelerator facility is not the operator of the facility because accelerators are operated by universities, research institutes, medical facilities and local or national governments. The stakeholders would prefer accelerator facilities to be decommissioned and released for unrestricted reuse in most cases due to the type of operators/users not being the same as in other nuclear facilities such as Power Plants, NFC facilities and Research Reactors (this is called in the practice *partial decommissioning*).

To decrease future dismantling costs, which might easily represent up to 4 times the purchase costs, it is important to quantify clearly the extent of this activation and to identify possible countermeasures to be taken during the construction phase of the accelerators. The subject of accelerator decommissioning has become important only in recent years: accelerator dismantling was generally handled in the past by setting up a plan of systematic measurements after the machine was shutdown. The in-depth study of machine and shielding activation in the construction phase allows also a better evaluation of the possible radiological burden put on workers and the public as a consequence of the dismantling and disposal options taken (European Commission, 1999). Regulations today require to consider decommissioning as part of the design and planning phase for each nuclear facility and this should be done for accelerator facilities as well. Operators of accelerators should identify difficulties that could be experienced during decommissioning so that solutions can be found in time and in some instances decommissioning of redundant parts/sections of the facility could be done while the facility is still in operation to reduce liabilities at the end of the life cycle. Nevertheless, there is a lack of references on specific procedures to follow during the decommissioning of particle accelerators. Although a number of guideline documents have been published with the radiological protection requirements during the operation of accelerators, the decommissioning of these facilities has not been addressed sufficiently: to date a univocal guideline, fully accepted by the scientific community, has not been published yet. Actually, even if the number of cyclotrons installed in the world is continuously increasing, only a few instances of decommissioning have been conducted over the world. In literature there is a lack of data about practical experiences of decommissioning of particle accelerators, particularly cyclotrons, and only a few reports try to collect all these information (European Commission, 1999; IAEA, 2004; Opelka, et al., 1979; Calandrino, et al., 2006; Birattari, et al., 1989; Carroll, 2002; Carroll, et al., 2001). Even if these data can be a valuable source of information, direct application of them in the planning of its own decommissioning strategy is not advisable due to the differences in the layout of the site, in the workload and technology of the different accelerators. The need to address the decommissioning of accelerators has been recognised by the IAEA and the writing of a reference text is currently ongoing.

As will be shown in the following chapters, Monte Carlo simulation allows to assess the level of activation of cyclotron components and shielding, to identify the most problematic radionuclides produced and to perform an optimal design of the whole site including the planning of an ad-hoc strategy of decommissioning.

# Chapter 2

## The Monte Carlo FLUKA code

Before introducing the Monte Carlo (MC) code used in this thesis it is necessary, in my opinion, to give to the reader three general but very important premises:

- *The perfect Monte Carlo code doesn't exist;*
- *Every Monte Carlo code has a more dedicated field of application;*
- *The experimental measurements validate the simulations and not vice versa.*

Are these three general sentences so important? Unfortunately, it is not uncommon to read in the scientific literature, or to listen in international congresses, sentences in opposition to the ones reported above. It has to be clear at any level, from the student that approaches for the first time the Monte Carlo simulation to the academic Professor with several years of experience, that the “simulation” gives a result that is “wrong” by nature. First of all it is necessary to consider some general remarks common to all the MC codes (and not only to them). These codes apply what is called the “*Monte Carlo Method*” that is, as it will be shown in detail in the next section, a numerical technique to evaluate integrals. As usual in physics, we are able to approximate exactly a phenomenon, which means to be able from a mathematical point of view to make equal to zero the rest of the approximation formula and from a physical point of view to take into account all the possible effects, only in a few general or idealized cases. What happens more frequently is that we are looking for a solution within a given precision, usually selected by us. Even in the case in which we are able to calculate analytically, and more precisely exactly, the solution we cannot finitely represent real numbers, which in theory have infinite digits: in this case we have both *truncation and rounding errors*. Moreover, we are not always able to take into account all the aspects of a physical problem: many times we need to neglect some aspects to obtain a closed formulation to solve a problem or to implement it in a script or a program that automatically performs the calculation. Different MC codes implement different nuclear models and not always a problem can be approached in the same way. A number of comparisons of different MC codes, on specific applications, have been published (OH, et al., 2011;

Alpat, et al., 2012; Gorbakov & Kryuchkov, 1996; Stekl, et al., 2000; Beskrovnaia, et al., 2008; Lee, et al., 2001). If one spends some time to understand the nuclear model implemented in a MC code, the limitation and the context in which this code has been developed, it will be clear that the different MC codes have a preferable field of application: i.e. it is not recommended to calculate  $k_{eff}$  eigenvalues for fissile systems with GEANT instead of MCNP, actually MCNP has been developed historically to solve neutron diffusion and multiplication problems in fission devices at Los Alamos National Laboratory (X-5 Monte Carlo Team, 2003); in opposition, the use of GEANT in the simulation of detector efficiency gives better results compared to MCNP (Karamanis, 2003). Finally, and more important, the result of a simulation has a physical meaning only if the model has been validated (in terms of physical and transport parameters) against experimental measurements or theoretical calculations in well-known problems in which an exact analytical solution can be evaluated. The result of a simulation should be never taken into account without any experimental confirmations. It is important to note that in this thesis the term "validation" is not related in any way to the nuclear models implemented in the code: it is supposed that this kind of validation has been done by the developers of the code and for the purpose of this work validation is intended only in term of physical and transport setup.

## 2.1 The Monte Carlo Method

Nowadays Monte Carlo codes are widely applied in radiation and particle transport. In addition to what reported above, it sometimes happens that people tend to spend a long time studying the different codes losing the mathematical basis on which they are founded. Other times, MC-users have not clear what really the Monte Carlo Method (MCM) is: the answer to the question "*What is the Monte Carlo Method?*" is often related to some aspects of the method, such as the generation of the random numbers, and not to what, from a mathematical point of view, this method really does. For these reasons, and to understand some aspect of the FLUKA code, a brief introduction to the MCM will be reported in the following. It is not a purpose of this work to go deeply into the details of the method but only to recall some fundamental aspects.

The Monte Carlo method was invented by John von Neumann, Stanislaw Ulam and Nicholas Metropolis (who named the method), and independently by Enrico Fermi. Originally it was not a simulation method, but a device to solve a multidimensional integro-differential equation by building a stochastic process such that some parameters of the resulting distributions would satisfy that equation. The equation itself did not necessarily refer to a physical process, and if it did, that process was not necessarily stochastic. It was soon realised, however, that when the

method was applied to an equation describing a physical stochastic process, such as neutron diffusion, the model (in this case a random walk) could be identified with the process itself. In these cases the method (analogue Monte Carlo) has become known as a simulation technique, since every step of the model corresponds to an identical step in the simulated process. Particle transport is a typical physical process described by probabilities (cross sections are interaction probabilities per unit distance). Therefore, it lends itself naturally to be simulated by Monte Carlo (Fassò, et al., 2009).

The analysis technique called Monte Carlo is, in essence, a methodology to use sample means to estimate population means. More broadly, Monte Carlo is a widely used numerical procedure that allows people to estimate answers to a wide variety of problems. In essence, Monte Carlo is a highly flexible and powerful form of quadrature<sup>7</sup>, or numerical integration, that can be applied to a very wide range of problems, both direct and inverse (Dunn & Shultis, 2012).

Before going deeply into the MCM, let briefly recall what a quadrature is. Consider the following definite integral in which  $f(x)$  is a real integrable function over the interval  $[a, b]$  (Quarteroni, et al., 2000)

$$I(f) = \int_a^b f(x)dx \quad \text{Equation 2-1}$$

There are several reasons for carrying out numerical integration of  $I(f)$ : the integrand  $f(x)$  may be known only at certain points, such as obtained by sampling (some embedded systems and other computer applications may need numerical integration for this reason); a formula for the integrand may be known, but it may be difficult or impossible to find an antiderivative that is an elementary function; finally it may be possible to find an antiderivative symbolically, but it may be easier to compute a numerical approximation than to compute the antiderivative. If the function  $f(x)$  is known, or can be evaluated, in a finite set of points  $\{x_i\}$ , fixed or selected, we can define a *quadrature rule* (or *quadrature formula*) as

$$\int_a^b f(x)dx \cong \sum_{i=1}^n \omega_i f(x_i) \quad \text{Equation 2-2}$$

---

<sup>7</sup>Quadrature is a historical mathematical term which means determining area. Quadrature problems have served as one of the main sources of problems for mathematical analysis. Mathematicians of ancient Greece, according to the Pythagorean doctrine, understood determination of area of a figure as the process of geometrically constructing a square having the same area (squaring). Thus the name quadrature for this process. The term numerical quadrature (often abbreviated to quadrature) is more or less a synonym for numerical integration, especially as applied to one-dimensional integrals.

where the (real) numbers  $\{x_i\}$  and  $\{\omega_i\}$  are called *nodes* and *weights* (or *coefficients*) of the quadrature rule respectively. In order that the linear combination of Equation 2-2 makes sense, the sum has to be convergent: in other words, it has to approach a given number for  $n \rightarrow \infty$ . The most common quadrature rules use an interpolating polynomial  $P_n(x)$ , of grade  $n-1$ , to approximate the function  $f(x)$  (*interpolatory quadrature rule*). When  $f(x)$  is a polynomial of grade  $n-1$  the interpolating polynomial corresponds to the integrand function and fitting error is null: in this case the quadrature rule is exact that means that the rest  $R_n(f)=0$ . The *degree of precision*  $d$  is the highest degree of the polynomial that can be exactly integrated by the quadrature rule. For highest degree the quadrature rule can equal the integral even if the interpolating polynomial is not coincident with the integrand function. When the quadrature rule is constructed at equally spaced points, the resulting formulas are called *Newton-Cotes* quadrature rules (Monegato, 1998). This kind of rule is the most basic method for approximating an integral: actually the Riemann integral is motivated by approximating the area under a curve by the area of rectangles that touch that curve, which gives a rough estimate that becomes increasingly accurate as the width of those rectangles shrinks. This amounts to approximating the function  $f(x)$  by a piecewise constant interpolant, and then computing the exact integral of the interpolant. When only one rectangle is used to approximate the entire integral, we have the simplest Newton-Cotes formula. This approach can be improved in two complementary ways: increasing the degree of the interpolating polynomial, and reducing the width of the subintervals over which each interpolating polynomial applies. The first approach leads to the *trapezoid rule* and *Simpson's rule*; the second yields *composite rules*, where the integral over  $[a,b]$  is split into the sum of integrals over subintervals (Embree, 2009). Another important class of quadrature rules are called *Gaussian quadrature* rules in which the nodes  $\{x_i\}$  are just the roots of a polynomial belonging to a class of *orthogonal polynomials*.

The summary reported below on MCM is based on the text “Exploring Monte Carlo Methods” (Dunn & Shultis, 2012) in which more details can be found. Our exploration of the Monte Carlo Method begins by considering continuous functions of a single variable. The methodology developed here can be applied also to discrete functions and to functions of several variables. Let consider the function  $z(x)$ , which is dependent on a stochastic (or random) variable  $x$ . Its *mean*, or *expected value*, or *population mean* is

$$\langle z \rangle = \int_a^b z(x) f(x) dx \quad \text{Equation 2-3}$$

where  $f(x)dx$  is the *probability* the random variable  $x$  has a value within  $dx$  about  $x$ .

The function  $f(x)$  is the *Probability Density Function*<sup>8</sup> (PDF) of a stochastic variable and has the following properties:

1. it is defined on an interval  $[a, b]$ , where  $b > a$ ;
2. it is non-negative on that interval, although it can be zero for some  $x \in [a, b]$ ;
3. it is normalized, i.e. the integral of  $f(x)$  over the interval  $[a, b]$  is equal to 1.

Here, it is assumed that values of  $x$  are in the range  $[a, b]$ , where  $a$  and  $b$  represent real numbers or infinite limits and the intervals can be either closed or open. The integral defined by

$$F(x) = \int_a^x f(x') dx' \quad \text{Equation 2-4}$$

where  $f(x)$  is a PDF over the interval  $[a, b]$  and  $F(x)$  is called the *Cumulative Distribution Function* (CDF) of  $f(x)$ . Note that, from this definition, a CDF has the following properties:

1.  $F(a)=0$ ;
2.  $F(b)=1$ ;
3.  $F(x)$  is monotone increasing, because  $f(x)$  is always non-negative.

The CDF is a direct measure of probability. The value  $F(x_i)$  represents the probability that a random sample of the stochastic variable  $x$  will assume a value between  $a$  and  $x_i$ , i.e.,  $\text{Prob}\{a \leq x \leq x_i\} = F(x_i)$ .

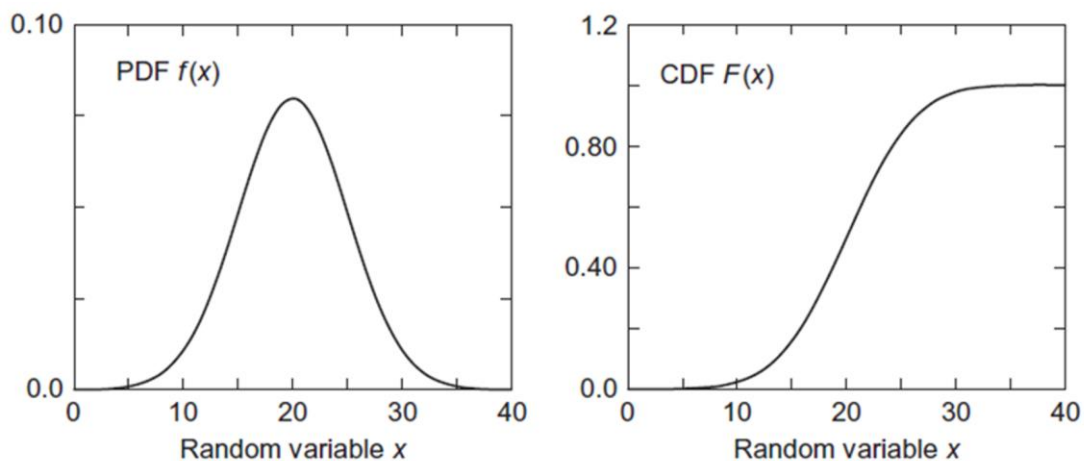


Figure 2-1 - The PDF and CDF for the normal or Gaussian distribution with  $\mu=20$  and  $\sigma=5$ .

<sup>8</sup> A PDF is a density function, i.e., it specifies the probability per unit of  $x$ , so that  $f(x)$  has units that are the inverse of the units of  $x$ .

A vast number of physical problems involve the evaluation of integral expressions such as Equation 2-3. The evaluation of  $\langle z \rangle$  from Equation 2-3 is far from the most complex problem to which Monte Carlo can be applied. However, it serves as a useful simple problem that allows to demonstrate, discuss and understand many of the essential features of the Monte Carlo. It will be shown later how Monte Carlo can be applied to problems with much more complexity than that of Equation 2-3. In this section, let consider the case in which the form of the integral of Equation 2-3 is known but the value of the integral is too difficult to be evaluated analytically. A quadrature scheme estimates the value of  $\langle z \rangle$  by constructing a summation of weighted evaluations of the integrand, namely,

$$\langle z \rangle \cong \sum_{i=1}^N \omega_i z(x_i) f(x_i) \quad \text{Equation 2-5}$$

Monte Carlo is a technique for estimating expected values, but since these can be expressed as integrals and almost any integral can be interpreted as an expectation, Monte Carlo can be used to estimate the values of definite integrals<sup>9</sup>. In the Monte Carlo approach to numerical quadrature, the abscissas are chosen randomly according to the PDF  $f(x)$  and the expected value is estimated from a sum such as in Equation 2-5. Explicitly, the straightforward Monte Carlo quadrature scheme proceeds as follows:

- generate  $N$  values  $\{x_i\}$  of the random variable  $x$  from the PDF  $f(x)$ ;
- define the quadrature abscissas as the sampled values  $\{x_i\}$ ;
- form the arithmetic average of the corresponding values of  $z(x)$ , i.e.,

$$\bar{z} \cong \frac{1}{N} \sum_{i=1}^N z(x_i) \quad \text{Equation 2-6}$$

where  $\bar{z}$  is the *sample mean* of a function  $z$  of a random variable  $x$ , that is an estimate of the population mean  $\langle z \rangle$  obtained from a finite number of  $N$  samples or “*histories*”. Note that the terms in the summation of Equation 2-6 do not include the PDF. In effect, the weight factors in this basic Monte Carlo scheme are of the form

$$\omega_i = \frac{1}{N \cdot f(x_i)} \quad \text{Equation 2-7}$$

Suppose one has to evaluate an integral such as in Equation 2-1 which is not in the

---

<sup>9</sup> The simple estimation of integrals by Monte Carlo has sometimes been called *deterministic* Monte Carlo to distinguish it from *probabilistic* or *analog* Monte Carlo.

form of an expected value. Such integral can be converted into the same form as Equation 2-3, for example, by rewriting the integral as

$$I = \int_a^b g(x)dx = (b-a) \int_a^b \frac{g(x)}{(b-a)} dx = (b-a) \int_a^b g(x)f(x)dx \quad \text{Equation 2-8}$$

$$I \cong \bar{I} = \frac{b-a}{N} \sum_{i=1}^N g(x_i) \quad \text{Equation 2-9}$$

In general, the expected value of a function  $z(x)$  with respect to a function  $h(x)$  can be expressed as follows

$$\langle z \rangle = \frac{\int_a^b z(x)h(x)dx}{\int_a^b h(x)dx} \quad \text{Equation 2-10}$$

Equations such as Equation 2-10, that it is not other than an integral average, can also be written in the form of Equation 2-3 by a simple normalization procedure as follows

$$M = \int_a^b h(x)dx \quad \text{Equation 2-11}$$

$$\langle z \rangle = \int_a^b z(x) \frac{h(x)}{M} dx \equiv \int_a^b z(x)f(x)dx \quad \text{Equation 2-12}$$

which is in the form of Equation 2-3 and thus can be estimated by Monte Carlo. This procedure may seem forced, because, if the integral of Equation 2-11 could be evaluated without Monte Carlo, then the integral in Equation 2-12 most likely could also be evaluated without Monte Carlo. However, this example merely is intended to demonstrate that Monte Carlo can be applied, in principle, to the evaluation of any definite integral. Further,  $\langle z \rangle$  could be estimated by using Monte Carlo to estimate both integrals in Equation 2-10 separately, i.e.,  $M$  could be evaluated by the basic Monte Carlo estimator as in Equation 2-9, where the  $\{x_i\}$  are sampled from the PDF  $1/(b-a)$ , and then  $\langle z \rangle$  could be estimated as in Equation 2-6, where the  $\{x_i\}$  are sampled from  $f(x)=h(x)/M$ . Thus, Monte Carlo can be applied to many problems indeed. Monte Carlo quadrature is not limited to estimate single integrals: in fact, Monte Carlo demonstrates its superiority to many other quadrature schemes when the integrals are highly multidimensional. Regardless of the *number of dimensions*  $m$ , the precision of the Monte Carlo estimator varies at worst as  $N^{1/2}$ , where  $N$  is the number of samples. Traditional quadrature rules, with prescribed abscissas and weights, have precisions that vary as  $N^{1/m}$  (Mosegaard & Sambridge, 2002). Hence,

Monte Carlo is superior to other quadrature schemes for integrals of dimension greater than two<sup>10</sup>!

Two important measures of any PDF  $f(x)$  are its population mean  $\mu(z)$  (the expected or average value of the function  $z(x)$  as defined in Equation 2-3) and *population variance*  $\sigma^2(z)$ . The variance of a random variable  $z(x)$  is defined<sup>11</sup> as

$$\sigma^2(z) = \langle [z(x) - \langle z \rangle]^2 \rangle = \int_a^b [z(x) - \langle z \rangle]^2 f(x) dx = \langle z \rangle^2 - \langle z \rangle^2 \quad \text{Equation 2-13}$$

Finally, the *standard deviation*  $\sigma(z)$  is defined as the square-root of the variance. From Equation 2-13 it is seen that the population variance  $\sigma^2(z)$  depends on  $\varpi$ , which often is not known. Thus, one must estimate the population variance with what is called the sample variance. To estimate the variance we can use Equation 2-6 by replacing the function  $z$  with  $[z-\varpi]^2$  obtaining

$$\sigma^2(z) \cong \frac{1}{N} \sum_{i=1}^N [z(x_i) - \langle z \rangle]^2 \quad \text{Equation 2-14}$$

However,  $\varpi$  is unknown that is, after all, what is being sought. What is usually done is to approximate  $\varpi$  by  $\bar{z}$ . This estimate of  $\sigma^2(z)$  with  $\varpi$  approximated by  $\bar{z}$  is called the *sample variance* and is denoted by  $s^2(z)$ . However, in replacing  $\varpi$  by  $\bar{z}$ , one degree of freedom has been used and, for reasons discussed below, the  $N$  in Equation 2-14 is, by convention, replaced by  $N-1$ . Thus, the sample variance is defined as

$$s^2(z) \equiv \frac{1}{N-1} \sum_{i=1}^N [z(x_i) - \bar{z}]^2 \quad \text{Equation 2-15}$$

The number of *degrees of freedom*<sup>12</sup>  $\nu$  is an often used but not always well understood parameter. In applications such as that being considered, where there

<sup>10</sup> Remember that the Transport Boltzmann's equation is, in its complete form, a 7-dimensions equation (3 variables for the position, 2 for the direction vector, 1 for energy and 1 for time)

<sup>11</sup> See (Dunn & Shultis, 2012) for the demonstration of the relationship.

<sup>12</sup> The original  $N$  samples were unconstrained (they were drawn independently) and, thus, in calculating the sample mean  $c=0$  and  $\nu=N$ ,  $N$  is used in the denominator of Equation 2-6. However, in forming the sample variance, one of the values of  $[z(x_i)-\varpi]^2$  is constrained ( $c=1$ ) by using  $\varpi$  to estimate  $\bar{z}$ . The differences in  $N-1$  cases are independent of each other; they are random samples from which a constant has been subtracted. However, the remaining difference must assume a constrained value, that value being the value that assures that the samples produce  $\bar{z}$ . In this sense, the sample mean used one degree of freedom and so  $c=1$  and  $\nu=N-1$ .

are  $N$  independent samples, the number of degrees of freedom is simply the number of independent variables less the number of *constraints*  $c$ .

In most Monte Carlo applications multiple random variables are involved that often depend on each other. Similar equations, as the ones reported above for a single random variable, can be obtained in a multidimensional approach for an array of  $n$  random variables  $\mathbf{x} = \{x_1, x_2, \dots, x_n\}$ . Hence, the Monte Carlo estimation of  $\varpi \pm \sigma(z)$  is calculated as

$$\begin{aligned} \langle z \rangle \pm \sigma(z) &= \int_V z(\mathbf{x})f(\mathbf{x})d\mathbf{x} \pm \sqrt{\int_V (z - \langle z \rangle)^2 f(\mathbf{x})d\mathbf{x}} \\ &\cong \bar{z} \pm \sqrt{\frac{\bar{z}^2 - \bar{z}^2}{N}} \end{aligned} \quad \text{Equation 2-16}$$

where the function  $f(\mathbf{x})$  is the *joint probability density function* of  $\mathbf{x}$  and  $V$  is the volume over which  $\mathbf{x}$  is defined.

Finally, it is important to discuss the real heart of the MCM that allows to use the equations reported above to find a solution that is the closest as possible to the real solution. Monte Carlo is based on two fundamental statistical results: the *law of large numbers* and the *central limit theorem* (CTL). As we have seen, Monte Carlo analysis is useful to calculate an expected value  $\varpi$  using its approximation  $\bar{z}$ . The law of large numbers states that, as long as the mean exists and the variance is bounded

$$\lim_{N \rightarrow \infty} \bar{z} = \langle z \rangle \quad \text{Equation 2-17}$$

This law states that eventually the normalized summation of Equation 2-6 approaches the expected value of Equation 2-3. Here, the quadrature nodes  $x_i$  are “sampled” from the PDF  $f(x)$  and the quadrature weights are equal to  $1/Nf(x)$ . One of the important features of Monte Carlo is that it allows to obtain both an estimate of an expected value (by the law of large numbers) and its uncertainty (by the central limit theorem). The Central Limit theorem states that for large values of  $N$ , the distribution of averages (normalised sum  $\bar{z}$ ) of  $N$  independent random variables identically distributed (according to any distribution with mean  $\varpi$  and variance  $\sigma^2(z) \neq \infty$ ) tends to a normal distribution with mean  $\varpi$  and variance  $\sigma^2(z)/N$ . In other words, “Given any observable  $A$ , that can be expressed as the result of a convolution of random processes, the average value of  $A$  can be obtained by sampling many values of  $A$  according to the probability distribution of the random processes” (Fassò, et al., 2009). The accuracy of MC estimator depends on the number of samples, that is

$$\sigma \propto \frac{1}{\sqrt{N}} \quad \text{Equation 2-18}$$

In an analogue Monte Carlo calculation, not only the mean of the contributions converges to the mean of the actual distribution, but also the variance and all moments of higher order:

$$\lim_{N \rightarrow \infty} \left[ \frac{\sum_1^N (z(x_i) - \langle z \rangle)^n}{N} \right]^{1/n} = \sigma_n \quad \text{Equation 2-19}$$

Then, partial distributions, fluctuations and correlations are all faithfully reproduced: in this case (and in this case only!) there is a real simulation (Fassò, et al., 2009).

## 2.2 The FLUKA code

### 2.2.1 FLUKA

In this work, the FLUKA code (Bohlen, et al., 2014; Ferrari, et al., 2005) was used to perform all the simulations. FLUKA is a fully integrated particle physics Monte Carlo simulation package. FLUKA is a general purpose tool for calculations of particle transport and interactions with matter, covering an extended range of applications spanning from proton and electron accelerator shielding to target design, calorimetry, activation, dosimetry, detector design, Accelerator Driven Systems, cosmic rays, neutrino physics, radiotherapy, radiobiology. It was developed and it is maintained under an INFN-CERN agreement. The highest priority in the design and development of FLUKA has always been the implementation and improvement of sound and modern physical models. Microscopic models are adopted whenever possible, consistency among all the reaction steps and/or reaction types is ensured, conservation laws are enforced at each step, and results are checked against experimental data at single interaction level. As a result, final predictions are obtained with a minimal set of free parameters fixed for all energy/target/projectile combinations. Therefore results in complex cases, as well as properties and scaling laws, arise naturally from the underlying physical models, predictivity is provided where no experimental data are directly available, and correlations within interactions and among shower components are preserved. The FLUKA physical models are described in several journal and conference papers (Fassò, et al., 2003; Ferrari, 2006; Battistoni, et al., 2007; Fassò, et al., 1995); on the technical side the stress has been put on four apparently conflicting requirements, namely efficiency, accuracy, consistency and flexibility. FLUKA can simulate with high accuracy the interaction and propagation in matter of about 60 different particles, including

photons and electrons from 1 keV to thousands of TeV, neutrinos, muons of any energy, hadrons of energies up to 20 TeV and all the corresponding antiparticles, neutrons down to thermal energies and heavy ions. The program can also transport polarised photons (e.g., synchrotron radiation) and optical photons. Time evolution and tracking of emitted radiation from unstable residual nuclei can be performed online. FLUKA can handle even very complex geometries, using an improved version of the well-known Combinatorial Geometry (CG) package. The FLUKA CG has been designed to track correctly also charged particles (even in the presence of magnetic or electric fields). Various visualization and debugging tools are also available. For most applications, no programming is required from the user. However, a number of user interface routines (in Fortran 77) are available for users with special requirements (FLUKA, 2010).

For many years FLUKA has been known as one of the main tools for designing shielding of proton accelerators in the multi-GeV energy range (its hadron event generator has been adopted by the majority of the existing high-energy transport codes, including those used for particle physics simulations). In the last years, however, FLUKA has gone through an important process of transformation which has converted it from a specialized to a multi-purpose program, not restricted to a limited family of particles or to a particular energy domain. If in its original high energy field FLUKA has few competitors, this is not the case in the intermediate and in the low energy range, where several well established transport codes exist. However, FLUKA can compare favourably with most of them, thanks to some important assets. One of them is the adoption of modern physical models, especially in the description of nuclear interactions. Some of these models have even been updated and extended with original contributions. Other advantages are the special care devoted to low-energy electromagnetic effects and the accurate combined treatment of multiple scattering and magnetic fields near material boundaries, essential for a correct simulation of many synchrotron radiation problems (Fassò, et al., 1995). In the last years, FLUKA has been widely used in the medical field to study different kinds of applications (Battistoni, 2012; Mairani, et al., 2013; Sommerer, et al., 2009; Parodi, et al., 2007a; Parodi, et al., 2007b; Infantino, et al., 2011; Infantino, et al., 2015a): even if FLUKA has been validated in the high energy range (Brugger, et al., 2004; Brugger, et al., 2006; Brugger, et al., 2007) no specific validations in the energy range of medical application have been published. As it will be shown in the following, in this work a carefully validation of FLUKA, in terms of physical and transport parameters, was conducted in the energy range of interest in the medical field.

FLUKA reads user input from an ASCII text file with extension *“.inp”*. The input consists of a variable number of *“commands”* (called also *“options”*), each consisting of one or more *“lines”* (called also *“cards”* for historical reasons). Each card contains one keyword (the name of the command), six floating point values called *WHATs*

and one character string called *SDUM*. The typical structure of a FLUKA input file is the following (Ferrari, et al., 2005):

- Titles and comments for documentation purposes (optional, but recommended)
- Description of the problem geometry (solid bodies and surfaces, combined to partition space into regions), (mandatory)
- Definition of the materials (mandatory unless pre-defined materials are used)
- Material assignments (correspondence material–region, mandatory)
- Definition of the particle source (mandatory)
- Definition of the requested “detectors”. Each of these is a phase space domain (region of space, particle direction and energy) where the user wants to calculate the expectation value of a physical quantity such as dose, fluence, etc. Various kinds of detectors are available, corresponding to different quantities and different algorithms used in the estimation (“estimators”). Detectors are optional, but one at least is expected, at least in the production phase
- Definition of biasing schemes (optional)
- Definition of problem settings such as energy cut-offs, step size, physical effects not simulated by default, particles not to be transported, etc. (optional)
- Initialisation of the random number sequence (mandatory if an estimation of the statistical error is desired)
- Starting signal and number of requested histories (mandatory)

In addition, special commands are available in FLUKA for more advanced problems involving magnetic fields, time-dependent calculations, writing of history files (so-called “collision tapes”), transport of optical photons, event-by-event scoring, calling user-written routines, etc. Details on the cards, the setup and the parameters used in this work will be given in the following chapters contextually to their use.

### 2.2.2 *Flair*

Flair (Vlachoudis, 2009) is an advanced user graphical interface for FLUKA, to enable the user to start and control FLUKA jobs completely from a GUI environment without the need for command-line interactions. It is an integrated development environment (IDE) for FLUKA, it does not only provide means for the post processing of the output but a big emphasis has been set on the creation and checking of error free input files. It contains a fully featured editor for editing the input files in a human readable way with syntax highlighting, without hiding the inner functionality of FLUKA from the users. It provides also means for building the executable, debugging the geometry, running the code, monitoring the status of one or many

runs, inspection of the output files, post processing of the binary files (data merging) and interface to plotting utilities like gnuplot and PovRay for high quality plots or photorealistic images. The program includes also a database of selected properties of all known nuclides and their known isotopic composition as well a reference database of ~300 predefined materials together with their Sterheimer parameters (Vlachoudis, 2009). Flair is also provided with a built-in Geometry Editor that allows for working on 2D cross sections of the geometry, the interactive visual editing of the geometry in 2D, debugging of bodies/regions in a graphical way and a fast 3D rendering of the geometry.

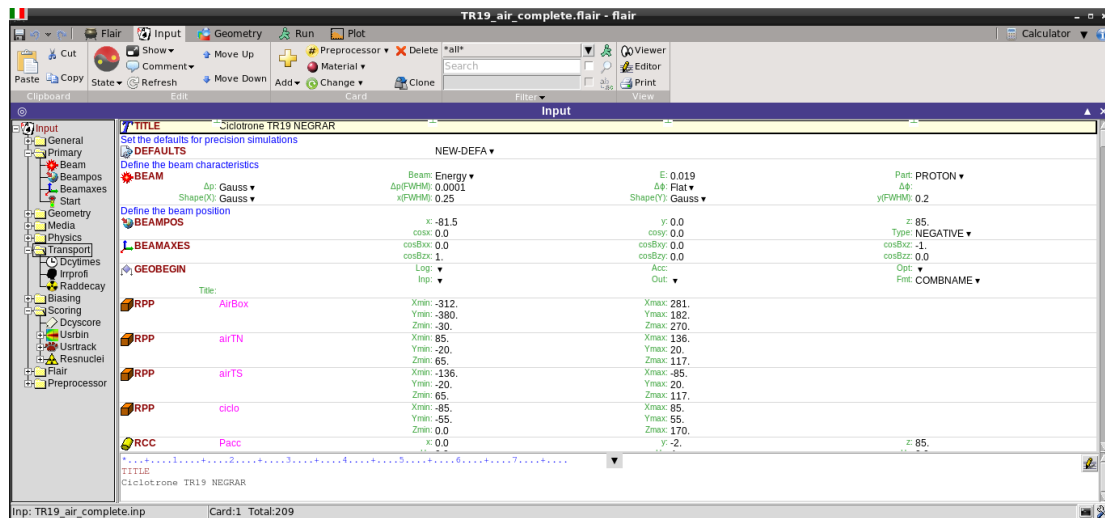


Figure 2-2 - The FLUKA graphical interface Flair (v 2.0-8).

### 2.2.3 SimpleGeo

SimpleGeo (Theis, et al., 2006) is an interactive 3D solid modeler which allows for flexible and easy creation of the models via drag & drop, as well as on-the-fly inspection. In addition it includes new debugging facilities, based on stochastic as well as deterministic methods, in order to validate the created geometry with immediate visual feedback of problematic regions. While the developing and the maintenance of Flair is strictly connected to the development of FLUKA, SimpleGeo is an independent project developed at CERN and specifically created to unify the various geometry modelling processes and syntaxes of radiation transport codes (Polz, 2014). Furthermore, even if with the last releases of Flair the potential of the geometry editor was continuously increased, SimpleGeo still remains very helpful in the developing of complex geometries. Implementing geometries for particle transport problems is one of the major time consuming tasks. The common approach of radiation transport codes is based on Constructive Solid Geometry (CSG) and requires textual input of the Boolean geometry tree. This makes the creation of models a tedious and error prone task, which is especially hard to master

for novice users. SimpleGeo allows the user to interactively build geometries using a number of basic primitives that are connected by boolean operations. To facilitate and enable parametric modeling SimpleGeo has a built in scripting language which can be used for procedural modeling. This language has access to most parts of the modeling kernel and thus, allows the user to implement additional specific functionality himself. SimpleGeo currently allows for importing and viewing of FLUKA (old and new syntax); in addition new geometries can be created from scratch and exported to FLUKA. A number of plugins are under development to extend the functionality of SimpleGeo beyond solid modeling. The plugins used in this work are the DaVis3D, which allows for displaying data on top of the geometry as well as data extraction and export to finite element software COMSOL, and the PipsiCAD 3D, which allows to display particle tracks in 3D, superimposed on top of the geometry.

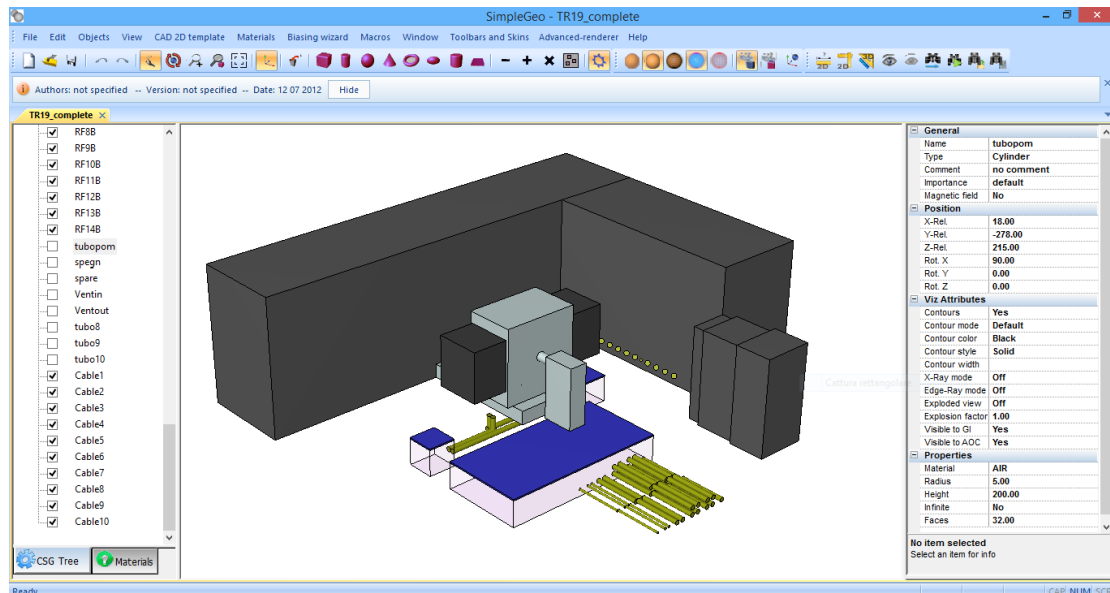


Figure 2-3 - Interface of the 3D solid modeler SimpleGeo (v 4.3.3).

# **Chapter 3**

## **Monte Carlo Model of the GE PETtrace Cyclotron**

### **3.1 The GE PETtrace Cyclotron**

The cyclotron used in the experimental tests and to which simulations setup refers, was a PETtrace (GE Medical System), a compact cyclotron with vertical acceleration plane, capable of accelerating negative hydrogen  $H^-$  and deuterium  $D^-$  ions up to an energy of 16.5 and 8.4 MeV respectively. Maximum beam intensity of 100  $\mu\text{A}$  and 60  $\mu\text{A}$  can be achieved (after a recent hardware upgrade) for hydrogen and deuterium ions respectively. The cyclotron is installed and used in the "S. Orsola-Malpighi" University Hospital (Bologna, IT) for the routine production of PET radionuclides. The beam of accelerated particles can be directed on one of the 6 output ports available. The cyclotron is equipped with several target assembly, the components in which nuclear reactions happen, for the routine production of the main radionuclides of interest for PET such as  $^{11}\text{C}$ ,  $^{13}\text{N}$ ,  $^{18}\text{F}$ ,  $^{18}\text{F}_2$  and  $^{64}\text{Cu}$ ; in addition production of non-standard radionuclides, such as  $^{89}\text{Zr}$  and  $^{99\text{m}}\text{Tc}$ , are conducted for research purposes. The cyclotron is able to operate in a *dual beam* condition, i.e. two target assembly can be irradiated at the same time.

In the following, details of the different cyclotron subsystems will be given; further information can be found in the accelerator manual (GE MEDICAL SYSTEMS, 2004). The PETtrace can be divided into several subsystems:

1. Magnet System;
2. Radio-Frequency (RF) System;
3. Ion Source System;
4. Beam Extraction System;
5. Beam Diagnostic System;
6. Vacuum system;
7. Target System

8. Secondary Water Cooling System
9. Power Distribution System

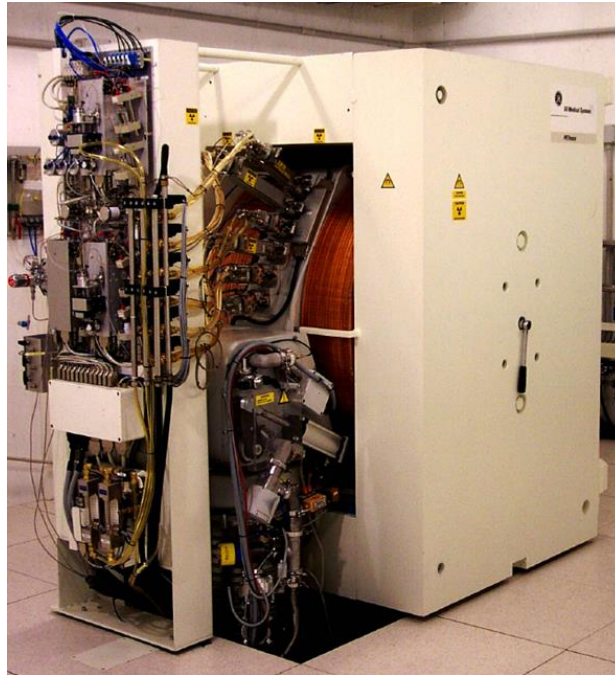


Figure 3-1 - The GE PETtrace cyclotron installed at "S. Orsola-Malpighi" Hospital.

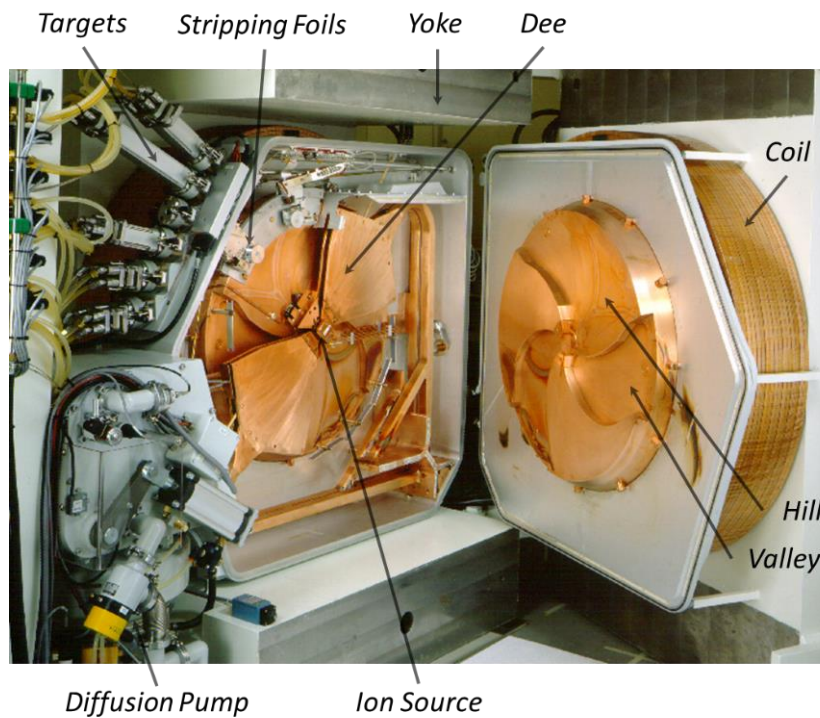


Figure 3-2 - Overview of the vacuum chamber and the main components of the GE PETtrace cyclotron.

The bearing structure of the magnet yoke is made of standard industrial steel with low content of carbon (<0.18%); the poles of the magnet, that are also of steel with a low carbon content (<0.05%), are a single piece forged. The poles of the magnet are divided into two different areas, the *hills* and *valleys*, the last ones created by removing radial sectors of the magnet. The magnetic field is induced by magnet coils made of hollow-core copper conductors inside which demineralized water circulates for refrigeration. A stabilized power supply (PSMC) provides the required current for the Magnet System. The magnet is vertically oriented. One of the side yokes, including the pole, is supported on hinges and can be opened like a door to provide access to the interior of the vacuum chamber.

The particles are accelerated by applying radio-frequency power to two resonators (*Dees*) within the vacuum chamber. The RF power is generated and transmitted by the RF System, comprising the following main parts:

- RF Power Generator (RFPG)
- RF Feeder Cable
- RF Cavity (RCAV)

The RFPG contains all of the necessary systems for providing RF power to the resonators including a highly stable frequency generator, preamplifier and power amplifier with associated output matching network to the feeder cable and dee voltage feedback control. The RFPG also includes a safety and interlock system. The RF power is fed to the resonators through a coaxial transmission line, the RF Feeder Cable. The two resonators are formed by two 75° Dees and supporting stems together with the cavity created by the cyclotron Vacuum Chamber and magnet pole faces. Finally, the RF system is controlled by the *Accelerator Control Unit (ACU)*.

The ion source is located in the center of the cyclotron and it is a cold-cathode-type *Penning ion gauge (PIG)* source. The ion source contains two separate chimneys, one for the production of  $H^-$  and the other for the  $D^-$ ; both particles are produced through the same technique. Within a cylindrical chamber, an electrical discharge is produced by a potential difference applied between the anode (side surface of the cylinder), connected to the ground, and two cathodes (bases of the cylinder), to which a negative voltage is applied while one of the source gasses, hydrogen or deuterium, is flowing. The plasma of ions and electrons which is created remains confined inside the chamber for the presence of the magnetic field. On one side of the chamber there is a small slit: the  $H^-$  or  $D^-$  ions exit the chamber when a positive voltage is applied to the dee which is located close to the slit. The slits for the two types of particles are located at opposite positions: the  $H^-$  are extracted from the dee mounted in the lower part of the cyclotron, while the  $D^-$  are extracted in the upper part.

The extraction of the beam is based on the *stripping foil* technique. Two electrons of the accelerating negative ions are stripped out during the passage of the beam through a thin foil of carbon (3  $\mu\text{m}$  thick). The charge of the accelerated particles changes from negative to positive, involving a change of the direction of rotation of the beam. The electrons collected by the foil allow a constant monitoring of the beam current. The PETtrace is equipped with two extraction units each of which can extract the beam to three of the six output ports. The extraction units slide on a curved rail mounted along the radius of extraction. Each foil carousel contains 6 carbon foils mounted on a revolver; The ACU automatically selects a new foil in case of a foil rupture by rotating the carousel. Having two extraction units allows the PETtrace to operate in *dual beam* in which two targets are irradiated simultaneously. The stripping foil technique allows an efficiency of extraction of the beam equal to 100%.

The Diagnostic System monitors the beam current at different positions within the cyclotron and in the Target System to control the beam intensity from the Ion Source to the target. The system includes a *flip-in probe* positioned at a small radius of the orbit of acceleration, the stripping foil, a collimator pair and the body of the target. All these systems are isolated from the ground to allow a correct measure of current. The internal flip-in probe located at a small radius, closed to the ion source, allows the beam current monitoring at the beginning of the irradiation. The extraction foils, in addition to changing the direction of rotation, allow a constant monitoring of the beam intensity, measuring the current created by the electrons stripped out from the negative accelerated ions. The collimators, a pair of foils in graphite, are placed in the inner part of the output ports and are used to center the beam by cutting each non-aligned tail. The body of the target, made of aluminum, is isolated from the ground to allow the measure of the effective current present on the target material during the production of radioisotopes. All the useful signals for the beam monitoring are connected to the multichannel Current Beam Analyzer (BCA).

The second  $H^-$  electron is fairly weakly bound (0.755 eV) and so may be lost due to interaction with the background gas (vacuum stripping), or by electro-magnetic disassociation. This lost beam causes heating and induces significant radioactivity in the cyclotron components. To reduce vacuum stripping, negative ion cyclotrons need to operate at vacuum pressures at least one order of magnitude better than positive machines (Milton, 1996). The vacuum is made with the aid of two pumps, a *rotary pump* to generate the pre-vacuum and a *diffusion pump* to bring the vacuum inside the chamber in optimum working conditions. The pumps are connected to the acceleration chamber of the cyclotron through a high-vacuum valve. To measure the wide range of pressure inside the vacuum chamber two pressure switches are installed: the Pirani pressure switch, capable of measuring pressures from 1 bar to  $10^3$  mbar and the Penning pressure switch for the measurement of high vacuum (<

$10^3$  mbar). The vacuum system is fully automated and controlled by the Vacuum Control Units (VCU) that constantly works.

When the particle beam has passed the selected extraction foil, it hits the corresponding target at the cyclotron beam exit. The targets, in terms of the total assembly, are mounted on a flange at the front of the cyclotron. The particle beam hits and transfers its energy to the target material and thus the nuclear reactions (required for the radionuclides production) take place. In the standard configuration, the cyclotron has six beam exit ports. Each beam exit is equipped with a vacuum gate valve (*Beam Exit Valve* or BEV) and a conical fitting for the target body. The target is locked into position by quick connections. All external connections to the targets, target pressure transducers and liquid target fillers (LTF) are located at the Target Panel. The Target Panel is mounted in front of the cyclotron, close to the targets. The Helium Cooling System is a closed system, which facilitates cooling of the target foils. The system includes the piping and valves for gas distribution, a heat exchanger, and a compressor for high-speed recirculation of the helium gas.

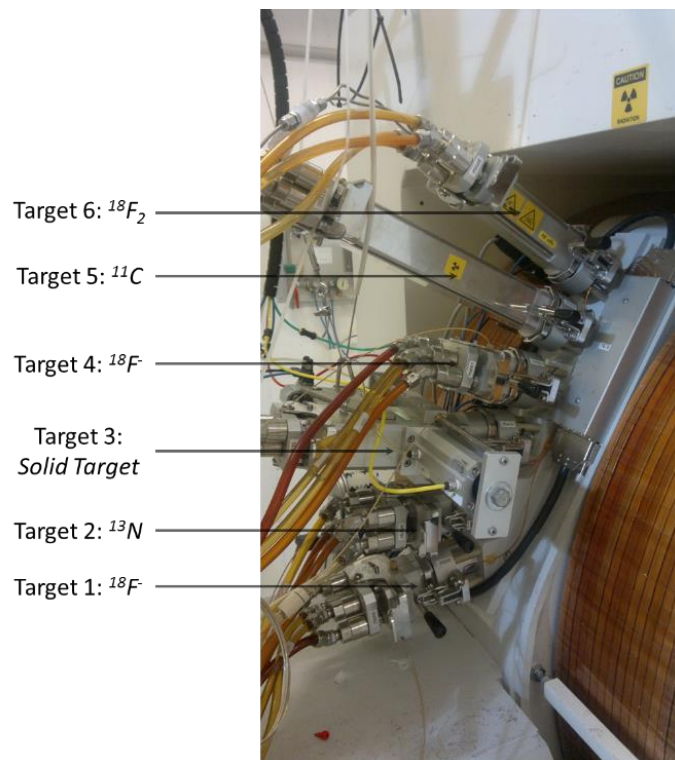


**Figure 3-3 - Targets currently mounted on the GE PETtrace cyclotron.**

Each target consists of a front flange for the connection to the cyclotron, a Helium cooling flange, a chamber where the target material is placed and a rear flange for connection to the different cooling and sorting supports. The front flange guides the target in the correct mounting position; all the targets can be easily installed and removed with a lever, which simplifies operations. The target chamber is separated

from the vacuum chamber of the cyclotron by two thin Havar™ foils (42.5% Co, 20% Cr, 17.86% Fe, 13% Ni, 2.8% W, 2% Mo, 1.6% Mn, 0.2% C, 0.04% Be), a non-magnetic resistant alloy. During the irradiation, helium circulates between the two Havar™ foils at a pressure of about 0.5 MPa, which allows the cooling of the metallic foils. The target material can be liquid, gaseous or solid depending on the nuclide to produce. The design and the type of material used for the construction of various targets is made in order to dissipate the heat developed by the interactions, to withstand the intense radiation beam to which the whole body of the target is subjected and especially to maximize the nuclear reaction of interest. The aluminum is chosen due to the excellent properties of activation of the metal, in fact, the activation products have a short half-life and are relatively few compared to those generated in alternative metals. The aluminum has a good ductility and a high thermal conductivity (247 W K m<sup>-1</sup>). All target supports (target material, water to cool the body of the target, helium for the cooling of the metallic foils) enter and leave the target through the rear flange. Because the target is made up of several pieces assembled together it is crucial to ensure an adequate sealing. The seal is obtained by interposing O-rings of plastic material, such as Viton, or metal (Helicoflex) between the surfaces. The GE PETtrace installed at "S. Orsola-Malpighi" University Hospital is equipped with an experimental solid target station, developed locally (Cicoria, et al., 2006).

The Secondary Water Cooling System provides a closed loop with deionized cooling water for the Cyclotron subsystems. This system consists of the Secondary Water Cooling Unit, which continuously deionizes the water, and two water manifolds that distribute the cooling water. A primary system for the cooling of the Secondary Cooling Unit must be provided by the customer. The Primary Cooling

**Table 3-1 - Main features of the radionuclides produced routinely and for research purpose at "S. Orsola-Malpighi" Hospital.**

<b>Target</b>	<b>Target Material (form)</b>	<b>Nuclear Reaction</b>	<b>Half-time</b>	<b>Chemical Form</b>
<i>Routine Production</i>				
<sup>18</sup> F	H <sub>2</sub> <sup>18</sup> O (liquid)	<sup>18</sup> O(p,n) <sup>18</sup> F	110 min	[ <sup>18</sup> F]F <sup>-</sup>
<sup>11</sup> C	N <sub>2</sub> + 1% O <sub>2</sub> (gas)	<sup>14</sup> N(p,α) <sup>11</sup> C	20 min	[ <sup>11</sup> C]CO <sub>2</sub>
<b>Solid Target</b>	<sup>64</sup> Ni (solid)	<sup>64</sup> Ni(p,n) <sup>64</sup> Cu	12.7 h	[ <sup>64</sup> Cu]Cu
<i>Available Routine Production</i>				
<sup>13</sup> N	H <sub>2</sub> O (liquid)	<sup>16</sup> O(p,α) <sup>13</sup> N	10 min	[ <sup>13</sup> N]NO <sub>x</sub>
<sup>15</sup> O	N <sub>2</sub> (gas)	<sup>14</sup> N(d,n) <sup>15</sup> O	2 min	[ <sup>15</sup> O]O <sub>2</sub>
<sup>18</sup> F <sub>2</sub>	<sup>20</sup> Ne + 1% F <sub>2</sub> (gas)	<sup>20</sup> Ne(d,α) <sup>18</sup> F	110 min	[ <sup>18</sup> F]F <sub>2</sub>
<i>Research Production</i>				
<b>Solid Target</b>	<sup>89</sup> Y (solid)	<sup>89</sup> Y(p,n) <sup>89</sup> Zr	78.4 h	[ <sup>89</sup> Zr]Zr
<b>Solid Target</b>	<sup>nat</sup> Mo or <sup>100</sup> Mo (solid)	<sup>100</sup> Mo(p,2n) <sup>99m</sup> Tc	6.01 h	[ <sup>99m</sup> Tc]Tc

System can consist of a water cooling tower or a refrigeration system. There should be a temperature regulation system in the Primary Cooling System to control the temperature of the Secondary Cooling System. Start-up and shutdown of the Secondary Water Cooling System is done automatically by the Control System. Flow switches in all of the secondary circuits provide interlock signals to the ACU.

The Mains Distribution Panel (MDP) handles the distribution of mains power to PETtrace subsystems, including the Power Distribution Unit. The Power Distribution Unit (PDU) handles the distribution of mains power to subsystems as the Vacuum System, the Helium Compressor (Target System), the Magnet door and others. The Accelerator electronics and power supplies are housed in equipment cabinets placed in the technical room outside the cyclotron vault.

The PETtrace system is computer-controlled. The Control System comprises four primary units:

- Master System exercises operational control over the tracer production runs and provides the primary interface between the PETtrace system and its operator.
- Accelerator Control Unit (ACU) provides the control interface between the Master System and the Accelerator.
- Chemistry Control System (CCS) provides the control interface between the Master System and the Radiochemistry System.
- PETtrace Service System (PSS) provides a dedicated maintenance terminal for system service.

### ***3.2 Monte Carlo Model of the GE PETtrace Cyclotron***

During the research period in which this work was conducted, several versions of FLUKA and Flair were released. At the time of writing the thesis, FLUKA 2011.2c.0 was released, while Flair 2.0-8 was available. Regarding the applications studied in this thesis, no significant differences were found between the different releases used. The geometry of the Monte Carlo model of the cyclotron, the target assembly and the cyclotron bunker were created using the solid modeler SimpleGeo version 4.3.3.

In this section the geometry, the definition of the material and the source term, aspects common to all the validation tests performed, will be described while details on the physical and transport parameters and on the scores used will be given contextually in the following subsections.

A detail MC model of the GE PETtrace cyclotron was realized. The model includes the magnet and magnet poles (Iron), the vacuum chamber (Aluminium), an approximation of the coils (Copper) and of the target filling stations panel (LTF) (Lead and Polyethylene), the cyclotron vault and the ducts through the vault walls. Data regarding the dimensions and features the cyclotron and its components were taken from technical sheets and reference manuals of the vendor (GE MEDICAL SYSTEMS, 2004). The geometry was created using simple geometrical entities, called “body”, (such as planes, cylinders and parallelepipeds) to create more complex space regions, called “REGION”, using the Boolean operations union, subtraction and intersection; one material was assigned to each region. The cyclotron was accurately positioned within the model of the vault, carefully reproduced on the basis of the original construction drawings and on measurements in the facility as built. The inner dimensions of the bunker are: 650 cm by 535 cm with a height of 350 cm and with 200 cm thick concrete walls. The target system modelled was the standard GE assembly comprised of a silver chamber filled with [ $^{18}\text{O}$ ]-water to produce Fluorine-18 by a ( $p,n$ ) reaction. The front of the target body (Aluminium) and 25  $\mu\text{m}$  thick Havar™ foils were modeled. The collimator was modeled as shown in Figure 3-8. The upper and lower collimators were modeled as only one piece in graphite, 1 cm thick; the hole in the center is 1 cm in width by 0.8 cm in height.

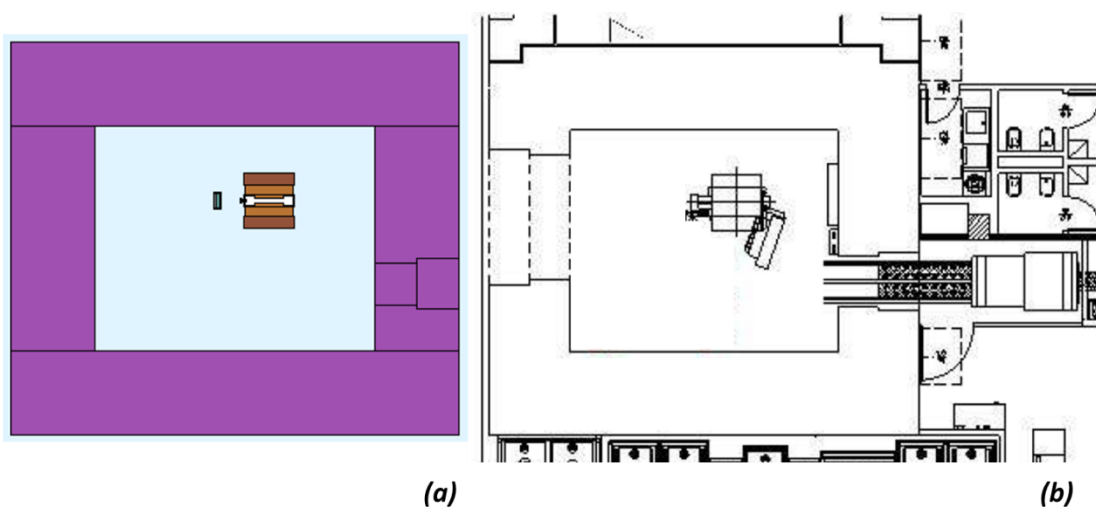
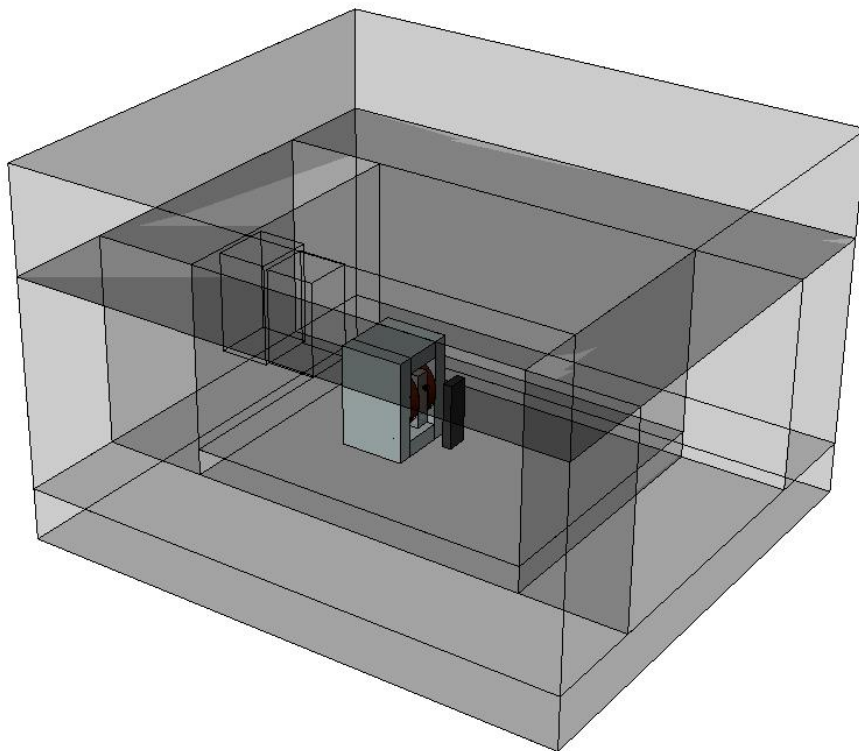
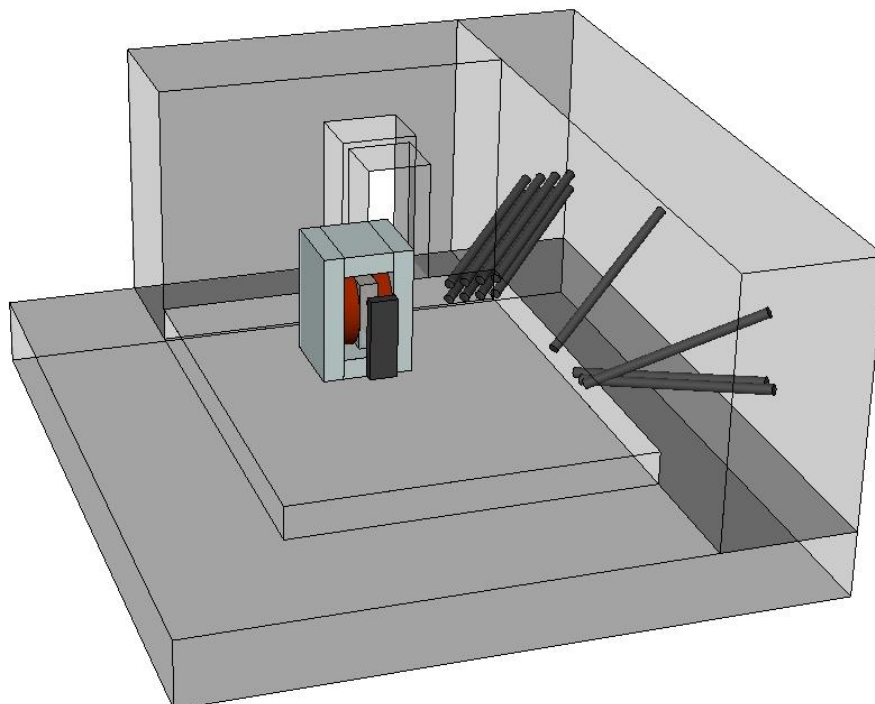


Figure 3-4 – Comparison of the FLUKA MC model of the GE PETtrace cyclotron and the cyclotron vault (a) of “S. Orsola-Malpighi” Hospital with an original technical drawing (b).



**Figure 3-5 – FLUKA Monte Carlo model of the cyclotron bunker of "S. Orsola -Malpighi" Hospital.**



**Figure 3-6 – FLUKA Monte Carlo model of the cyclotron bunker of "S. Orsola -Malpighi" Hospital: detail of the cyclotron and the ducts through the vault walls.**

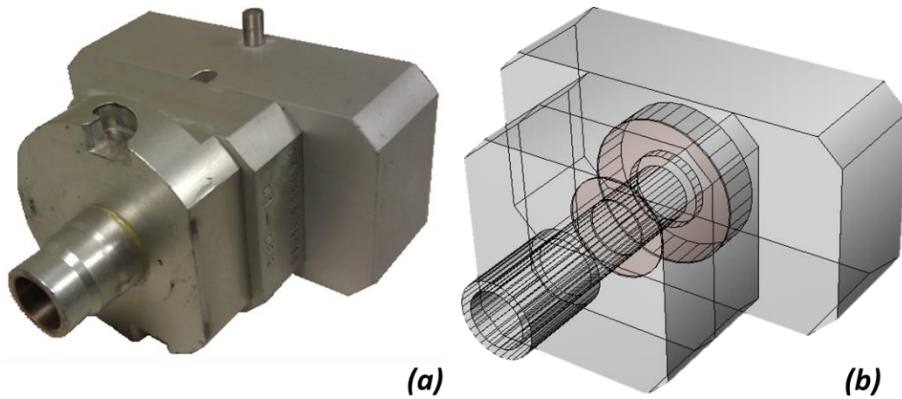


Figure 3-7 – Comparison between the real (a) and modeled (b) <sup>18</sup>F target assembly of the GE PETtrace cyclotron.

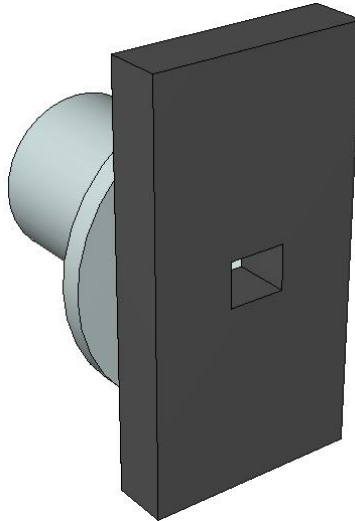


Figure 3-8 – FLUKA MC model of the PETtrace collimator.

Materials were assigned to each *REGION* of the input by a dedicated *ASSIGNMA* card: the assigned material was selected from the Flair material database or created when necessary. The [<sup>18</sup>O]-water material, 97% enriched, was created within Flair using the dedicated *MATERIAL* and *COMPOUND* cards as shown in Figure 3-9.

<b>MATERIAL</b>	Z: 8.	Name: O-18	#	p: 0.001429
		Am: 18.	A: 18.	dE/dx: ▼
<b>LOW-MAT</b>		Mat: O-18 ▼	LowMat: 16O, Oxygen 16, 296K ▼	
Water18O				
<b>MATERIAL</b>	Z:	Name: Water18O	#	p: 1.1
		Am: Water18O ▼	A:	dE/dx: ▼
<b>COMPOUND</b>		Name: Water18O ▼	Mix: Atom ▼	Elements: 1,3 ▼
	f1: 2.0	M1: HYDROGEN ▼	f2: 1.0	M2: O-18 ▼
	f3:	M3: ▼		
<b>MATERIAL</b>	Z:	Name: TarSol	#	p: 1.1
		Am: TarSol ▼	A:	dE/dx: ▼
<b>COMPOUND</b>		Name: TarSol ▼	Mix: Volume ▼	Elements: 1,3 ▼
	f1: 97.0	M1: Water18O ▼	f2: 3.0	M2: WATER ▼
	f3:	M3: ▼		

Figure 3-9 - Definition of the [<sup>18</sup>O]-water material in Flair.

The *LOW-MAT* card allows to assign the cross section of Oxygen-16 to the new created material  $^{18}\text{O}$ .

The composition of the air volume within the bunker was modeled selecting the standard “*AIR*” material from the Flair material database, which mostly refers to the NIST database (NIST, 2014). Composition of the *AIR* material is reported in Table 3-2.

**Table 3-2 - Composition of “Air, Dry (near sea level)” as reported from NIST database.**

<b>Element</b>	<b>Fraction by weight</b>
C	0.000124
N	0.725267
O	0.231781
Ar	0.012827

The walls of the bunker were simulated of standard concrete Portland, with a density of  $2.35 \text{ g/cm}^3$ . Both Havar and Portland materials were selected from the Flair material database and imported to input file (Figure 3-10).

470 Havar  
see Porter, NIM 89 (1970) 237; Goodfellow (via Google)  
0.04% Be contribution omitted

**MATERIAL** Name: Havar # p: 8.3  
Z: Am: A: dEdx: Elements: 7..9

**COMPOUND** Name: Havar Mix Mass Elements: 7..9  
M1: CARBON M2: CHROMIUM  
M3: MANGANESE M4: IRON  
M5: COBALT M6: NICKEL  
M7: MOLYBDEN M8: TUNGSTEN  
M9:

Concrete portland

**MATERIAL** Name: PORTLAND # p: 2.35  
Z: Am: A: dEdx: Elements: 10..12

**COMPOUND** Name: PORTLAND Mix Mass Elements: 10..12  
M1: HYDROGEN M2: CARBON  
M3: OXYGEN M4: SODIUM  
M5: MAGNESIUM M6: ALUMINIUM  
M7: SILICON M8: POTASSIUM  
M9: CALCIUM M10: IRON  
M11: M12:

**Figure 3-10 - Definition of Havar and Portland materials. Composition is reported in mass fraction.**

A 16.5 MeV proton beam, elliptically shaped in the direction perpendicular to beam direction, was simulated with a Gaussian distribution in energy ( $\text{FWHM}_{\Delta E} = 0.08 \text{ MeV}$ ) both on the x and y axis. In Figure 3-11 the definition of the proton beam is shown. Several variables were defined using different *#define* cards: *dx* and *dy* are the maximum dimension, in cm, of the beam spot in the x and y direction respectively; *dE* is the *energy spread* of the beam of  $\pm 0.1 \text{ MeV}$ ; *dp* is the corresponding *momentum spread*<sup>13</sup> calculated using the built-in function *dE2dp*. These variables were used in the *BEAM* card for the definition of the proton beam while the *BEAMPOS* card was used to set the starting point of the beam and the direction. Since in FLUKA the beam is directed by default along the z-direction, the *BEAMAXES* was used to rotate the beam reference frame and to correctly orient the beam.

<sup>13</sup> While it is possible to select the energy of the beam particle, the energy spread must be given to the *BEAM* card as momentum spread (Ferrari, et al., 2005).

#define dx	1.4		
#define dy	1.2		
#define dE	=0.1*MeV		
#define dp	=dE2dp(0.0165, dE, mPROTON)		
Define the beam characteristics			
*BEAM	Beam: Energy ▾	E: 0.0165	Part: PROTON ▾
	Δp: =(2.355/6)*dp	Δφ: Flat ▾	Δφ: Δφ: =(2.355/6)*dy
	Shape(X): Gauss ▾	Shape(Y): Gauss ▾	
	Δx: =(2.355/6)*dx		
Define the beam position			
*BEAMPOS	x: -15.	y: 0.0	z: 120.
	cosx: 0.0	cosy: 0.0	Type: POSITIVE ▾
*BEAMAXES	cosBxx: 0.0	cosBxy: 0.0	cosBxz: -1.
	cosBzx: 1.	cosBzy: 0.0	cosBzz: 0.0

Figure 3-11 - Definition of the proton beam.

The  $x$  and  $y$ -dimensions of the beam spot, that approximate the real beam, were found from the result of a sensitivity analysis: the maximum dimension on both  $x$  and  $y$ -direction was varied in order to compare the current released on the collimators and target assembly, scored using the current estimator *USRBDX*, with experimental measurements.

*USRBDX	Type: I1_LinE_LinΩ ▾	Reg: PacIn ▾	Unit: 60 BIN ▾	Name: Icoll
	Part: BEAMPART ▾	Emin: 0.0	to Reg: CollP ▾	Area: 1.
		Ωmin: 0.0	Emax: 17.	Ebins: 17.
			Ωmax: 6.28	Ωbins: 1.
*USRBDX	Type: I1_LinE_LinΩ ▾	Reg: Hav2 ▾	Unit: 60 BIN ▾	Name: Itar
	Part: BEAMPART ▾	Emin: 0.0	to Reg: Target ▾	Area: 1.
		Ωmin: 0.0	Emax: 17.	Ebins: 17.
			Ωmax: 6.28	Ωbins: 1.

Figure 3-12 - USRBDX cards used in the modelling of the PETtrace beam spot: proton current was measured both on the collimator and on the target material.

The *beam wide* is a parameter routinely monitored during the daily irradiations and defined as

$$BW = 100 \cdot \frac{\frac{1}{2}(I_{upper} + I_{lower})}{I_{targ}} \quad \text{Equation 3-1}$$

where  $I_{upper}$ ,  $I_{lower}$  and  $I_{targ}$  are the proton current measured on the upper and lower collimators and the target respectively. An average beam wide of 11% was considered for the comparison. Note that, since the upper and the lower collimators were modeled as a one piece, the *USRBDX* card “Icoll” (Figure 3-12) gave directly the total current  $I_{upper} + I_{lower}$ . The FWHM in the  $x$  and  $y$ -direction was calculated using the well-known relationship

$$FWHM = 2.355 \cdot \sigma = 2.355 \cdot \frac{d_{max}}{6} \quad \text{Equation 3-2}$$

where  $d_{max}$  is the maximum dimension of the spot in the  $x$  or  $y$  direction, considered equals to  $6\sigma$ .

Radiation decay was enabled, through the *RADDECAY* card (Figure 3-13), in “active” mode meaning that the time evolution is calculated analytically and all daughter nuclei and all associated radiations are considered, but at fixed times: it is possible to perform on-line time evolution of decay radiation, and to score all

standard quantities (energy deposition, residuals, etc.) according to a user-defined irradiation profile (*IRRPROFI*) and one or more user-defined decay times (*DCYTIMES*). Radiation transport is performed only once, and the evolution is applied as a weight depending on the setting of the estimator, to be defined with the *DCYSCORE* card (Ferrari, et al., 2005). In other word, in active mode the decay radiation is evaluated analytically, using the well-known exponential equation, but only at a given time instants set through the *DCYTIMES* card. The *IRRPROFI* card (Figure 3-13) was used to set an irradiation profile of 1hour-1μA proton current (expressed in particle/s as requested in the card). This irradiation profile was used for all the simulations to compare results from simulations with experimental results coming from different irradiations and reference values available in literature. Finally, the *DCYTIMES* card (Figure 3-13) was used to set  $t=0$ , meaning the *End of Bombardment* (EOB), as the only cooling time used: again this choice was done to compare results from simulations with experimental and reference values.

<b>RADDECA</b> h/μ Int: ignore ▼ e-e+ LPB: ignore ▼	Decays: Active ▼ h/μ LPB: ignore ▼ e-e+ WW: ignore ▼ decay cut: 0.0	Patch Isom: off ▼ h/μ WW: ignore ▼ Low-n Bias: ignore ▼ prompt cut: 0.0	Replicas: e-e+ Int: ignore ▼ Low-n WW: ignore ▼ Coulomb corr: ▼
<b>IRRPROFI</b>	Δt: 3600. Δt: Δt:	p/s: 6.21E+12 p/s: p/s:	
<b>DCYTIMES</b>	t1: 0.0 t4:	t2: t5:	t3: t6:

Figure 3-13 - Cards *RADDECA*, *IRRPROFI* and *DCYTIMES* used in the simulations.

The *START* card (Figure 3-14) was used to set the number of primary histories to be simulated in each cycle. In FLUKA, each run is composed by a user-defined number of cycles (default = 5): once a run had been performed, the files generated in each cycle were processed, meaning that they were averaged to obtain a final file with higher statistic respect to the files obtained in each cycle. This strange FLUKA feature it is not other than a computational way to apply the law of large numbers and the central limit theorem explained in section 2.1. Knowledge of the total number of primary particles simulated is extremely important for the post-processing of the results since these are generally normalized per primary particle<sup>14</sup>. Usually we know the total number of primary to be simulated and so we are interested in calculating the number of primary particles to set in *START*: knowing the number of cycles per run and the number of jobs<sup>15</sup>, the primary particles in *START* can be calculated as

$$\#N \text{ primary in } START = \frac{\#N \text{ primary to be simulated}}{\#N \text{ cycles} \cdot \#N \text{ Jobs}} \quad \text{Equation 3-3}$$

<sup>14</sup> Results are generally normalized per unit primary weight. If no bias is used, the primary weight is equal to 1 and the total number of primary particle simulated is equal to the sum of primary weights.

<sup>15</sup> The number of jobs is the number of run performed in parallel. In essence is the number set, within Flair, in the run menu into the field “spawn”.

The *RANDOMIZ* card sets the seeds for the double-precision random number generator while *STOP* stops the execution of the program. Default settings were used for these cards.



Figure 3-14 - Cards *START*, *RANDOMIZE* and *STOP*.

In the following, where not explicitly indicated, simulations were conducted simulating a total of  $10^9$  primary particles to achieve, in most of the cases, uncertainties on the final result less than 1%.

## 3.3 Validation of the Model

### 3.3.1 Production of $^{18}\text{F}$

The production of  $^{18}\text{F}$  by the well-known reaction  $^{18}\text{O}(p,n)^{18}\text{F}$  was studied to find the set of physical and transport parameters that allowed to obtain the best result with minimum cpu-time usage. A basic beam transport line, consisting in a target of a water solution (1.3 g) 97% enriched in  $^{18}\text{O}$ , was modelled and initially used to perform a sensitivity analysis to find the optimal combination of default, physic and transport parameters. A perfect pencil beam was simulated at this stage to reproduce ideal beam conditions. Three different sets of defaults, predefined transport settings for the most common problems, were set using the dedicated *DEFAULTS* card (Figure 3-15) and compared:

- **NEW-DEFA** in which a reasonable minimal set of physical mechanisms (such as transport of electrons, positrons and photons; low energy neutron transport; delta ray production; heavy particle bremsstrahlung) is enabled;
- **HADROTHER** for hadrotherapy calculations;
- **PRECISIO** for maximum precision simulations.

The defaults used in this validation differ not only in the physical mechanisms enabled but also in the production and transport energy thresholds of primary and secondary particles.



Figure 3-15 - *DEFAULT* card

The assessment of the saturation yield, already defined in section 1.2.3, of  $^{18}\text{F}$  was performed using the *RESNUCLE* card (Figure 3-16) to score the activity produced at EOB. Results were compared with the recommended saturation activity for  $1\ \mu\text{A}$  ( $A_2$ ) provided in the IAEA database for medical radioisotopes production: for 16.5 MeV protons  $A_2$  results to be 13.078 GBq/ $\mu\text{A}$  (IAEA, 2001a). To allow the calculation of the activity of  $^{18}\text{F}$  produced at EOB, *RESNUCLE* card was “connected”, through the *DCYSCORE* card (Figure 3-16), to the cooling time  $t=0$ .

<b>DCYSCORE</b>	Cooling t: 0.0 ▾ Det: AcTar ▾	Kind: RESNUCLE ▾ to Det: ▾	Step:
<b>RESNUCLE</b> Max Z:	Type: All ▾ Max M:	Unit: 30 BIN ▾ Req: Target ▾	Name: AcTar Vol: 1

Figure 3-16 - *RESNUCLE* and *DCYSCORE* cards.

For each simulation two *PHYSICS* cards (Figure 3-17) were used to enable coalescence mechanisms and the new FLUKA evaporation model, with heavy fragment evaporation (Ferrari, et al., 2011); for some simulations, *PART-THR* card (Figure 3-17) was used to overwrite the default particle transport threshold for one or more types of particles. In this case, proton transport threshold was set to 1 MeV instead the default value of 10 MeV of the *NEW-DEFA* default.

<b>PHYSICS</b>	Type: COALESCE ▾	Activate: On ▾	# Dstack:
<b>PHYSICS</b>	Type: EVAPORAT ▾	Model: New Evap with heavy frag ▾	
<b>PART-THR</b>	Type: Energy ▾ Part: PROTON ▾	E: 0.001 to Part: PROTON ▾	Step: 1.

Figure 3-17 - *PHYSICS* and *PART-THR* cards.

Simulations were performed on a core™ i7 laptop with four physical cores and hyper-thread enabled.

Results of the sensitivity analysis performed on defaults, physical and transport parameters are summarized in Table 3-3.

Table 3-3 - Validation of the physics and transport parameters in the energy range of medical applications: assessment of the saturation yield of  $^{18}\text{F}$ .

DEFAULTS	NEW-DEFA	NEW-DEFA	NEW-DEFA	HADROTHE	HADROTHE	PRECISIO	PRECISIO
<b>TRANSPORT</b>	PART-THR: as default (10 MeV)	PART-THR: 0.1 MeV	PART-THR: 1 MeV for protons	PART-THR: as default (0.1 MeV)	PART-THR: 10 MeV	PART-THR: as default (0.1 MeV)	PART-THR: 10 MeV
<b>Simulation Time [h]</b>	1.05	5.04	3.12	25.17	3.43	25.48	2.26
<b><math>Y_{\text{sat}}^{18\text{F}}</math> [GBq/<math>\mu\text{A}</math>]</b>	6.521 ± 0.006	13.166 ± 0.009	13.161 ± 0.009	13.169 ± 0.010	6.508 ± 0.005	13.200 ± 0.010	6.486 ± 0.006
<b><math>A_2/Y_{\text{FLUKA}}</math></b>	2.01 ± 0.20	0.99 ± 0.10	0.99 ± 0.10	0.99 ± 0.10	2.01 ± 0.20	0.99 ± 0.10	2.02 ± 0.20

From Table 3-3, *NEW-DEFA* default and a proton transport threshold set at 1 MeV proved the best combination giving an excellent agreement with the IAEA recommended value in the shortest simulation time (Infantino, et al., 2015a). Actually, considering the production cross section of the  $^{18}\text{O}(p,n)^{18}\text{F}$  reaction retrieved from the IAEA charged-particle cross section database for medical radioisotope production (IAEA, 2011a), it is possible to see how a large part of the area under the curve is lost when protons are not transported below 10 MeV (remember that the integral of this curve is proportional to the activity produced).

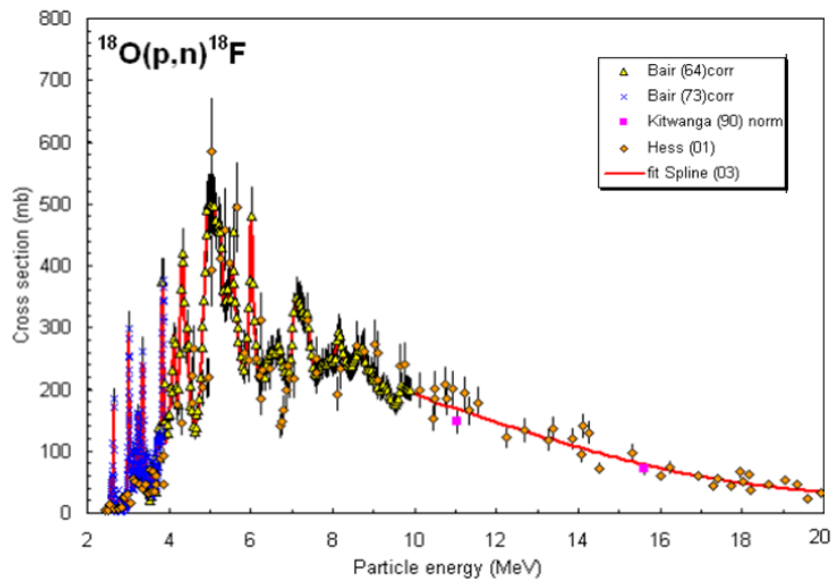


Figure 3-18 - Cross section of the  $^{18}\text{O}(p,n)^{18}\text{F}$  reaction (IAEA, 2011a).

In a previous work conducted in 2010 the production of  $^{89}\text{Zr}$ , via the  $^{89}\text{Y}(p,n)^{89}\text{Zr}$  reaction, was studied using FLUKA (Infantino, et al., 2011) to develop a target capable of maximizing the production yield. In this work a very simple cylindrical target, including the Yttrium foil, the target baking, the cooling Helium and the Havar foil was modeled. The *NEW-DEFA* set was used; a spread out 16.5 MeV proton beam was defined. Finally, activity produced after 1hour-1 $\mu\text{A}$  irradiation was scored using the *RESNUCLE* card. Simulations were compared with experimental measurements (Ciarmatori, et al., 2011) and a theoretical assessment conducted using the TALYS code (Koning, et al., 2007): experimental to FLUKA and TALYS to FLUKA ratios of  $1.09 \pm 0.15$  and  $1.07 \pm 0.16$  were found respectively.

### 3.3.2 Assessment of the Neutron Ambient Dose Equivalent

Measurements of the neutron ambient dose equivalent  $\text{H}^*(10)$  were taken around the PETtrace to further validate the model with another quantity of radiological interest. The experimental setup adopted refers to a previous work conducted at “S. Orsola-Mapighi” Hospital (Gallerani, et al., 2008) where

measurements of ambient dose equivalent  $H^*(10)$ , from thermal and fast neutrons, were conducted within the cyclotron vault. Measurements were taken in 12 points located along 8 directions at the same height of target n°1, used in the  $^{18}\text{F}$ -production (Figure 3-19): a set of 3 dosimeters for fast neutrons (CR-39) and 3 for thermal neutrons (GR-200 and GR-207), all provided by ENEA, was used at each measurement point to improve measurement statistics.

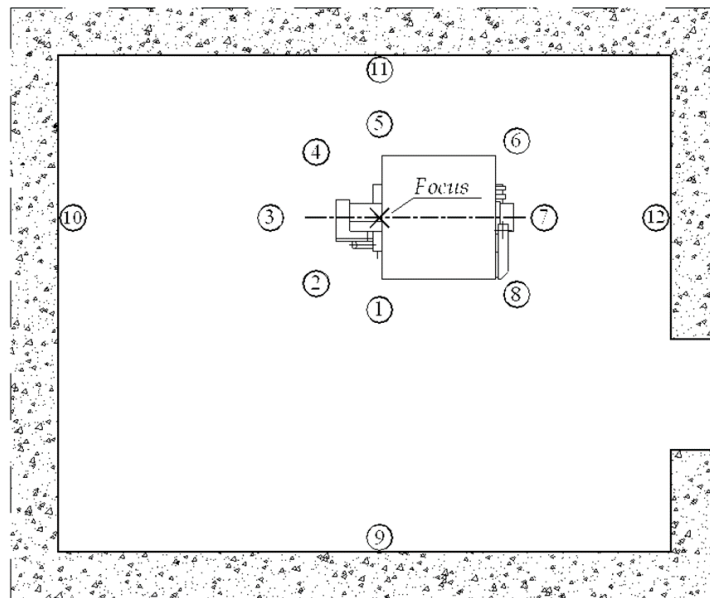


Figure 3-19 - Experimental setup used in the measurement campaign: numbers indicate the position of the dosimeters (Gallerani, et al., 2008).

A new measurement campaign was conducted using a neutron rem-counter FHT-752 (Thermo Scientific) provided with a  $\text{BF}_3$  proportional-counter and a PE-moderator, calibrated in  $H^*(10)$  and a new set of 12 TLD dosimeters, type CR39 (ENEA). The main features of the detectors (ENEA, 2013; Thermo Scientific, 2013) used in the measurement campaign are reported in Table 3-4. To obtain dose rates in the measurement range of the detectors and thus limiting the effects of dead time, irradiation tests were conducted with an integrated current between 0.005 and 0.0016  $\mu\text{Ah}$ . Results were compared with Monte Carlo simulations performed in the same conditions of irradiation.

Table 3-4 - Main features of the detectors used in the measurement of the neutron ambient dose equivalent.

	FHT-752 (Thermo Scientific)	CR39 (ENEA)
<b>Measured Quantity</b>	$H^*(10)$	$H^*(10)$ , $H_p(10)$
<b>Energy Range</b>	0.025 eV – 20 MeV	200 keV – 14 MeV
<b>Measuring Range</b>	1 nSv/h – 0.4 Sv/h	0.1 – 20 mSv
<b>Detector</b>	$\text{BF}_3$ (1 bar)	CR39 (25x36x1.4 mm)
<b>Response</b>	Neutron: $0.5 \text{ s}^{-1}/(\mu\text{Sv/h})$ for Cf-252 Gamma: $<10^{-5}$ at 1Sv7h for Cs 137	Energy dependence: $\pm 50\%$ Angular dependence: $\pm 15\%$

Simulations were performed using the *NEW-DEFA* set; proton transport threshold was set to 1 MeV, according to the results reported above, using the *PART-THR* card. Finally, a 1hour-1 $\mu$ A irradiation profile was simulated and results were normalized to the total charge in  $\mu$ Ah. The spread out beam described in section 3.2 was used. Neutron ambient dose equivalent was assessed in FLUKA using the *USRBIN* and the *AUXSCORE* cards. The *USRBIN* card scores the distribution of several quantities (such as energy deposited, dose, activity, specific activity, displacements per atom, non-ionising energy losses, dose equivalent, fluence) in a regular spatial structure (binning detector) independent from the geometry (Ferrari, et al., 2011). The *AUXSCORE* card allows to associate scoring detectors of given estimator types with dose equivalent conversion factors and to filter scoring detectors according to auxiliary (generalised) particle distributions or isotope ranges (Ferrari, et al., 2011).

 <b>USRBIN</b>	Type: R- $\Phi$ -Z Part: DOSE-EQ	Rmin: 0.0 X: 0.0 Zmin: 0.0	Unit: 41 BIN Rmax: 200. Y: 0.0 Zmax: 200.	Name: dosePol NR: 200. NP: 72. NZ: 200.
 <b>USRBIN</b>	Type: X-Y-Z Part: DOSE-EQ	Xmin: -600. Ymin: -450. Zmin: -200.	Unit: 42 BIN Xmax: 600. Ymax: 650. Zmax: 600.	Name: doseCar NX: 240. NY: 220. NZ: 160.
 <b>AUXSCORE</b>	Delta: $\downarrow$	Type: USRBIN Det: dosePol	Part: NEUTRON to Det: doseCar	Set: AMB74 Step: 1.

**Figure 3-20 - USRBIN cards used for the assessment of the neutron ambient dose equivalent  $H^*(10)$ .**

To reproduce the positioning of the dosimeters two different USRBIN cards were set (Figure 3-20): in the first one a cylindrical mesh R- $\Phi$ -Z was created in an area close to the cyclotron with a pitch of 1 cm along the radial direction and the height of the cylinder and with a pitch of 5° on the polar angle; in the second one, a Cartesian mesh, on the whole cyclotron vault, with a pitch of 5 cm along the x, y, and z-direction was created. The *AUXSCORE* card allowed to filter the dose equivalent from neutrons only and to apply the fluence-to-dose equivalent conversion coefficients to obtain results in ambient dose equivalent  $H^*(10)$ : the set “*AMB74*” based on ICRP74 (ICRP, 1996) and Pelliccioni (Pelliccioni, 2000) data was used. Results of the simulation are reported in Figure 3-21 and Figure 3-22.

From the cylindrical mesh (Figure 3-22) data for positions 1-8 were taken while positions 9-12 were calculated using an exponential attenuation; data from the Cartesian mesh (Figure 3-21) were taken, for all the positions, in the same coordinates as the real dosimeters. Comparison of the simulated and measured values of ambient dose equivalent is reported in Table 3-5 (Infantino, et al., 2014a; Infantino, et al., 2015a).

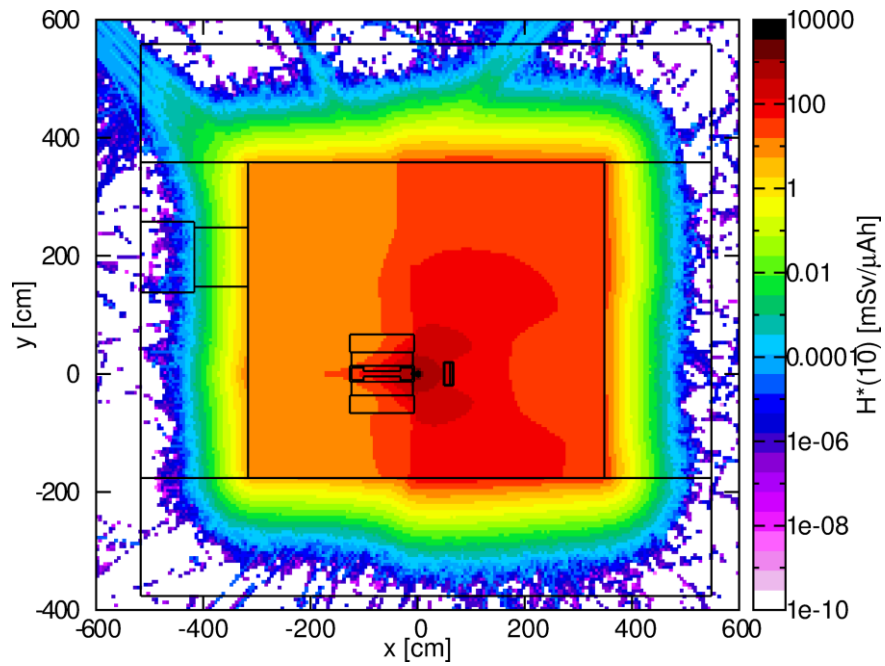


Figure 3-21 – FLUKA assessment of the neutron ambient dose equivalent  $H^*(10)$  over the whole cyclotron vault (Cartesian mesh).

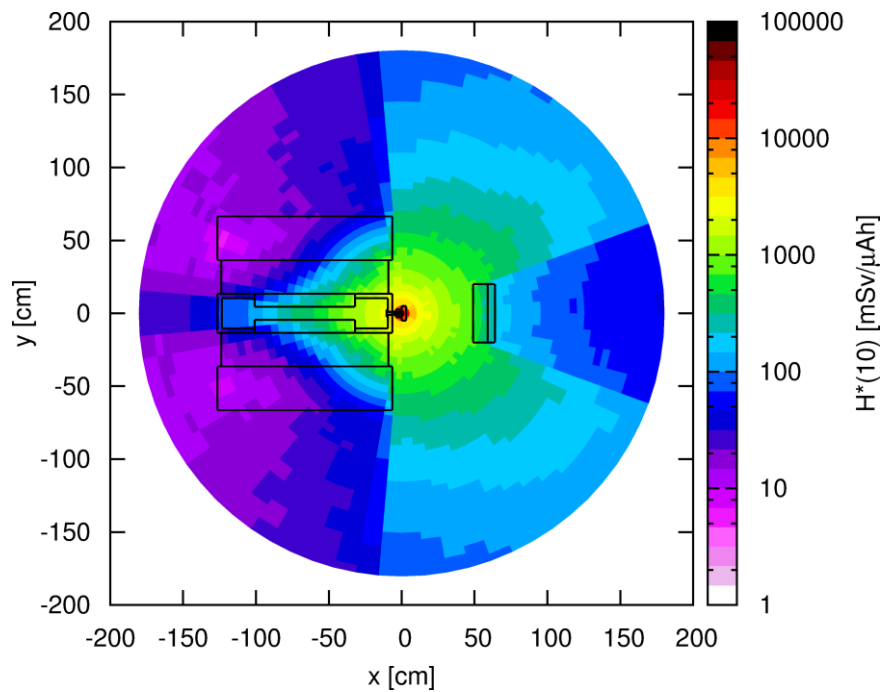


Figure 3-22 - FLUKA assessment of the neutron ambient dose equivalent  $H^*(10)$  in an area close to the cyclotron (cylindrical mesh).

**Table 3-5 - Comparison of neutron ambient dose equivalent obtained with simulation and experimental measurements.**

Position	Gallerani et al.	FLUKA (R $\Phi$ Z)	FLUKA (XYZ)	FHT-752	CR39
	Dose $\pm$ Uncertainty [mSv/ $\mu$ Ah]				
<b>1</b>	230 $\pm$ 70	307.9 $\pm$ 2.9	308.8 $\pm$ 0.5	330 $\pm$ 50	400 $\pm$ 200
<b>2</b>	300 $\pm$ 100	453.9 $\pm$ 3	464.4 $\pm$ 0.6	430 $\pm$ 60	300 $\pm$ 200
<b>3</b>	43 $\pm$ 13	110.6 $\pm$ 1.6	97.82 $\pm$ 0.26	93 $\pm$ 14	60 $\pm$ 30
<b>4</b>	300 $\pm$ 100	459 $\pm$ 3	480.0 $\pm$ 0.6	420 $\pm$ 60	400 $\pm$ 200
<b>5</b>	300 $\pm$ 100	316.9 $\pm$ 2.7	330.9 $\pm$ 0.5	330 $\pm$ 50	400 $\pm$ 200
<b>6</b>	6.2 $\pm$ 2.6	19.7 $\pm$ 0.5	20.87 $\pm$ 0.11	27 $\pm$ 4	6 $\pm$ 5
<b>7</b>	37 $\pm$ 12	55.0 $\pm$ 1.1	75.69 $\pm$ 0.24	32 $\pm$ 4	19 $\pm$ 13
<b>8</b>	2.1 $\pm$ 0.9	19.0 $\pm$ 0.5	18.87 $\pm$ 0.10	23 $\pm$ 4	6 $\pm$ 5
<b>9</b>	19 $\pm$ 6	27.43 $\pm$ 0.26	52.93 $\pm$ 0.19	55 $\pm$ 8	31 $\pm$ 18
<b>10</b>	5.9 $\pm$ 2.3	10.70 $\pm$ 0.14	46.61 $\pm$ 0.17	45 $\pm$ 7	38 $\pm$ 22
<b>11</b>	100 $\pm$ 30	131.9 $\pm$ 1.3	169.6 $\pm$ 0.3	190 $\pm$ 28	130 $\pm$ 70
<b>12</b>	13 $\pm$ 4	19.6 $\pm$ 0.4	38.00 $\pm$ 0.17	22 $\pm$ 3	50 $\pm$ 29

As it possible to see from Table 3-5, the uncertainty associated with the CR39 dosimeters is quite high: this is substantially due to a significant dependence on the energy response of the instrument in a intense and complex radiation field as the one within the cyclotron vault during an irradiation. On the other hand, the use of an electronic instrument like the rem-counter allows to improve the counting statistics thanks to the greater dimensions of the probe, compared with the TLDs, even if the correct positioning might be affected from a significative uncertainty. The total uncertainty<sup>16</sup> associated with the neutron rem-counter was assessed by a quadratic propagation of the uncertainty on the reading of the proton current ( $\sim$ 5%), on the irradiation time ( $<$  3s), on the calibration factor ( $\sim$ 5%) and on the differences from the calibration spectra ( $\sim$ 5%): a total uncertainty of 15% was considered.

Finally, the ratio between FLUKA (Cartesian mesh) and the measurements obtained using the FHT-752, the TLDs (average of Gallerani et al. and the new measurement campaign) and the total average of the experimental measurements (FHT-752 + CR39 + Gallerani et al.) was calculated for each position. Results are reported in Table 3-6. The average for each position and for the global agreement considering all positions was calculated by weighting the single uncertainties of the measurements using the following equations:

<sup>16</sup> Sometimes the quantitative assessment of the uncertainty is impossible or quite complex: in this case, the uncertainty can be assessed on the basis of the experience of the scientist that performs the measurement as suggested in the standard ANSI N42.14-1999 (ANSI, 1999).

$$\bar{x} = \frac{\sum_{i=1}^N x_i \left(\frac{1}{\sigma_i}\right)^2}{\left(\frac{1}{\sigma_{\bar{x}}}\right)^2} = \frac{\sum_{i=1}^N x_i \left(\frac{1}{\sigma_i}\right)^2}{\sum_{i=1}^N \left(\frac{1}{\sigma_i}\right)^2} \quad \text{Equation 3-4}$$

$$\left(\frac{1}{\sigma_{\bar{x}}}\right)^2 = \sum_{i=1}^N \left(\frac{1}{\sigma_i}\right)^2 \quad \text{Equation 3-5}$$

where  $\bar{x}$  is the *weighted average* and  $\sigma_{\bar{x}}$  is the *standard deviation of the mean* (SDOM) (Taylor, 1997).

As shown in Table 3-6, using the physics and transport parameters found to optimal in the previous section, the assessment of the neutron ambient dose equivalent resulted in optimal agreement with the experimental measurements obtained with the neutron rem-counter. Compared to the measurements obtained with the TLDs FLUKA overestimates, on average, the dose rate of about 55%: from a radiation protection point of view FLUKA gives a safe condition, useful during the design of shielding even if, as reported above, the measurement of the dose equivalent with this type of dosimeter is not recommended.

**Table 3-6 - Ratio between FLUKA (XYZ) values and experimental measurements.**

<b>Position</b>	<b>Fluka/FHT-752</b>	<b>Fluka/Average TLD</b>	<b>Fluka/Average Exp</b>
<b>1</b>	0.94 ± 0.14	1.3 ± 0.3	1.03 ± 0.14
<b>2</b>	1.08 ± 0.16	1.5 ± 0.4	1.20 ± 0.16
<b>3</b>	1.04 ± 0.16	2.2 ± 0.6	1.47 ± 0.21
<b>4</b>	1.13 ± 0.17	1.5 ± 0.4	1.24 ± 0.16
<b>5</b>	1.01 ± 0.15	1.03 ± 0.28	1.01 ± 0.13
<b>6</b>	0.78 ± 0.12	3.4 ± 1.2	1.9 ± 0.3
<b>7</b>	2.4 ± 0.4	2.6 ± 0.8	2.4 ± 0.3
<b>8</b>	0.81 ± 0.12	9 ± 3	5.6 ± 1.4
<b>9</b>	0.97 ± 0.15	2.6 ± 0.8	1.64 ± 0.24
<b>10</b>	1.04 ± 0.16	7.5 ± 2.7	4.6 ± 1.0
<b>11</b>	0.89 ± 0.13	1.7 ± 0.5	1.18 ± 0.16
<b>12</b>	1.69 ± 0.25	2.7 ± 0.9	1.98 ± 0.27
<i>Total Average</i>			
	0.99 ± 0.04	1.55 ± 0.15	1.30 ± 0.06

### 3.3.3 Comparison with Tesch's Data

As reported in section 1.2.2, for many years the work published by Tesch (Tesch, 1985) was widely employed in the design of shielding, especially regarding the assessment of the source term. In this context, it was interesting to compare the neutron yields obtained by Tesch in 1980's with FLUKA Monte Carlo simulations. A basic beam transport line was modelled to study the radiation field produced in the irradiation of a cylindrical thick target of copper, iron, graphite, tantalum and aluminium. An ideal pencil beam without any spread in energy and direction was simulated. The number of neutrons produced per primary incident proton was evaluated at energies characteristic of PET cyclotrons in addition to the ones above 50 MeV reported by Tesch to cover the entire energy range of biomedical cyclotrons. Proton range in the different target materials was assessed using SRIM code (Ziegler, et al., 2010) to create a target region thick enough to completely stop the proton beam. The number of neutrons produced per simulated primary particle is available in the standard FLUKA output (\*.out file): to improve the statistic the neutron yield, at a given energy, was calculated from the average of the corresponding value retrieved from all the \*.out files generated during the simulation.

A summary of the results obtained from simulations, for the different materials, is reported in Table 3-7 and in Figure 3-23.

**Table 3-7 - FLUKA neutron yields obtained for several target materials.**

Energy [MeV]	Graphite	Aluminum	Iron	Copper	Tantalum
	<i>Neutron yield (neutrons/incident proton)</i>				
<b>16.5</b>	(4.8322±0.0012)E-05	(5.381±0.016)E-04	(1.927±0.21)E-03	(2.37±0.03)E-03	(2.40±0.06)E-03
<b>19</b>	(6.7527±0.0016)E-05	(9.77±0.04)E-04	(3.12±0.04)E-03	(3.69±0.06)E-03	(4.35±0.10)E-03
<b>24</b>	(1.3818±0.0004)E-04	(2.458±0.014)E-03	(6.22±0.05)E-03	(6.96±0.11)E-03	(1.061±0.029)E-02
<b>30</b>	(4.7514±0.0028)E-04	(4.93±0.03)E-03	(1.104±0.017)E-02	(1.237±0.022)E-02	(2.12±0.06)E-02
<b>50</b>	(5.173±0.014)E-03	(1.957±0.020)E-02	(3.65±0.07)E-02	(4.07±0.09)E-02	(8.00±0.27)E-02
<b>100</b>	(4.19±0.03)E-02	(8.91±0.12)E-02	(1.391±0.028)E-01	(1.72±0.04)E-01	(3.89±0.15)E-01
<b>150</b>	(1.145±0.012)E-01	(1.97±0.03)E-01	(2.99±0.06)E-01	(3.74±0.10)E-01	(8.9±0.4)E-01
<b>200</b>	(2.098±0.028)E-01	(3.01±0.05)E-01	(4.84±0.11)E-01	(6.02±0.16)E-01	(1.47±0.06)E+00
<b>250</b>	(3.30±0.05)E-01	(4.88±0.09)E-01	(7.39±0.17)E-01	(9.17±0.25)E-01	(2.28±0.09)E+00

Neutron yields were compared with data reported by Tesch (1985) (Figure 1-6): in the 50 – 250 MeV energy range the average ratio between Tesch data and FLUKA simulations was  $0.99 \pm 0.12$  for graphite,  $1.17 \pm 0.14$  for aluminum,  $1.15 \pm 0.14$  for iron,  $1.00 \pm 0.12$  for copper and  $0.94 \pm 0.10$  for tantalum. In the energy range of interest for proton therapy the overall agreement with Tesch was very good. Below 30 MeV the agreement was not as satisfactory (i.e.  $1.28 \pm 0.26$  for iron and  $2.0 \pm 0.4$

for aluminum at 19 MeV); Tesch reported only limited data in this range of energy which is likely due to the limited diffusion of PET cyclotrons during the 1970's and 1980's. A validated Monte Carlo model can fill this gap, supplying accurate prediction of neutron yield in this low energy region as well (Infantino, et al., 2015a).

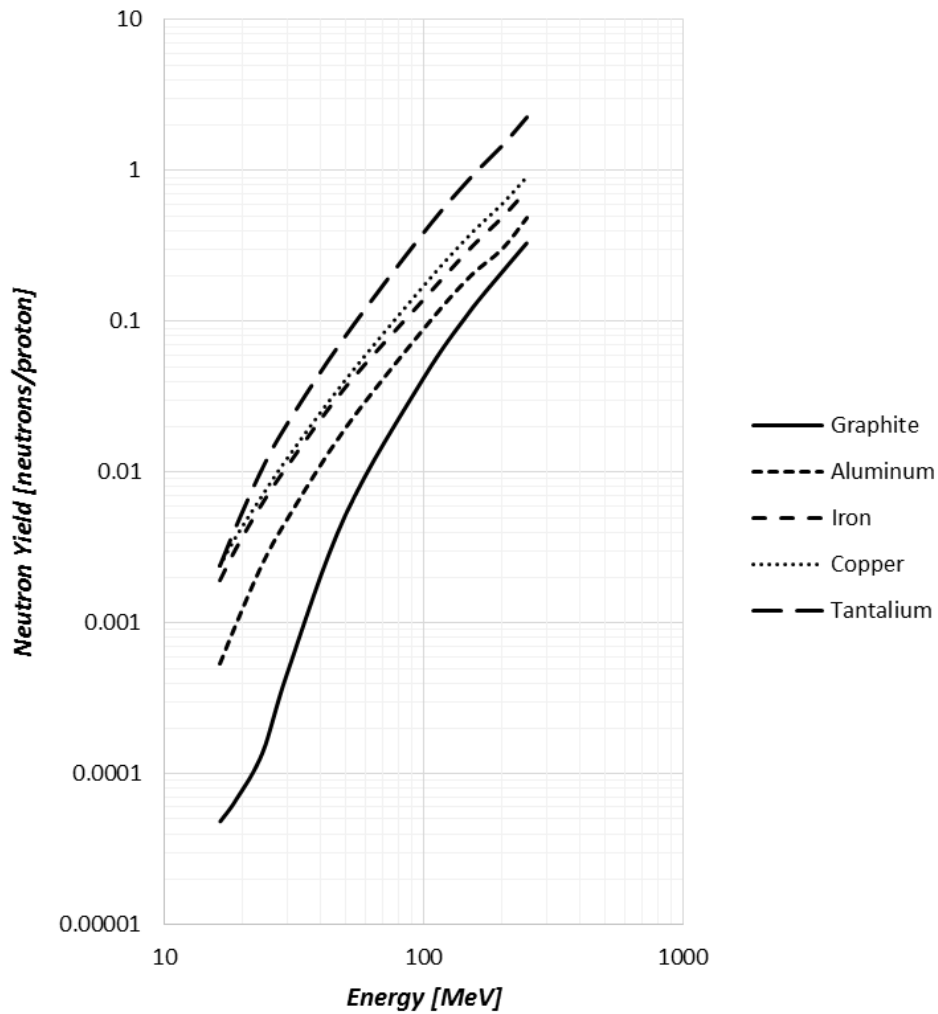
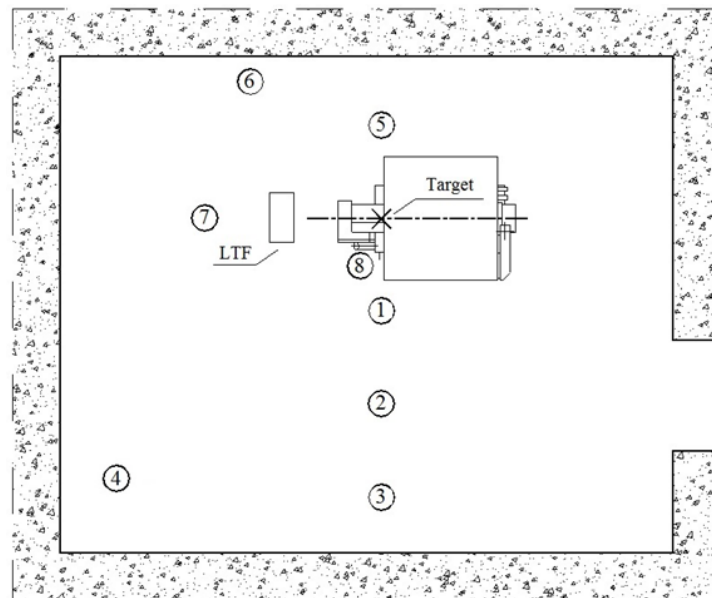


Figure 3-23 – FLUKA total neutron yield per incident proton for different target materials.

### 3.4 Experimental Measurements of $^{41}\text{Ar}$

In the use of biomedical cyclotrons, the activation of air during irradiation and the consequent release in the external atmosphere of radioactive effluents is a radiation protection topic still at the heart of the debate within the scientific community. In particular, the production, and consequent release in the external atmosphere of  $^{41}\text{Ar}$  is an important aspect of the radiation protection of workers and representative persons of the population. In a medical cyclotron facility,  $^{41}\text{Ar}$  ( $t_{1/2} = 109.34\text{m}$ ) is produced by the activation of air due to secondary neutron flux during irradiation, according to the  $^{40}\text{Ar}(n,\gamma)^{41}\text{Ar}$  reaction which has a cross section of  $\sim 660$  mb at thermal energy (0.025 eV) (ENDF, 2014). In literature, some analytical assessments of the  $^{41}\text{Ar}$  production in air were published, based on assumptions or experimental measurement of the neutron flux. A theoretical model of the production of  $^{41}\text{Ar}$  in a cyclotron vault and its release in atmosphere was studied by Birattari et al. (Birattari, et al., 1985; Birattari, et al., 1987b), where hypothesis on the shape and the energy distribution of the neutron field were done. Gutermuth et al. (Gutermuth, et al., 2005) and Biju et al. (Biju, et al., 2013; Biju, et al., 2012) have performed FLUKA Monte Carlo assessment of  $^{41}\text{Ar}$  concentration around proton accelerators in the 0.1-1 GeV energy range; in these works, Monte Carlo simulations were compared with results of analytical estimations, according to methods described in the IAEA Report 283 (IAEA, 1988) or NCRP Report 144 (NCRP, 2003) respectively. An estimation of the production of  $^{41}\text{Ar}$  due to photoneutrons near a 15 MV linear accelerator was performed by Chao et al. (Chao, et al., 2007), based on experimental measurement of the neutron flux using Indium foils. Some experimental results are available as regards  $^{41}\text{Ar}$  release from nuclear reactors (Lauritzen, et al., 2003; Mladin, et al., 2013). However, there are not reports on direct measurement of air activation around biomedical cyclotrons.

To measure the activity concentration of  $^{41}\text{Ar}$  inside the cyclotron bunker, an extensive measurement campaign was performed: Marinelli beakers of  $1000\text{ cm}^3$  were placed inside the bunker, during a routine production of  $^{18}\text{F}$ , in a series of marked positions as reported in Figure 3-24. Beakers 1, 2, 3, 4 were placed at a distance of 1, 2, 3, 4 m from the target respectively; beaker 5 was placed at 1 m while beakers 6 and 7 at 2 m from the target; beaker 8 was placed "in contact" with the target. All the beakers were placed at the same height of the target assembly used in the irradiations. To assess the average value of  $^{41}\text{Ar}$  concentration within the entire bunker, beakers were placed in a variety of different position. Marinelli beakers were sealed to simulate the absence of the ventilation (normally present within the cyclotron vault and fixed at 15 air changes per hour): under the hypothesis of thin plastic thickness of the beaker, the activation of the air inside the beaker is equal to activation of air outside the beaker. At the end of the irradiation, after a measured waiting time of 10 to 20 minutes, that allow to enter the bunker



**Figure 3-24 - Sampling positions adopted during the measurement campaign of  $^{41}\text{Ar}$  within the bunker.**

and remove the samples, the beakers were measured in gamma-ray spectrometry using a HPGe N-Type detector. The high-resolution gamma-ray spectrometry system is based on digital electronics (Areva Canberra, distributed in Italy by TNE, Milan). The HPGe detector has a 30 % relative efficiency and a resolution of 1.8 keV at 1332 keV. The spectrometry system was calibrated in the 59-1836 keV range by means of a multi-radionuclide certified reference solution, obtained from an accredited Standardization Laboratory (Areva CERCA LEA, Pierrelatte Cedex, France). The calibration process was performed accordingly to the IEC 61452 standard (IEC, 1995), using the Genie 2000 software. A dual logarithmic polynomial efficiency curve was used.

The method implemented in the software accounts for the propagation of the uncertainties in the calibration of the reference source (1-2% at 1 sigma level, depending on the peak in the mixture), in the tabulated yield (typically <1%), in the net peak area (<1% for calibration peaks) and in the interpolation of the curve (typically <3%). The calibration uncertainties results thus of about 4-5% at 1 sigma level (Zagni, et al., 2014). Samples were measured for 1800 seconds and all the experimental measurements were decay corrected to EOB. The different density of the samples compared to the calibration source, was taken into account: the efficiency curve for an equivalent gaseous Marinelli calibration source was evaluated using the software Labsocs (Bronson, 2003; Venkataraman, et al., 2005) provided with the acquisition package Genie2000 (Canberra). A correction factor for efficiency for the 1294 keV peak, the most important gamma line for  $^{41}\text{Ar}$ , was calculated and applied to the experimental measurements.

A FLUKA MC model reproducing the measurement setup was created (Figure 3-26). *NEW-DEFA* default and proton transport threshold set to 1 MeV were used; an irradiation profile of 1hour-1 $\mu$ A was simulated. Coalescence and evaporation of heavy fragment were enabled through *PHYSICS* cards; *RADDECAY* card was set in “active” mode. Two different types of score were used: *RESNUCLE* and *USRTRACK* scores. The *RESNUCLE* was used to directly score the activity concentration of  $^{41}\text{Ar}$  in the air volume at EOB. Several *RESNUCLE* cards were used to score the activity of  $^{41}\text{Ar}$  in the whole air volume, within the Marinelli beakers and in 1m<sup>3</sup>-volumes centred in the same position as the Marinelli beakers. The *USRTRACK* score was used to assess the differential neutron fluence distribution in energy within the target region, in an energy-binning basis. To reach a high statistic, 10<sup>10</sup> primary particles were simulated running 16 parallel jobs on a remote cluster<sup>17</sup>: in this way it was possible to reduce the total CPU-time usage (running times were about 20 hours for each job) and to reduce the variance.

DCYSCORE	Cooling t: 0.0	Kind: RESNUCLE	Step: 1
	Det: AcAir	to Det: AcAir	Name: AcAir
RESNUCLE	Type: All	Unit: 30 BIN	Vol: 121560333.
Max Z:	Max M:	Reg: AirB	Name: specN
USRTRACK	Reg: AirB	Unit: 50 BIN	Vol: 121560333.
Type: Linear	Emin: 0.0	Emax: 0.02	Bins: 200.
Part: NEUTRON			

Figure 3-25 - *RESNUCLE* and *USRTRACK* scores used in the assessment of  $^{41}\text{Ar}$  concentration.

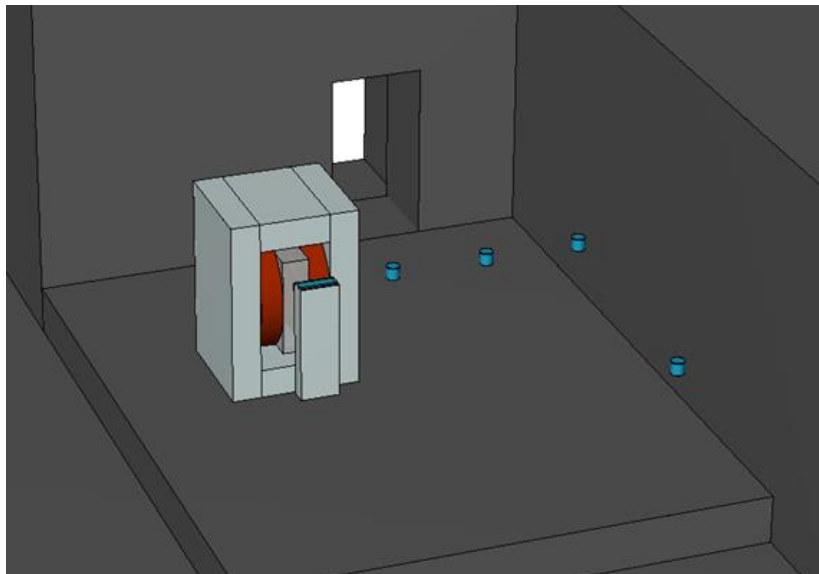


Figure 3-26 - Section of the FLUKA Monte Carlo model used in the simulations: The model reproduces one of the experimental setup adopted.

<sup>17</sup> The remote cluster used for these simulation was an 8-physical processors Intel® Xeon® E5410 (@ 2.33 GHz) provided with 4 cores each.

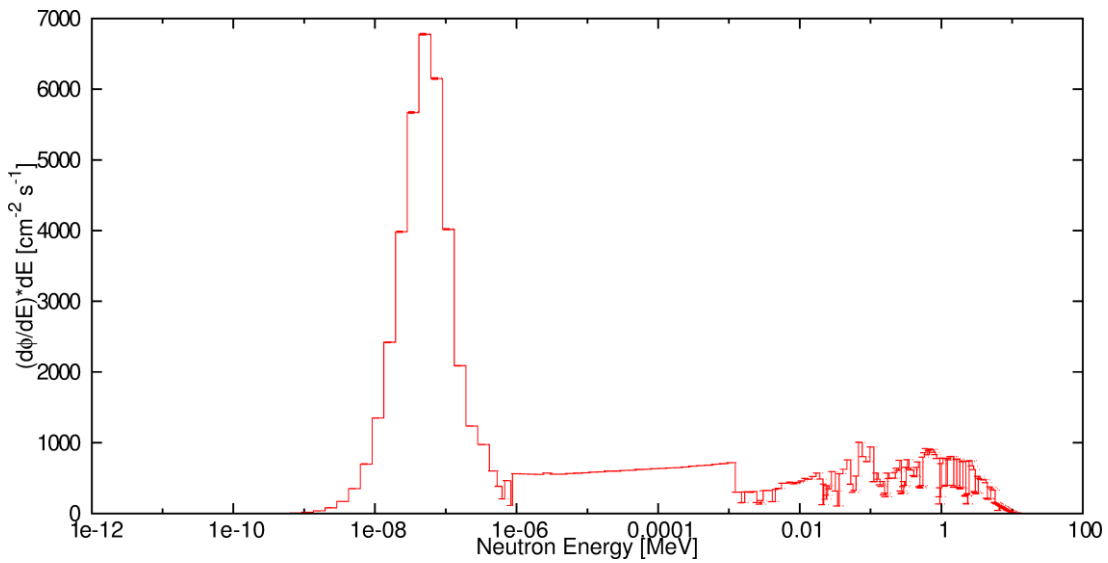


Figure 3-27 - Neutron spectra in the whole air volume within the cyclotron vault.

Figure 3-27 shows the neutron spectrum in the whole air volume within the cyclotron vault. It is possible to see how neutrons are generated around 1 MeV and then slowed down to thermal energy with a peak around  $\sim 4 \times 10^{-7}$  MeV.

One of the main features of FLUKA is the possibility to calculate the residual nuclei produced in inelastic interactions in a defined region. To assess the radionuclide inventory, FLUKA bases its calculation on inelastic hadronic interaction models except for low-energy neutrons where tabulated cross sections are used (Brugger, et al., 2007). Transport of neutrons with energies lower than a predefined threshold energy is performed in FLUKA by a multigroup algorithm: for neutrons with energy lower than 20 MeV, as in the case of interest, FLUKA uses a specific neutron cross section library in which the energy range is divided into 260 energy groups of approximately equal logarithmic width (31 of which are thermal), and containing more than 250 different materials. This library has a larger number of groups and a better resolution in the thermal energy range in respect to the original one (Ferrari, et al., 2011). In addition to direct assessment performed with *RESNUCLE* score, the production yield was calculated also “off-line”, using ENDF/B-VII.0 cross sections library (ENDF, 2014) in combination with neutron fluence data obtained with the *USRTRACK* score. The saturation activity can be written in this case as

$$A_{sat} = \int_{E_{260}}^{E_1} n_{^{40}\text{Ar}} \phi(E) \sigma_{(n,\gamma)}(E) dE \quad \text{Equation 3-6}$$

where  $n_{^{40}\text{Ar}}$  is the number of  $^{40}\text{Ar}$  atoms in the target material;  $\phi(E)$  is the neutron flux distribution in energy and  $\sigma_{(n,\gamma)}$  is the cross section of the  $^{40}\text{Ar}(n,\gamma)^{41}\text{Ar}$  reaction.

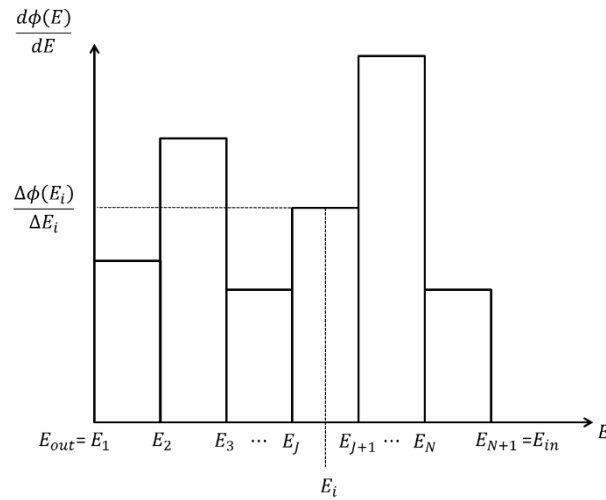


Figure 3-28 - Example of a generic spectrum obtained with the *USRTRACK* score of *FLUKA*.

Using the *USRTRACK* score, it is possible to obtain directly the differential distributions of fluence in energy  $d\phi(E)/dE$  in units of  $cm^{-2} GeV^{-1}$  per incident primary unit weight<sup>18</sup>. Actually, considering a generic spectrum obtained with *USRTRACK* (Figure 3-28) and  $N+1$  points in energy ( $j=1, \dots, N+1$ ), that correspond to  $N$  energy bins ( $i=1, \dots, N$ ), we can transform the integral of Equation 3-6 into a sum over the *FLUKA* 260 energy bins<sup>19</sup>

$$\begin{aligned}
 A_{sat} &= \rho V \omega_{40Ar} \frac{N_A}{A_{40Ar}} \int_{E_{260}}^{E_1} \phi(E) \sigma_{(n,\gamma)}(E) dE \\
 &\cong \rho V \omega_{40Ar} \frac{N_A}{A_{40Ar}} \sum_{i=260}^1 \frac{\Delta\phi(E_i)}{\Delta E_i} \sigma_{(n,\gamma)}(E_i) \Delta E_i
 \end{aligned}
 \tag{Equation 3-7}$$

where  $\rho$  is the density of the target material (air);  $V$  is the volume of the target region;  $\omega_{40Ar}$  is the mass fraction of  $^{40}Ar$  in air (Table 3-2);  $A_{40Ar}$  is the atomic weight of  $^{40}Ar$ ;  $N_A$  is Avogadro's number and  $\Delta E_i$  is the width of the  $i^{th}$  energy bin. Calling  $F(E_i)$  the differential neutron fluence distribution as a function of energy, in the  $i^{th}$  bin, obtained using the *USRTRACK* score we can obtain

<sup>18</sup> In most of the cases each primary particle simulated has a weight equal to 1 and the sum of the primary unit weights equals the total number of the primary particles simulated. It is important to remember that generally this is not true, in example when a bias is used.

<sup>19</sup> Note that the energy groups are numbered in order of decreasing energy (group 1 corresponds to the highest energy).

$$A_{sat} \cong \rho V \omega_{^{40}\text{Ar}} \frac{N_A}{A_{^{40}\text{Ar}}} N_P \sum_{i=260}^1 F(E_i) \sigma_{(n,\gamma)}(E_i) \Delta E_i \quad \text{Equation 3-8}$$

where  $N_P$  is the number of primary particles per second defined in the IRRPROFI card. The off-line calculation of the saturation activity using external cross section data was called “*External Cross Section Method*” (ECSM) (Infantino, et al., 2015b). Since the constrain of the fixed energy structure, Equation 3-8 was implemented in a spreadsheet that first “*adapted*” the ENDF cross sections to the “*Low Energy Neutrons*”<sup>20</sup> (LEN) structure; then the convolution was performed and activity concentration for 1hour-1 $\mu\text{A}$  irradiation was calculated. The adapted CS were calculated by weighting the ENDF CS respect to particle energy (Equation 3-9).

$$\bar{\sigma}_i = \bar{\sigma}|_{E_i}^{E_{i+1}} = \frac{\sum_{k=E_i}^{E_{i+1}} \sigma(k) \cdot \frac{1}{k}}{\sum_{k=E_i}^{E_{i+1}} \frac{1}{k}} \quad \left\{ \begin{array}{l} \forall i = 1, \dots, 260 \\ \forall k = E_i, \dots, E_{i+1} \end{array} \right. \quad \text{Equation 3-9}$$

In Figure 3-29 it is possible to see how considering only the cross section value at 0.0025 eV, as it was done in the past in the already published works, significantly underestimate the production of  $^{41}\text{Ar}$ .

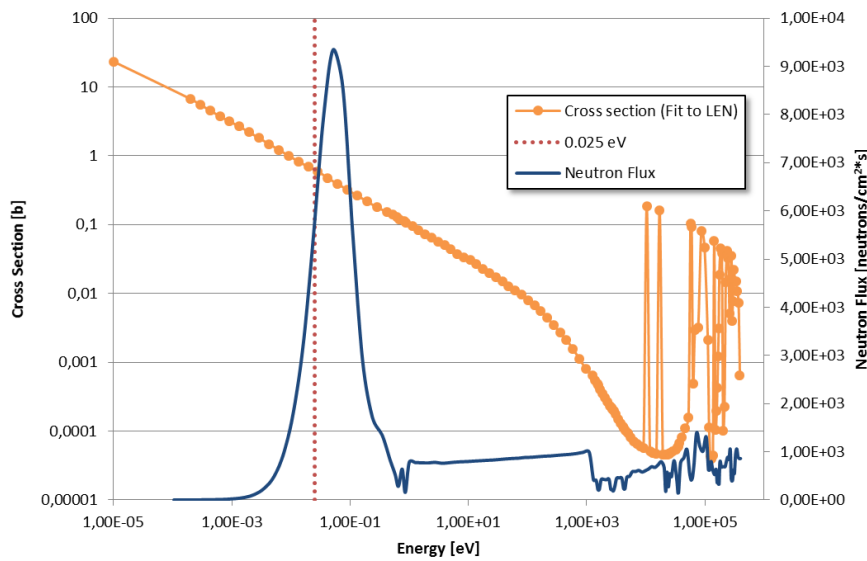


**Figure 3-29 - Differential neutron fluence distribution as a function of energy and fit of the  $^{40}\text{Ar}(n,\gamma)^{41}\text{Ar}$  cross section to the low energy neutrons structure. The figure gives an idea of the convolution process.**

About 68 samples, distributed in 8 different positions in the bunker and during different 17 irradiations, were taken to reach a good statistic. The values of activity

<sup>20</sup> FLUKA considers “Low Energy Neutrons” all the neutrons with an energy less than 20 MeV.

**Table 3-8 - Results of the experimental measurements of  $^{41}\text{Ar}$  in the different positions. For each beaker the weighted average, over 17 samples, and standard deviation of the mean were calculated.**

<b>Beaker</b>	<b>Weighted average <math>\pm</math> SDOM [Bq/dm<sup>3</sup>*<math>\mu</math>Ah]</b>
<b>1</b>	0.721 $\pm$ 0.023
<b>2</b>	0.69 $\pm$ 0.03
<b>3</b>	0.711 $\pm$ 0.025
<b>4</b>	0.82 $\pm$ 0.03
<b>5</b>	1.00 $\pm$ 0.05
<b>6</b>	1.01 $\pm$ 0.05
<b>7</b>	1.07 $\pm$ 0.06
<b>8</b>	0.83 $\pm$ 0.04
<b>Total</b>	0.86 $\pm$ 0.15

of  $^{41}\text{Ar}$  corrected to the EOB were then normalized for the charge accumulated on the target in each bombardment, expressed in  $\mu\text{A}\cdot\text{h}$ . Average  $^{41}\text{Ar}$  concentration in each position, including the standard deviation of the mean (SDOM), are listed in Table 3-8. The values of activity concentration in air show some differences between the different positions of sampling; this is considered due to the position relative to the walls: the closer to the wall, the greater the fluence of thermal neutrons. Despite these differences, the values show a substantial uniformity, being the coefficient of variation of the results 19.4%; it was considered thus practical to express the results in a synthetic form using an overall average, and its standard deviation, of the activity concentration of  $^{41}\text{Ar}$  produced in air, that results  $0.86 \pm 0.15 \text{ Bq/dm}^3\cdot\mu\text{Ah}$ .

Direct activation of the air within the cyclotron vault, obtained with the RESNUCLE score, can be represented as a bi-dimensional map (atomic vs mass number) of the radionuclides produced (Figure 3-30). As the figure shows, traces of other radionuclides can be produced in air during irradiation (Table 3-9); however, the order of magnitude of the activity concentration at EOB of these radionuclides is at least two order of magnitude less than that of  $^{41}\text{Ar}$ , and this only in the case of radionuclides with half-lives of seconds or minutes. For all the other, longer lived radionuclides, the evaluated activity concentrations are 5 or more order of magnitude less than  $^{41}\text{Ar}$ ; their production can then be neglected. The  $^{41}\text{Ar}$  concentrations obtained directly using the RESNUCLE card (already reported in Table 3-9), and indirectly by the neutron fluence-to-cross section convolution, both over the whole air volume ( $\sim 120 \text{ m}^3$ ), are compared in Table 3-10, as well as the ratio of the simulated concentration to the experimental average.

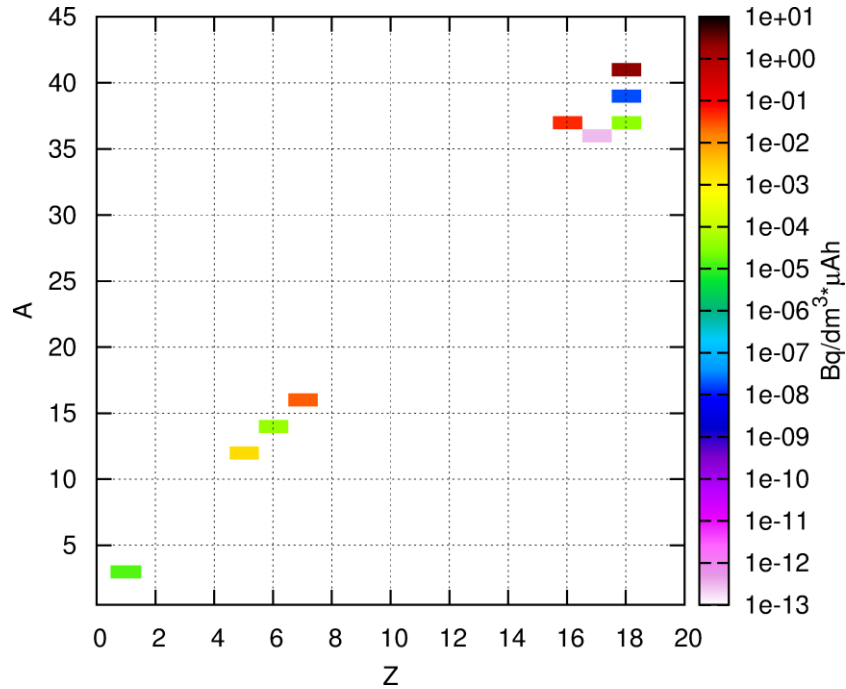


Figure 3-30 - Bi-dimensional map of the radionuclides produced during irradiation in the air volume within the cyclotron vault: Concentrations were normalized for the charge accumulated on the target, expressed in  $\mu\text{Ah}$ .

Table 3-9 - Activity concentration, at EOB, of the radionuclides produced in air during irradiation.

Isotope	$t_{1/2}$	Activity Concentration [ $\text{Bq/dm}^3 \cdot \mu\text{Ah}$ ]
$^{41}\text{Ar}$	109.34 m	$(2.18 \pm 0.11)\text{E}+00$
$^{39}\text{Ar}$	269 y	$(1.76 \pm 0.63)\text{E}-08$
$^{37}\text{Ar}$	35.04 d	$(3.3 \pm 1.2)\text{E}-05$
$^{37}\text{S}$	5.05 m	$(4.9 \pm 1.6)\text{E}-02$
$^{36}\text{Cl}$	$3.01\text{e}5$ y	$(2.9 \pm 2.9)\text{E}-13$
$^{16}\text{N}$	7.13 s	$(2.5 \pm 0.7)\text{E}-02$
$^{14}\text{C}$	5730 y	$(4.235 \pm 0.012)\text{E}-05$
$^{12}\text{B}$	20.20 ms	$(1.9 \pm 1.9)\text{E}-03$
$^3\text{H}$	12.33 y	$(1.39 \pm 0.04)\text{E}-05$

Table 3-10 - FLUKA assessment of the  $^{41}\text{Ar}$  concentration: total air volume.

	$^{41}\text{Ar}$ Concentration [Bq/dm <sup>3</sup> *μAh]	Ratio FLUKA/Exp
<b>Direct (RESNUCLE)</b>	2.18 ± 0.11	2.5 ± 0.5
<b>Convolution (USRTRACK)</b>	2.19 ± 0.07	2.5 ± 0.5

The ratio between the FLUKA simulated concentration of  $^{41}\text{Ar}$  (direct assessment, *FD*, and convolution fluence-to-CS, *FC*) and the experimental measurements was compared for Marinelli beaker and 1m<sup>3</sup>-volume in positions 1-4 (Table 3-11).

Table 3-11 - FLUKA assessment of the  $^{41}\text{Ar}$  concentration: ratio of the simulated concentrations for Marinelli beakers and 1m<sup>3</sup>-volumes over experimental measurements.

Beaker	Marinelli Beakers		1m <sup>3</sup> -volumes	
	<i>FD/Exp</i>	<i>FC/Exp</i>	<i>FD/Exp</i>	<i>FC/Exp</i>
<b>1</b>	n/a	3.58 ± 0.18	7 ± 4	3.01 ± 0.14
<b>2</b>	n/a	3.51 ± 0.20	3.5 ± 1.2	3.13 ± 0.16
<b>3</b>	n/a	3.56 ± 0.19	3.0 ± 1.3	3.05 ± 0.14
<b>4</b>	n/a	3.36 ± 0.19	2.6 ± 0.8	2.99 ± 0.16

Even if the results reported in Table 3-11 are substantially equal within the uncertainties, a tendency can be observed: the larger is the volume in which direct and fluence-to-CS convolution assessment of  $^{41}\text{Ar}$  concentration is performed, the less is the ratio of FLUKA simulations to the experimental measurements. This trend is due to the very low reaction rate of the  $^{40}\text{Ar}(n,\gamma)^{41}\text{Ar}$  reaction: actually, direct assessment in the Marinelli beakers (10<sup>-3</sup> m<sup>3</sup>) did not produce any results while in the 1m<sup>3</sup>-volumes  $^{41}\text{Ar}$  was produced in a detectable quantity. Regarding the results obtained from fluence-to-cross section convolution, again it is possible to see how increasing the volume of integration the ratio FLUKA to experimental decreases and tends to the ratio obtained considering the whole air volume inside the cyclotron vault (~120 m<sup>3</sup>).

In conclusion, sampling air within a bunker in irradiation conditions is a relatively complex task; all the main aspects were addressed, including significance of the sampling, timing between sampling and gamma ray spectrometry analysis, correction of the efficiency calibration accounting for sample's density. Individual measurement resulted affected by uncertainties of the order of 5 % at 1 sigma level; being the results quite similar in the different sampling positions, it was possible to evaluate an overall average, within a variability of less than 20 %. These results were considered satisfactory and useful, particularly to support the planning stage of new facilities and the choices regarding proper regulation of the ventilation system.

As a first, relevant result, it was confirmed that, as expected, production of  $^{41}\text{Ar}$  is the only significant air activation process. Nevertheless, we only obtain an agreement within a factor of 2 – 3 between simulations and experimental results. A similar level of discrepancy has been observed in other attempts to model activation in materials not directly interested by the primary beam (Vincke, et al., 2011; Biju, et al., 2013; Gutermuth, et al., 2005; Brugger, et al., 2007).

The reasons for these differences should be investigated in low energy physical models used in current Monte Carlo programs, particularly when applied to target nuclei present at a very low concentration in a compound media.

However, it has to be noted that analytical approaches to calculate  $^{41}\text{Ar}$  production in air require a relatively complex series of calculations, based on rough approximations of the real geometry, neutron spectra and fluence distribution. Their accuracy cannot be expected to be better than those obtained using Monte Carlo methods, based on a more accurate description of the real problem.

Monte Carlo simulations can instead allow for an accurate geometrical description of the real setup, and provide an elegant solution to the problem of assessing air activation, while in the same time provide information on other relevant radiation protection quantities, like neutron fluence, ambient dose distribution, activation of cyclotron structures and perimetral walls (Infantino, et al., 2015a).

Finally, simulations produced an overestimation, by a factor measurable in an order of magnitude of about 2, of the concentration of  $^{41}\text{Ar}$  produced in air. Further studies are necessary in order to improve the precision of Monte Carlo simulations, as regards activation of materials due to secondary radiation; however, the observed discrepancies being in terms of a cautious overestimation, the results confirmed the usefulness of FLUKA in the perspective evaluation of the radiological impact of new cyclotron installations.

### **3.5 Cyclotron Production of $^{99m}\text{Tc}$**

The established method for the production of  $^{99}\text{Mo}$ , based on fission in nuclear reactors, is still critical due to the plants aging and the significant investments needed for maintenance or for their renewal. Much research work is thus in progress on the study of alternative methods for the production of  $^{99m}\text{Tc}$  in quantities and with the degree of purity required for clinical use. Between them, the cyclotron production of  $^{99m}\text{Tc}$  via the  $^{100}\text{Mo}(p,2n)^{99m}\text{Tc}$  reaction has turned out as the most attractive alternative and several works have already proved its feasibility

using medical cyclotrons accelerating protons up to 19 MeV. One critical aspect regarding the direct production of  $^{99m}\text{Tc}$  with cyclotron is the need for a robust and reliable production process leading to a target capable of withstanding high beam currents and long irradiation time and granting the production of large amounts of  $^{99m}\text{Tc}$ . Several techniques have been indicated as extremely promising; however these methods require specialized instrumentation and complex operations to be performed handling activated materials in order to recover irradiated Mo. Although several groups (Morley, et al., 2012; Gagnon, et al., 2011; Hanemaayer, et al., 2014; Richards, et al., 2013; Qaim, et al., 2014; Lebeda, et al., 2012; Lucconi, et al., 2013) have already investigated alternative techniques, a reliable production methodology is far from being established and this aspect is still an open issue (Lucconi, et al., 2014).

The development of a low-cost target, producible through a relatively fast and easy methodology and capable of granting a local supply was studied using MC simulation. In particular FLUKA was used to find the best material that maximize the production yield of  $^{99m}\text{Tc}$  (minimizing the radionuclide impurities) and the optimal target thickness to be irradiated. A detailed MC model of the solid target assembly, including the PETtrace collimator (Figure 3-8) and the copper backing for the positioning and the cooling of the solid target, was created (Figure 3-31). Figure 3-32 shows the MC model of the two different target setups modeled. Different target setups (including material composition and dimension of the target) were simulated.

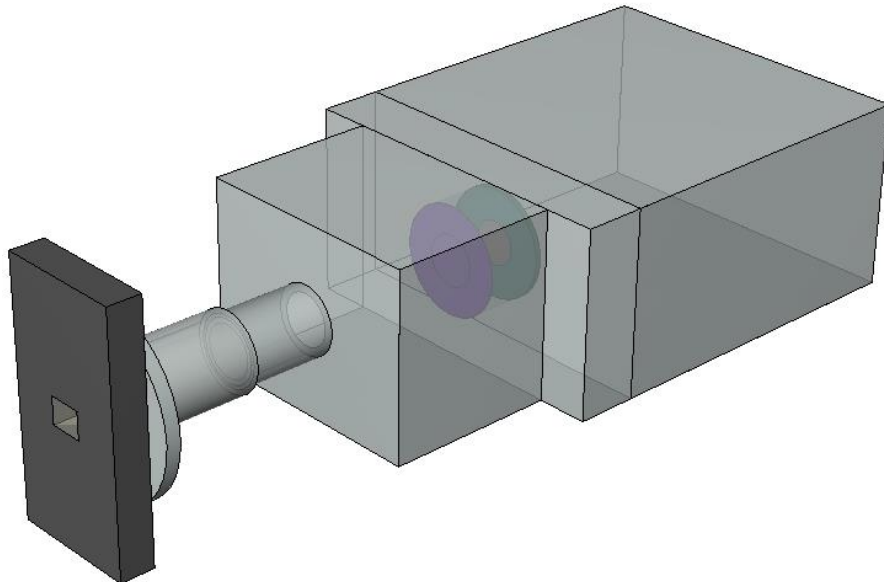


**Figure 3-31 - FLUKA MC model of the solid target assembly mounted on the GE PETtrace cyclotron.**

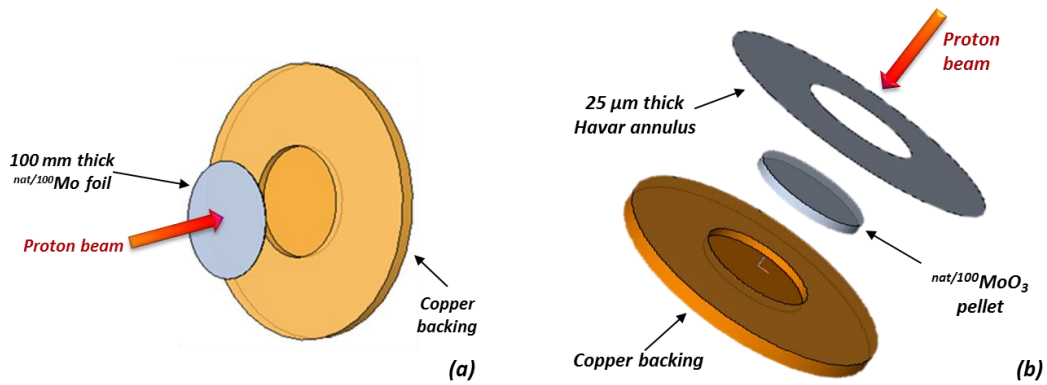


Figure 3-32 - Target setups used in the simulation: <sup>nat</sup>/<sup>100</sup>Mo foil (a) and <sup>nat</sup>/<sup>100</sup>MoO<sub>3</sub> pellet (b).

Table 3-12 - Data of the different targets simulated. For the <sup>100</sup>MoO<sub>3</sub> pellet target impurities reported in the batch certificate were modeled.

Target	Thickness	Diameter [mm]	Density [g/cm <sup>3</sup> ]
<sup>nat</sup> Mo foil	100 μm	13	10.22
<sup>100</sup> Mo foil (99.01% enriched)	100 μm	13	10.22
<sup>nat</sup> MoO <sub>3</sub> pellet	1 mm	13	4.69
<sup>100</sup> MoO <sub>3</sub> pellet (99.01% enriched)	1 mm	13	4.69

MATERIAL	Name: <b>92Mo</b>	#	ρ: 10.22
Z: 42.	Am:	A: 92.	dE/dx: ▼
MATERIAL	Name: <b>94Mo</b>	#	ρ: 10.22
Z: 42.	Am:	A: 94.	dE/dx: ▼
MATERIAL	Name: <b>95Mo</b>	#	ρ: 10.22
Z: 42.	Am:	A: 95.	dE/dx: ▼
MATERIAL	Name: <b>96Mo</b>	#	ρ: 10.22
Z: 42.	Am:	A: 96.	dE/dx: ▼
MATERIAL	Name: <b>97Mo</b>	#	ρ: 10.22
Z: 42.	Am:	A: 97.	dE/dx: ▼
MATERIAL	Name: <b>98Mo</b>	#	ρ: 10.22
Z: 42.	Am:	A: 98.	dE/dx: ▼
MATERIAL	Name: <b>99Mo</b>	#	ρ: 10.22
Z: 42.	Am:	A: 99.	dE/dx: ▼
MATERIAL	Name: <b>100Mo</b>	#	ρ: 10.22
Z: 42.	Am:	A: 100.	dE/dx: ▼
LOW-MAT	Mat: <b>92Mo ▼</b>	LowMat: Mo. Natural Molybdenum (2), 296K ▼	
LOW-MAT	Mat: <b>94Mo ▼</b>	LowMat: Mo. Natural Molybdenum (2), 296K ▼	
LOW-MAT	Mat: <b>95Mo ▼</b>	LowMat: Mo. Natural Molybdenum (2), 296K ▼	
LOW-MAT	Mat: <b>96Mo ▼</b>	LowMat: Mo. Natural Molybdenum (2), 296K ▼	
LOW-MAT	Mat: <b>97Mo ▼</b>	LowMat: Mo. Natural Molybdenum (2), 296K ▼	
LOW-MAT	Mat: <b>98Mo ▼</b>	LowMat: Mo. Natural Molybdenum (2), 296K ▼	
LOW-MAT	Mat: <b>99Mo ▼</b>	LowMat: Mo. Natural Molybdenum (2), 296K ▼	
LOW-MAT	Mat: <b>100Mo ▼</b>	LowMat: Mo. Natural Molybdenum (2), 296K ▼	
MATERIAL	Name: <b>Moarr</b>	#	ρ: 10.22
Z:	Am:	A:	dE/dx: ▼
COMPOUND	Name: <b>Moarr ▼</b>	Mk: Mass ▼	Elements: 7.9 ▼
f1: 0.09	M1: <b>92Mo ▼</b>	f2: 0.06	M2: <b>94Mo ▼</b>
f3: 0.1	M3: <b>95Mo ▼</b>	f4: 0.11	M4: <b>96Mo ▼</b>
f5: 0.08	M5: <b>97Mo ▼</b>	f6: 0.55	M6: <b>98Mo ▼</b>
f7: 99.01	M7: <b>100Mo ▼</b>	f8:	M8: ▼
f9:	M9: ▼		
MATERIAL	Name: <b>TriMo</b>	#	ρ: 4.69
Z:	Am:	A:	dE/dx: ▼
COMPOUND	Name: <b>TriMo ▼</b>	Mk: Atom ▼	Elements: 1.3 ▼
f1: 1.0	M1: <b>Moarr ▼</b>	f2: 3.0	M2: <b>OXYGEN ▼</b>
f3:	M3: ▼		

Figure 3-33 - Example of the definition of the target material (<sup>100</sup>MoO<sub>3</sub>) using the MATERIAL and COMPOUND cards.

Table 3-13 - Natural isotopic abundance for natural and enriched Molybdenum used in the simulations.

Isotope (A)	<sup>nat</sup> Mo	<sup>100</sup> Mo
	Fraction (%)	Fraction (%)
92	14.84	0.09
94	9.25	0.06
95	15.92	0.1
96	16.68	0.1
97	9.55	0.08
98	24.13	0.55
100	9.63	99.01

Data on the different targets simulated are reported in Table 3-12 while isotopic compositions for <sup>nat</sup>Mo (De Bievre & Taylor, 1993) and <sup>100</sup>Mo are reported in Table 3-13. The different target materials were created using several MATERIAL and COMPOUND cards (Figure 3-33).

A 16.5 MeV proton beam was modeled using the BEAM and BEAMPOS cards: a spread out beam, elliptical-shaped, with FWHM<sub>x</sub>=0.71 cm, FWHM<sub>y</sub>=0.51 cm, FWHM<sub>ΔE</sub>=0.0785 MeV and FWHM<sub>Δφ</sub>=0.001 mrad was set to reproduce an average experimental BW of 12.5%. On average 79.8% of the extracted current hit the target material.

NEW-DEFA set with proton transport threshold set to 1 MeV was used; coalescence and evaporation of heavy fragment were enabled through PHYSICS cards and 1hour-1μA irradiation was simulated. Assessment of the saturation yield was conducted off-line through the convolution of proton fluence within the target material to cross section obtained from TALYS simulations (Figure 3-35).

#define	volTar	:=pi*b(target,7)**2*b(target,4)	Unit: 50 BIN	Name: fluence
USRTRACK	Type: Linear	Reg: Target	Emin: =12*MeV	Vol: =volTar
	Part: BEAMPART		Emax: =16.5*MeV	Bins: 18.

Figure 3-34 - Scores used in the assessment of the production of <sup>99m</sup>Tc.

Compared to the results of section 3.3.1 and 3.4 for the <sup>18</sup>F and <sup>41</sup>Ar respectively, in this case we were interested in scoring a nuclide that is in a metastable state. At the moment, FLUKA is not able to reproduce the correct branching ratio between ground and metastable states. By enabling the "Patch Isom" flag in the RADDECAY card it is possible to split (half-half) the production of a specific isotope between ground and isomeric states (if the latter exists). Furthermore other than <sup>99m</sup>Tc, a large number of possible impurities can be produced in a metastable state (Figure 3-35).

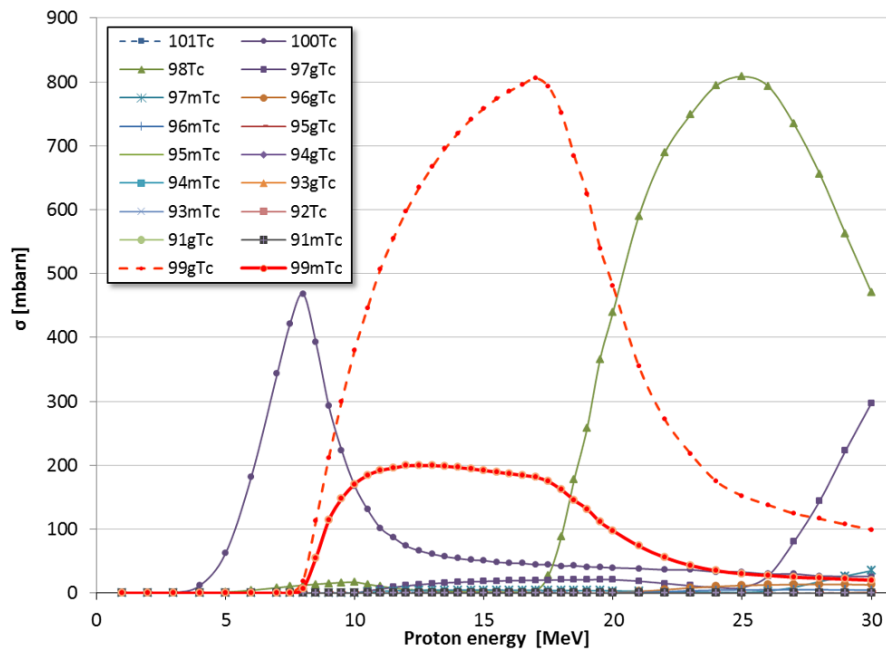


**Figure 3-35 - Cross section data obtained from TALYS simulation for the irradiation with 16.5 MeV protons of a 99.01%  $^{100}\text{Mo}$ -enriched target.**

Considering this aspect, it was decided to switch off the “Patch Isom” flag and to produce all the isotopes at ground state. ECSM takes into account the different branching ratio between ground and metastable states since saturation activity is directly calculated from the correct production cross section.

Moreover, another important aspect is that  $^{99m}\text{Tc}$  can be produced from more than one reaction channel: in the energy range considered the two most probable reactions are  $^{100}\text{Mo}(p,2n)^{99m}\text{Tc}$  and  $^{98}\text{Mo}(p,\gamma)^{99m}\text{Tc}$ . The ECSM was modified to take into account all the reaction channels. The saturation activity for  $^{99m}\text{Tc}$  can be written as

$$A_{sat}(^{99m}\text{Tc}) = \rho V \omega_{100} \frac{N_A}{A_{100}} \int_{E_{out}}^{E_{in}} \phi(E) \sigma_{(p,2n)}(E) dE + \rho V \omega_{98} \frac{N_A}{A_{98}} \int_{E_{out}}^{E_{in}} \phi(E) \sigma_{(p,\gamma)}(E) dE \quad \text{Equation 3-10}$$

Transforming integrals into sum it possible to obtain

$$A_{sat}({}^{99m}\text{Tc}) = \rho V N_A \left[ \sum_{i=E_{out}}^{E_{in}} \phi(E_i) \sigma_{(p,2n)}(E_i) \frac{\omega_{100}}{A_{100}} + \sum_{i=E_{out}}^{E_{in}} \phi(E_i) \sigma_{(p,\gamma)}(E_i) \frac{\omega_{98}}{A_{98}} \right] \quad \text{Equation 3-11}$$

The two terms can be summed up since they work on the same index

$$A_{sat}({}^{99m}\text{Tc}) = \rho V N_A \left[ \sum_{i=E_{out}}^{E_{in}} \phi(E_i) \left( \sigma_{(p,2n)}(E_i) \frac{\omega_{100}}{A_{100}} + \sigma_{(p,\gamma)}(E_i) \frac{\omega_{98}}{A_{98}} \right) \right] \quad \text{Equation 3-12}$$

We can extend what it was found for  ${}^{99m}\text{Tc}$  in Equation 3-12 in a more general formulation over  $M$  reaction channels as reported in Equation 3-13

$$A_{sat} = \rho V N_A \left[ \sum_{i=E_{out}}^{E_{in}} \phi(E_i) \left( \sum_{j=Ch_1}^{Ch_M} \sigma_j(E_i) \frac{\omega_j}{A_j} \right) \right] \quad \text{Equation 3-13}$$

The second sum of Equation 3-13 shows how, for each energy  $E_i$ , the total production cross section, for a given radionuclide, is obtained weighting the single cross sections for all the reaction channels and for the isotopic abundance of the target material. Differential proton fluence distributions in energy obtained using the USRTRACK score are reported in Figure 3-36 and Figure 3-37 for the foil and the pellet respectively.

Results of the simulations were compared with experimental tests conducted from the group of the Medical Physics Department of "S. Orsola-Malpighi" Hospital (Lucconi, et al., 2013; Lucconi, et al., 2014). Measurements were performed through gamma-ray spectrometry using the same detector reported in section 3.4.

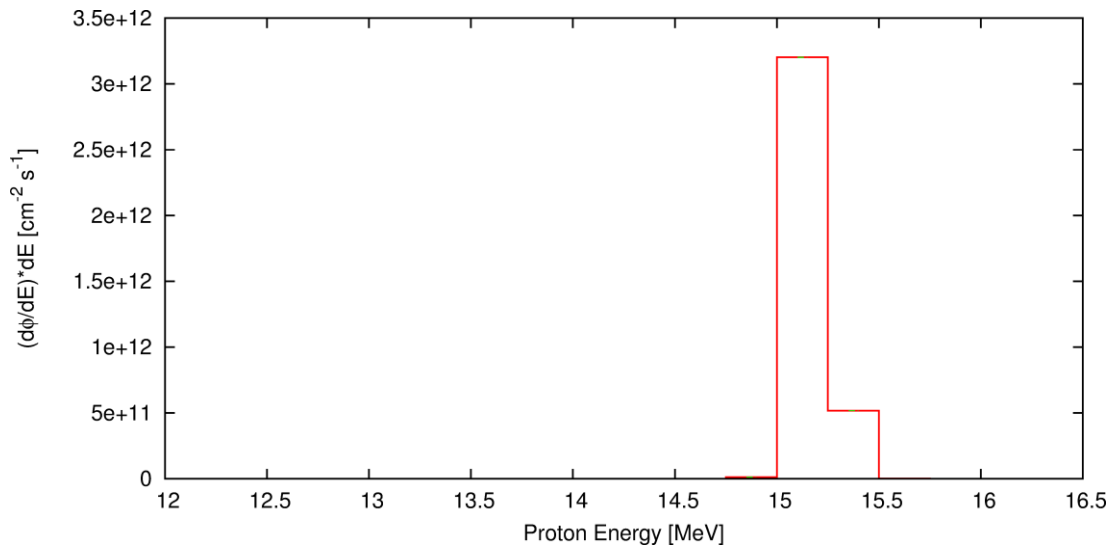


Figure 3-36 - Differential proton fluence distribution in energy within a 100  $\mu\text{m}$  thick  $^{nat}\text{Mo}$  foil target (bin each 0.25 MeV). A similar proton spectrum, within the random uncertainty, was obtained for the enriched target.

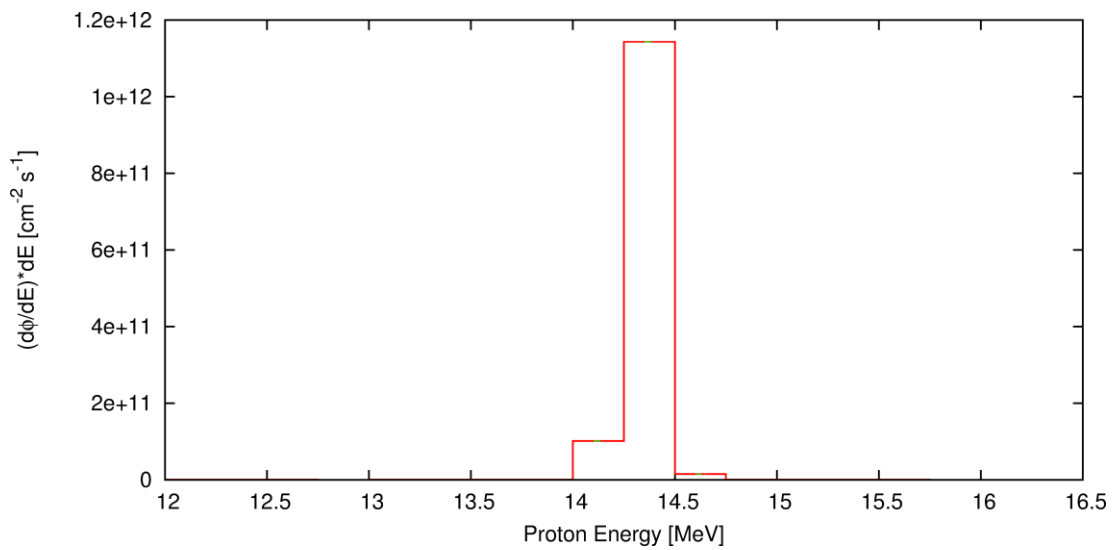


Figure 3-37 - Differential proton fluence distribution in energy within a 1 mm thick  $^{nat}\text{MoO}_3$  pellet (bin each 0.25 MeV). A similar proton spectrum, within the random uncertainty, was obtained for the enriched target.

Table 3-14 - Results of FLUKA simulation of a 100  $\mu\text{m}$  thick  $^{\text{nat}}\text{Mo}$  foil and comparison with experimental measurements.

	$Y_{\text{exp}}$ [MBq/ $\mu\text{A}$ ]	$Y_{\text{FLUKA}}$ [MBq/ $\mu\text{A}$ ]	$Y_{\text{exp}}/Y_{\text{FLUKA}}$
$^{99\text{m}}\text{Tc}$	$110.2 \pm 1.5$	$73.0499 \pm 0.0018$	$1.509 \pm 0.021$
$^{97\text{m}}\text{Tc}$	$170 \pm 90$	$181.584 \pm 0.004$	$0.9 \pm 0.5$
$^{96\text{g}}\text{Tc}$	$388 \pm 4$	$284.431 \pm 0.007$	$1.364 \pm 0.014$
$^{96\text{m}}\text{Tc}$	$375 \pm 13$	$153.227 \pm 0.004$	$2.45 \pm 0.08$
$^{95\text{g}}\text{Tc}$	$448 \pm 5$	$479.743 \pm 0.012$	$0.934 \pm 0.010$
$^{95\text{m}}\text{Tc}$	$166.0 \pm 2.0$	$163.320 \pm 0.004$	$1.016 \pm 0.012$
$^{94\text{g}}\text{Tc}$	$160.0 \pm 2.0$	$425.356 \pm 0.010$	$0.376 \pm 0.005$
$^{94\text{m}}\text{Tc}$	$262.0 \pm 5.0$	$89.2254 \pm 0.0022$	$2.94 \pm 0.06$
$^{93\text{g}}\text{Tc}$	$69.0 \pm 1.0$	$95.2014 \pm 0.0024$	$0.725 \pm 0.011$
$^{93\text{m}}\text{Tc}$	$11.2 \pm 0.4$	$17.5946 \pm 0.0004$	$0.637 \pm 0.023$
$^{92}\text{Tc}$	$290 \pm 60$	$227.032 \pm 0.005$	$1.28 \pm 0.26$
$^{95\text{g}}\text{Nb}$	$12.0 \pm 0.4$	$3.34993 \pm 0.00008$	$3.58 \pm 0.12$
$^{92\text{m}}\text{Nb}$	$3.96 \pm 0.14$	$7.02240 \pm 0.00017$	$0.564 \pm 0.020$
$^{99}\text{Mo}$	$6.18 \pm 0.10$	$2.95731 \pm 0.00007$	$2.09 \pm 0.03$

Table 3-14 shows the results obtained, in terms of saturation yield, for the  $^{\text{nat}}\text{Mo}$  foil target, including the ratio of experimental measurements to FLUKA simulations; an average ratio, weighted on uncertainties, of  $0.664 \pm 0.003$  was found. In Table 3-14, FLUKA results were reported only for the radionuclides found in the experimental measurements.

Regarding the  $^{100}\text{Mo}$  foil, direct experimental measurements were not performed. To assess the saturation yield for the enriched target it is in general necessary to take into account the ratio between the mass fractions of the target isotope into the target material. Actually, considering only one reaction channel, for example the  $^{100}\text{Mo}(p,2n)^{99\text{m}}\text{Tc}$ , the ratio between saturation activity of  $^{99\text{m}}\text{Tc}$  obtained from a  $^{\text{nat}}\text{Mo}$  ( $N$ ) target and a  $^{100}\text{Mo}$ -enriched ( $E$ ) target can be written as

$$\frac{A_{\text{sat}}^N(^{99\text{m}}\text{Tc})}{A_{\text{sat}}^E(^{99\text{m}}\text{Tc})} = \frac{\rho V \omega_{100}^N \frac{N_A}{A_{100}} \int_{E_{\text{out}}}^{E_{\text{in}}} \phi(E) \sigma_{(p,2n)}(E) dE}{\rho V \omega_{100}^E \frac{N_A}{A_{100}} \int_{E_{\text{out}}}^{E_{\text{in}}} \phi(E) \sigma_{(p,2n)}(E) dE} = \frac{\omega_{100}^N}{\omega_{100}^E} \quad \text{Equation 3-14}$$

Unfortunately, as already explained above,  $^{99\text{m}}\text{Tc}$  can be produced from more than one reaction channel. Considering the  $^{100}\text{Mo}(p,2n)^{99\text{m}}\text{Tc}$  and the  $^{98}\text{Mo}(p,\gamma)^{99\text{m}}\text{Tc}$  reaction channels, the ratio of Equation 3-14 becomes

$$\frac{A_{Sat}^N(^{99m}\text{Tc})}{A_{Sat}^E(^{99m}\text{Tc})} = \frac{\rho V N_A \left[ \phi(E_1) \left( \sum_{j=Ch_1}^{Ch_M} \sigma_j(E_1) \frac{\omega_j^N}{A_j} \right) + \phi(E_2) \left( \sum_{j=Ch_1}^{Ch_M} \sigma_j(E_2) \frac{\omega_j^N}{A_j} \right) + \dots \right]}{\rho V N_A \left[ \phi(E_1) \left( \sum_{j=Ch_1}^{Ch_M} \sigma_j(E_1) \frac{\omega_j^E}{A_j} \right) + \phi(E_2) \left( \sum_{j=Ch_1}^{Ch_M} \sigma_j(E_2) \frac{\omega_j^E}{A_j} \right) + \dots \right]} \quad \text{Equation 3-15}$$

Equation 3-15 shows how it is incorrect, in this case, to get the saturation activity for the enriched target, from the value obtained in the irradiation of a natural target, simply considering the different isotopic composition. Table 3-15 shows the experimental saturation yields, calculated from the ones obtained for the natural target, the results of FLUKA simulations and the ratio of experimental to simulation. An average ratio, weighted on uncertainties, of  $0.664 \pm 0.003$  was found for the  $^{100}\text{Mo}$ -enriched foil target.

Table 3-16 shows the results obtained, in terms of saturation yield, for the  $^{\text{nat}}\text{MoO}_3$  pellet target, including the ratio of experimental measurements to FLUKA simulations; an average ratio, weighted on uncertainty, of  $0.486 \pm 0.013$  was found. In Table 3-16, FLUKA results were reported only for the radionuclides found in the experimental measurements.

Table 3-17 shows the results obtained, in terms of saturation yield, for the  $^{100}\text{MoO}_3$  pellet target, including the ratio of experimental measurements to FLUKA simulations; an average ratio, weighted on uncertainty, of  $0.274 \pm 0.008$  was found. In Table 3-17, FLUKA results were reported only for the radionuclides found in the experimental measurements.

**Table 3-15 - Results of FLUKA simulation of a 100  $\mu\text{m}$  thick  $^{100}\text{Mo}$  foil and comparison with experimental measurements.**

	$Y_{exp}$ [MBq/ $\mu\text{A}$ ]	$Y_{FLUKA}$ [MBq/ $\mu\text{A}$ ]	$Y_{exp}/Y_{FLUKA}$
$^{99m}\text{Tc}$	$1127 \pm 15$	$746.954 \pm 0.019$	$1.509 \pm 0.021$
$^{97m}\text{Tc}$	$3.8 \pm 2.0$	$4.04222 \pm 0.00010$	$0.9 \pm 0.5$
$^{96g}\text{Tc}$	$3.07 \pm 0.03$	$2.25031 \pm 0.00006$	$1.364 \pm 0.014$
$^{96m}\text{Tc}$	$2.95 \pm 0.10$	$1.20348 \pm 0.00003$	$2.45 \pm 0.08$
$^{95g}\text{Tc}$	$2.93 \pm 0.03$	$3.14188 \pm 0.00008$	$0.934 \pm 0.010$
$^{95m}\text{Tc}$	$1.091 \pm 0.013$	$1.07317 \pm 0.00003$	$1.016 \pm 0.012$
$^{94g}\text{Tc}$	$1.014 \pm 0.013$	$2.69664 \pm 0.00007$	$0.376 \pm 0.005$
$^{94m}\text{Tc}$	$1.66 \pm 0.03$	$0.564788 \pm 0.000014$	$2.94 \pm 0.06$
$^{93g}\text{Tc}$	$0.465 \pm 0.007$	$0.641427 \pm 0.000017$	$0.725 \pm 0.011$
$^{93m}\text{Tc}$	$0.0756 \pm 0.0027$	$0.118712 \pm 0.000003$	$0.637 \pm 0.023$
$^{92}\text{Tc}$	$1.8 \pm 0.4$	$1.37751 \pm 0.00004$	$1.28 \pm 0.26$
$^{95g}\text{Nb}$	$0.279 \pm 0.009$	$0.0778783 \pm 0.0000020$	$3.58 \pm 0.12$
$^{92m}\text{Nb}$	$0.0250 \pm 0.0009$	$0.0443453 \pm 0.0000011$	$0.564 \pm 0.020$
$^{99}\text{Mo}$	$66.7 \pm 1.1$	$31.9083 \pm 0.0008$	$2.09 \pm 0.03$

**Table 3-16 - Results of FLUKA simulation of a 1 mm thick <sup>nat</sup>MoO<sub>3</sub> pellet and comparison with experimental measurements.**

	$Y_{exp}$ [MBq/ $\mu$ A]	$Y_{FLUKA}$ [MBq/ $\mu$ A]	$Y_{exp}/Y_{FLUKA}$
<sup>101</sup> Tc	1.8 ± 0.7	0.608001 ± 0.000013	2.9 ± 1.2
<sup>99m</sup> Tc	137 ± 8	115.7608 ± 0.0024	1.18 ± 0.07
<sup>97m</sup> Tc	350 ± 40	288.069 ± 0.006	1.21 ± 0.12
<sup>96g</sup> Tc	690 ± 30	470.276 ± 0.010	1.46 ± 0.07
<sup>96m</sup> Tc	790 ± 90	264.201 ± 0.005	3.0 ± 0.3
<sup>95g</sup> Tc	640 ± 40	731.543 ± 0.015	0.87 ± 0.05
<sup>95m</sup> Tc	267 ± 14	247.107 ± 0.005	1.08 ± 0.06
<sup>94g</sup> Tc	152 ± 9	607.675 ± 0.012	0.251 ± 0.015
<sup>94m</sup> Tc	300 ± 40	130.8284 ± 0.0027	2.3 ± 0.3
<sup>93g</sup> Tc	35.4 ± 2.3	40.2793 ± 0.0008	0.88 ± 0.06
<sup>93m</sup> Tc	6.2 ± 1.7	1.39206 ± 0.00005	4.5 ± 1.2
<sup>92</sup> Tc	500 ± 200	322.827 ± 0.007	1.7 ± 0.6
<sup>97</sup> Nb	2.4 ± 0.4	1.62126 ± 0.00003	1.48 ± 0.26
<sup>95g</sup> Nb	17.7 ± 1.1	3.85728 ± 0.00008	4.59 ± 0.29
<sup>95m</sup> Nb	10.1 ± 0.6	0.644841 ± 0.000013	15.6 ± 0.9
<sup>92m</sup> Nb	8.0 ± 0.4	10.32713 ± 0.00021	0.78 ± 0.04
<sup>89g</sup> Nb	2900 ± 500	1.85071 ± 0.00004	1545 ± 290
<sup>99</sup> Mo	11.9 ± 0.6	2.36190 ± 0.00005	5.06 ± 0.27

**Table 3-17 - Results of FLUKA simulation of a 1 mm thick <sup>100</sup>MoO<sub>3</sub> pellet and comparison with experimental measurements.**

	$Y_{exp}$ [MBq/ $\mu$ A]	$Y_{FLUKA}$ [MBq/ $\mu$ A]	$Y_{exp}/Y_{FLUKA}$
<sup>101</sup> Tc	3.9 ± 0.5	6.42349 ± 0.00013	0.60 ± 0.07
<sup>99m</sup> Tc	1320 ± 80	1218.373 ± 0.025	1.08 ± 0.07
<sup>96g</sup> Tc	2.74 ± 0.15	3.75279 ± 0.00008	0.73 ± 0.04
<sup>96m</sup> Tc	15 ± 5	2.09361 ± 0.00004	7.0 ± 2.4
<sup>95g</sup> Tc	2.05 ± 0.11	4.88305 ± 0.00010	0.419 ± 0.024
<sup>95m</sup> Tc	0.82 ± 0.05	1.66230 ± 0.00003	0.496 ± 0.029
<sup>94g</sup> Tc	0.51 ± 0.04	3.96893 ± 0.00008	0.128 ± 0.010
<sup>94m</sup> Tc	0.93 ± 0.12	0.857017 ± 0.000018	1.09 ± 0.14
<sup>93g</sup> Tc	0.27 ± 0.10	0.267992 ± 0.000005	1.0 ± 0.4
<sup>97</sup> Nb	21.5 ± 2.1	17.1286 ± 0.0003	1.26 ± 0.12
<sup>95g</sup> Nb	0.252 ± 0.019	0.0903441 ± 0.0000018	2.79 ± 0.21
<sup>95m</sup> Nb	0.077 ± 0.008	0.0151033 ± 0.0000003	5.1 ± 0.5
<sup>92m</sup> Nb	0.0230 ± 0.0027	0.0666878 ± 0.0000014	0.35 ± 0.04
<sup>99</sup> Mo	108 ± 6	24.9534 ± 0.0005	4.31 ± 0.23

In conclusion the data reported from Table 3-14 to Table 3-17 show that using the ECMS the saturation yield of  $^{99m}\text{Tc}$  is reproduced, considering all the targets, with an overall average experimental to FLUKA ratio of  $1.13 \pm 0.05$ . Even if  $^{99m}\text{Tc}$  is reproduced with a good agreement this it is not true for all the radionuclides produced during the irradiation: the average agreement, for the different targets, resulted spanning in the range 0.3-0.7. The reasons of these results have to be searched both in the experimental measurements and in simulations. Problems in obtaining an accurate measure of activity, in a so complex spectrum, are related to the large number of peaks that can give, in some cases, interference; another critical aspect is the correction of the amount of measured activity due to the possible decay from a parent radionuclide, as happens for example for  $^{99}\text{Mo}/^{99m}\text{Tc}$ . Regarding the simulations, the main source of error might be, in this particular case, to be searched in the cross-section data obtained from TALYS simulation. On the other hand, TALYS was used instead of experimental cross sections since the wide range of data, not always in agreement each other, available in literature.



# ***Chapter 4***

## ***Modeling of TRIUMF TR13 Liquid and Solid Target Assembly***

In this chapter a summary of a project conducted at TRIUMF - Canada's national laboratory for particle and nuclear physics, in the period from 1<sup>st</sup> November 2013 to 28<sup>th</sup> February 2014, under the supervision of Dr. Cornelia Hoehr is reported.

The Monte Carlo code FLUKA was used to simulate the production of a number of established and emerging positron emitting radionuclides,  $^{18}\text{F}$ ,  $^{13}\text{N}$ ,  $^{94}\text{Tc}$ ,  $^{44}\text{Sc}$ ,  $^{68}\text{Ga}$ ,  $^{86}\text{Y}$ ,  $^{89}\text{Zr}$ ,  $^{56}\text{Co}$ ,  $^{52}\text{Mn}$ ,  $^{61}\text{Cu}$  and  $^{55}\text{Co}$ , on a small medical cyclotron with a proton beam energy of 13 MeV. Direct simulated yields agree well with experimental data collected at the TR13 cyclotron at TRIUMF as well as with the convolution of simulated proton fluence and cross sections from literature. A summary of the results obtained is available in (Infantino, et al., 2014b; Infantino, et al., 2015b).

TRIUMF's TR13 cyclotron (FIG) is a self-shielded external ion source cyclotron that accelerates negative hydrogen ions to 13 MeV. The TR13 cyclotron has two extraction ports each with a target selector. On each target selector, four targets can be mounted. The selector is mounted on a bellows and can be moved horizontally and vertically: when a target is selected for irradiation, the bellows moves it into position in the proton beam. Protons are extracted from the cyclotron via carbon extraction foils, stripping off the two electrons, thereby reversing the electric charge of the ion and bending outwards its trajectory in the magnetic field; 25  $\mu\text{A}$  can be routinely extracted onto one target. Details of the cyclotron are given in (Laxdal, et al., 1994; Buckley, et al., 2000). Since the main purpose of the project was the assessment of the saturation yield for the radionuclides reported above, it was decided to model only the liquid and solid target assembly and the collimation system: actually these are the parts which the beam interact with after the extraction.

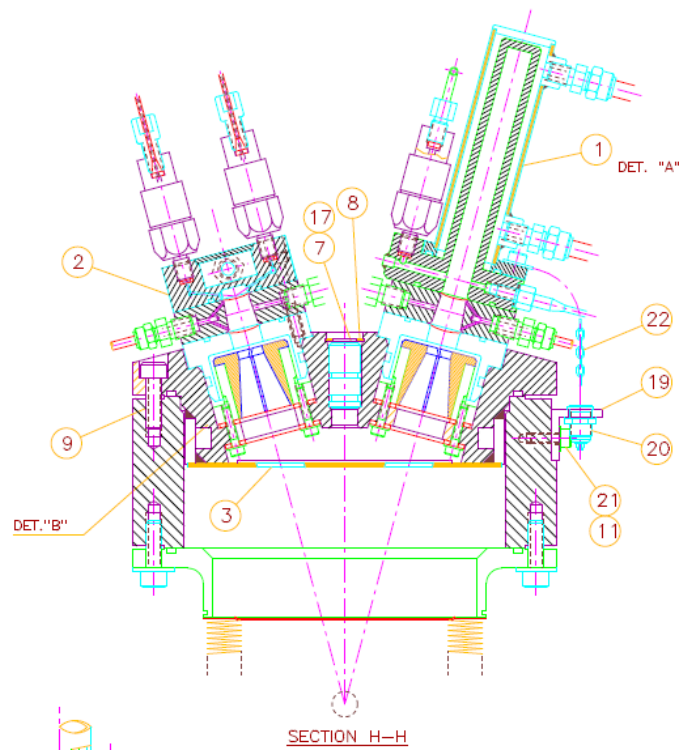


Figure 4-1 - The TRIUMF TR13 cyclotron.

## **4.1 Monte Carlo Model of the TR13 Liquid and Solid Target Assembly**

### **4.1.1 Geometrical model of the targets**

The collimation system and the target assembly, for the liquid and the solid target, of the TR13 cyclotron were modeled on the basis of information taken from original technical drawings. Figure 4-2 shows a section of the target selector in which two different targets are mounted: a liquid (left) and a gas (right) target assembly for the production of  $^{18}\text{F}$  and  $^{11}\text{C}$  respectively. Figure 4-3 shows a detail of the main two components of the TR13 collimation system: the baffle plate and the four pieces-conical collimator.



**Figure 4-2 – Section of the of the target plate: in the figure it is possible to recognize the baffle, two collimator rings (two for each target), the conical collimator (one for each target) composed from four pieces, the liquid and the gas target.**

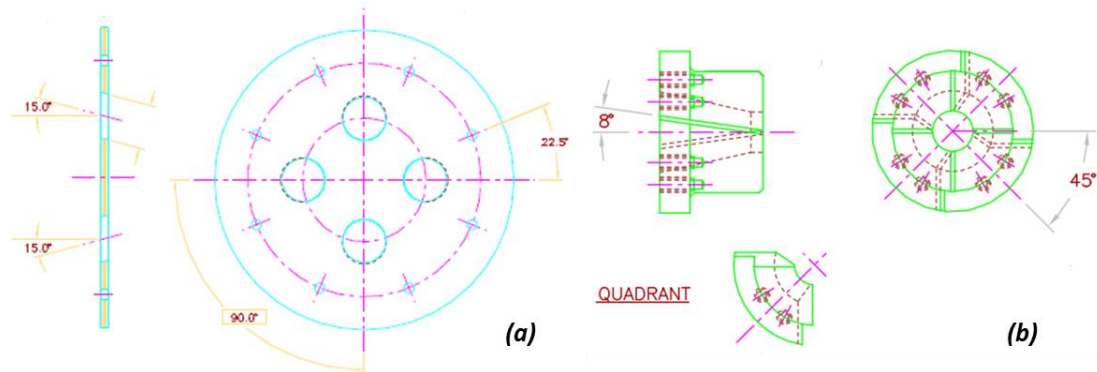


**Figure 4-3 - Detail of the TR13 baffle (a) and four pieces-conical collimator (b).**

The target plate is mounted on a bellows which can be moved horizontally and vertically. On the plate, four targets can be mounted: when a target is selected for irradiation, the bellows moves it in position into the proton beam. The proton beam is first collimated by the baffle (graphite) and then is further collimated by two collimator rings (anodized aluminum) mounted closely together. The proton beam then goes through a conical shaped collimator (graphite) composed from four isolated pieces.

Let now consider the liquid target on the left of Figure 4-2 and Figure 4-4 (a): the target is mounted on the target plate via the insulator flange (anodized aluminum). Then the beam goes through a 32 mm in diameter, 25  $\mu\text{m}$  thick aluminum foil that separates the vacuum from the target assembly. The foil is cooled with a helium flow (10 psi) through the Helium window. Because the helium has to be separated from the target material, a foil of HAVAR, 32 mm in diameter and 39  $\mu\text{m}$  thick, is installed. At the end, the proton beam enters the liquid target material that is contained in a chamber 12 mm in diameter, 8 mm deep. The target body is made out of niobium.

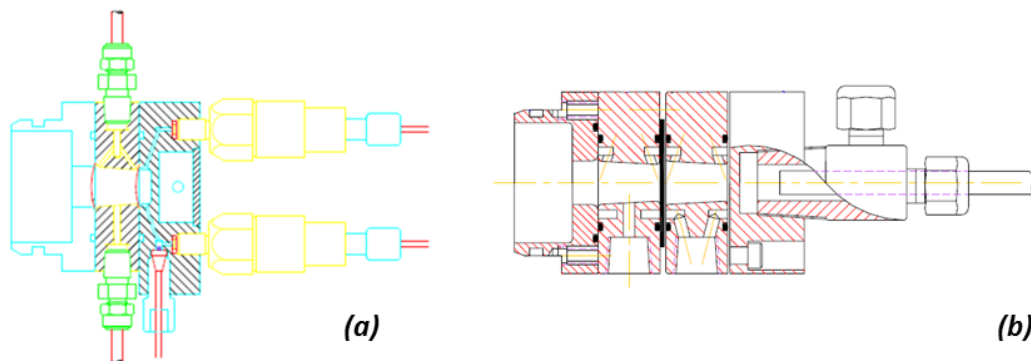


**Figure 4-4 – Section of the original technical drawings of the TR13 liquid (a) and solid (b) target assembly (Buckley, 2006).**

The solid target (Figure 4-4 (b)) is, substantially, a modified liquid target: the target foil, 32 mm in diameter, is mounted instead of the HAVAR foil and another helium window is installed after the target foil to provide cooling from the back. At the end, water cooled aluminum block, acting as beam dump, is mounted close to the system.

Figure 4-5 shows the final FLUKA MC model of the TR13 liquid (a) and the solid (b) target assembly, as they appear in Flair; Figure 4-6 and Figure 4-7 show the 3D obtained using SimpleGeo.

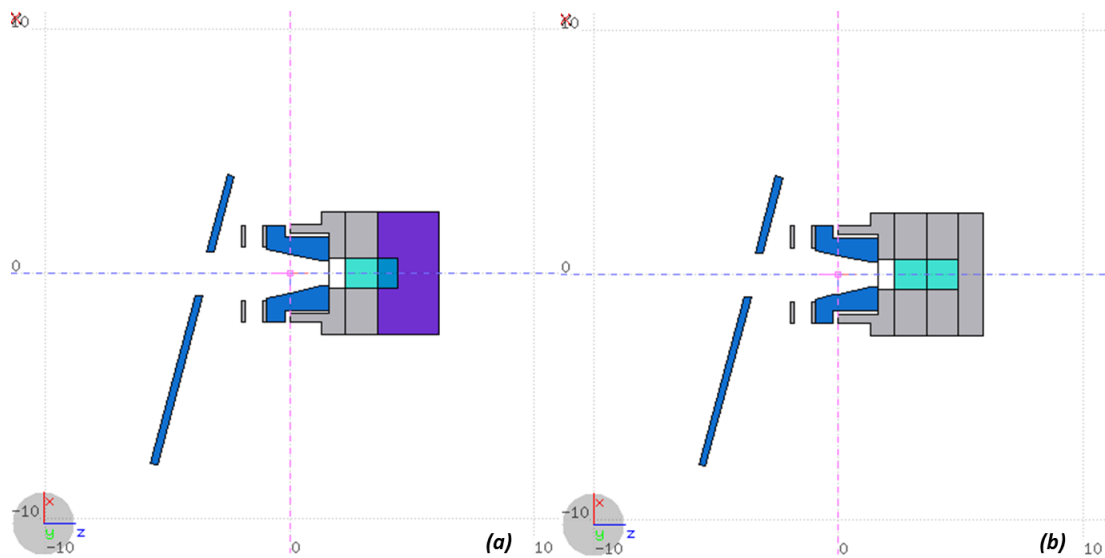


Figure 4-5 – Section of the FLUKA MC model of the liquid (a) and solid (b) target assembly (plane ZX).

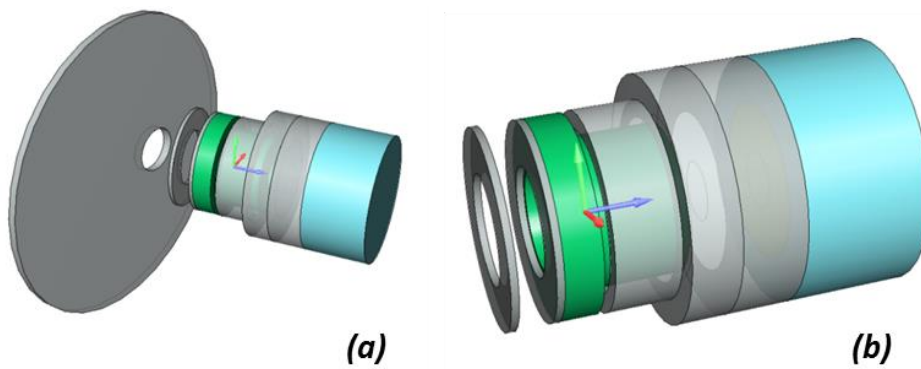


Figure 4-6 – 3D of the FLUKA MC model of the TR13 liquid target with (a) and without (b) the baffle plate.

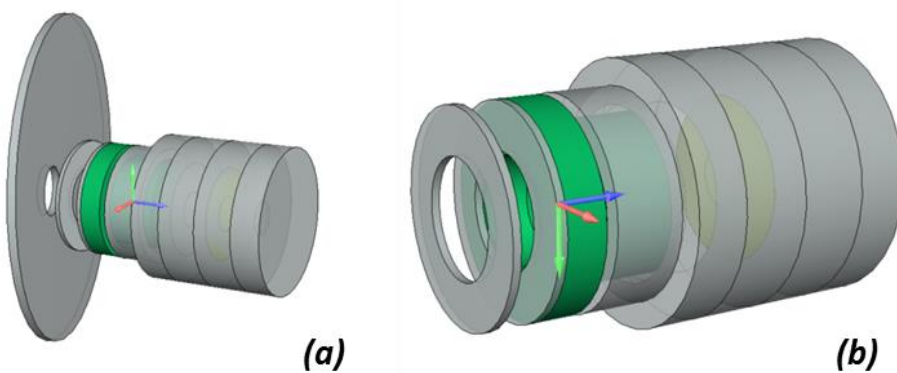


Figure 4-7 – 3D of the FLUKA MC model of the TR13 solid target with (a) and without (b) the baffle plate.

### 4.1.2 Composition of the Targets

In this section, the target composition and specification, as implemented in FLUKA, are presented. A number of nuclear reactions were studied such as  $^{18}\text{O}(p,n)^{18}\text{F}$ ,  $^{nat}\text{O}(p,x)^{13}\text{N}$ ,  $^{nat}\text{Mo}(p,x)^{94m}\text{Tc}$ ,  $^{nat}\text{Ca}(p,x)^{44}\text{Sc}$ ,  $^{nat}\text{Zn}(p,x)^{68}\text{Ga}$ ,  $^{nat}\text{Sr}(p,x)^{86}\text{Y}$ ,  $^{nat}\text{Y}(p,x)^{89}\text{Zr}$ ,  $^{nat}\text{Fe}(p,x)^{56}\text{Co}$ ,  $^{nat}\text{Cr}(p,x)^{52}\text{Mn}$ ,  $^{nat}\text{Zn}(p,x)^{61}\text{Cu}$ ,  $^{nat}\text{Ni}(p,x)^{55}\text{Co}$ . Due to the large number of radionuclide productions studied in this work, the target materials were divided into two overarching categories: liquid targets, which include the water solutions of several salts and solid targets. FLUKA uses the natural isotopic abundance for all elements, but it was decided to input the natural isotopic compositions from the literature (De Bievre & Taylor, 1993) into the code to know the exact atomic content: all the isotopes of an element were created with several *MATERIAL* cards while the final natural element were created using the *COMPOUND* card where the isotopic mass fraction was given. For all the liquid targets, the mass fraction of all the components of the target mixture was calculated and inserted into FLUKA for the definition of the target material. The main features of the target materials used in this work are reported in the following.

Note: The density is the one used inside FLUKA			
<b>MATERIAL</b>	Name: 16O	#	p: 0.001429
z: 8.	Am:	A: 16.	dEdx: ▼
LOW-MAT	Mat: 16O ▼	LowMat: 16O, Oxygen 16, 296K ▼	
<b>MATERIAL</b>	Name: 17O	#	p: 0.001429
z: 8.	Am:	A: 17.	dEdx: ▼
LOW-MAT	Mat: 17O ▼	LowMat: 16O, Oxygen 16, 296K ▼	
<b>MATERIAL</b>	Name: 18O	#	p: 0.001429
z: 8.	Am:	A: 18.	dEdx: ▼
LOW-MAT	Mat: 18O ▼	LowMat: 16O, Oxygen 16, 296K ▼	
<b>MATERIAL</b>	Name: Onat	#	p: 0.001429
z:	Am:	A:	dEdx: ▼
<b>COMPOUND</b>	Name: Onat ▼	Mic: Mass ▼	Elements: 1,3 ▼
f1: 99.757	M1: 16O ▼	f2: 0.038	M2: 17O ▼
f3: 0.205	M2: 18O ▼		
Natural Water	Name: Wat_nat	#	p: 1.0
<b>MATERIAL</b>	Am: Wat_nat	A:	dEdx: ▼
z:			
Material H2_natO	Name: Wat_nat ▼	Mic: Atom ▼	Elements: 1,3 ▼
<b>COMPOUND</b>	M1: HYDROGEN ▼	f2: 1.0	M2: Onat ▼
f1: 2.0	M2: ▼		
f3:			
Hydrogen Peroxide	Name: Peroxi	#	p: 1.11
<b>MATERIAL</b>	Am: Peroxi	A:	dEdx: ▼
z:			
Hydrogen Peroxide	Name: Peroxi ▼	Mic: Atom ▼	Elements: 1,3 ▼
<b>COMPOUND</b>	M1: HYDROGEN ▼	f2: 2.0	M2: OXYGEN ▼
f1: 2.0	M2: ▼		
f3:			
Target Solution mix	Name: TarSol	#	p: 1.
<b>MATERIAL</b>	Am: TarSol	A:	dEdx: ▼
z:			
Target Solution 99.5% Natural Water and 0.5% Hydrogen Peroxide	Name: TarSol ▼	Mic: Mass ▼	Elements: 1,3 ▼
<b>COMPOUND</b>	M1: Wat_nat ▼	f2: 0.006	M2: Peroxi ▼
f1: 0.994	M2: ▼		
f3:			

Figure 4-8 - Example of the definition of a complex target material: a solution of water+HNO<sub>3</sub> was created using several MATERIAL and COMPOUND cards.

#### 4.1.2.1 O-18

The target was composed of enriched  $^{18}\text{O}$ -water (96% in volume) with a solution density of  $1\text{ g/cm}^3$ . The mass fractions calculated were  $\omega_{^{18}\text{O}\text{wat}}=0.96$  and  $\omega_{\text{wat}}=0.04$  respectively.

#### 4.1.2.2 O-nat

The target was composed of deionised water with 0.5% in volume of hydrogen peroxide ( $\text{H}_2\text{O}_2$ ) with a solution density of  $1\text{ g/cm}^3$ . The mass fractions calculated

were  $\omega_{\text{wat}}=0.994$  and  $\omega_{\text{per}}=0.006$  respectively. The natural isotopic abundance used in the simulation for Oxygen is reported in Table 4-1.

*Table 4-1 - Natural isotopic abundance of natural Oxygen.*

<i>Isotope (A)</i>	<i>Fraction (%)</i>
16	99.757
17	0.038
18	0.205

#### 4.1.2.3 Mo-nat

The salt used as target was ammonium molybdate tetrahydrate  $(\text{NH}_4)_6^{\text{nat}}\text{Mo}_7\text{O}_{24}\cdot 4\text{H}_2\text{O}$ : 19.9 g of salt were dissolved in 12 ml water and 1.2 ml hydrogen peroxide ( $\text{H}_2\text{O}_2$ ). The salt density was  $2.498 \text{ g/cm}^3$  while the final solution density was  $0.995 \text{ g/cm}^3$ . The mass fractions calculated were  $\omega_{\text{salt}}=0.599$ ,  $\omega_{\text{wat}}=0.361$  and  $\omega_{\text{per}}=0.040$  respectively. The natural isotopic abundance used in the simulation for natural Molybdenum is reported in Table 4-2 (Hoehr, et al., 2012).

*Table 4-2 - Natural isotopic abundance of natural Molybdenum.*

<i>Isotope (A)</i>	<i>Fraction (%)</i>
92	14.84
94	9.25
95	15.92
96	16.68
97	9.55
98	24.13
100	9.63

#### 4.1.2.4 Ca-nat

Two different targets were simulated: a liquid target (a salt of Calcium dissolved in water) and a solid target. The natural isotopic abundance of Calcium is reported in Table 4-3. The salt used as target was Calcium nitrate tetrahydrate  $^{\text{nat}}\text{Ca}(\text{NO}_3)_2\cdot 4\text{H}_2\text{O}$ : 54 g of salt were dissolved in 25 ml water.

*Table 4-3 - Natural isotopic abundance of natural Calcium.*

<i>Isotope (A)</i>	<i>Fraction (%)</i>
40	96.940
42	0.647
43	0.135
44	2.086
46	0.004
48	0.187

The salt density was 1.82 g/cm<sup>3</sup> while the final solution density was 1.55 g/cm<sup>3</sup>. The mass fractions calculated were  $\omega_{\text{salt}}=0.684$  and  $\omega_{\text{wat}}=0.316$  respectively. The solid target was a foil, 1.26 cm<sup>2</sup> of surface and 2.5 mm thick, of Ca 99.99% pure. An Aluminum foil, same surface as the target and 0.0125 mm thick, was placed in front of the target to protect the cyclotron from the vaporized calcium (Severin, et al., 2012). The density of Calcium was 1.55 g/cm<sup>3</sup>.

#### 4.1.2.5 Zn-nat

Two different targets were simulated: a liquid target (a salt of Zinc dissolved in water) and a solid target. The natural isotopic abundance of Zinc is reported in Table 4-4. The salt used as target was Zinc nitrate hexahydrate <sup>nat</sup>Zn(NO<sub>3</sub>)<sub>2</sub>·6H<sub>2</sub>O: 75 g of salt were dissolved in 22.7 ml of water and 2.3 ml of HNO<sub>3</sub> 1M. The salt density was 2.065 g/cm<sup>3</sup> while the final solution density was 1.56 g/cm<sup>3</sup>. The mass fractions calculated were  $\omega_{\text{salt}}=0.743$ ,  $\omega_{\text{wat}}=0.225$  and  $\omega_{\text{acid}}=0.032$  respectively. The solid target was a foil, 32 mm in diameter and 0.1 mm thick, of Cr 99.95% pure. The density of Zinc was 7.133 g/cm<sup>3</sup>.

Table 4-4 - Natural isotopic abundance of natural Zinc.

Isotope (A)	Fraction (%)
64	48.63
66	27.90
67	4.10
68	18.75
70	0.62

#### 4.1.2.6 Sr-nat

The salt used as target was strontium nitrate <sup>nat</sup>Sr(NO<sub>3</sub>)<sub>2</sub>: 43.6 g of salt were dissolved in 25 ml water. The salt density was 2.98 g/cm<sup>3</sup> while the final solution density was 1.43 g/cm<sup>3</sup>. The mass fractions calculated were  $\omega_{\text{salt}}=0.636$  and  $\omega_{\text{wat}}=0.364$  respectively. The natural isotopic abundance of Strontium is reported in Table 4-5.

Table 4-5 - Natural isotopic abundance of natural Strontium.

Isotope (A)	Fraction (%)
84	0.56
86	9.86
87	7.00
88	82.58

#### 4.1.2.7 Y-nat

The salt used as target was Yttrium (III) nitrate hexahydrate <sup>nat</sup>Y (NO<sub>3</sub>)<sub>3</sub>·6H<sub>2</sub>O: 37.46 g of salt were dissolved in 33.735 ml water and 2.265 ml of HNO<sub>3</sub> 1M. The salt

density was  $2.682 \text{ g/cm}^3$  while the final solution density was  $1.43 \text{ g/cm}^3$ . The mass fractions calculated were  $\omega_{\text{salt}}=0.504$ ,  $\omega_{\text{wat}}=0.454$  and  $\omega_{\text{acid}}=0.043$  respectively. The natural isotopic abundance of Yttrium is reported in Table 4-6.

*Table 4-6 - Natural isotopic abundance of natural Yttrium.*

<i>Isotope (A)</i>	<i>Fraction (%)</i>
89	100

#### **4.1.2.8 Fe-nat**

The target was a foil, 32 mm in diameter and 0.1 mm thick, of Fe 99.99% pure. An additional collimator in Aluminum, 32 mm in diameter and 0.7 mm thick, with a hole of 5 mm in diameter at the centre was placed in front of the target. Simulations were performed with and without the Al collimator. The density of Iron was  $7.784 \text{ g/cm}^3$  and its natural isotopic abundance is reported in Table 4-7.

*Table 4-7 - Natural isotopic abundance of natural Iron.*

<i>Isotope (A)</i>	<i>Fraction (%)</i>
54	5.845
56	91.754
57	2.119
58	0.282

#### **4.1.2.9 Cr-nat**

The target was a foil, 32 mm in diameter and 0.5 mm thick, of Cr 99.99% pure. The density of Chromium was  $7.18 \text{ g/cm}^3$  and its natural isotopic abundance is reported in Table 4-8.

*Table 4-8 - Natural isotopic abundance of natural Chromium.*

<i>Isotope (A)</i>	<i>Fraction (%)</i>
50	4.4
52	83.8
53	9.5
54	2.4

#### **4.1.2.10 Ni-nat**

The target was a foil, 32 mm in diameter and 0.25 mm thick, of Ni 99.98% pure. The density of Nickel was  $8.902 \text{ g/cm}^3$  and its natural isotopic abundance is reported in Table 4-9.

Table 4-9 - Natural isotopic abundance of natural Nickel.

Isotope (A)	Fraction (%)
58	68.07
60	26.22
61	1.114
62	3.63
64	0.93

### 4.1.3 Beam Analysis and Modelling

A high level of detail was reached in the geometrical model, and an accurate modeling of the source term, the proton beam, was necessary. In FLUKA, the BEAM card can easily model a particle beam: as shown in section 3.2 this card requires several parameters such as particle energy, momentum spread, beam divergence, and beam shape. To find the parameters that best approximate the real beam, data were taken from (Laxdal, et al., 1994), (Papash, 1993) and from in-house experimental measurements. The control system of the cyclotron records the current measured on the extraction foil, the baffle, the conical collimator and the target throughout the entire irradiation. To find reference values for the mean behavior of a realistic beam, data from eight different irradiations on three different targets mounted on both extraction ports over the course of a week with proton beam currents on the targets ranging from 10  $\mu\text{A}$  to 25  $\mu\text{A}$  were averaged normalized to the sum of the total extracted current.

The beam was then simulated with FLUKA, starting from the theoretical data as discussed in (Laxdal, et al., 1994) and (Papash, 1993), with a Gaussian distribution in energy and in divergence, and an elliptical shape in the plane perpendicular to the direction of the beam, with a Gaussian distribution on both the x and y-direction, perpendicular to the beam-direction z. Through an iterative process, the beam parameters in the simulation were adjusted and the beam currents on the baffle, collimator and target assessed via the current estimator *USRBDX* until the current on these components best matched the experimental data. The *USRBDX* score gave directly the ratio  $I_I$  between the particles crossing the surface (current) of the region considered and the total primary particles simulated. Since the very short range of protons in the materials which composed the baffle, the collimation system and the target, at the energy considered, it is possible to assume that all the particles that enter a region are absorbed and consequently give a current signal to the measurement system. An assessment of the proton range in these materials was conducted using the software SRIM (Ziegler, et al., 2010). If we call  $I_R$  the current in the region of interest,  $I_S$  the proton current at the probe and if we consider a unitary surface, we can write the following relationship between the currents:

$$I_1 \left[ \frac{\text{beam particles}}{\text{primary particles}} \right] = \frac{I_R [\mu A]}{I_S [\mu A]} \quad \text{Equation 4-1}$$

The agreement between the averaged experimental measurements and FLUKA simulations is summarized in Table 4-10.

**Table 4-10 - Comparison of extracted beam currents on several extraction elements between FLUKA and the averaged experiment (at 2-sigma level). The beam currents on the different elements are normalized to the sum of the total extracted current (Infantino, et al., 2015b).**

	Baffle	Conical collimator (sum of 4 pieces)	Target
	Normalized current (%)		
<b>FLUKA simulation</b>	$0.33 \pm 0.16$	$13.63 \pm 0.16$	$85.9881 \pm 0.0026$
<b>Experiment (k=2)</b>	$0.61 \pm 0.28$	$14.0 \pm 2.4$	$90 \pm 6$

A *USRBIN* score, Cartesian mesh, was added to visualize the fluence of primary particle as additional check (Figure 4-9 and Figure 4-10). From this study, the best parameters to approximate the mean behavior of the beam were found to be  $\text{FWHM}_x=0.69$  cm and  $\text{FWHM}_y=0.41$  cm, an energy spread  $\text{FWHM}_{\Delta E}=298.3$  keV and a beam divergence of  $\text{FWHM}_{\Delta\theta}=11.775$  mrad.

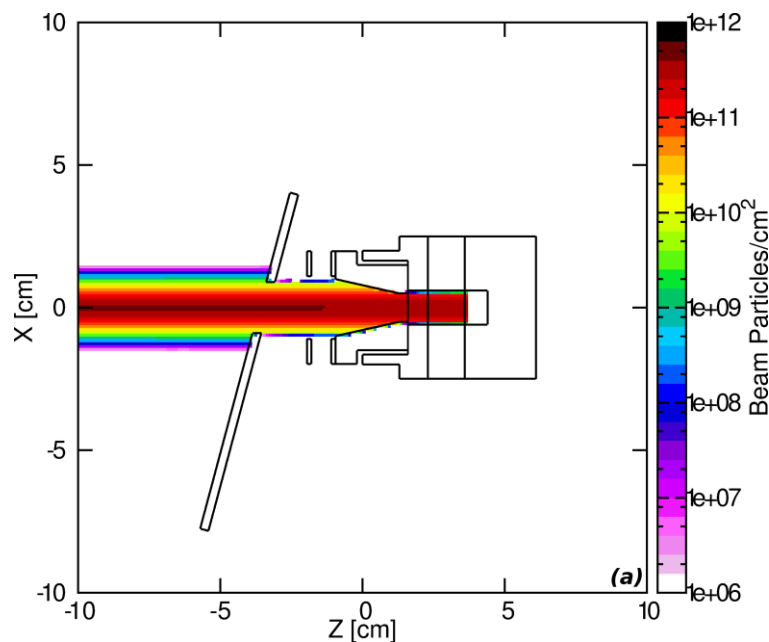


**Figure 4-9 - Proton beam intensity impinging onto the collimator and target in the xz plane (y=0).**

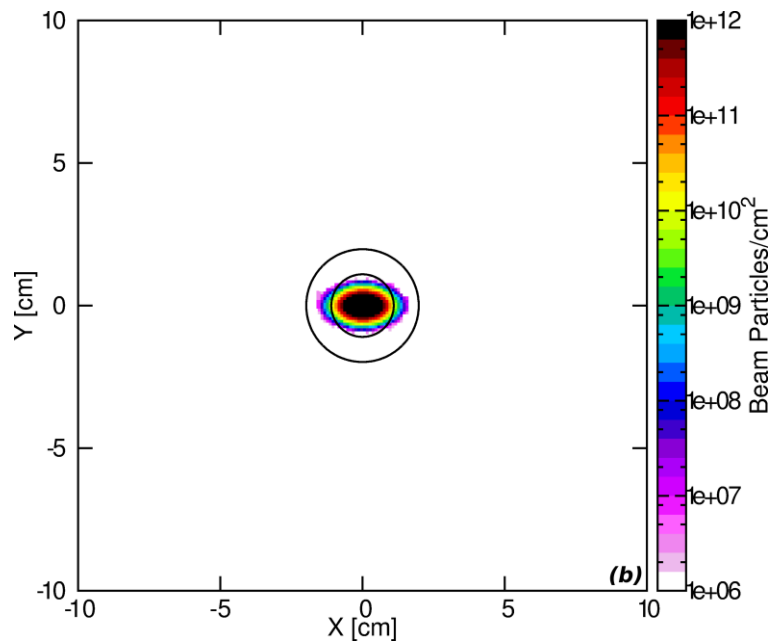


Figure 4-10 - Proton beam intensity impinging onto the collimator and target in the  $xy$  plane ( $z=0$ ).

Proton beam energies of 12 and 12.5 MeV were set for liquid and solid targets respectively. In Figure 4-11 the definition of the beam used in the simulation is reported.

#define	xmax	:1.75			
#define	ymax	:1.05			
#define	Eprot	:12*MeV			
#define	dE	:380*keV			
#define	dpmx	:dE2dp(Eprot, dE, mPROTON)			
Define the beam characteristics					
BEAM	Beam: Energy	:E	:0.012	Part: PROTON	
	Δp: Gauss	:Δp:=(2.355/(2*1.644))*dpmx	Δφ: Gauss	Δφ:11.775	
	Shape(X): Gauss	Δx:=(2.355/6)*xmax	Shape(Y): Gauss	Δy:=(2.355/6)*ymax	
Define the beam position					
BEAMPOS	x:	0.0	y:	0.0	z:-12.93
	cosx:	0.0	cosy:	0.0	Type: POSITIVE

Figure 4-11 - Definition of the proton beam used in the simulation of the TR13 liquid target assembly.

#### 4.1.4 Physical Parameters and Scores

The *NEW-DEFA* default was used and proton transport threshold was set to 1 MeV through the *PART-THR* card. Radiation decay was activated in analogue mode (*RADDECAY* card) and all the isotopes were simulated to be produced in their ground state. An irradiation profile of 1hour-1μA was set for all the simulations. For the calculation of the differential proton fluence distribution  $d\phi(E)/dE$  inside the target region, two more cards were added: with the card *MCSTHRES* the Multiple Coulomb Scattering (MCS) for primary and secondary protons was enabled while with the card *FLUKAFIX* the loss of energy at every step, for charged hadrons, was set to 0.01 (1% of the initial energy). The *FLUKAFIX* card does not modify the number of

protons<sup>21</sup> in the volume but only the resolution of the spectrum since in FLUKA, energy loss for protons is treated as a discrete process (Ferrari, et al., 2011).



Figure 4-12 – MCSTHRES and FLUKAFIX cards used in the simulation of the TR13 target assembly.

Two different score types were used: the *RESNUCLE* and the *USRTRACK* score. The *RESNUCLE* card allowed to directly assess the activity produced at the end of bombardment. The *USRTRACK* score was used to calculate the differential proton fluence distribution in energy inside the target region on an energy-binning basis to apply the external cross section method: the size of the binning was chosen on the basis of the cross section data retrieved from the IAEA (IAEA, 2011a) and EXFOR (IAEA, 2014) database. To achieve high statistics and a lower than 1% uncertainty in the activity and proton fluence scored,  $10^{10}$  primary particles were simulated for all the reactions. Simulations were performed on the WestGrid Cluster (WestGrid, 2013).

## 4.2 Results of the Simulations

### 4.2.1 Reference Values

The experimental (and literature) values used for the comparison with FLUKA are listed in Table 4-11. For each isotope, the saturation yield  $Y_{exp}$  and the number of irradiations conducted are reported. The  $^{44g}\text{Sc}$  (solid target) measurement is not related to TR13 but is added to compare the liquid target performance to a solid target. The notation “TR13” was used for unpublished experimental values. The saturation yields were normalized to the beam current on the target material. For all the experimental values, a statistical analysis was conducted. Since the large fluctuation on the irradiation parameters from an irradiation to another, the mean value of the saturation yield and the standard deviation of the mean, for each isotope, was calculated by weighting the single uncertainties of the measurements using Equation 3-4 and Equation 3-5. Experimental values were obtained from gamma-ray spectrometry analysis: all the calculations were performed starting from the raw data of activity at the EOB and from the uncertainties in the single measurements.

<sup>21</sup> This was verified by the comparison of the integral of several spectra obtained with different values of the FLUKAFIX option.

Table 4-11 - Experimental (and literature) values of the saturation yield for the radioisotopes of interest.

<i>Isotope</i>	<i>Y<sub>exp</sub></i> <i>[MBq/μA]</i>	<i>Number of</i> <i>Irradiations</i>	<i>Reference</i>
<b>Liquid targets</b>			
<sup>44</sup> Sc	4.9 ± 0.3	9	(Hoehr, et al., 2013)
<sup>68</sup> Ga	137.8 ± 1.7	3	TR13
<sup>86</sup> Y	36.4 ± 0.6	3	TR13
<sup>94</sup> Tc	49 ± 6	3	(Hoehr, et al., 2012)
<sup>89</sup> Zr	346.4 ± 2.4	6	TR13
<sup>18</sup> F	4930 ± 60	9	TR13
<sup>13</sup> N	259 ± 3	12	TR13
<b>Solid targets</b>			
<sup>44</sup> Sc (Solid target)	215 ± 15	n/a	(Severin, et al., 2012)
<sup>56</sup> Co	1400 ± 200	5	(Buckley, 2006)
<sup>52</sup> Mn	900 ± 100	4	(Topping, et al., 2013)
<sup>61</sup> Cu	130 ± 17	3	TR13
<sup>55</sup> Co	181 ± 22	1	(Ferreira, et al., 2007)

### 4.2.2 Direct Assessment

The direct assessment of the saturation yields with FLUKA was performed using two different setups of the BEAM card: in the first case, a perfect pencil beam was simulated; the second case refers to a spread out beam in both direction and energy as determined in section 4.1.3.

The model was validated by comparing the result obtained for the  $^{18}\text{O}(p,n)^{18}\text{F}$  reaction ( $8191.2 \pm 2.2$  MBq/μA) with the recommended saturation yield provided by the IAEA Nuclear Data Service (9527 MBq/μA) (IAEA, 2011a). The ratio of simulated yield using a pencil beam to IAEA was  $0.86 \pm 0.09$ .

The comparison of the results obtained with FLUKA to the experimental values is reported in Table 4-12 where  $Y_P$  and  $Y_{SE}$  refer to the saturation yields obtained with the pencil beam and the spread out beam, respectively. The saturation yields are both normalized to the current reaching the target material. Given the limitation of FLUKA to predict the correct branching ratio for the production of metastable states, the experimental value for <sup>44</sup>Sc (Liquid target) and <sup>94</sup>Tc was given as the sum of the saturation yield of the ground and the metastable states. For all isotopes, the experimental saturation yield was smaller than the simulated saturation yield. This can be explained again with losses in the transfer system for the liquid target, as well as losses in the vials when the solid targets are dissolved before the gamma spectroscopy takes place.

**Table 4-12 - Comparison of the saturation yields obtained with FLUKA with the pencil beam ( $Y_P$ ) and the spread out beam in direction and energy ( $Y_{SE}$ ) to the experimental values ( $Y_{exp}$ ). The saturation yields are both normalized to the current on the target material.**

Isotope	$Y_{exp}/Y_P$	$Y_{exp}/Y_{SE}$
<b>Liquid targets</b>		
<sup>44</sup> Sc	0.43 ± 0.03	0.42 ± 0.03
<sup>68</sup> Ga	0.972 ± 0.012	0.969 ± 0.012
<sup>86</sup> Y	1.108 ± 0.018	1.111 ± 0.018
<sup>94</sup> Tc	0.65 ± 0.08	0.65 ± 0.08
<sup>89</sup> Zr	1.152 ± 0.008	1.151 ± 0.008
<sup>18</sup> F	0.601 ± 0.007	0.601 ± 0.007
<sup>13</sup> N	0.1686 ± 0.0020	0.1659 ± 0.0019
<b>Solid targets</b>		
<sup>44</sup> Sc	0.82 ± 0.06	0.83 ± 0.06
<sup>56</sup> Co	0.61 ± 0.07	1.29 ± 0.15
<sup>52</sup> Mn	0.211 ± 0.024	0.211 ± 0.024
<sup>61</sup> Cu	0.32 ± 0.04	0.32 ± 0.04
<sup>55</sup> Co	3.3 ± 0.4	3.4 ± 0.4

The only exception was <sup>55</sup>Co with an experimental saturation yield about 3 times higher than both simulated saturation yields. From the EXFOR database it was possible to retrieve data about the cross section of the <sup>58</sup>Ni( $p, \alpha$ )<sup>55</sup>Co reaction (Levkovskij, 1991). No resonances or an energy threshold in the energy range of interest are reported that could explain the discrepancy. Results obtained for the production of <sup>55</sup>Co from references (Brugger, et al., 2007; Brugger, et al., 2006; Brugger, et al., 2004) were in good agreement with experimental values within a factor of 2: in these references the production was for a higher energy range and with different starting material, therefore using completely different cross sections. In conclusion, the model implemented in FLUKA may not adequately predict the production of <sup>58</sup>Ni( $p, \alpha$ )<sup>55</sup>Co at low energies.

From Table 4-12 it is possible to calculate the average ratio for both liquid and solid targets as well as the total average for all the radionuclides studied. These data are reported in Table 4-13.

**Table 4-13 - Average values of the ratio of the  $Y_{exp}$  to  $Y_P$  and  $Y_{SE}$  for both liquid and solid targets and total average for all the radionuclides studied.**

	$Y_{exp}/Y_P$	$Y_{exp}/Y_{SE}$
<b>Liquid targets</b>	0.7 ± 0.4	0.7 ± 0.4
<b>Solid targets</b>	1.1 ± 1.3	1.2 ± 1.3
<b>Total average</b>	0.9 ± 0.8	0.9 ± 0.9

From Table 4-13, one can see that there is reasonably good agreement between the simulated and the experimental data for liquid targets and a somewhat less consistent agreement for solid targets. Especially regarding liquid targets, the results obtained are very good if we consider that Monte Carlo does not take into account factors such as thermal and fluid-dynamic effects such as a density reduction, as well as loss of activity during delivery from the cyclotron in the transfer system. Results obtained for solid targets might be affected also from the very small thickness of the target material.

In Table 4-14, the comparison between the saturation activities obtained using the pencil beam, the spread out beam and the experimental values is reported. It is important to remember that in the pencil beam setup, the beam is in ideal conditions: the beam is perfectly aligned with the target and there is no spread in direction and energy; moreover, there is no loss or scattering of particles in the collimation system. Therefore, when the spread out beam is used, the simulated proton beam is much closer to the experimental beam and the agreement is better. In (Brugger, et al., 2006) the ability of FLUKA to predict the induced activity in a medium was reported: a proton beam of 120 GeV on different target materials (copper, iron, titanium, stainless steel, aluminum, and concrete) was simulated and the results were compared with experimental values. In this publication a comparison of the results obtained with a pencil beam to a Gaussian beam gave a difference of about 30%. In this work the difference between the saturation

**Table 4-14 - Comparison of the saturation activities obtained with FLUKA with the pencil beam ( $A_{satP}$ ) and the spread out beam in direction and energy ( $A_{satSE}$ ). The saturation activities take into account the current on the target material.**

<i>Isotope</i>	$A_{satP}$ [MBq/ $\mu$ A]	$A_{satSE}$ [MBq/ $\mu$ A]	$A_{satSE}/A_{satP}$
<b>Liquid targets</b>			
<sup>44</sup> Sc	11.39 ± 0.08	9.98 ± 0.08	0.876 ± 0.010
<sup>68</sup> Ga	141.7 ± 0.3	122.20 ± 0.28	0.863 ± 0.003
<sup>86</sup> Y	32.90 ± 0.15	28.20 ± 0.14	0.857 ± 0.006
<sup>94</sup> Tc	75.58 ± 0.22	65.28 ± 0.21	0.864 ± 0.004
<sup>89</sup> Zr	300.7 ± 0.4	258.7 ± 0.4	0.8605 ± 0.0018
<sup>18</sup> F	8191.2 ± 2.2	7047.0 ± 2.1	0.8603 ± 0.0003
<sup>13</sup> N	1536.4 ± 1.0	1342.8 ± 1.0	0.8740 ± 0.0008
<b>Solid targets</b>			
<sup>44</sup> Sc	260.7 ± 0.4	223.4 ± 0.4	0.8571 ± 0.0020
<sup>56</sup> Co	2349.6 ± 1.2	860.0 ± 0.8	0.3660 ± 0.0004
<sup>52</sup> Mn	4154.0 ± 1.7	3572.7 ± 1.5	0.8601 ± 0.0005
<sup>61</sup> Cu	407.3 ± 0.5	349.6 ± 0.5	0.8584 ± 0.0016
<sup>55</sup> Co	54.13 ± 0.18	46.38 ± 0.18	0.857 ± 0.004

activities obtained with the pencil beam,  $A_{satP}$ , and the spread out beam in direction and energy,  $A_{satSE}$ , was about 15%, showing the same trend as Brugger *et al.* The  $^{56}\text{Co}$  production differs from this trend as  $A_{satSE}/A_{satP}$  is 0.3660 instead of the average  $\sim 0.86$  for all other reactions. This is due to the presence of an additional collimator in front of the target foil to limit the size of the activation area on the foil. The additional collimator is a disk of aluminum, 0.7 mm thick with a 5 mm inner diameter. The energy spectrum in the target disk obtained in FLUKA with this additional collimator shows that protons are not completely stopped by the collimator, but only have their energy reduced to 5.3 MeV. This is close to the energy threshold for the  $^{nat}\text{Fe}(p,x)^{56}\text{Co}$  reaction (Al-Abyad, et al., 2009). While with a pencil beam all protons passing through the collimator might contribute to the  $^{56}\text{Co}$  production in the simulation, in the case of the spread-out beam only a portion might have enough energy. The effect of the reduced proton flux might be larger than the increased energy of some of the protons in the FLUKA-internal production mechanism, resulting in a much reduced saturation activity.

### 4.2.3 External Cross Sections Method (ECSM)

Similarly to what seen in section 3.4, the external cross section method was applied to all the reactions studied. Actually, the saturation activity can be written as

$$A_{sat} \cong \rho V \omega_x \frac{N_A}{A_x} N_p \sum_{i=E_{out}}^{E_{in}} F(E_i) \sigma_{xy}(E_i) \Delta E_i \quad \text{Equation 4-2}$$

where  $E_{in}$  and  $E_{out}$  are the energies of the incoming and outgoing proton beam respectively. The other symbols have the same meaning of Equation 3-8. When possible the cross section data and the recommended saturation yields, used in the validation of the method, were retrieved from the IAEA Nuclear Data Service (IAEA, 2011a; IAEA, 2011b). The *USRTRACK* score was set to have the same energy bin size (in general 0.1 MeV) and the same energy range as in the IAEA cross section data. In all the other cases, the cross section data was retrieved from the EXFOR database (IAEA, 2014) and was chosen considering the year of publication and the energy range. To automatically perform the folding between the external cross sections and the fluence data of the *USRTRACK*, a dedicated MATLAB script was written. The script worked with ASCII cross section files formatted as in the IAEA Nuclear Data Services database. Moreover the script provided also the fitting of the cross section data to have the corresponding value every 0.1 MeV, an assessment of the *coefficient of determination*  $R^2$  of the fitting and the *uncertainty of the convolution*,  $\delta A_{sat}$ , calculated by the propagation of the independent uncertainties of the cross section data and the fluence. Finally, the saturation yield  $Y_{CS}$  in MBq/ $\mu\text{A}$  was calculated as the ratio of the saturation activity  $A_{sat}$  to the irradiation current  $I$ .

$$R^2 = 1 - \frac{SSE}{SS_{yy}} = 1 - \frac{\sum_i (y_i - \hat{y}_i)^2}{\sum_i (y_i - \bar{y})^2} \tag{Equation 4-3}$$

$$\delta A_{sat} = n_x \cdot \sqrt{\sum_{j=1}^{N+1} \left( \sqrt{\left(\frac{\delta F}{F}\right)^2 + \left(\frac{\delta \sigma}{\sigma}\right)^2} \right)_j^2 \cdot [ |F \cdot \sigma|_j \cdot N_p \cdot 10^{-27} \cdot (E_{j+1} - E_j) ]^2} \tag{Equation 4-4}$$

where in Equation 4-3  $SSE$  is the deviation of the observations from their predicted values while  $SS_{yy}$  is the deviation of the observations from their mean. To assess the differential proton fluence distribution as a function of energy, within the target material, all the simulations were performed simulating  $10^8$  primary particles that allowed, for this score and in these conditions, to achieve an uncertainty on fluence data less than 1 %. Typical proton spectra obtained for liquid and solid targets are reported in Figure 4-14 and Figure 4-15: the artefacts at the higher energies of the proton spectra are due to the way in which FLUKA treats the loss of energy of charged particles: actually, above a pre-set threshold, charged particle energy loss (ionization) is modeled by FLUKA in a discrete way as a  $\delta$ -ray production (Ferrari, et al., 2011).

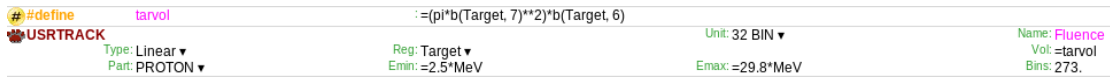


Figure 4-13 - USRTRACK score used in the assessment of proton fluence distribution in energy within the target material.

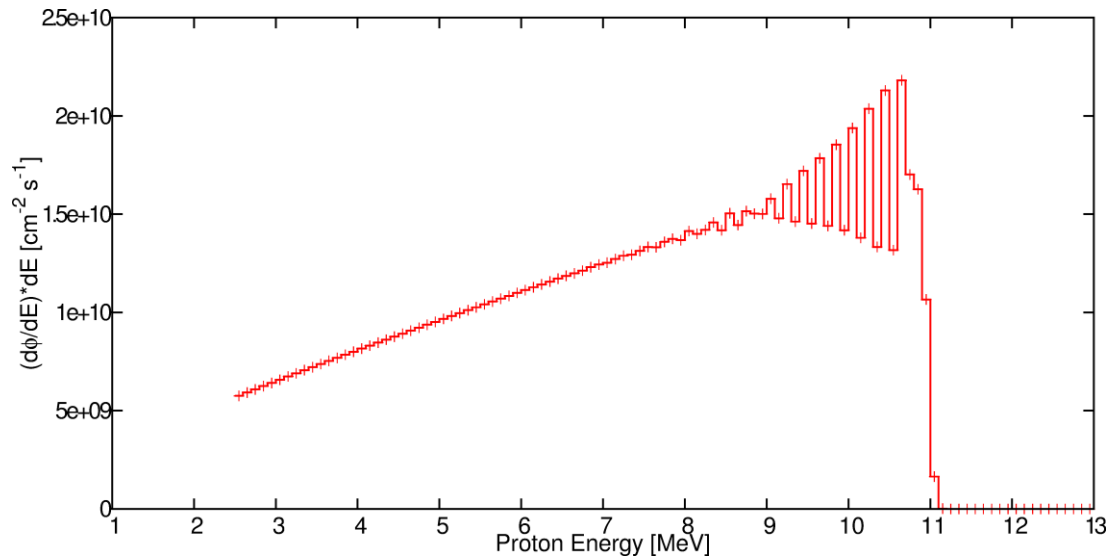


Figure 4-14 - Proton flux distribution in energy in a liquid target of  $H_2^{18}O$ .

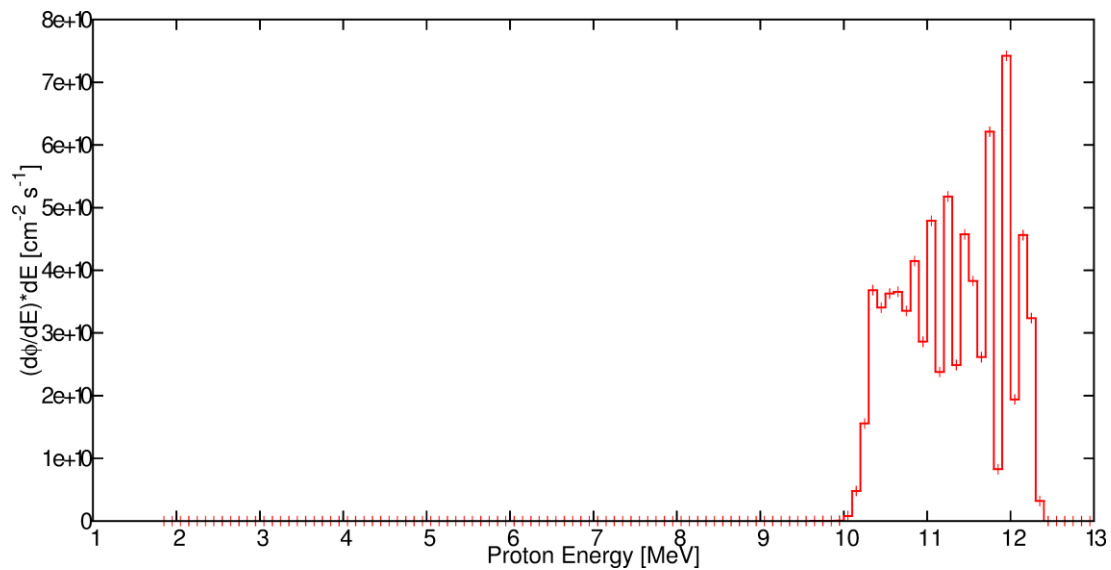


Figure 4-15 - Proton flux distribution in energy in a solid target of  $^{nat}\text{Fe}$ .

The calculation was validated again using the well-known reaction from the IAEA Nuclear Data Service,  $^{18}\text{O}(p,n)^{18}\text{F}$ . The ECSM-calculated yield for  $^{18}\text{F}$  was  $6780 \pm 120$  MBq/ $\mu\text{A}$ ; the literature value is 9527 MBq/ $\mu\text{A}$  (IAEA, 2011a), resulting in a ratio  $Y_{\text{IAEA}}/Y_{\text{CS}}$  of  $0.71 \pm 0.07$ . This is a good agreement given that liquid targets have complicated internal thermodynamic behavior and losses in the transfer. The calculation was then repeated for all radioisotopes investigated where external cross sections were available in the discussed energy range, and the results were

Table 4-15 - Saturation yields obtained with the external cross section method ( $Y_{\text{CS}}$ ) and comparison to the direct assessment with FLUKA  $Y_{\text{P}}$  and the experimental values  $Y_{\text{exp}}$  where cross section data is available.

Isotope	Cross Section Reference	Reaction	$Y_{\text{CS}}$ [MBq/ $\mu\text{A}$ ]	Uncertainty %	$Y_{\text{P}}/Y_{\text{CS}}$	$Y_{\text{exp}}/Y_{\text{CS}}$
<b>Liquid targets</b>						
$^{44}\text{Sc}$	(Krajewski, et al., 2013)	$^{44}\text{Ca}(p,n)$	7.1E+00	3.1	1.6	0.68
$^{68}\text{Ga}$	(Al-Saleh, et al., 2007)	$^{nat}\text{Zn}(p,x)$	9.2E+01	2.2	1.8	1.5
$^{86}\text{Y}$	(IAEA, 2011b)	$^{86}\text{Sr}(p,n)$	1.5E+02	1.8	0.21	0.24
$^{89}\text{Zr}$	(Omara, et al., 2009)	$^{89}\text{Y}(p,n)$	8.5E+02	2.0	0.35	0.41
$^{18}\text{F}$	(IAEA, 2011a)	$^{18}\text{O}(p,n)$	6.8E+03	1.8	1.2	0.73
$^{13}\text{N}$	(IAEA, 2011a)	$^{16}\text{O}(p,\alpha)$	4.6E+02	3.5	3.3	0.56
<b>Solid targets</b>						
$^{44}\text{Sc}$	(Al-Saleh, et al., 2007)	$^{44}\text{Ca}(p,n)$	5.3E+01	2.2	4.9	4.0
$^{56}\text{Co}$	(Al-Abyad, et al., 2009)	$^{56}\text{Fe}(p,n)$	1.7E+03	4.5	1.4	0.86
$^{52}\text{Mn}$	(Tanaka & Furukawa, 1959)	$^{52}\text{Cr}(p,n)$	3.0E+03	2.3	1.4	0.29
$^{61}\text{Cu}$	(Levkovskij, 1991)	$^{64}\text{Zn}(p,\alpha)$	1.6E+02	2.6	2.5	0.81
$^{55}\text{Co}$	(Levkovskij, 1991)	$^{58}\text{Ni}(p,\alpha)$	9.1E+01	1.9	0.53	2.0

compared with the data obtained from the direct assessment with FLUKA and with literature values. Furthermore, since the RESNUCLE score gives information about the radionuclidic inventory inside the target region, the calculation was extended to  $^{43}\text{Sc}$ ,  $^{67}\text{Ga}$ ,  $^{54}\text{Mn}$ , and  $^{88}\text{Y}$ . Results are reported in Table 4-15.

It should be mentioned that the literature cross section data used refer to the most probable reaction that can take place in the target volume, for example the  $^{18}\text{O}(p,n)^{18}\text{F}$  or the  $^{16}\text{O}(p,\alpha)^{13}\text{N}$ , while other reactions, which can contribute to the production of the radioisotope investigated, were not taken into account. The assumption was that only the main reaction contributes significantly to the production of the desired radioisotope, while the contribution of other reactions is negligible; this assumption is justified in the energy range of the TR13 cyclotron of 12 – 0 MeV. Since FLUKA uses nuclear models to assess the radioactivity induced in the target region, the yield calculation automatically takes into account all particles that can be found in the target region while, for the ECSM, only protons as projectiles were considered. Again, for the energy range of the TR13 it can be assumed that only protons significantly contribute to the activation of the target material. The final uncertainties were calculated propagating the independent uncertainties of the cross sections and the fluence data; it is important to note that while the uncertainty in the fluence data was less than 1%, the uncertainty in the cross section values was in the range of 10-20%. This uncertainty translates into a large uncertainty in  $Y_{CS}$ . The data in Table 4-15 show relatively good agreement between the  $Y_{CS}$  and the experimental data or the direct assessment of the saturation yield with FLUKA. The agreement achieved was strongly dependent on the quality of the cross sections. The cross section data have to fit certain requirements, including a large set of data points ideally spanning the energy range from cross-section threshold to 13 MeV with small uncertainties. Slightly better results were obtained with the very well-known reactions and the solid target materials which confirm again the impossibility to take into account the thermal and fluid-dynamic effects as well as the unloading efficiency with the Monte Carlo method. In the case of  $^{56}\text{Co}$  the convolution of the cross sections with the fluence data resulted in better agreement with the experimental value: in this particular case indirect assessment of the residual nuclei with FLUKA was able to better reproduce the experimental data compared with the direct assessment.

# ***Chapter 5***

## ***Application of the Developed Model***

### ***5.1 Planning of a New PET Facility***

In this section the application of the validated Monte Carlo model (Chapter 3 ) to the design of the new PET facility of “Sacro Cuore-Don Calabria” Hospital (Negrar, IT) is presented. The calculations performed with the developed MC model were added to the radiation protection technical report used for the licensing of the site. Actually, the licensing of such kind of facility requires, in Italy, a complex request of approval coordinated by the Ministry of the Economic Development in agreement with the Ministry of Interior, the Ministry of Health, the Ministry of Labour, the Ministry of the Environment, the national institute for the environmental protection and research (ISPRA) and the Italian regions of interest. The facility was built in between 2013-2014 and the first beam was extracted in January 2015, after the licensing approval.

#### ***5.1.1 Description of the New PET Facility***

##### ***5.1.1.1 Layout of the New PET Facility***

A new building, composed of three floors, was built within the complex of “Sacro Cuore-Don Calabria” Hospital to hold the cyclotron bunker; the technical room containing the equipment for the cyclotron; the control room; a micro-PET scanner and the laboratory for the injection of the animals; four laboratories for the synthesis of radiopharmaceuticals ( $^{18}\text{F}$ -labeled,  $^{11}\text{C}$ -labeled, peptides and research); a quality control (QC) laboratory; several offices. The cyclotron was installed at ground floor: in Figure 5-1 it is possible to recognize in particular the cyclotron vault (006); the control room (008); the technical room (007) and the water package room (010). At first floor (Figure 5-2) the main rooms of interest, for the design of shielding, are: the hot cells technical room (104); the  $^{18}\text{F}$ -labeled (112) and  $^{11}\text{C}$ -labeled (109) laboratory;  $^{68}\text{Ga}$ -labeled and peptides laboratory (105); a research laboratory (108) and the QC laboratory (122).

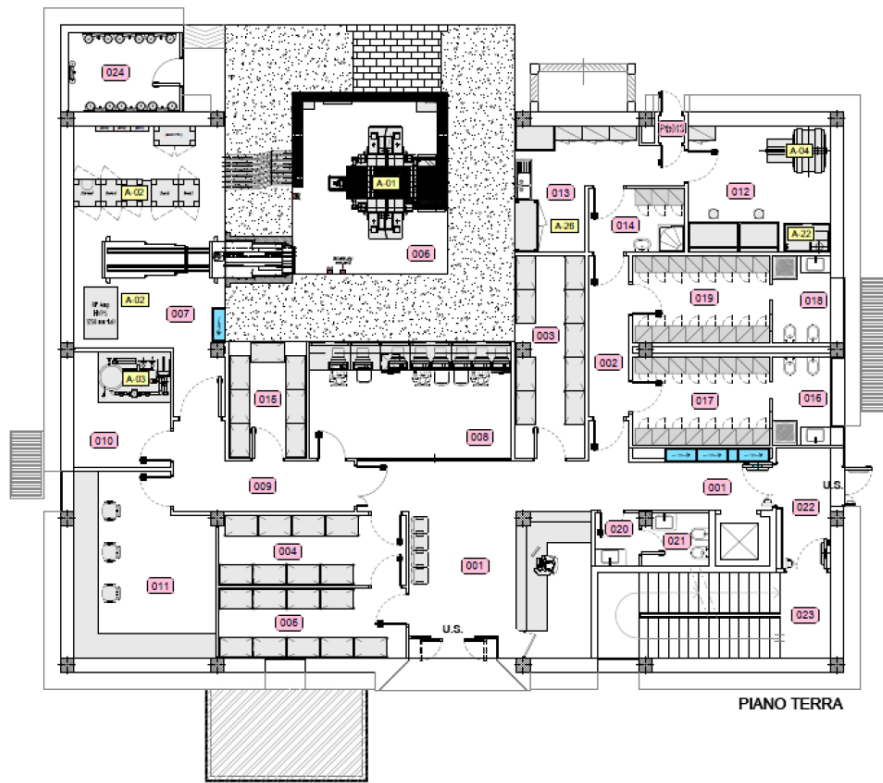


Figure 5-1 - Layout of the ground floor new PET facility of "Sacro Cuore-Don Calabria" Hospital.

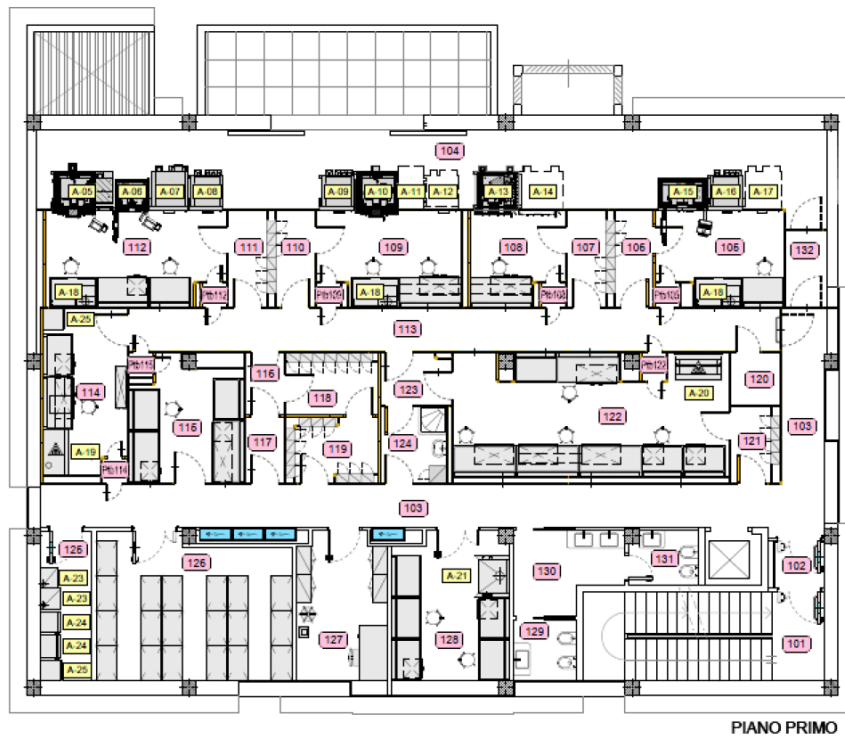


Figure 5-2 - Layout of first floor of the new PET facility of "Sacro Cuore-Don Calabria" Hospital.

### 5.1.1.2 The TR19 Cyclotron

The cyclotron installed at “Sacro Cuore-Don Calabria” Hospital is an ACSI TR19 (Figure 5-3), an external ion source cyclotron that accelerates negative hydrogen ions up to 19 MeV, provided with two target selectors able to host 4 targets assembly each, that allow a dual beam irradiation, and two local shields composed of a proprietary mixture that allow a significant reduction of the dose field around the target selectors. The main features of the TR19 cyclotron are reported in Table 5-1.

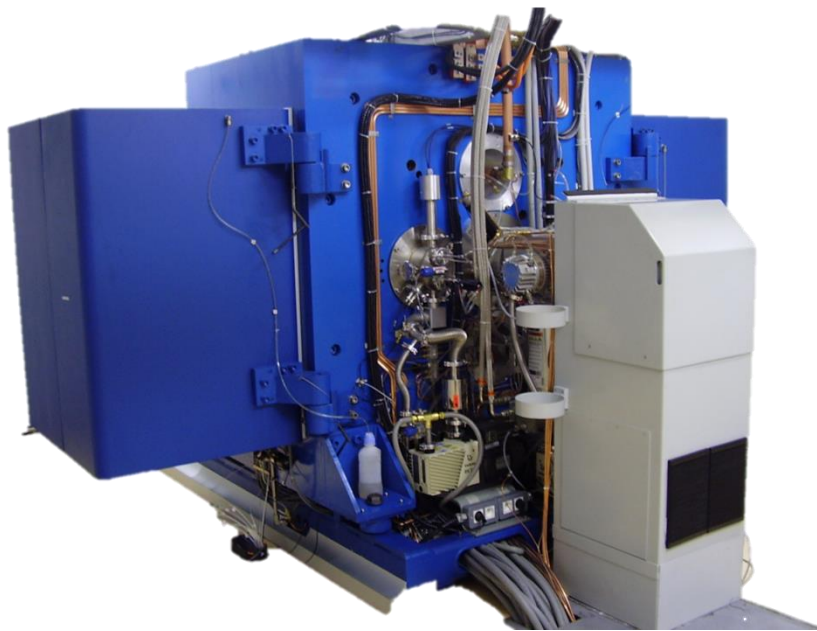


Figure 5-3 - The ACSI TR19 cyclotron.

Table 5-1 - Overview of the main features of the TR19 cyclotron (ACSI, 2014).

<b>TR19 Specifications</b>			
<b>Type of cyclotron</b>	Negative Hydrogen External Ion Source 2 Extracted Beams 8 External Targets	<b>RF System</b>	Number of Dees: 2 (45 degrees) Dee Voltage: 50 kV RF Frequency: 13 kW Energy per Rev.: 200 keV
<b>Beam current</b>	Nominal: 150 $\mu\text{A H}^-$	<b>Ion Source</b>	Type: Multi-cusp Output Current: 2.8 mA
<b>Beam Energy</b>	Energy range: 13 to 19 MeV $H^-$	<b>Vacuum System</b>	Operating Pressure: $5 \times 10^{-7}$ Torr Base Pressure: $2 \times 10^{-7}$ Torr Pumps: 2 Cryopumps, 1 Turbomolecular, 2 Two stage Rotary Vane
<b>Magnet</b>	Weight: 22 Tons Geometry: 4 Sectors Hill Angle: 45 degrees Magnet Power: 19 kW Pole Radius: 57 cm	<b>Shielding</b>	Local shielding on each target selector

In the following, a detailed description of the TR19 subsystems is provided: the information reported below, retrieved from the TR19 manual (ACSI, 2014), is helpful in understanding the developed MC model.

The main magnet consists of a magnet yoke made of low-carbon steel, two nickel plated poles made of low-carbon steel, and two magnet coil assembly, each mounted in the yoke and connected to water cooling headers. In the TR19 the  $H^-$  ions are accelerated on a vertical plane. The main magnet assembly weighs 22,000 kg and has an outside dimension of 1700x1700x100 mm. The poles of the magnet have a radius of 600 mm. The magnet yoke opens along its longitudinal axis to provide access to the main vacuum tank and the interior of the cyclotron. The four sector radial ridge magnetic poles have four Hills and four Valleys. The average magnetic field strength is 1.2 Tesla (at nominal operating conditions of 490 A), with Hill and Valley average magnetic field strength of 1.9 and 0.55 Tesla respectively. The Hill gap varies with radius, but is about 40 mm, and the Valley gap is 200 mm. The Hill angle varies from 40° to 45°. Each magnet coil assembly consists of five modular coils or pancakes. These coils are made of hollow-core, low resistivity, copper conductors. The conductors are glass-fiber insulated and cast in epoxy. The coils are cooled by circulating de-ionized water in the hollow-core conductors. The Main Magnet power supply requirement is 60 kVA (480 Volts / 3 phase) with voltage stability of  $\pm 5\%$ . It is connected to the coils through four power cables. The Main Magnet requires 22 kW of DC power. One of the Main Magnet yokes is mobile on a rail allowing to be opened for maintenance purposes.

The Radio-Frequency (RF) System on the TR19 cyclotron is a single frequency system that resonates at 74MHz for protons. The negative ions  $H^-$  are accelerated in the TR19 at the fourth harmonic of their rotation frequency. The RF control system is designed to allow the TR19 to be run by the computer control system, without any Operator intervention. The RF system can also be operated in manual mode for operational, maintenance and diagnostic purposes. The RF system on the TR19 consists of a resonator, a power amplifier, and a coaxial transmission line from the power amplifier to the cyclotron, a real-time RF control system and a radio frequency generator. The radio frequency parameters are monitored through pick-ups inside the resonator cavity. Inside the TR19 cyclotron are two Dees, with Dee angles that vary from 40° to 45°. The Dees are precisely machined out of low resistivity copper and are designed to optimize the energy transfer from the RF system to the accelerating hydrogen ions. The shape of the Dees serves to reduce the capacitive losses due to edge effects, impedance and the attenuation interaction between the Dees and the Dee liners. The nominal Dee voltage is 50 kV for protons. The Dees and Dee stems are water cooled as is the power amplifier using flow and temperature controlled de-ionized water. The power amplifier is based on an EIMAC water cooled triode running in a grounded grid configuration. The power amplifier is driven by a commercially available solid state amplifier built to Mil-Spec

requirements. The frequency is generated by a high stability frequency synthesizer. The other components that make up the RF amplifier are proven, commercially available components such as the power supply, instrumentation and read-back devices. The RF Control System is interlocked with the computerized Control System to monitor the RF amplitude, frequency and phase.

To reduce beam degradation, minimize neutron activation and residual radiation within the cyclotron, and to minimize maintenance and operating costs, the TR19 vacuum system is designed around high efficiency cryopumps. The main tank cryopump is inserted into the magnet to utilize its high water vapor pumping speed of 4000 l/s. By using cryopumps, there are few sources of contamination within the TR19 cyclotron. A key feature of the vacuum system is its modularized design that permits the different subsystems on the cyclotron to be valved off from the main vacuum tank. Maintenance on the targets and extraction system can be done while the main tank remains at high vacuum. Also, the externally mounted ion source eliminates the need to vent and access the vacuum tank to perform maintenance on the ion source and injection system. Venting to atmosphere is done using a dry nitrogen system. The main vacuum tank is formed by the two nickel plated magnet poles and an aluminum ring called the vacuum wall. The vacuum tank is designed for operation down to a high vacuum of  $5 \times 10^{-7}$  Torr. Unless the cyclotron is being serviced, the main tank is normally kept at high vacuum.

The  $H^-$  ion source (IS) is made up of a cylinder 10 cm in diameter, and 17 cm long. Hydrogen gas is fed into the ion source from bottles mounted next to the cage. Between the  $H_2$  bottles and the flow controller is a copper tube, while between the ion source and the needle valve is a plastic pipe to insulate against the electric potential of the Ion Source (25 kV). A tungsten filament is situated in the middle of the ion source body. The filament is heated by the filament current and biased to -100 V, with respect to the ion source body, by the arc power supply. Electrons are evaporated off the hot tungsten filament to produce an arc between the filament and the body. The arc heats the  $H_2$  gas and converts the gas into a plasma of energetic ions. The voltage and current settings of the arc can be set to control the dynamic resistance of the plasma which in turn determines the beam current and emittance from the ion source. Surrounding the ion source and filament are permanent magnets which produce a magnetic field which contains the plasma. The permanent magnets are high field strength rare earth magnets. As a result of the manufacturing process, these rare earth magnets are very brittle. These magnets are also sensitive to heat and must be kept below 100°C. The ion extraction optics consists of a series of electrodes set at specific voltages which are used to extract and focus the negative  $H^-$  ions before they pass into the injection line. Between each electrode is an insulator. Next is the Injection Beam Stop (IBS). The IBS is a disk that can either be retracted from, or inserted into, the path of the beam. The IBS is used as a shutter to change the status of the cyclotron from "beam off" to "beam on".

When retracted, and provided the ion source gate valve is open, the beam is allowed to be injected into the cyclotron. The ion source is mounted in a vacuum chamber that is pumped by a turbomolecular pump on the source side, and a cryopump on the injection line side of the extraction electrodes.



*Figure 5-4 - The external ion source of the TR19 cyclotron.*

The TR19 cyclotron is equipped with two beam extractors (Figure 5-5), 180° apart, so that two beams can be extracted simultaneously. Extraction is achieved by stripping the electrons off the hydrogen ions using a thin-film pyrolytic carbon foil. The two variable energy extraction probes allow simultaneous extraction of beams with beam currents variable in ratios from 1:100 to 1:1 at a variable energy of 13 MeV to 19 MeV. The extracted beams exit the TR19 cyclotron along two extraction ports, which are designated as Target Selectors 1 and 2. The extraction probes also have an azimuthal motion of  $\pm 4$ mm for steering the beam down the center of the target selector. This adjustment plus the target selector positioning are used together to position the target in the middle of the beam and align the angle of the beam so it comes straight into the target. The correct alignment is mostly an issue for the longer gas targets where the beam should go straight down the target and not hitting the sides.

Each of the two target selectors (Figure 5-5) can position any one of the four mounted targets into the beam for a total of eight targets. The target bodies supplied with the TR19 share a common interface with the target selector. The

targets are modularized and interchangeable, and are designed to allow rapid attachment and removal from the target selector. To minimize residual activity, the target selectors are made primarily from aluminum and baffles and collimators are made from graphite. The targets are moved into position by a gimbal arrangement. The gimbal has two pivot axes which allow the selector to move in either a horizontal or vertical direction. A stainless steel bellows is used as a flexible beam tube that maintains vacuum while allowing the gimbal freedom to move. Each target selector and extraction probe can be isolated from the main vacuum tank by a vacuum isolation gate valve. The vacuum isolation valve allows the targets to be changed or maintenance to be done on the targets without affecting the high vacuum in the main tank. The cooling of target windows is done by spraying high velocity, turbulent, helium gas over the surface of the two windows. The closed loop helium cooling system is located in the utility cabinet. Water cooling to the targets and target selector is from the same cooling circuit as for the cyclotron.



**Figure 5-5 – TR19 target selector with two targets mounted. In the top of the picture it is possible to see also one of the extraction probes.**

All the target bodies supplied with the TR19, without regard for the specific isotope being produced, share a common interface with the target selector. The

targets are designed to allow rapid attachment and removal from the target selector. The target bodies are water cooled to carry away the heat produced by the beam current absorbed by the target bodies. Most target bodies are made of aluminum. Niobium is used in the [ $^{18}\text{F}$ ]FDG production targets because it is relatively inert with respect to fluoride ions. The first portion of the target assembly consists of a solid aluminum plug pierced by a 10 mm hole. The outside of the plug has a groove in which is mounted the O-ring used to make the vacuum seal between the target body and the target selector. Between the plug and the target body is a disk with windows on both sides. The two thin foil windows separate the target material from the high vacuum within the cyclotron. The first window is the vacuum window for the beamline, and the second one is the target window. The windows are cooled by high speed streams of helium gas supplied by a recirculating closed loop cooling system located in the target services cabinet. The Target bodies are insulated from ground to allow the measurement of beam current.

Advanced Cyclotron Systems Inc. has developed a compact, composite shielding material. The shielding material is a mixture of high density and low density materials, along with a neutron sink, that permits the composite material to act as a compact and effective shield for both gamma radiation and neutrons. A composite borated material is included in the composition of the local-shielding (Figure 5-6), two doors that completely enclose the target selector on each side, to absorb thermal neutrons. The composite local-shield that is supplied with the TR19 cyclotron helps to minimize the shielding requirements. Because of its high density it is extremely effective in reducing the attenuation length of the 6 MeV gamma rays to be approximately the same as that for neutrons.

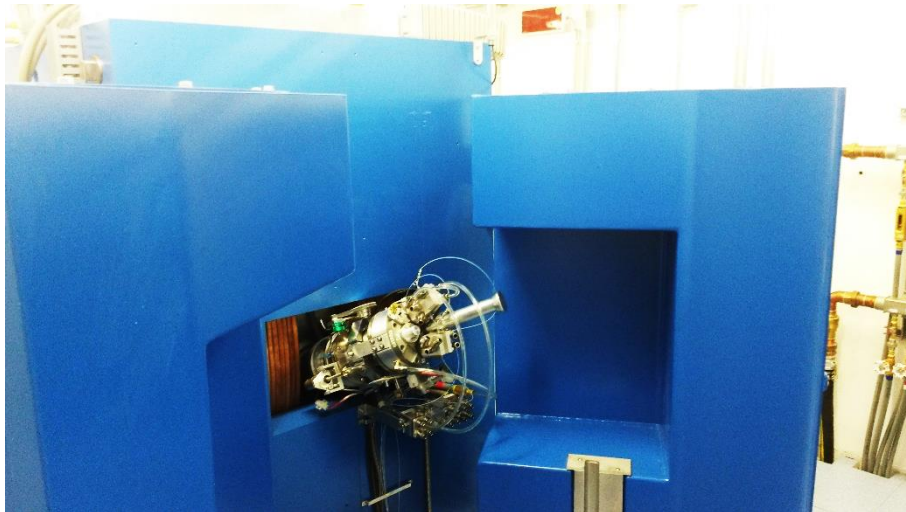


**Figure 5-6 - TR19 local-shielding: when closed, the local-shield encloses the target selector completely.**

### 5.1.2 Monte Carlo Model of the TR19 Cyclotron

The FLUKA MC model of the TR19 cyclotron and the cyclotron vaults were created using SimpleGeo and then exported to Flair. The main components of the cyclotron were modeled including the yoke, the magnet poles and the magnet coils, a simplified model of the collimation system and the target selector, a  $^{18}\text{F}$  target assembly for each side, the two local shielding, and the external ion source (Figure 5-7). The layout of the cyclotron vault was accurately reproduced from original technical drawings; after the assessment of the required thickness of the vault walls, ducts were accurately reproduced to perform the study of dose transmission through them. The inner dimensions of the bunker are: 460 cm by 540 cm with a height of 380 cm and with 200 cm thick concrete walls (after design of the shielding). Figure 5-8 shows the final geometrical model. A  $^{18}\text{F}$  liquid target assembly was modeled including the Havar foils, the Helium cooling window and the  $^{18}\text{O}$ -enriched water target (Figure 5-9). The average composition and density of the local-shielding was modeled from private communications with the manufacturer to preserve the proprietary mixture.

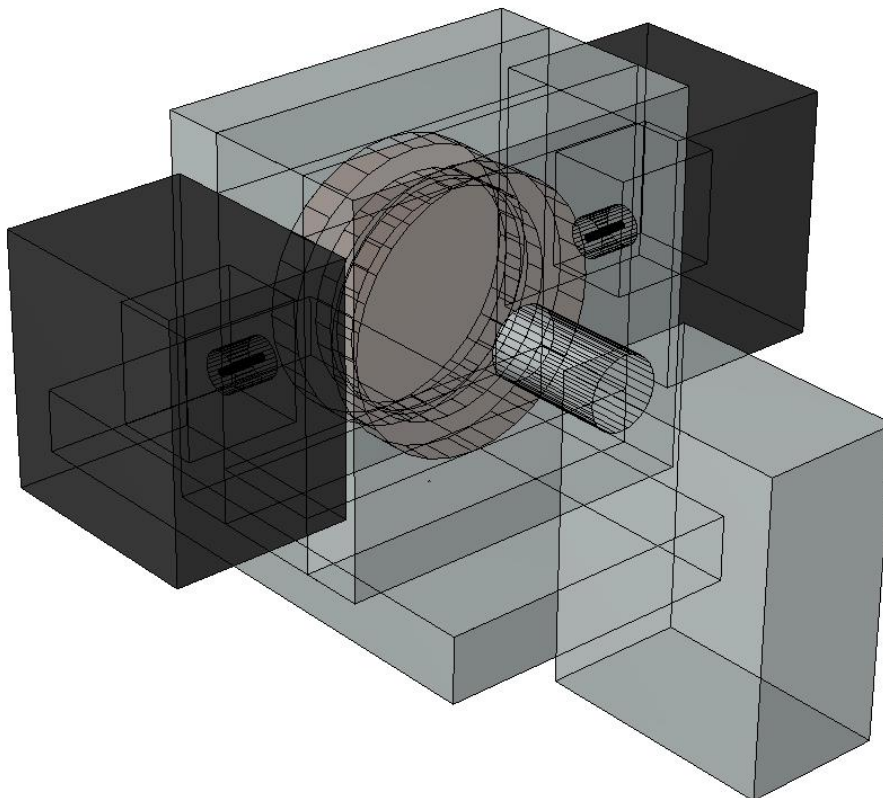


Figure 5-7 - 3D of the FLUKA MC model of the TR19 cyclotron.

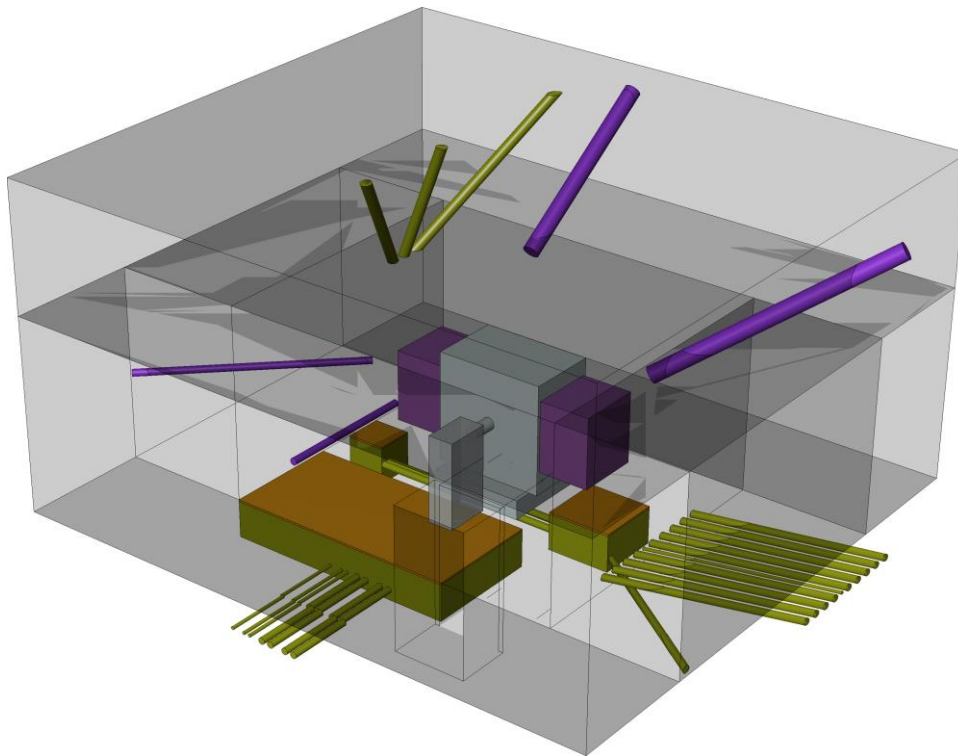


Figure 5-8 - 3D of the FLUKA MC model of the TR19 cyclotron, the cyclotron vault and the ducts through the vault walls.

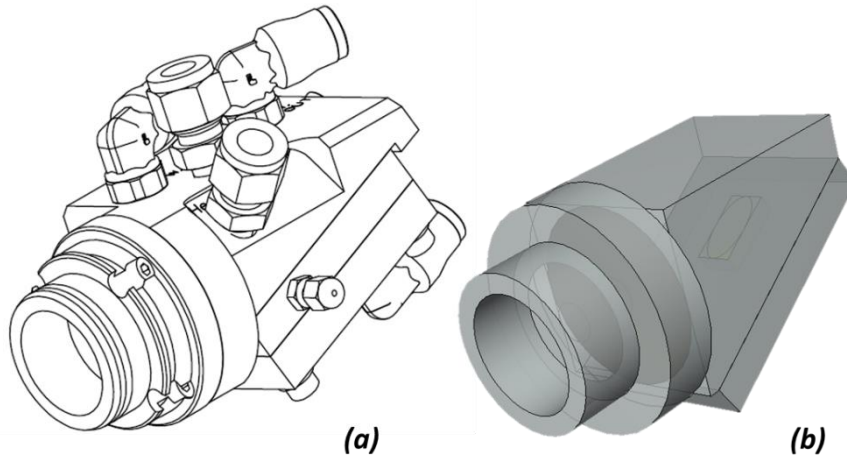


Figure 5-9 - Comparison between the original technical drawing (a) and modeled (b)  $^{18}\text{F}$  target assembly of the TR19 cyclotron.

A 19 MeV proton beam was modeled using the *BEAM* and *BEAMPOS* cards: a spread out beam, elliptical-shaped, with  $\text{FWHM}_x=0.25$  cm,  $\text{FWHM}_y=0.2$  cm,  $\text{FWHM}_{\Delta E}=0.0001$  GeV/c was set. *BEAMAXES* card was used to rotate the beam reference frame according to the geometry reference frame. Dual beam was simulated merging the scores obtained simulating the irradiation of a target selector at a time.

*NEW-DEFA* default and coalescence and evaporation of heavy fragment were enabled through *PHYSICS* cards. An irradiation profile of 1hour-1 $\mu$ A was simulated and *RADDECAY* card was set in “active” mode. Simulations were performed in high statistic simulating  $10^9$  primary particles for each target selector.

### 5.1.3 Design of shielding and ducts

The design of the required thickness of the cyclotron vault was conducted by the assessment of the ambient neutron dose equivalent  $H^*(10)$  around the accelerator in a dual beam irradiation; in a second step, an optimization of ducts trough the vault walls was performed. Activation of air within the bunker was studied to assess the production of  $^{41}\text{Ar}$  due to the secondary neutrons as well as the activation of shielding and cyclotron components to plan decommission strategies as requested by the Italian national regulation on radiation protection.

The targets are the dominant source of radiation within the TR19. It is important to bear in mind that for the  $(p,n)$  reactions used in proton cyclotrons for the production of PET radioisotopes, the amount of radiation produced in the target is a direct function of the production rate of the radioactive isotopes. In a proton cyclotron the neutron flux is maximum during the irradiation of  $^{18}\text{O}$  to produce  $^{18}\text{F}$ . For this reason, all the simulations were conducted simulating the irradiation of a  $^{18}\text{O}$ -water target.

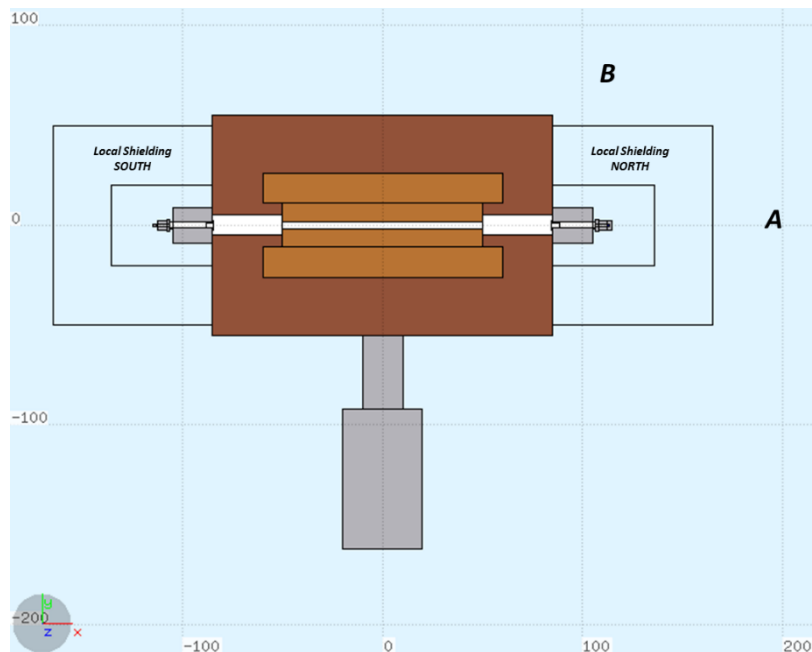


**Figure 5-10 - Assessment of the attenuation factor of the local shield. In the picture, local shields are made of air, simulating their absence. Point A ( $0^\circ$ ) and point B ( $90^\circ$ ) are both at 1m from the target.**

In a first step, the efficacy of the local shield was verified by evaluating the attenuation factor: this step was fundamental since the composition and the density of the local shield were not completely known. The neutron ambient dose equivalent  $H^*(10)$  was assessed around the cyclotron through USRBIN (Cartesian mesh, pitch 10 cm) and AUXSCORE cards. The cyclotron was simulated with and without the local shield (simply switching the material to air); at this stage the cyclotron vault was not simulated. The neutron ambient dose equivalent  $H^*(10)$  was scored in two points, both 1 m from the target: point "A" was at  $0^\circ$  (beam direction) from target while point "B" at  $90^\circ$  (see Figure 5-10). Local shielding, as well as the targets selectors, were labeled "NORTH" and "SOUTH" according to the direction of the beam along the x-axis: "NORTH" referred to positive x-direction. This notation was used also for the walls of the cyclotron vault. Results of the simulations are reported in Table 5-2: results are reported only for the local shielding "NORTH" but similar results, within the random uncertainty, were obtained for the local shielding "SOUTH" irradiating the corresponding target selector. An average attenuation factor of  $146 \pm 8$  was found: the manufacturer reported an average attenuation factor of about 100. Since the variability in the composition of the mixture within the local shield it was decided, at this stage, to retain acceptable the modeled composition.

**Table 5-2 - Assessment of the attenuation factor of the local shield.**

	A	B
<b><math>H^*(10)</math> Without LS [mSv/<math>\mu</math>Ah]</b>	$592 \pm 7$	$431 \pm 7$
<b><math>H^*(10)</math> With LS [mSv/<math>\mu</math>Ah]</b>	$3.73 \pm 0.27$	$3,21 \pm 0,27$
<b>Attenuation factor</b>	$159 \pm 11$	$134 \pm 12$
<b>Average</b>	$146 \pm 8$	

Using USRTRACK score it was possible to assess the differential neutron fluence distribution in energy in air around the cyclotron (Figure 5-11). In a very first stage of the design, the inner dimensions of the bunker were modeled following the indication of the cyclotron manufacturer; an air box of about  $68 \text{ m}^3$  was thus created around the model of the accelerator. Figure 5-12 and Figure 5-13 show the neutron spectra obtained: the presence of the local shield thermalizes part of the neutrons and shifts the peak from about 1 MeV (production peak) to about 0.1 MeV. As shown in the following, the thermalization effect is higher when concrete walls are included in the model.



**Figure 5-11 - USRTRACK score used in the assessment of the neutron fluence distribution in air.**

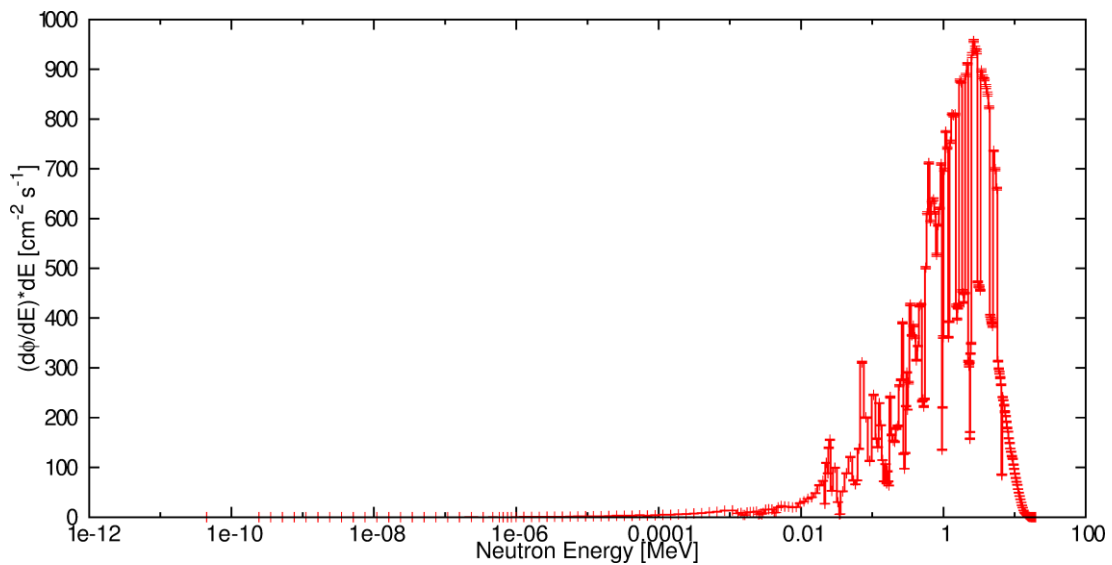


**Figure 5-12 - Differential neutron fluence distribution in energy, in air, without local shielding.**

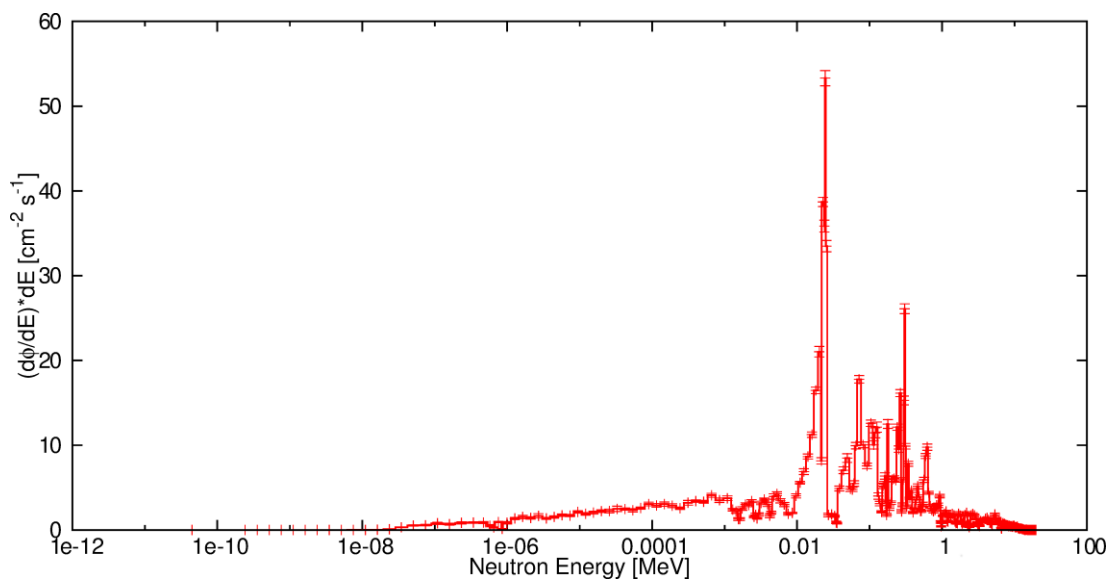


**Figure 5-13 - Differential neutron fluence distribution in energy, in air, with local shielding.**

The design of shielding of the cyclotron vault was performed according to the thus assessed neutron dose field. The expected dose equivalent  $H_{exp}(\theta, \bar{d})$ , in the direction  $\theta$  at the distance  $\bar{d}$  from the source without any barrier, was assessed for several points (Figure 5-14), located along different directions. In addition to the points reported in Figure 5-14 a point in the roof and one in the floor were considered.

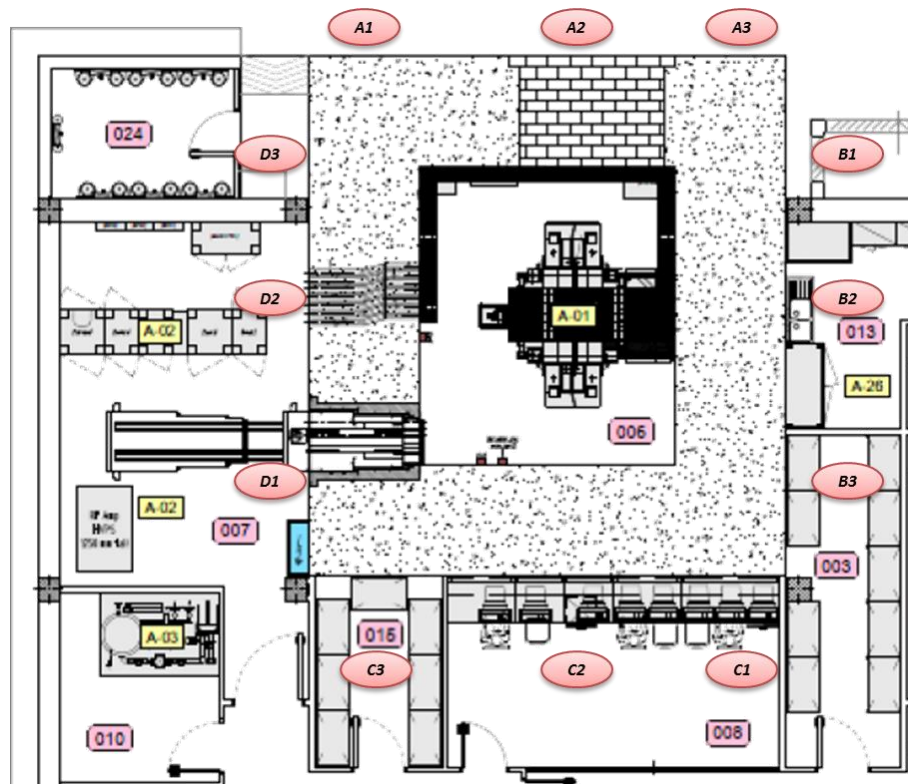


**Figure 5-14 - Design of shielding: the expected dose equivalent  $H_{exp}(\theta, r)$  was assessed in several points, along different direction, to assess the required thickness of the walls.**

The shielding design goal was fixed to 1 mSv/y (yearly dose limit for the population prescribed by D.Lgs 230/95) for points from B1 to D3, including the roof and the floor; in the external area (A1 to A3) a safety goal of 0.5 mSv/y was used. The reference dose equivalent  $H_{ref}(\theta, 100)$ , in the direction  $\theta$  at the reference distance of 100 cm from the target, was assessed from FLUKA simulations: neutron ambient dose equivalent  $H^*(10)$  was assessed using USRBRIN scores (cylindrical mesh; 5 cm pitch in both R and z-direction; 5° pitch in angle) and AUXSCORE card to filter the contribution of neutron only (Figure 5-15 and Figure 5-16). From Figure 5-15 and Figure 5-16  $H^*(10)$  was taken along all the directions of the points A1 to D3; then the expected dose equivalent  $H_{exp}(\theta, d)$  was computed using Equation 1-2 and data reported in Table 5-3. The transmission factor  $B(t_b)$  of the shielding was computed, for all the points, using Equation 1-1. The thickness of the barrier, in concrete, was computed choosing  $TVL_l=31.8$  cm (for 20 MeV neutrons) and  $TVL_e=28.5$  cm (for 1 MeV neutrons) (IAEA, 1988): an average effective thickness of  $132 \pm 22$  cm, including the additional HVL to shield scattering radiation, was calculated. To take into account a safety factor of 20% and the inaccuracy of the composition of the local shield, it was decided to add an additional HVL thus building 200 cm thick concrete walls.

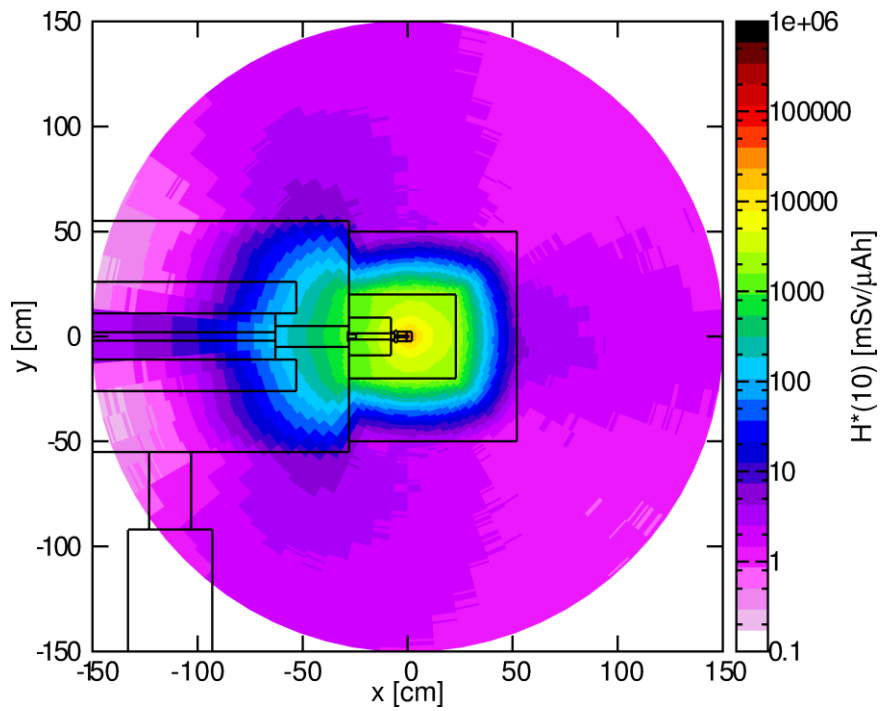


Figure 5-15 - Assessment of the neutron ambient dose equivalent  $H^*(10)$  around the target selector "NORTH" using a USBIN score with a fine cylindrical mesh.

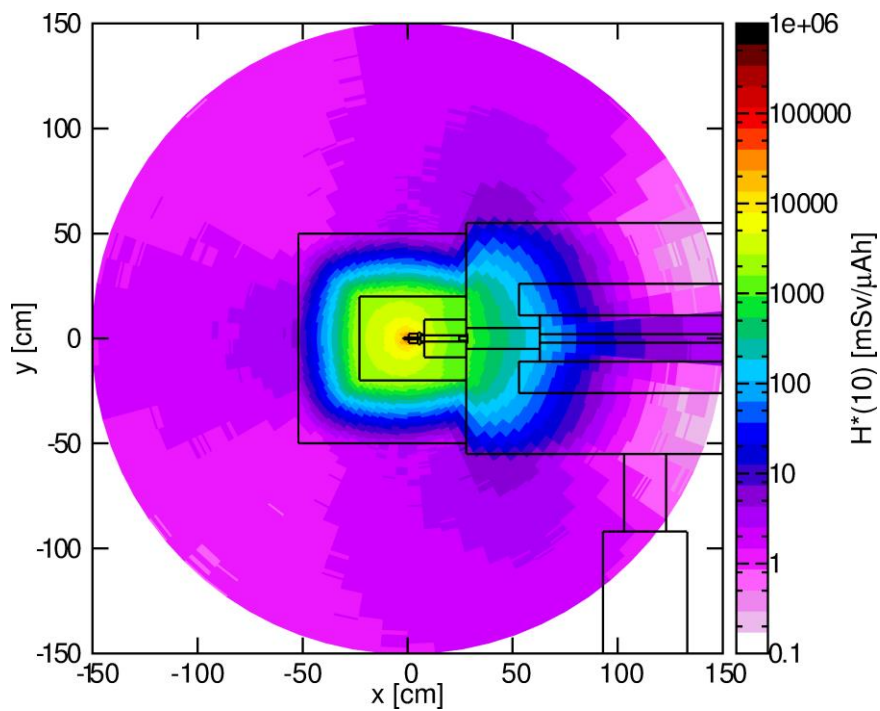


Figure 5-16 - Assessment of the neutron ambient dose equivalent  $H^*(10)$  around the target selector "SOUTH" using a USBIN score with a fine cylindrical mesh.

Table 5-3 – Data used to compute the expected dose equivalent  $H_{exp}(\theta,d)$ .

Point	FLUKA	Distance from Target d [cm]	Use Factor U	Occupancy Factor T
	$H_{ref}(\theta,100)$ [mSv/ $\mu$ Ah]			
<b>A1</b>	2.2 ± 0.4	490	1	1/16
<b>A2</b>	3.7 ± 0.6	420	1	1/16
<b>A3</b>	2.3 ± 0.3	490	1	1/16
<b>B1</b>	1.61 ± 0.26	390	1	1/16
<b>B2</b>	7.4 ± 0.3	390	1	1/16
<b>B3</b>	2.26 ± 0.29	390	1	1/16
<b>C1</b>	2.4 ± 0.4	490	1	1
<b>C2</b>	3.5 ± 0.4	420	1	1
<b>C3</b>	1.98 ± 0.27	490	1	1
<b>D1</b>	1.70 ± 0.24	450	1	1
<b>D2</b>	6.4 ± 0.4	450	1	1
<b>D3</b>	1.50 ± 0.29	450	1	1
<b>Roof</b>	0.130 ± 0.019	450	1	1
<b>Floor</b>	0.130 ± 0.019	400	1	1/40

The 200 cm thick walls were added to the MC model and the neutron fluence distribution in energy was assessed using USRTRACK score (Figure 5-17): compared to Figure 5-12 and Figure 5-13 it is possible to see how the presence of concrete walls improve the slowing down, and the thermalization, of neutrons.

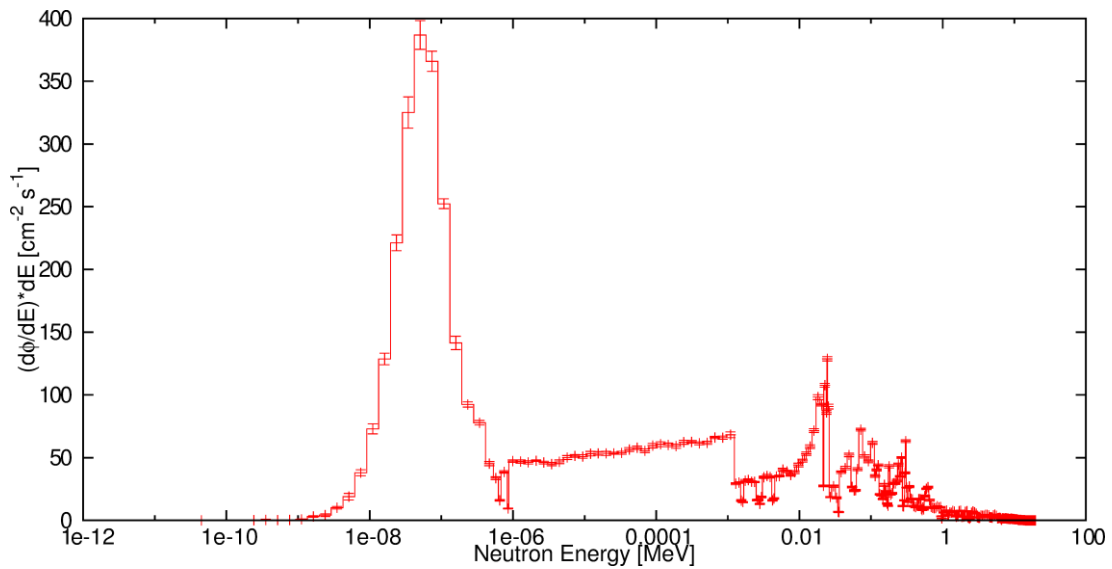
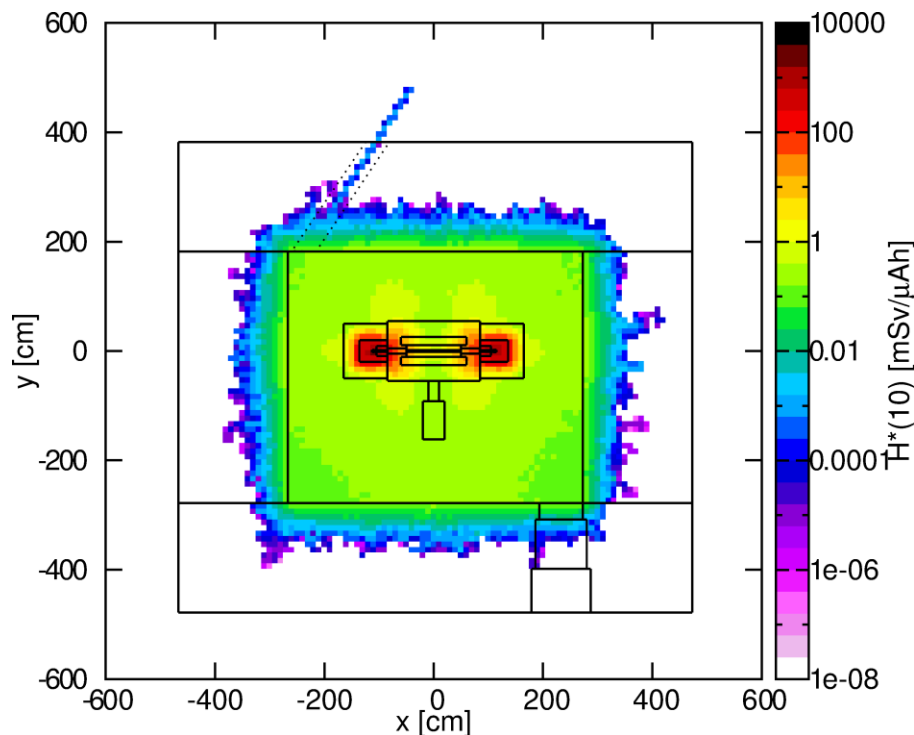


Figure 5-17 – Differential neutron fluence distribution in energy, in air within the cyclotron vault, during a dual beam irradiation with closed local shield.

One of the features of MC simulation in planning new cyclotron facilities is the ability to predict possible transmission of dose through ducts and mazes. In particular, in a complex site like the one reported in this section, there are several ducts (used to bring cables, pipes, etc. into the cyclotron vault) that can be critical points in which neutrons can find an easy way to escape from the cyclotron vault. Fixing these problems once the bunker is already built is quite complicated and expensive while the identification of critical situations during the design allows to avoid post-construction interventions. After the design of shielding, an accurate evaluation of the transmission of dose through the ducts was performed. Figure 5-8 shows the ducts modeled on the basis of the original technical drawing of the site. The neutron ambient dose equivalent  $H^*(10)$  during a dual beam irradiation was assessed in the whole bunker using a USBIN score (Cartesian mesh; 5 cm pitch) and AUXSCORE card. The result of the simulation is reported in Figure 5-18.



**Figure 5-18 – First version of the planning of the cyclotron vault: transmission of the dose through the pipe of the out-coming ventilation was identified.**

In a first stage of the design of the ducts, a possible transmission of neutron dose was found through the pipe of exhaust air in the ventilation system. Alternative solutions were then studied, according to the engineers working on the design of the ventilation system, and implemented in the Monte Carlo model: the position and the orientation of the pipe through the wall were changed to satisfy planning and radiation protection requirements. Figure 5-19 shows the final configuration adopted: no significant transmission through the duct was observed.

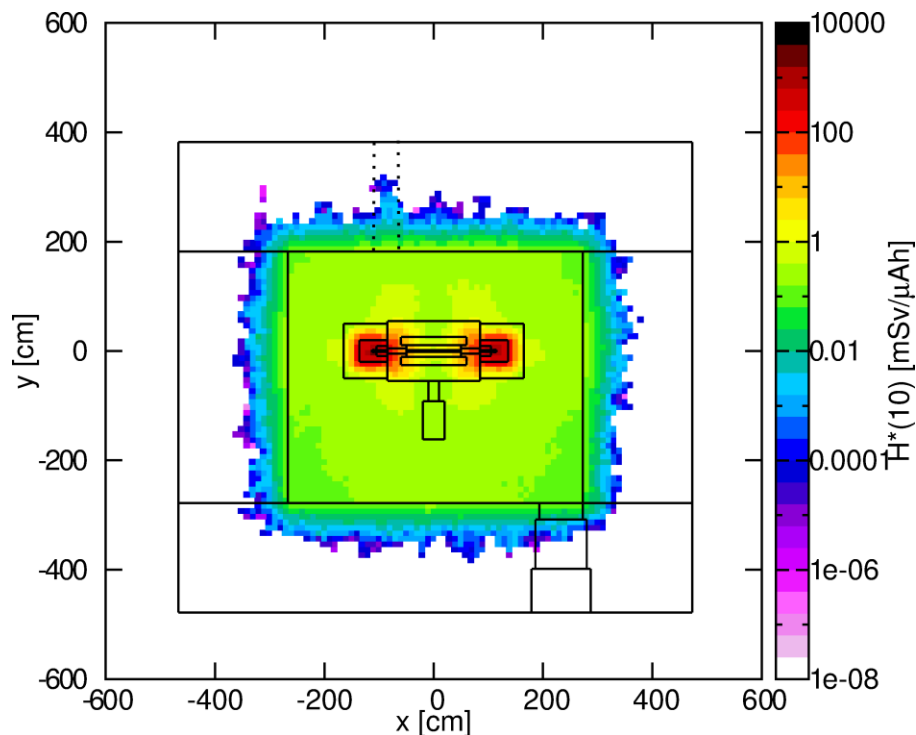


**Figure 5-19 – Optimization of the position and the orientation of the pipe through the wall allows avoiding any significant transmission of dose.**

It is important to note that, even if from Figure 5-18 and Figure 5-19 one could think that neutrons are completely absorbed in less than 1 m of concrete, this is not true! The meaning of these plots is different: at this level of statistic ( $2 \times 10^9$  primary particles simulated) and without any BIAS, it is quite difficult to score neutrons outside the cyclotron vault and to obtain a statistically significant measurement. It is also important to remember that  $10^9$  primary particles correspond to a huge number of histories simulated and increasing this number requires a huge amount of cpu-power without a significant increasing of the information obtained. Actually, assessing the dose outside the cyclotron vault is sufficient to obtain an accurate value of the dose incident to the inner side of the wall (remember that MC simulation allows to reproduce the source term better than analytical methods) and then use an exponential law, taking into account an average TVL.

All the ducts planned in the cyclotron vault were tested and no significant transmission was observed. As an example, the assessment of the dose transmission through the RF and power supply ducts and the pipe for the loading of the enriched-water target are reported in the following. Dedicated fine mesh were set for all the ducts with several USBIN cards.

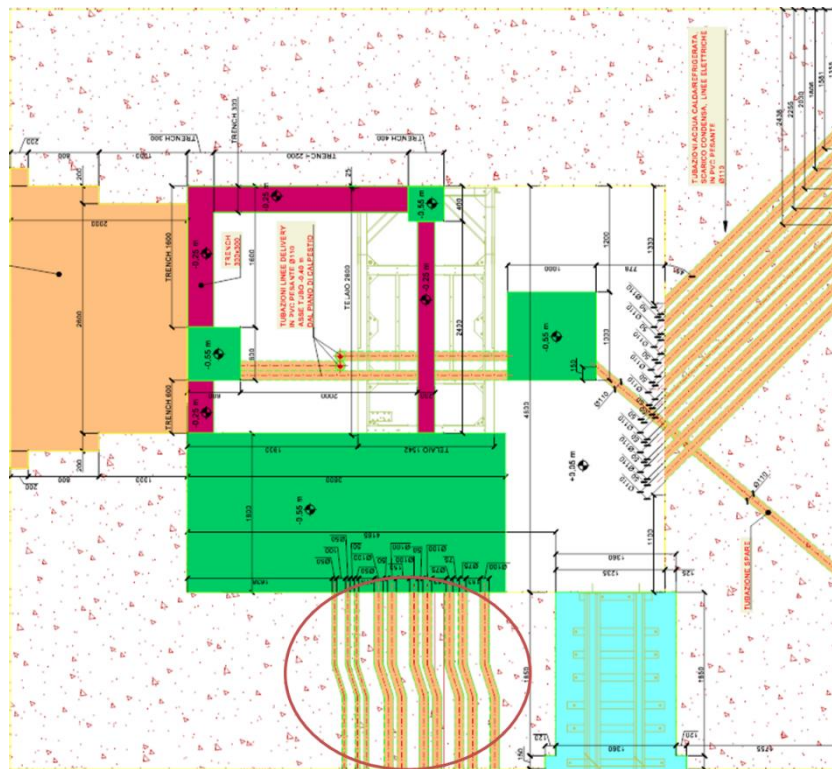


Figure 5-20 - Ducts through the cyclotron vault walls for the RF and power supply (original technical drawing).

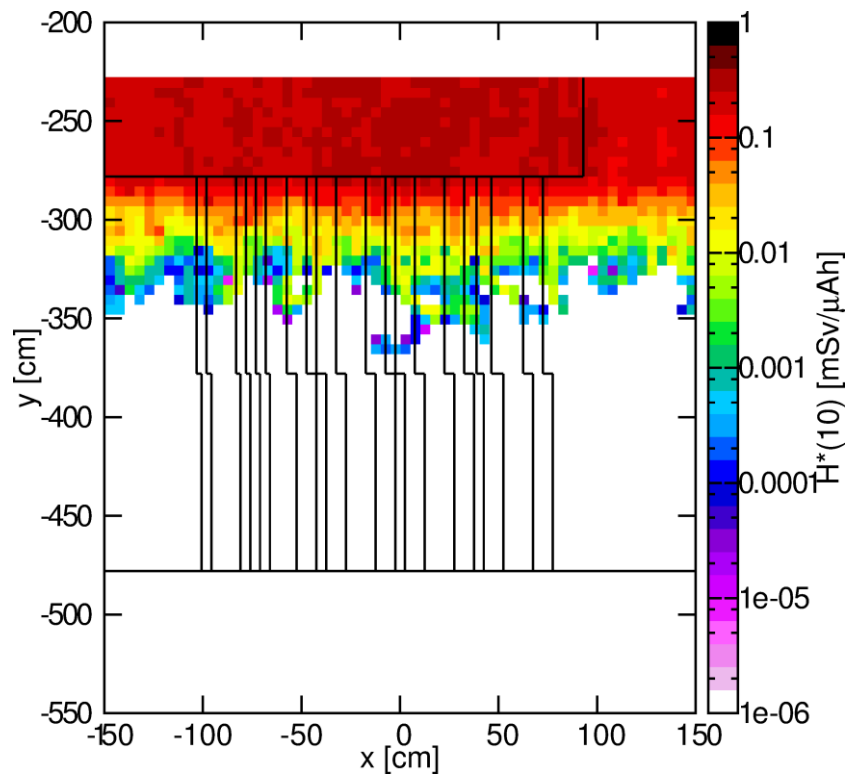
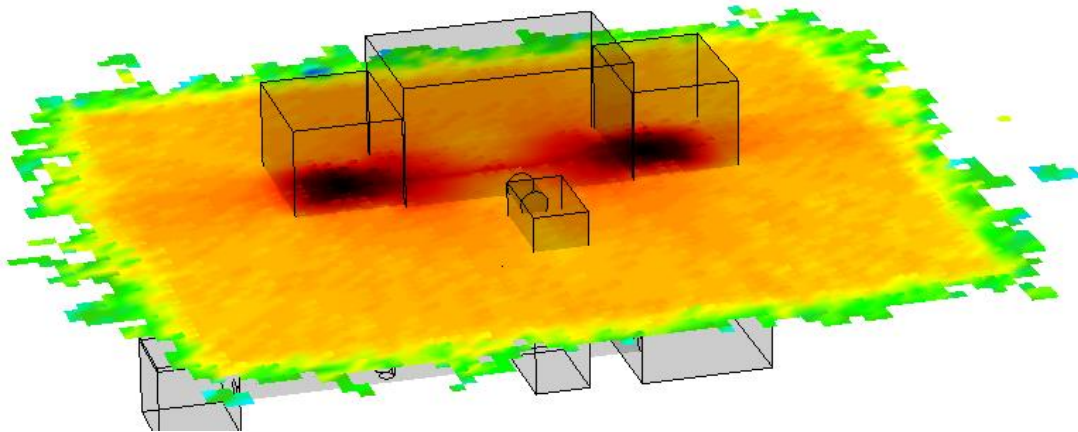


Figure 5-21 - Assessment of the dose transmission through the ducts: detail of the RF and power supply ducts.



It is important to note that no assumptions were made about the build-up factor. Actually one of the advantages of MC simulation is the possibility to accurately reproduce the source term of radiation, the geometry and the interaction of radiations with matter: the dose scored by means MC simulations already takes into account scattered radiation and build-up effect and no further assumptions are required.

An interesting feature of SimpleGeo is the DaVis 3D plugin that allows to overlap the result of a USBIN score over a 3D geometry. Examples of that feature are reported in Figure 5-24 to Figure 5-26.



**Figure 5-24 – Overlap of the neutron ambient dose equivalent  $H^*(10)$  over a 3D geometry: dose field around the TR19 cyclotron.**

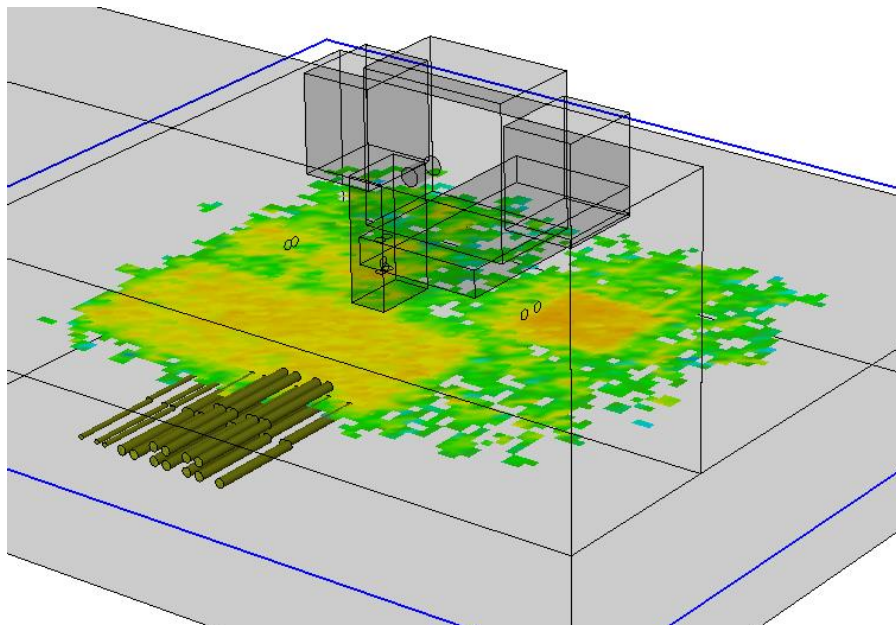


**Figure 5-25 – Overlap of the neutron ambient dose equivalent  $H^*(10)$  over a 3D geometry: dose field through the RF and power supply ducts.**

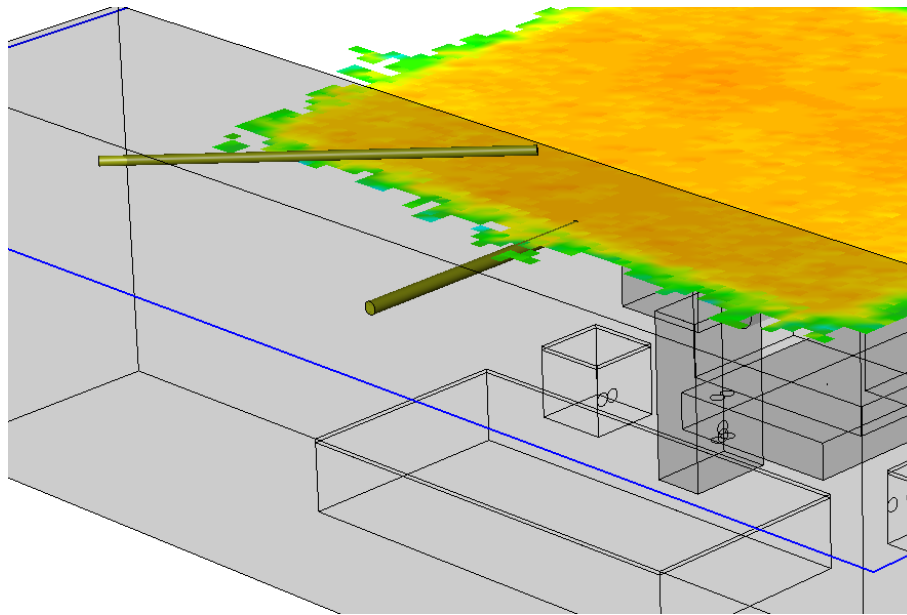


Figure 5-26 – Overlap of the neutron ambient dose equivalent  $H^*(10)$  over a 3D geometry: dose field through the pipe for the loading of the  $^{18}\text{O}$ -water target.

### 5.1.4 Release of $^{41}\text{Ar}$

The production of  $^{41}\text{Ar}$  during a dual beam irradiation was studied to assess the release in atmosphere and the radiological impact in the area close to the hospital. The amount of  $^{41}\text{Ar}$  produced in a 1hour-1 $\mu\text{A}$  dual beam irradiation, without ventilation within the bunker, was assessed using RESNUCLE score (Figure 5-27): an average “static concentration”  $C_S(^{41}\text{Ar})$  of  $0.045 \pm 0.026 \text{ Bq/dm}^3 \cdot \mu\text{Ah}$  (sum of the two target) was found at EOB.



Figure 5-27 - Assessment of  $^{41}\text{Ar}$  within the cyclotron vault without ventilation.

The release of  $^{41}\text{Ar}$  in the external atmosphere was assessed using a simple dilution model. Considering a ventilation rate within the bunker of  $r_v=10$  exchanges per hour; an air density of  $\rho_a=0.00129 \text{ g/cm}^3$ ; a dual beam irradiation at a total current level of  $150 \mu\text{A}$  it is possible to calculate the “dynamic concentration”  $C_D(^{41}\text{Ar})$  of  $^{41}\text{Ar}$ , in Bq/g, using the following relationship:

$$C_D(^{41}\text{Ar}) = \frac{C_S(^{41}\text{Ar}) \cdot I}{\rho_a \cdot r_v} \tag{Equation 5-1}$$

The resulting dynamic concentration was  $0.52 \text{ Bq/g}$ , that is under the limit of  $1 \text{ Bq/g}$  recommended by the Italian national regulation. It is important to note that this

value represents the concentration of  $^{41}\text{Ar}$  coming out from the bunker and not from the installation! The exhaust of the bunker is then summed up with the exhaust of the hot cells: from technical data of the ventilation system a total out-coming flow rate of  $2390 \text{ m}^3/\text{h}$  was evaluated. In a first approximation it is possible to assess an equivalent ventilation rate, within the bunker, of about  $2390/68=35$  exchanges per hour: under this hypothesis the dynamic concentration of  $^{41}\text{Ar}$  releasing in the external atmosphere is about  $0.15 \text{ Bq/g}$ .

The radiological impact of the continuous release of  $^{41}\text{Ar}$  in atmosphere was assessed using the validated code HotSpot 2.05 (Homann & Aluzzi, 2013). The HotSpot Health Physics codes were created to provide Health Physics personnel with a fast, field-portable calculation tool for evaluating accidents involving radioactive materials. HotSpot codes provide a first-order approximation of the radiation effects associated with the atmospheric release of radioactive materials. Four general programs, *PLUME*, *EXPLOSION*, *FIRE*, and *RESUSPENSION*, calculate a downwind assessment following the release of radioactive material resulting from a continuous or puff release, explosive release, fuel fire, or an area contamination event.

A Gaussian plume of  $^{41}\text{Ar}$  was studied using as source term the activity concentration coming out from the cyclotron vault, calculated above for a dual beam irradiation, to consider the worst scenario. Meteorological data, in particular the probability distribution of the wind direction, was taken from the Italian regional agency for the prevention and the environment (ARPA) in the year preceding the building of the facility.

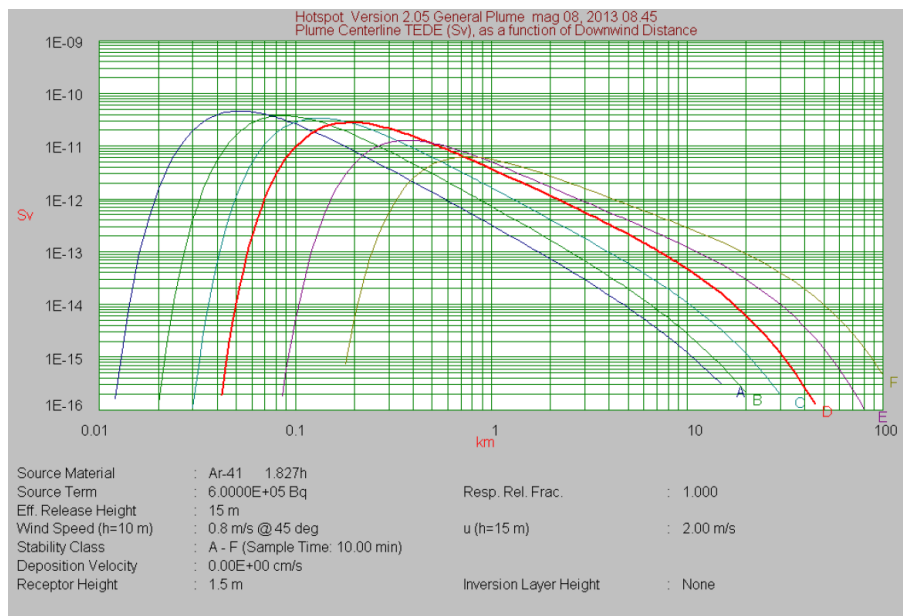


**Figure 5-28 - Radiological impact assessment, for the representative person of the population, of the release of  $^{41}\text{Ar}$  in the external atmosphere.**

The simulation was repeated for different atmospheric stability classes and 2000 working hours/year were considered. The result of the radiological impact assessment is reported in Figure 5-28. Results in Figure 5-28 are reported as Total Effective Dose (TED), taking into account the internal and external exposure and the distance from the point of emission: the maximum TED scored was less than 0.08  $\mu\text{Sv}$ . It is important to remember that, from the results of section 3.4, FLUKA overestimates the production of  $^{41}\text{Ar}$  and the result found is further conservative.

### 5.1.5 Activation of Walls and Local Shield

Long-term activation of local shields and vault walls was studied to assess the order of magnitude of activity after 10 years in operation and to plan strategies of decommissioning. A 10-years irradiation was simulated (Figure 5-29): an average proton current of 2.3  $\mu\text{A}$  was calculated taking into account a realistic workload of the accelerator. The radionuclidic inventory within the two local shields and the cyclotron vault walls was assessed using several RESNUCLE cards; activity was scored at different cooling times spanning from 0 to 6 weeks from EOB.

<b>IRRPROFI</b>	$\Delta t$ : =year*10	$p/s$ : =2.3*6.21E12	
	$\Delta t$ :	$p/s$ :	
	$\Delta t$ :	$p/s$ :	
<b>DCYTIMES</b>	$t1$ : 0.0	$t2$ : =week*1	$t3$ : =week*2
	$t4$ : =week*3	$t5$ : =week*4	$t6$ : =week*6

Figure 5-29 - Irradiation profile used in the assessment of the long-term activation of local shields and cyclotron vault walls.

The radionuclidic inventory assessed within the two local shields is reported in Figure 5-30 using the typical 2D maps (atomic number to mass number) obtainable using RESNUCLE score. When an average irradiation profile is simulated, the order of magnitude of the activity produced of long half-life radionuclides is well reproduced. Generally the cyclotron works some hours during the days, depending on the workload of the facility, but between two irradiations (let say between two working days) long half-life radionuclides do not decay significantly: the total effect during 1 year working is an accumulation of the activity produced. Vice versa this fact is not true for the short half-life radionuclides: as shown in Figure 5-30, the total activity present within the two local shields at EOB is overestimated due to the presence of radionuclides with a short half-life such as  $^{13}\text{N}$  ( $t_{1/2}=7.1$  s),  $^{38}\text{Cl}$  ( $t_{1/2}=37.2$  m),  $^{53}\text{Fe}$  ( $t_{1/2}=8.51$  m),  $^{55}\text{Cr}$  ( $t_{1/2}=3.5$  m),  $^{57}\text{Mn}$  ( $t_{1/2}=85$  s),  $^{58}\text{Mn}$  ( $t_{1/2}=3$  s), etc. After a waiting time large enough to allow the decay of radionuclides with half-life from seconds to a few days, for example 4 weeks, the radionuclidic inventory of Figure 5-30 is much more realistic than at EOB. On the other hand, in real case, during the decommissioning of a site it is not realistic that the dismantling operations on the cyclotron begin the day after the last production. Actually it is more realistic that operations on the accelerator begin only after some weeks, in which furniture and other secondary equipment are taken away from the site. From a radiation protection point of view we are interested in assessing the order of magnitude of

the long half-life radionuclides that might be managed by workers involved in the decommissioning.

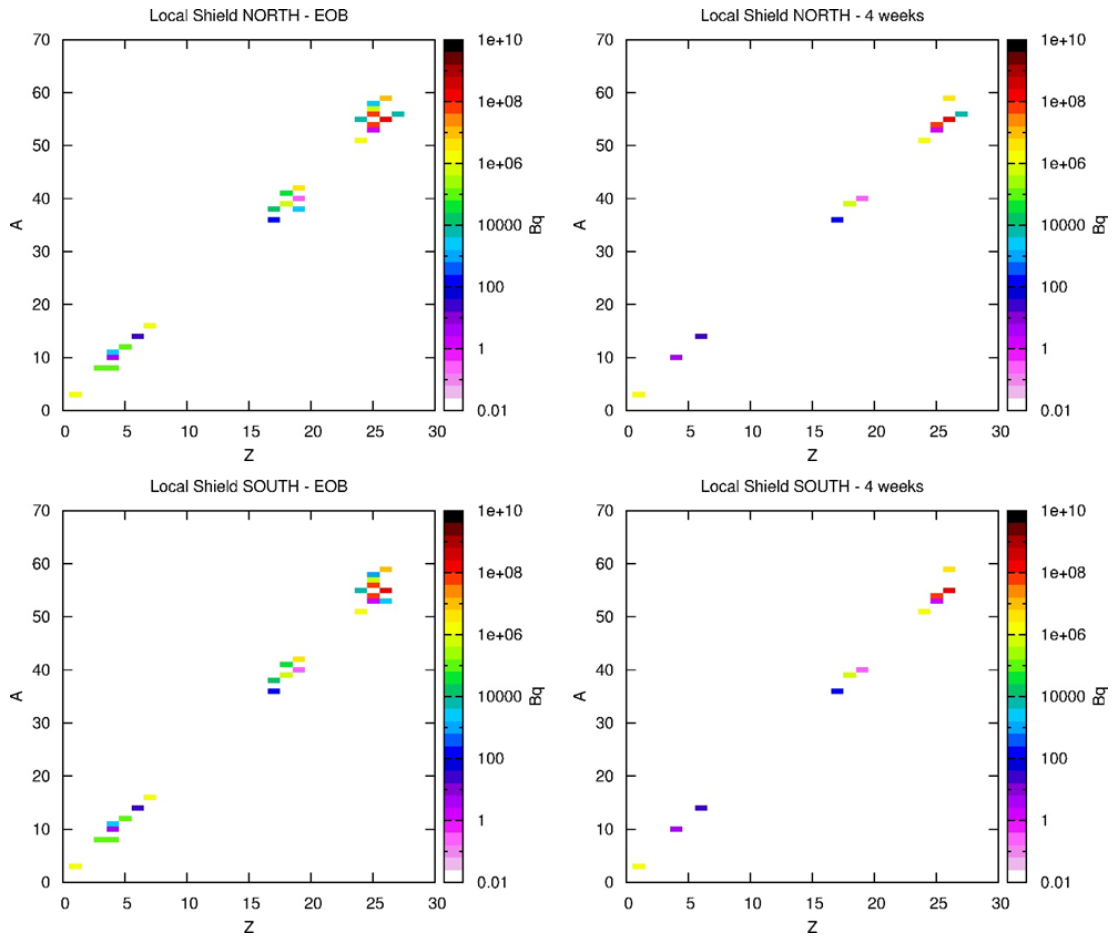


**Figure 5-30 – Long-term activation of local shields: the radionuclidic inventory was assessed at EOB and 4 weeks after EOB.**

Similar considerations can be done regarding the activation of the cyclotron vault walls. Considering the decommissioning of a site, the assessment of the activity induced within the concrete walls is one of the most important radiation protection problems. Quantification of long half-life radionuclides is important again not only for the radiation protection of workers but also to assess the volume of radioactive waste: actually the D.Lgs 203/95 prescribes that a mixture of radionuclides needs to be treated as radioactive waste if the sum of the ratio between the activity concentration of a given radionuclide and the limit activity concentration is greater than 1 or if radionuclides with a half-life greater than 75 days are present in the mixture. Figure 5-31 and Figure 5-32 show the results obtained for the cyclotron vault walls.

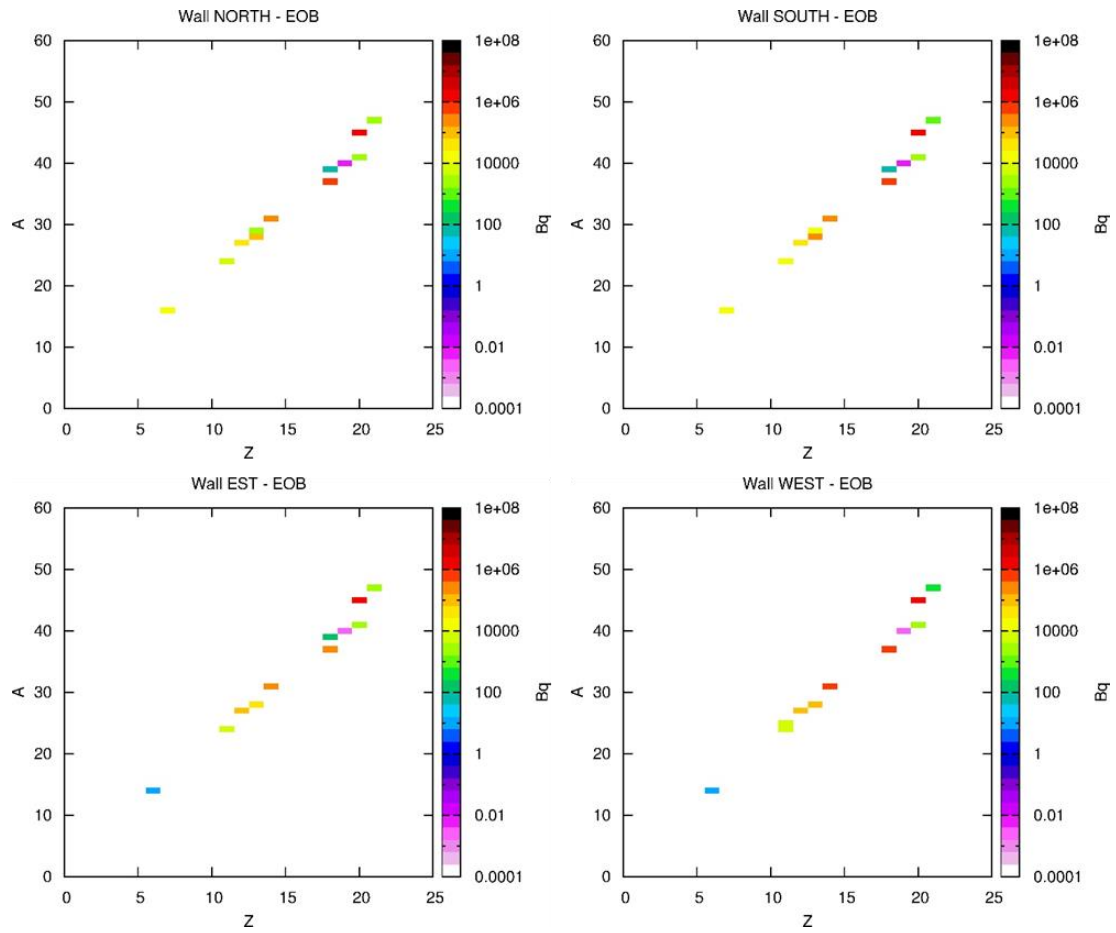


Figure 5-31 - Long-term activation of cyclotron vault walls: the radionuclidic inventory was assessed at EOB.

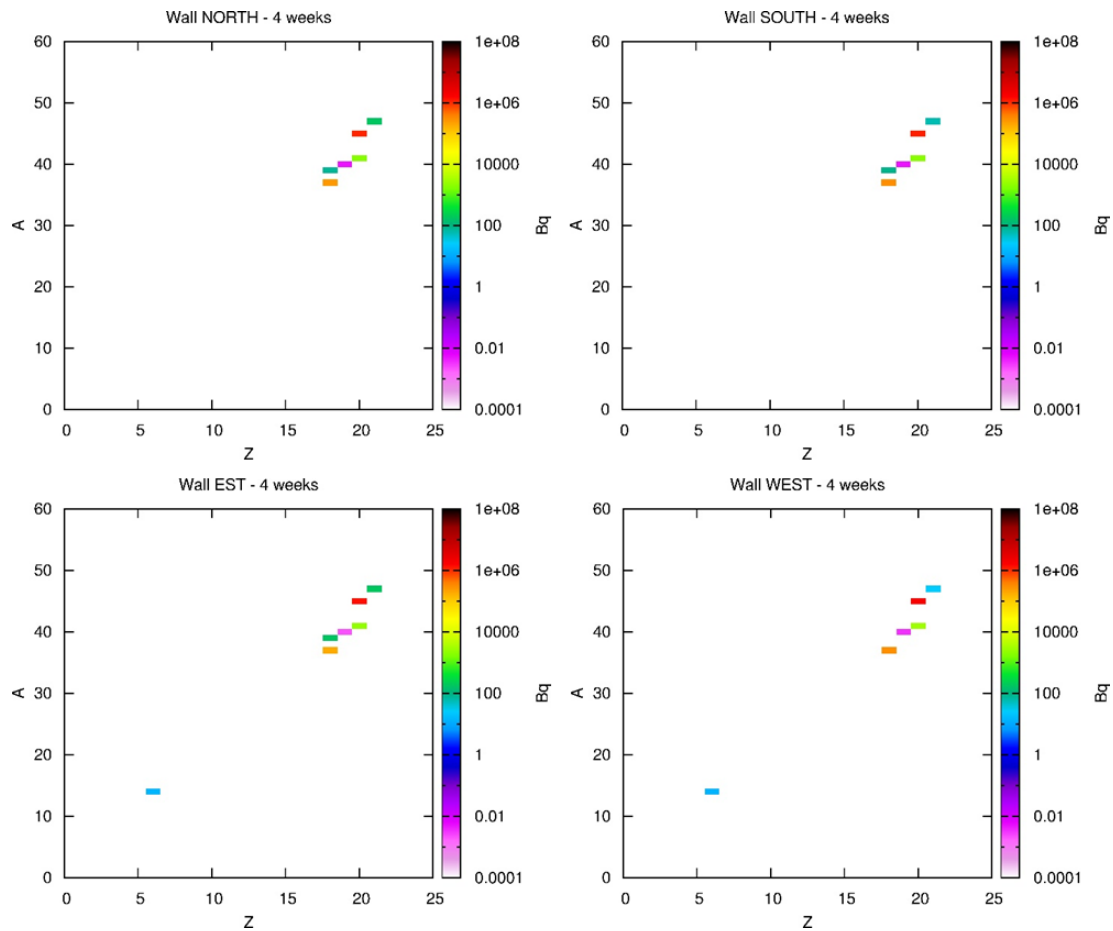
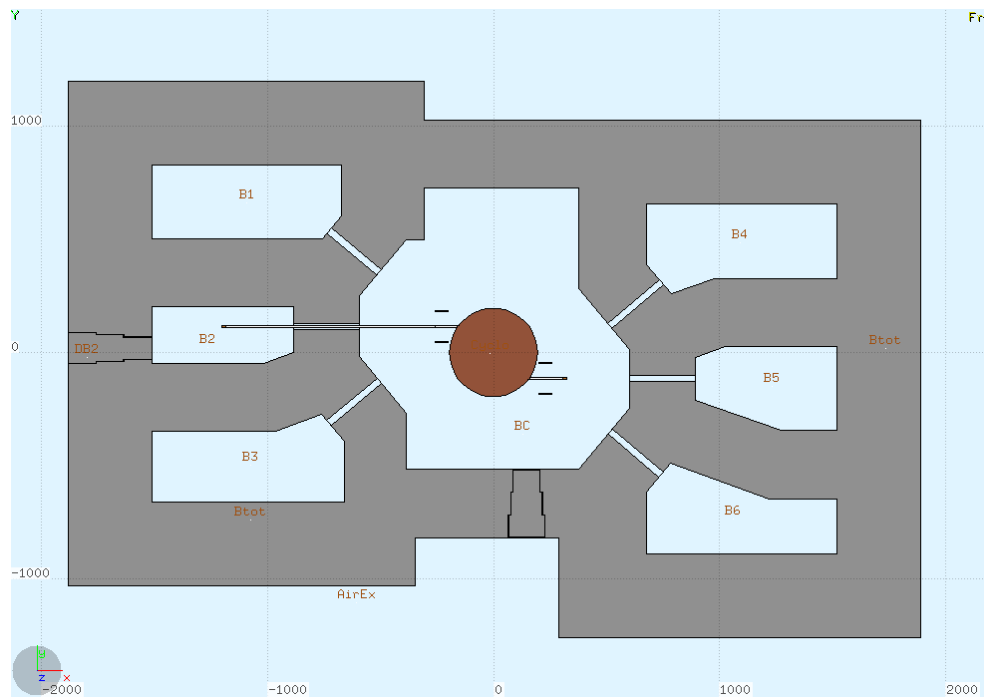


Figure 5-32 - Long-term activation of cyclotron vault walls: the radionuclidic inventory was assessed 4 weeks after EOB.

## 5.2 Assessment of the dose transmission through several types of plug-doors

In this section, the assessment of the dose transmission through several types of plug-doors, in planning a new cyclotron facility, is reported. In Figure 5-33 the FLUKA MC model of the new facility is reported: a 70 MeV cyclotron, provided with two extraction ports, is placed in the main vault (BC); on each extraction port a dipole allows to direct the beam through different vaults (B1 to B6), where target stations are mounted, by a beam line. The aim of this section is to find the optimal plug-door solution for the cyclotron and the target vaults. A detailed MC model of the bunkers and the plug-doors (Figure 5-34), including the air gap between the door and its housing, were created; a detailed model of the cyclotron was not necessary in this

study and a simplified one was created to reproduce the average dose field within the cyclotron vault.



**Figure 5-33 - Layout of the new cyclotron facility.**

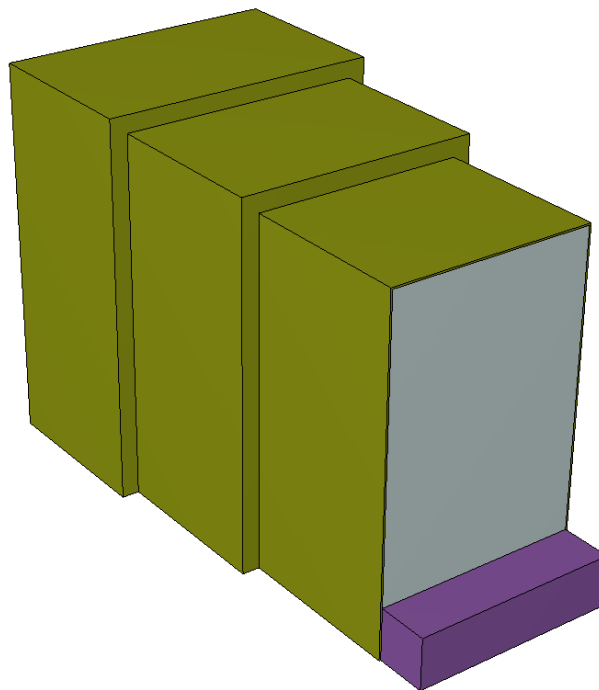


**Figure 5-34 - FLUKA MC model of plug-door studied: the figure shows the solution with a borated-PE block in front of the door.**

All the plug-doors studied (160 cm width; 220 cm height; 300 and 370 cm long for the cyclotron and the targets vaults respectively) are made of concrete with a steel cover of different thickness. Differences in the solutions studied are reported in the following:

- **Solution "A"**: Standard plug-door with a steel cover of 6 mm; top and lateral air gap of 10 mm; bottom air gap of 20 mm;
- **Solution "B"**: Plug-door of solution "A" and an addition step of 100 mm in the vault side;
- **Solution "C"**: Standard plug-door with a top and lateral steel cover of 6 mm and 16 mm in the bottom; air gap of 10 mm in all the directions. A block of 30% borated-polyethylene (PE) (30x30x160 cm) was added in front the door in the vault side.

All the simulations were performed using a 70 MeV proton pencil beam hitting a cylindrical beam dump made of copper: the dimension of the beam dump was calculated using the SRIM code (Ziegler, et al., 2010) to allow the complete absorption of the particle beam. An irradiation profile of 1 hour at the maximum current level of 350  $\mu\text{A}$  was simulated. Neutron and gamma ambient dose equivalent  $H^*(10)$  was assessed using several USBIN cards: in setting the different cards a 10 cm and 2 cm pitch were used to allow the scoring over a coarse and fine Cartesian mesh respectively.

The different plug-doors solutions were tested for two different bunkers: the cyclotron vault (BC) and the vault n°2 (B2). From a radiation protection point of view, the presence of a beam dump within BC is not realistic but allowed to create a more intense radiation field; B2 was selected as the worst case of the six target vaults considering the relative position of the plug-door respect to the direction of the proton beam. Comparison of the different solutions will be presented for the two bunkers studied. Once again, as final remark, MC simulations allow to take into account the build-up effect without any further assumption on the radiation field.

### 5.2.1 Bunker BC

Results obtained for the cyclotron vault are reported in Figure 5-35 and Figure 5-36, for the three different solutions studied. Figure 5-35 shows how using the standard plug door (solution "A") a dose transmission through the bottom air gap (Figure 5-36) might be possible. The dose transmission is reduced when a step is introduced in solution "B" and even more using the borated-PE block of solution "C". Similar results were found for gamma radiation with a dose field about a factor  $10^2$  smaller than the neutron field reported below. Again, as reported in section 5.1.3, the number of primary particles simulated does not allow to quantify, with good accuracy, the dose rate due to the neutrons transmitted below the plug-door.

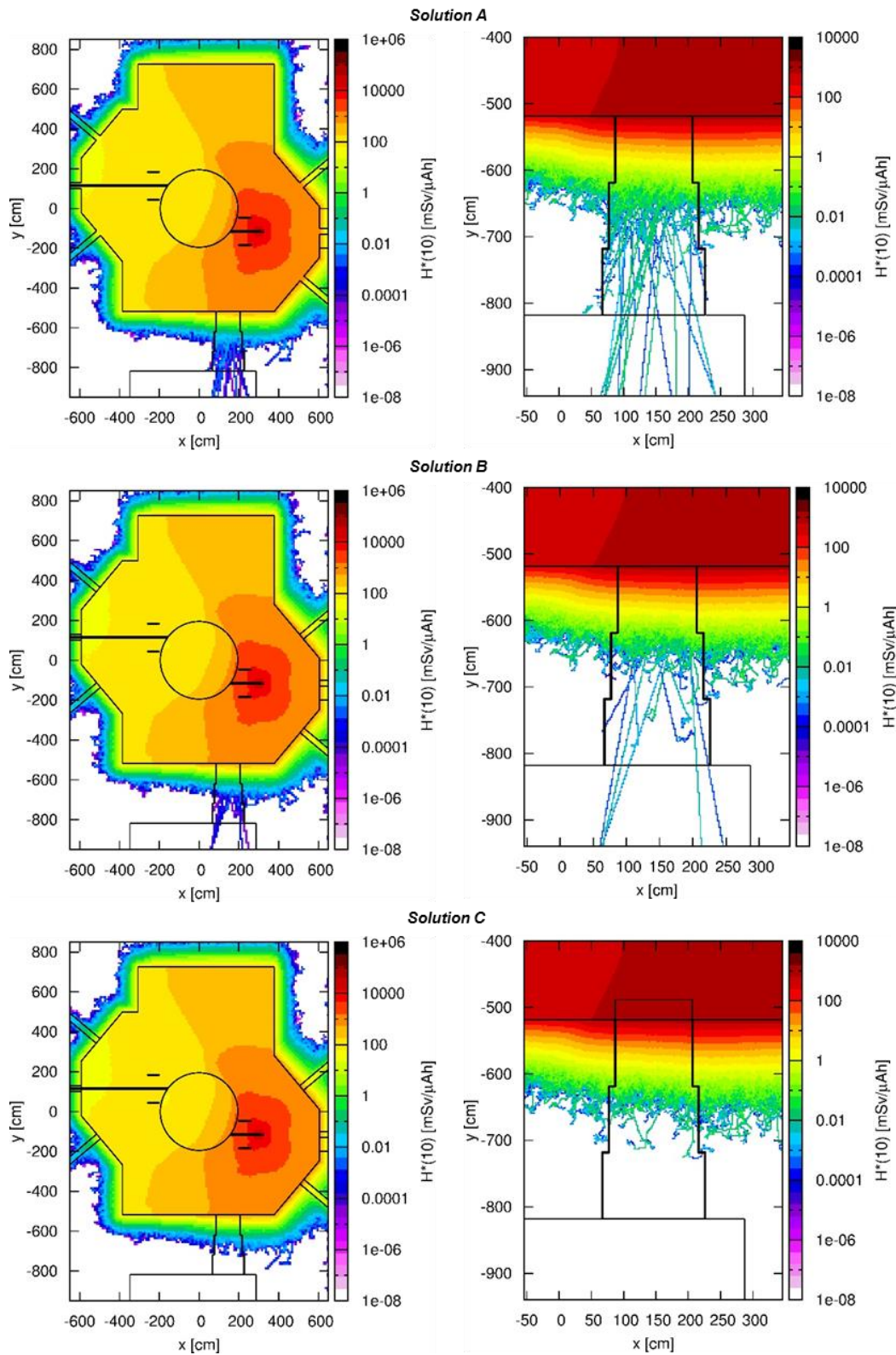
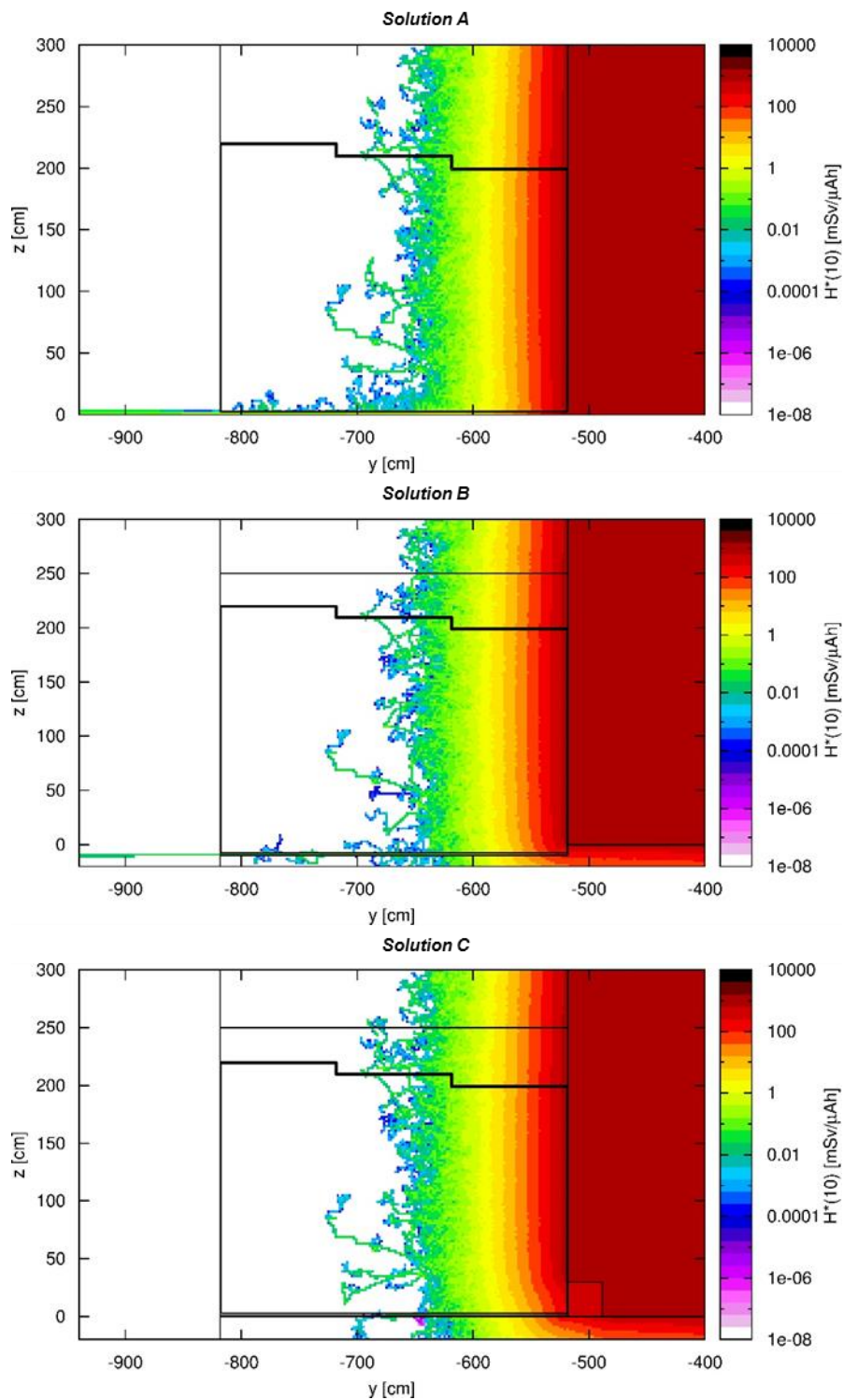


Figure 5-35 – Comparison of the different solutions of plug-doors studied: assessment of the neutron ambient dose equivalent over the whole BC (coarse mesh) and detail of the plug-door (fine mesh).



**Figure 5-36 – Comparison of the different solutions of plug-doors studied: assessment of the neutron ambient dose equivalent over the BC plug-door in the transverse direction (fine mesh).**

On the other hand, the quantification of the order of magnitude of the average dose rate outside the plug-door in contact with the wall and at a height of 150 cm can be

performed from the knowledge of the dose rate incident to the inner side of the door and from general considerations on the neutron spectra and the TVL: for a 300  $\mu\text{A}$  irradiation a dose rate of  $\sim 0.21 \mu\text{Sv}$  was found.

### 5.2.2 Bunker B2

Results obtained for the cyclotron vault are reported in Figure 5-37 to Figure 5-39, for the three different solutions studied.

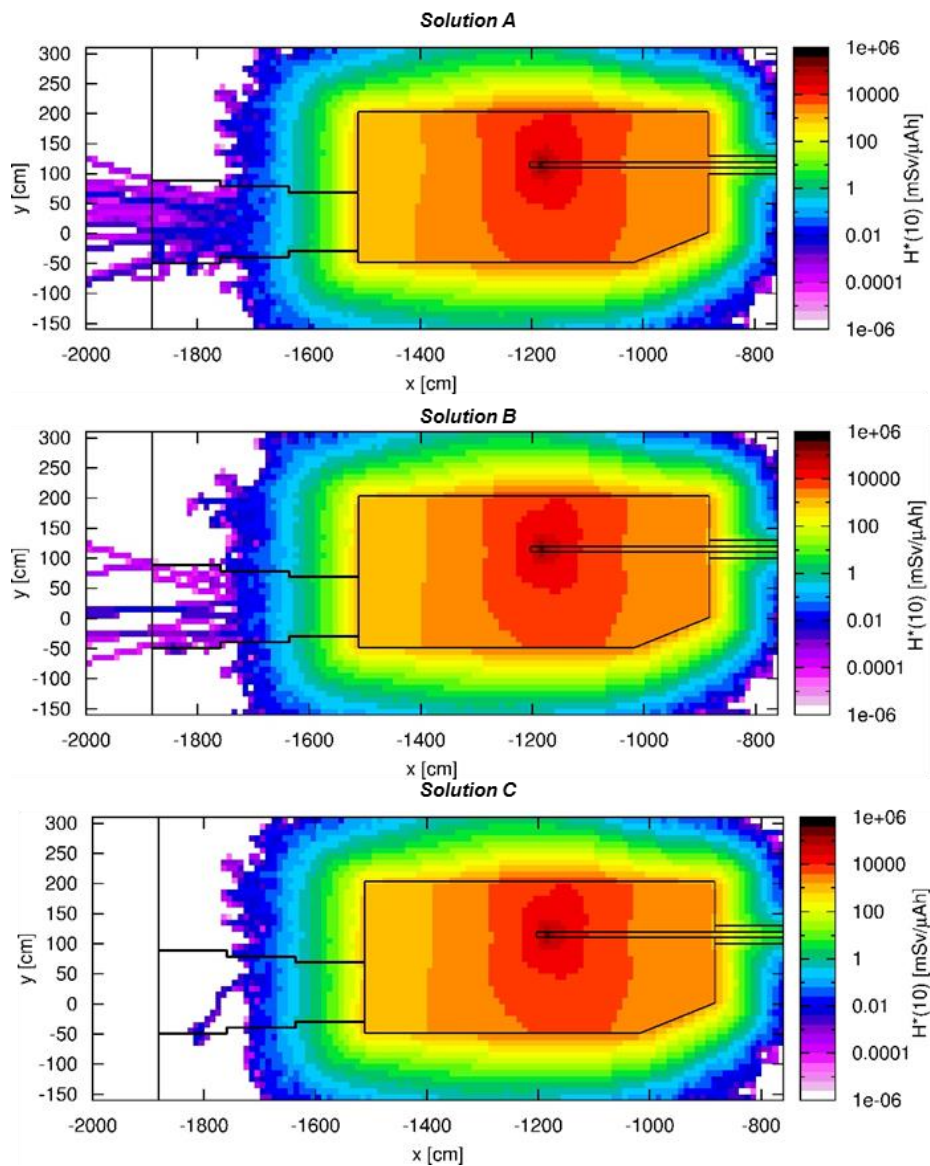


Figure 5-37 – Comparison of the different solutions of plug-doors studied: assessment of the neutron ambient dose equivalent over the whole bunker B2 (coarse mesh)

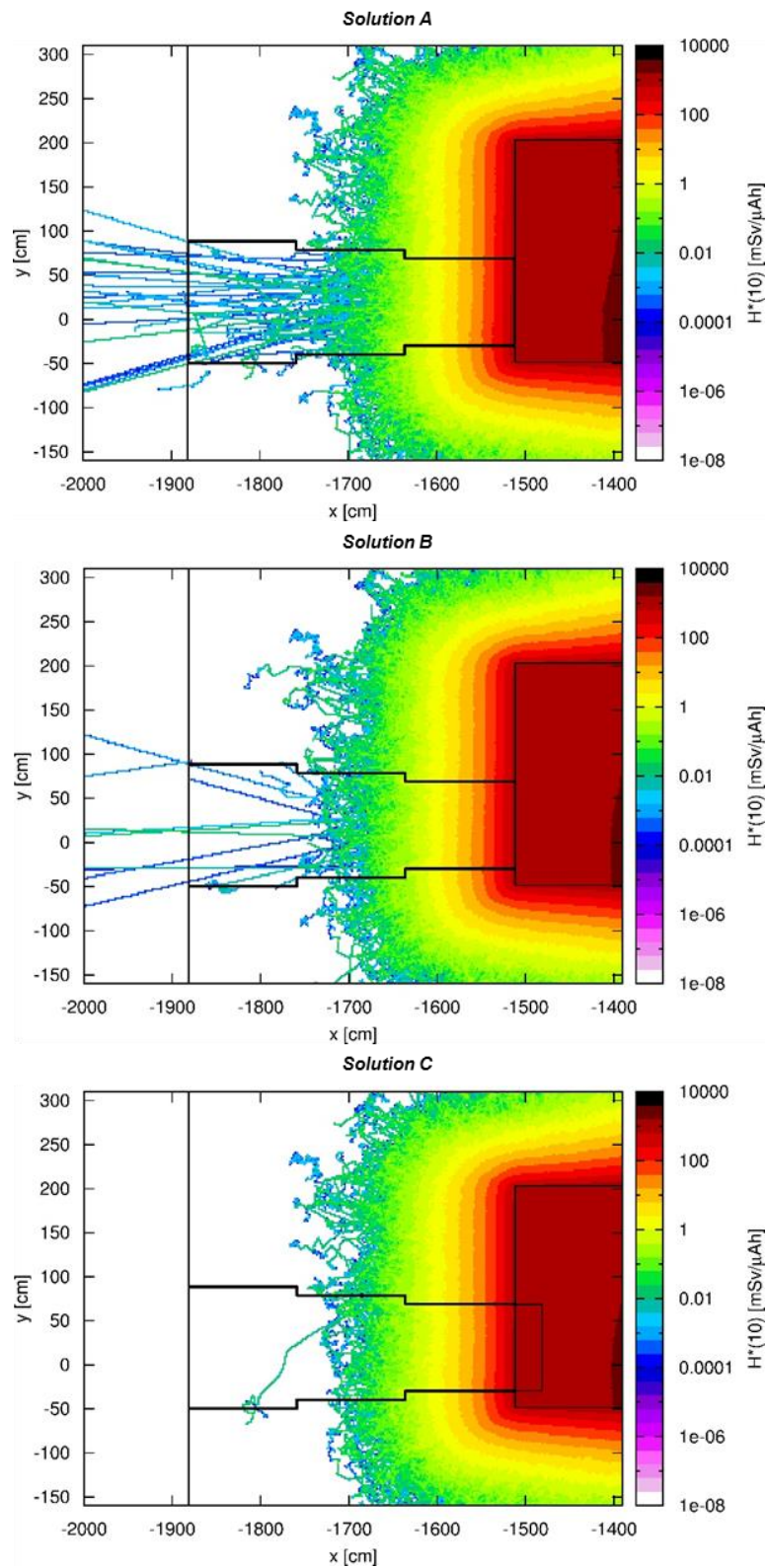
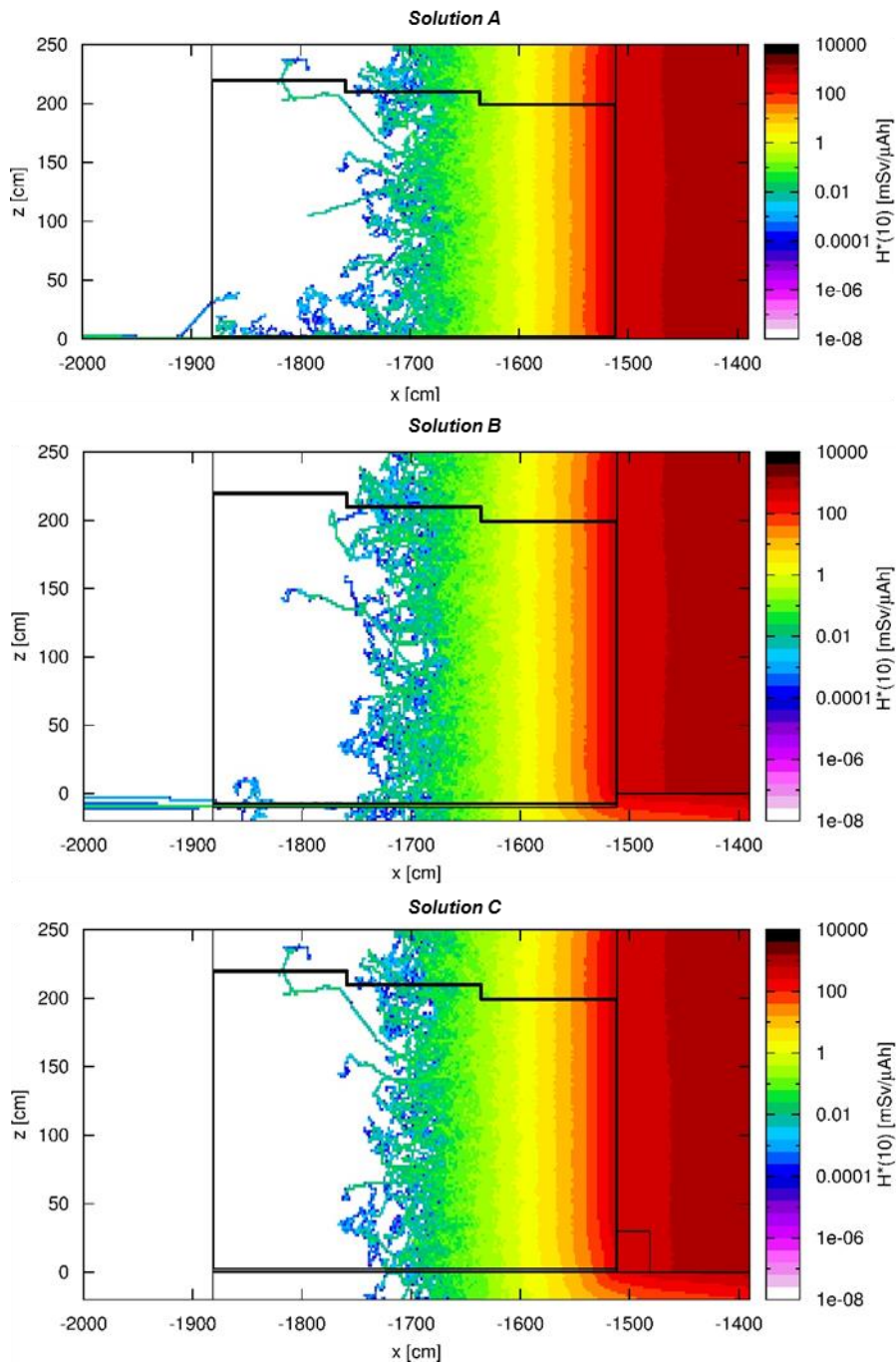


Figure 5-38 – Comparison of the different solutions of plug-doors studied: detail of the assessment of the neutron ambient dose equivalent over the B2 plug-door (fine mesh).



**Figure 5-39 - Comparison of the different solutions of plug-doors studied: assessment of the neutron ambient dose equivalent over the B2 plug-door in the transverse direction (fine mesh).**

Similarly to the results obtained for the BC, Figure 5-37 and Figure 5-38 show how using the standard plug door (solution “A”) a dose transmission through the bottom air gap (Figure 5-39) might be possible. The dose transmission is reduced when a step is introduced in solution “B” and even more using the borated-PE block of solution “C”. Similar results were found for gamma radiation with a dose field about

a factor  $10^2$  smaller than the neutron field reported below. On average outside the plug-door in contact with the wall and at a height of 150 cm a dose rate of  $\sim 0.12 \mu\text{Sv}$  (order of magnitude) was found for a  $300 \mu\text{A}$  irradiation.

### **5.3 Replacement of Scanditronix MC17 with a TR19 cyclotron**

The partial decommissioning of a PET facility and the replacement of a Scanditronix MC17 cyclotron (Figure 5-40) with a new ACSI TR19 unit were evaluated using FLUKA. The MC17 cyclotron can accelerate  $H^+$  and  $D^+$  ions up to 17 and 8.5 MeV respectively; maximum current available is  $75 \mu\text{A}$  for  $H^+$  ions (typical irradiation current is  $50 \mu\text{A}$ ) and  $50 \mu\text{A}$  for  $D^+$  ions. An average workload of 15 h/week for radionuclides production was considered (IAEA, 2006).



**Figure 5-40 - The Scanditronix MC17 cyclotron.**

The partial decommissioning of the site and the replacement of the cyclotron with a new TR19 unit were studied. A detailed FLUKA MC model of the cyclotron and the cyclotron vault were created from original technical drawings (Figure 5-42).

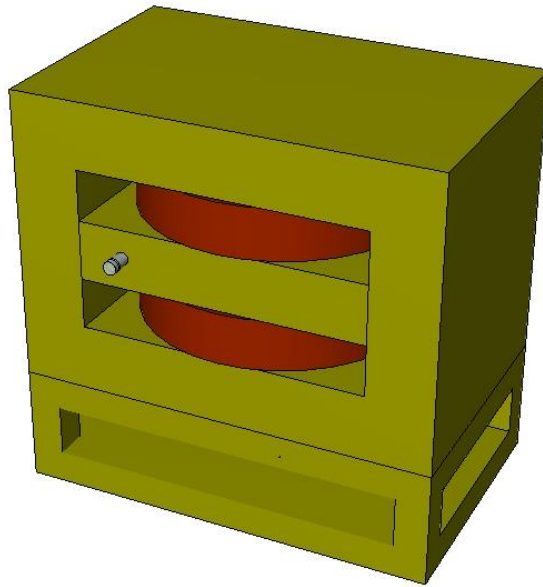


**Figure 5-41 - FLUKA MC model of the Scanditronix MC17 cyclotron.**

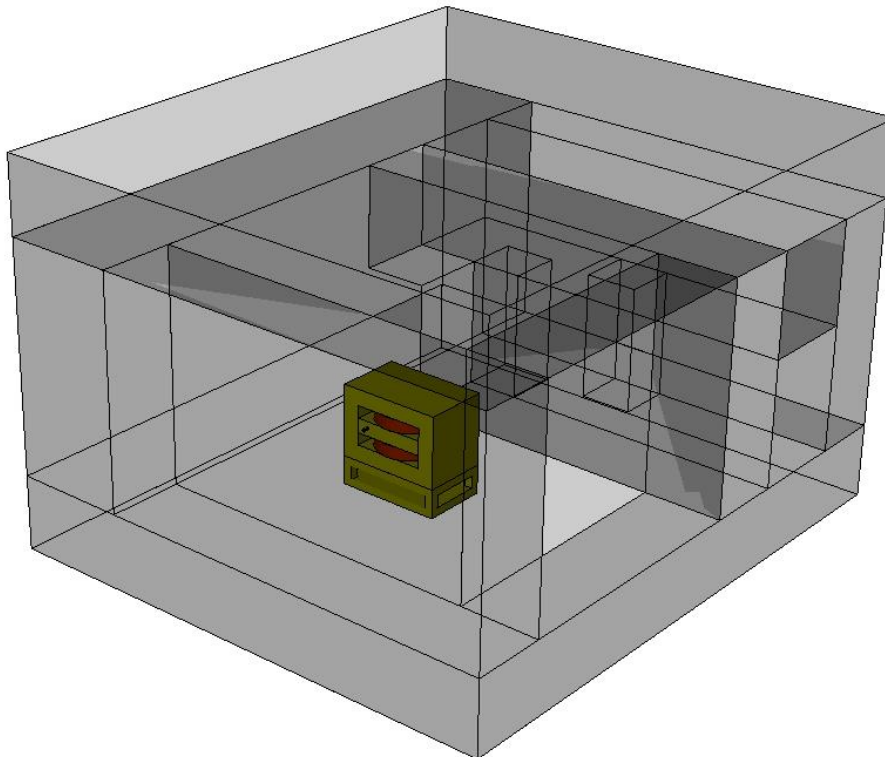


**Figure 5-42 - FLUKA MC model of a Scanditronix MC17 cyclotron and the cyclotron vault.**

A 17 MeV proton pencil beam was simulated and NEW-DEFA default was used with proton transport threshold set to 1 MeV using a dedicated *PART-THR* card. Coalescence and evaporation of heavy fragment were enabled using two *PHYSICS* cards. The vault walls were made of PORTLAND concrete with addition of traces of Eu (1e-6 %) and Co (1e-4 %). *RADDECAY* was enabled in active mode and a 1hour-1 $\mu$ A irradiation was simulated. Neutron ambient dose equivalent  $H^*(10)$  was assessed using *USRBIN* (Cartesian mesh, 5 cm pitch) and *AUXSCORE* cards. Long-term activation was evaluated, using several *RESNUCLE* cards, by splitting the first 60 cm of the vault walls into 10 cm thick slabs; wall "NORTH" (in the direction of the proton beam) was additionally divided in blocks of 1 m<sup>2</sup>. An irradiation profile of 5 years at an average current level of 0.57  $\mu$ A, calculated from evaluations on the effective workload of the accelerator, was simulated; activity was scored 1 year after EOB to allow for the decay of short half-life radionuclides.  $10^{10}$  primary particles were simulated. The assessment of the neutron ambient dose equivalent  $H^*(10)$  is reported in Figure 5-43; Figure 5-44 shows the long-term activation in the blocks in front of the target assembly.

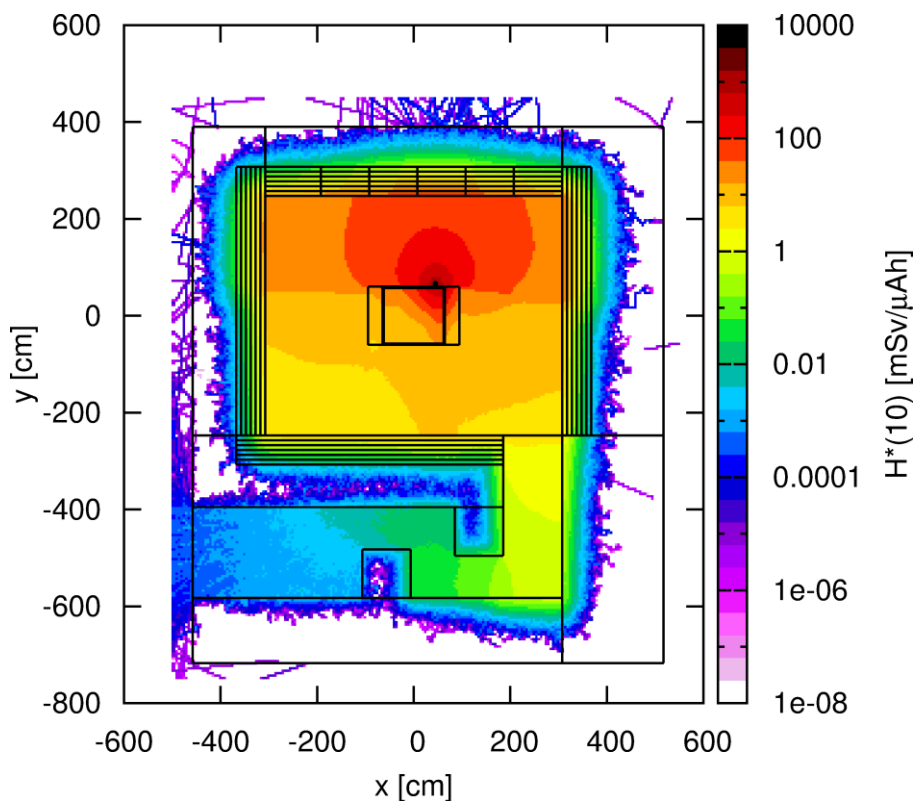


**Figure 5-43 - Assessment of the neutron ambient dose equivalent  $H^*(10)$  produced by the MC17 cyclotron over the whole cyclotron vault.**

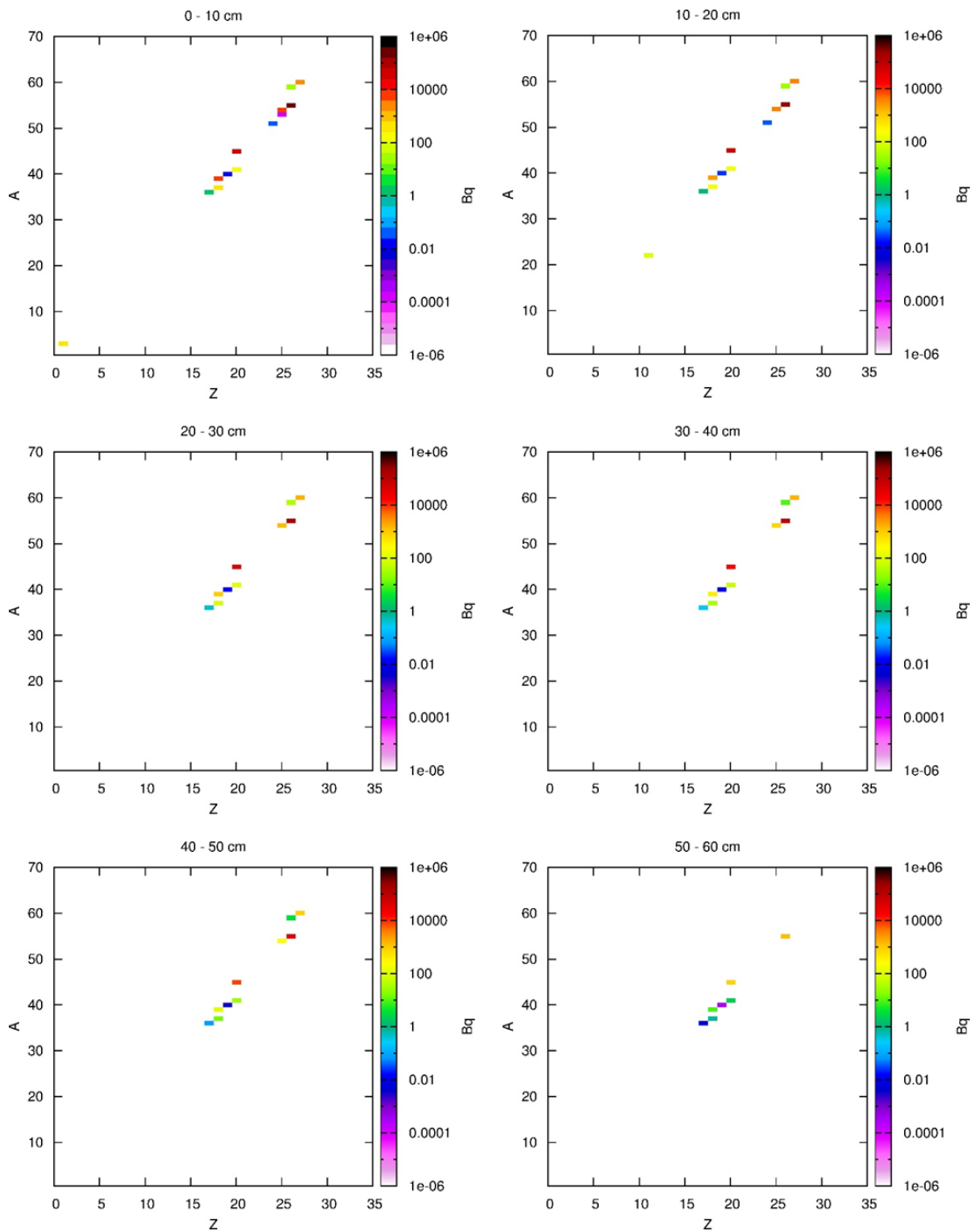


**Figure 5-44 - Long-term activation of the part of wall NORTH in front of the target assembly.**

Figure 5-43 shows once again how MC simulation allows to assess the dose field more accurately than analytical methods in bad geometry condition as in example the maze of the bunker. From Figure 5-44, it was possible to identify the radionuclides involved in the long-term activation and to assess the order of magnitude of the activity produced. To make the plots of Figure 5-44 more readable,

$^{152}\text{Eu}$  and  $^{154}\text{Eu}$  were not plotted even if traces of these two radionuclides were found in several slabs ( $\sim 1$  kBq and  $\sim 300$  Bq respectively in the first 10 cm). From the decommissioning point of view the most important long half-life radionuclides found, considering the first 10 cm, are  $^{60}\text{Co}$  ( $\sim 2$  kBq),  $^{55}\text{Fe}$  ( $\sim 220$  kBq),  $^{54}\text{Mn}$  ( $\sim 1.5$  kBq),  $^{45}\text{Ca}$  ( $\sim 50$  kBq).

The possibility to install a new TR19 unit, using the same layout of the cyclotron vault, was studied replacing the MC17 cyclotron in the MC model with the new accelerator. The result of the assessment of the neutron ambient dose equivalent  $H^*(10)$  is reported in Figure 5-45.

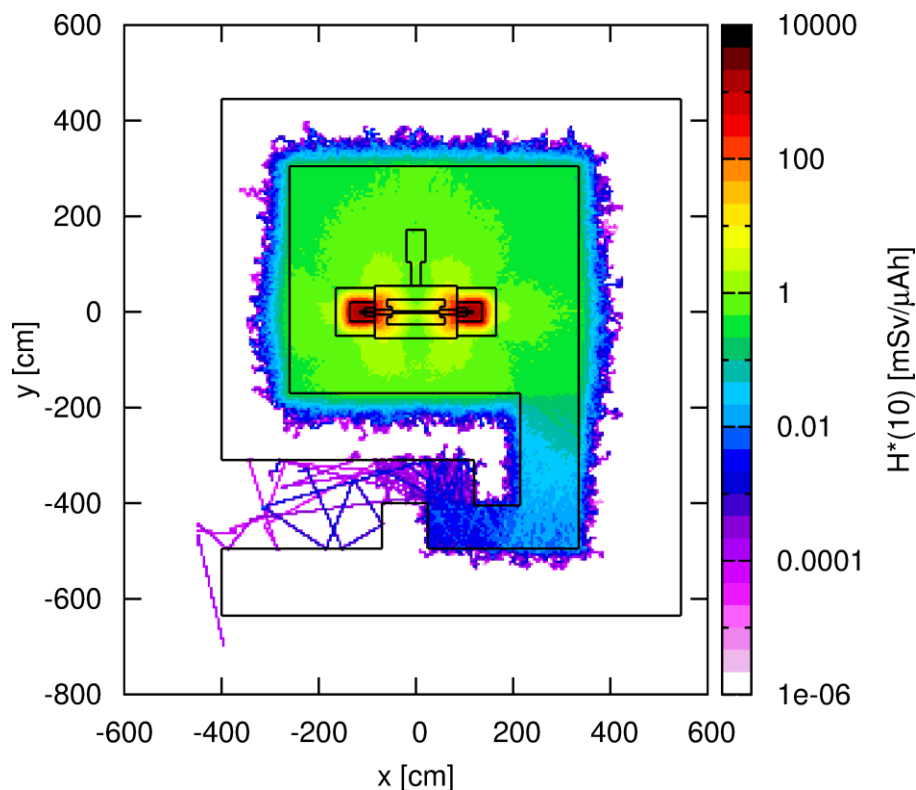


**Figure 5-45 – Replacement of a MC17 cyclotron with a TR19: Assessment of the neutron ambient dose equivalent  $H^*(10)$  using the existing layout of the cyclotron vault.**

The two local shields of TR19 therefore allow to use the existing layout of the cyclotron vault. From Figure 5-43 and Figure 5-45 it was possible to assess the order of magnitude of the dose rate at the entrance of the maze (the first of the two columns): the MC17 produced an average dose rate of  $0.13 \pm 0.05$  mSv/ $\mu\text{Ah}$  while for TR19, thanks to its local shields, the average dose rate was  $0.41 \pm 0.19$   $\mu\text{Sv}/\mu\text{Ah}$ , about a factor  $\sim 300$  smaller.

## 5.4 Ambient dose assessment around an energy degrader for proton therapy

In the previous sections, it was shown how Monte Carlo simulation allows an accurate modeling of cyclotron facilities. However, as partially seen in section 5.1.3, MC can be extremely useful when some general requirements of a new facility are known and it is necessary to provide other people involved in the planning with data essential to proceed with the installation. For example at the beginning of the planning civil engineers typically need a rough estimation of the cyclotron vault dimensions to give us a more detailed layout. In this context it was interesting to assess the dose field around an energy degrader for proton therapy application to evaluate the  $H_{ref}(\theta, r)$  term of Equation 1-2. Actually, in a real case, the degrader would be one of the components in which the beam interacts thus producing a significant dose emission and activation.

A general and simplified model of an energy degrader was created based on existing commercial devices. The degrader is composed of a Stainless Steel vacuum box in which a beam collimation assembly in Copper and two rows of wedges are hosted: by moving the wedges the total thickness of graphite crossing by the beam is varied and the out-coming proton energy is changed. At this stage the wedges were modeled as a variable thickness of graphite. Part of the beam line was modeled to allow the beam entering the degrader (Figure 5-46). Finally, the model was placed in an air box to allow the assessment of a non-shielded dose field.

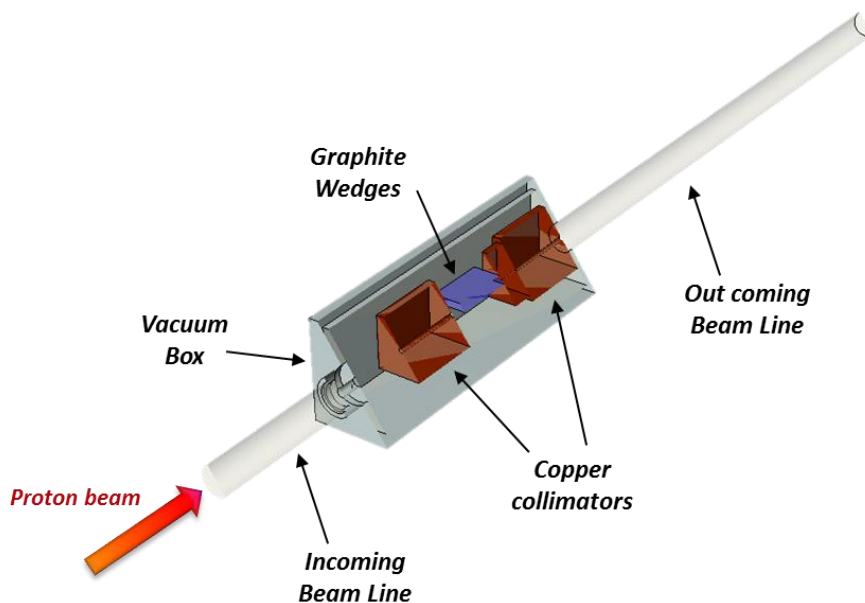


Figure 5-46 - Section of the 3D FLUKA MC model of a degrader for proton therapy application (45° clipping plane).

To obtain different out-coming proton energies, the degrader wedges were simulated as a variable thickness of graphite: several clinical values of the out-coming proton energy were chosen and the thickness of the wedges was assessed using the SRIM code (Ziegler, et al., 2010). Table 5-4 reports, for each energy, the corresponding value of the thickness simulated.

Table 5-4 - Thickness of the degrader wedges for different out-coming proton energies.

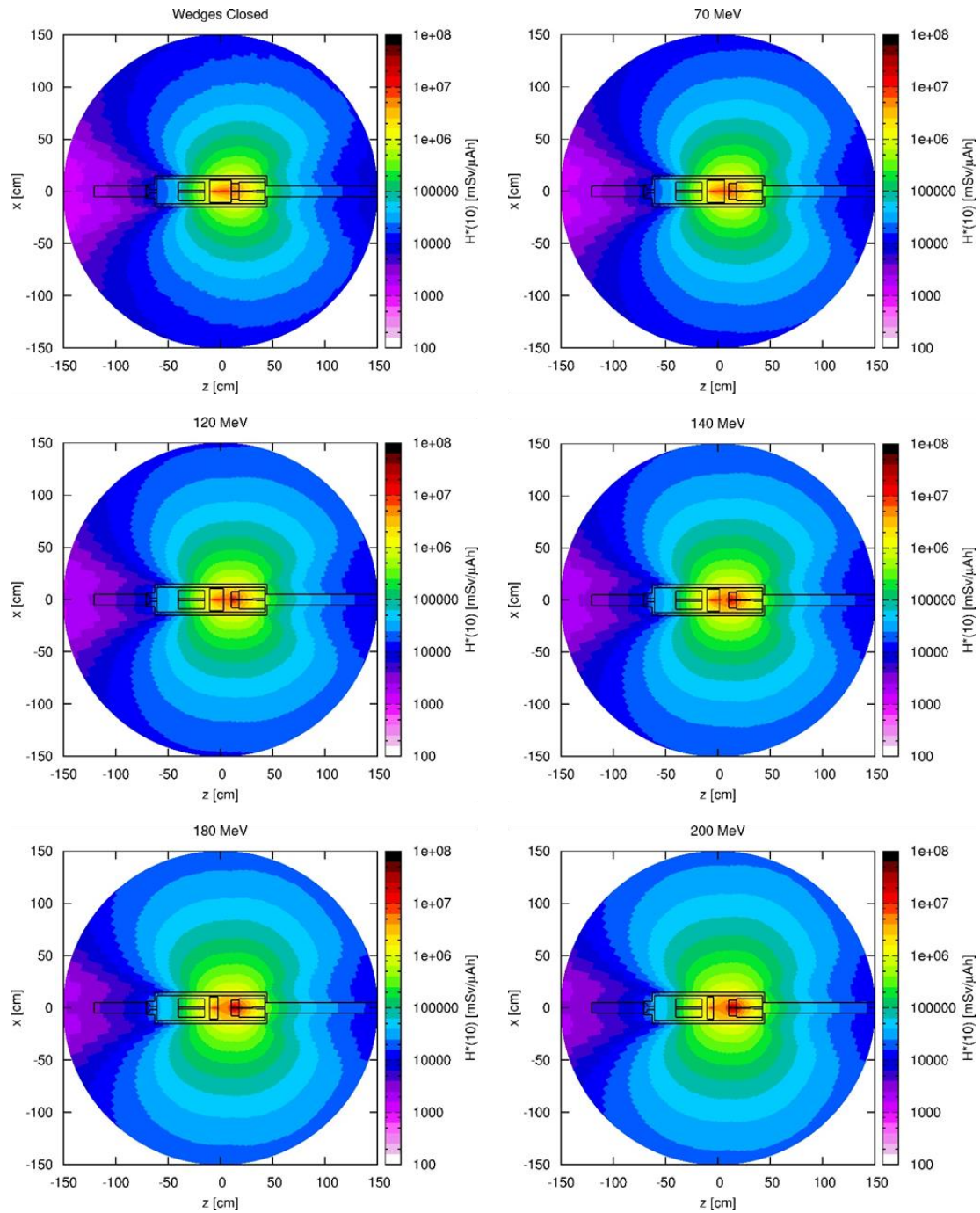
Out-coming Proton Energy [MeV]	Wedges Thickness $\Delta z$ [cm]
Wedges Closed	20.600
70	16.691
120	13.452
140	11.816
180	8.304
200	5.910

A 250 MeV proton beam was modeled using *BEAM* and *BEAMPOS* cards: a spread out beam, elliptical-shaped, with  $FWHM_x=0.25$  cm,  $FWHM_y=0.2$  cm,  $FWHM_{\Delta p}=0.0001$  GeV/c was set. NEW-DEFA default was used and coalescence and evaporation of heavy fragment were enabled using two *PHYSICS* cards; *RADDECAY* was enabled in active mode and a 1hour-1 $\mu$ A irradiation was simulated. Neutron and gamma ambient dose equivalent  $H^*(10)$  was assessed using *USRBIN* (cylindrical mesh; 1 cm pitch on R and z-direction; 2.5° pitch on angle) and *AUXSCORE* cards. Since the *USRBIN* cylindrical mesh has by default the height oriented along the z-axis, *ROT-DEFI* and *ROTPRBIN* cards were used to rotate some *USRBIN* scores to have the height of the mesh oriented along the y-axis.

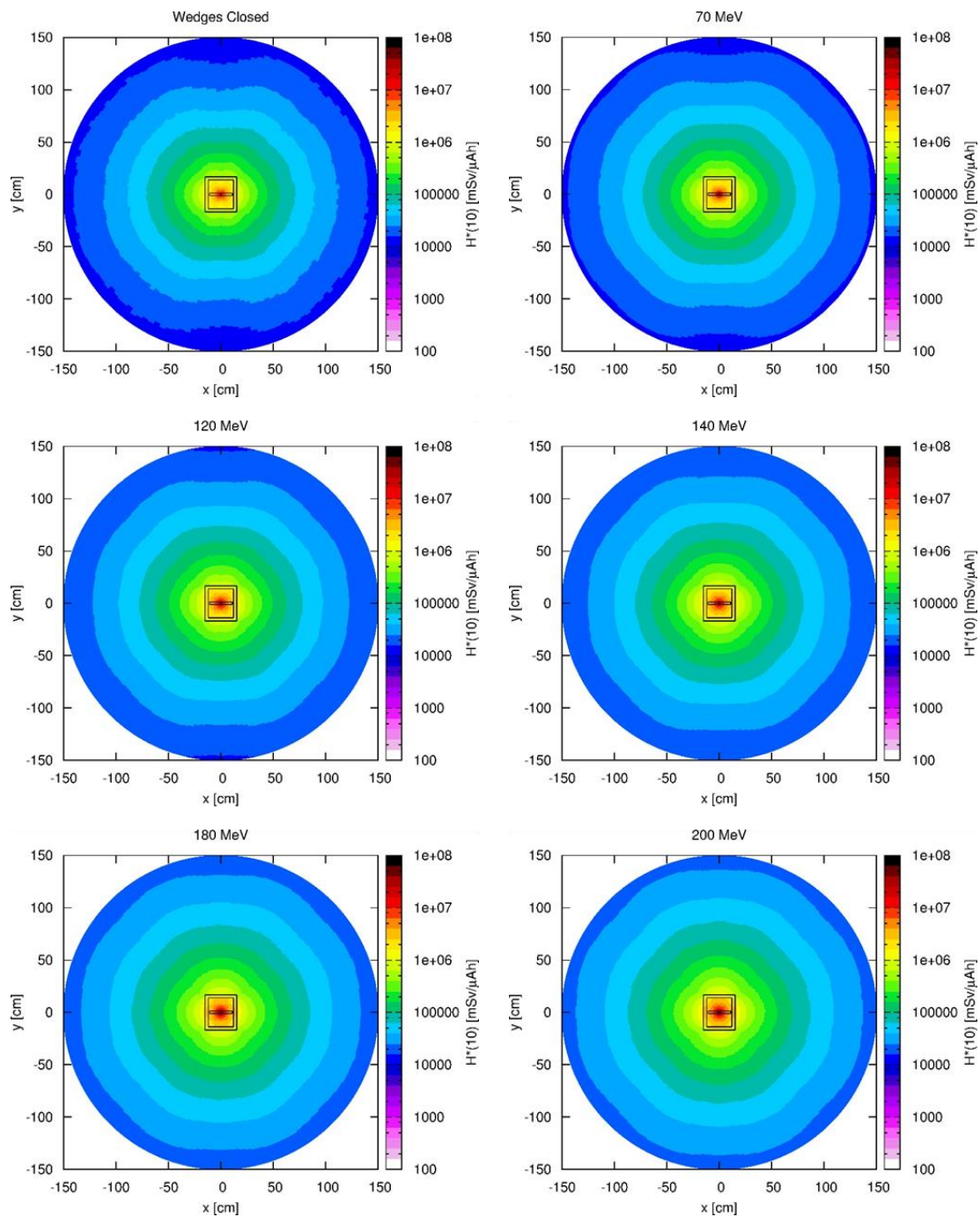
<b>ROT-DEFI</b>	Axis: X Polar: 0.0 $\Delta x$ : 0.0	Id: 1 Azim: 90. $\Delta y$ : 0.0	Name: rot90 $\Delta z$ : 0.0
<b>ROTPRBIN</b>	Storage: Bin: doseNy	to Bin: doseGy	Rot: rot90 Step: 2.
<b>USRBIN</b>	Type: R- $\Phi$ -Z Part: DOSE-EQ Rmin: 0.0 X: 0.0 Zmin: -20.	Unit: 30 BIN Rmax: 150. Y: 0.0 Zmax: 20.	Name: doseN NR: 150. N $\Phi$ : 144. NZ: 40.
<b>USRBIN</b>	Type: R- $\Phi$ -Z Part: DOSE-EQ Rmin: 0.0 X: 0.0 Zmin: -20.	Unit: 32 BIN Rmax: 150. Y: 0.0 Zmax: 20.	Name: doseNy NR: 150. N $\Phi$ : 144. NZ: 40.
<b>AUXSCORE</b>	Delta: Type: USRBIN Det: doseN	Part: NEUTRON to Det: doseNy	Set: AMB74 Step: 1.
<b>USRBIN</b>	Type: R- $\Phi$ -Z Part: DOSE-EQ Rmin: 0.0 X: 0.0 Zmin: -20.	Unit: 31 BIN Rmax: 150. Y: 0.0 Zmax: 20.	Name: doseG NR: 150. N $\Phi$ : 144. NZ: 40.
<b>USRBIN</b>	Type: R- $\Phi$ -Z Part: DOSE-EQ Rmin: 0.0 X: 0.0 Zmin: -20.	Unit: 33 BIN Rmax: 150. Y: 0.0 Zmax: 20.	Name: doseGy NR: 150. N $\Phi$ : 144. NZ: 40.
<b>AUXSCORE</b>	Delta: Type: USRBIN Det: doseG	Part: PHOTON to Det: doseGy	Set: AMB74 Step: 1.

Figure 5-47 - USRBIN score used in the simulation of the energy degrader.

Results of the assessment of the neutron ambient dose equivalent  $H^*(10)$ , for the different out-coming proton energies, are reported in Figure 5-48 and Figure 5-49.



**Figure 5-48 - Assessment of the neutron ambient dose equivalent  $H^*(10)$  for the different out-coming proton energies in the longitudinal plane.**



**Figure 5-49 - Assessment of the neutron ambient dose equivalent  $H^*(10)$  for the different out-coming proton energies in the transverse plane.**

Similar plots were obtained in the assessment of the gamma ambient dose equivalent that resulted about a factor  $\sim 10^2$  smaller than neutron ambient dose equivalent. The average neutron and gamma dose equivalent at the reference distance of 100 cm was assessed and reported in Table 5-5.

Table 5-5 – Assessment of the neutron and gamma dose equivalent at the reference distance of 100 cm.

Out-coming Proton Energy	Neutron $H_{ref}(100)$ [Sv/ $\mu$ Ah]	Gamma $H_{ref}(100)$ [mSv/ $\mu$ Ah]
<b>Wedges Closed<sup>22</sup></b>	30.03 $\pm$ 0.03	238.5 $\pm$ 0.4
<b>70</b>	32.474 $\pm$ 0.003	252.55 $\pm$ 0.04
<b>120</b>	37.170 $\pm$ 0.004	264.92 $\pm$ 0.04
<b>140</b>	39.512 $\pm$ 0.004	275.40 $\pm$ 0.04
<b>180</b>	44.834 $\pm$ 0.004	275.40 $\pm$ 0.04
<b>200</b>	47.403 $\pm$ 0.004	274.71 $\pm$ 0.04

Results in Table 5-5 were obtained averaging the dose values at 100 cm for all the angles. Actually from Figure 5-49 it is possible to see that in the xy-plane there is a certain symmetry in the neutron (and gamma) dose field: since the purpose of this kind of calculation was to obtain a reference value to use in a very first assessment of the shielding, the dose field was considered as perfectly symmetric at this stage.

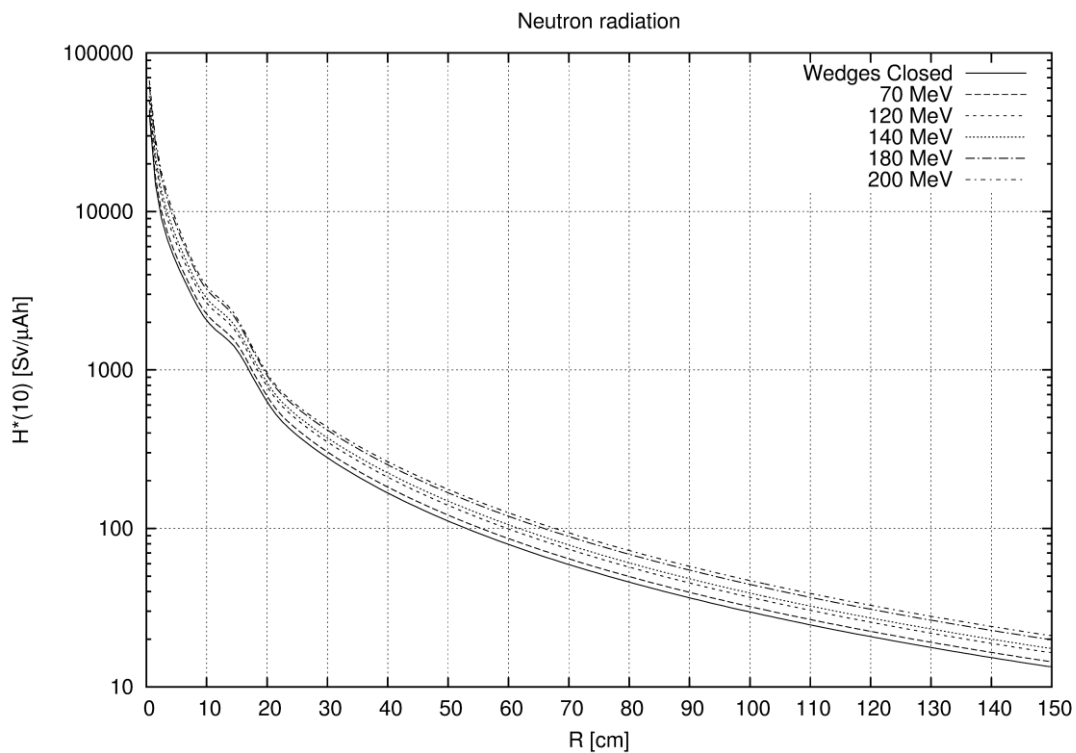
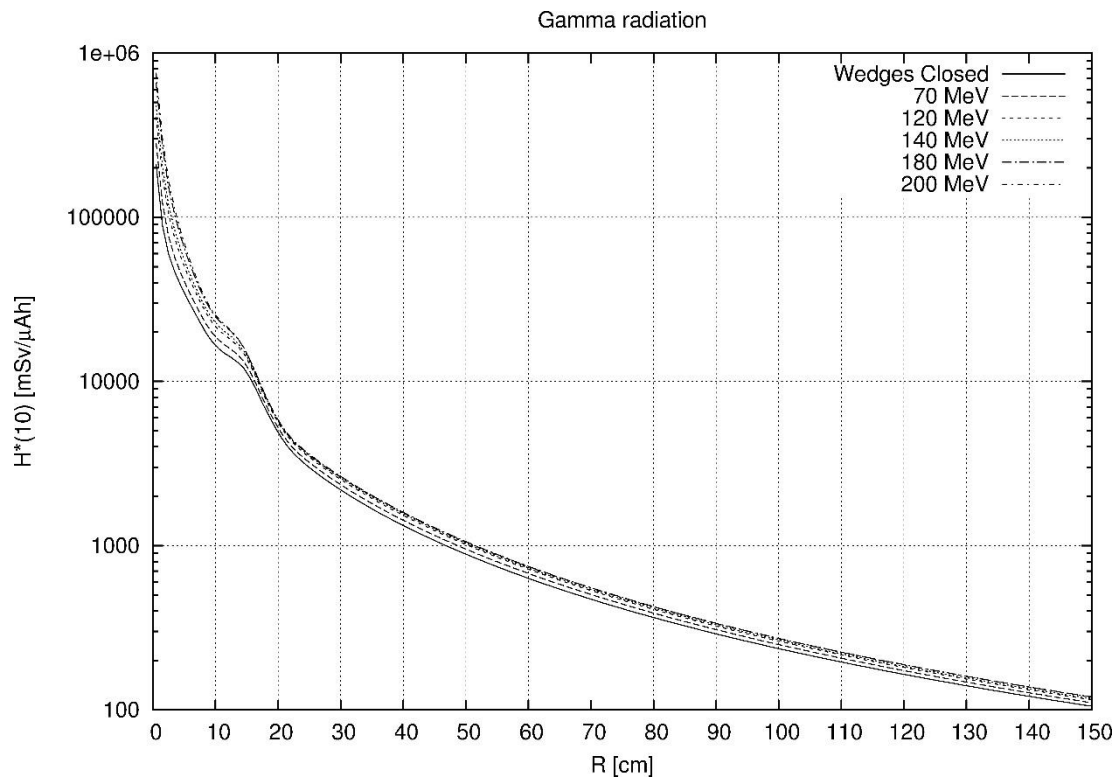


Figure 5-50 – Average neutron dose equivalent, as a function of the radial distance from the beam spot, for the different out-coming proton energies.

<sup>22</sup> Results obtained simulating  $10^7$  primary particles.



**Figure 5-51 – Average gamma dose equivalent, as a function of the radial distance from the beam spot, for the different out-coming proton energies.**

Figure 5-50 and Figure 5-51 show the average neutron and gamma dose equivalent, as a function of the radial distance from the beam spot, for the different out-coming proton energies. As already pointed out in the previous sections MC simulation allows to take into account the build-up effect without any further assumption on the radiation field.

Finally, the SimpleGeo PipsiCAD 3D plugin was used to overlap particle tracks over the 3D model of the degrader (Figure 5-52). This particular feature, even if does not provide any quantitative information, allows to obtain qualitative information about the type, the direction and the number of particles produced during the irradiation and interacting with the components of the degrader, in particular the wedges and the collimators.

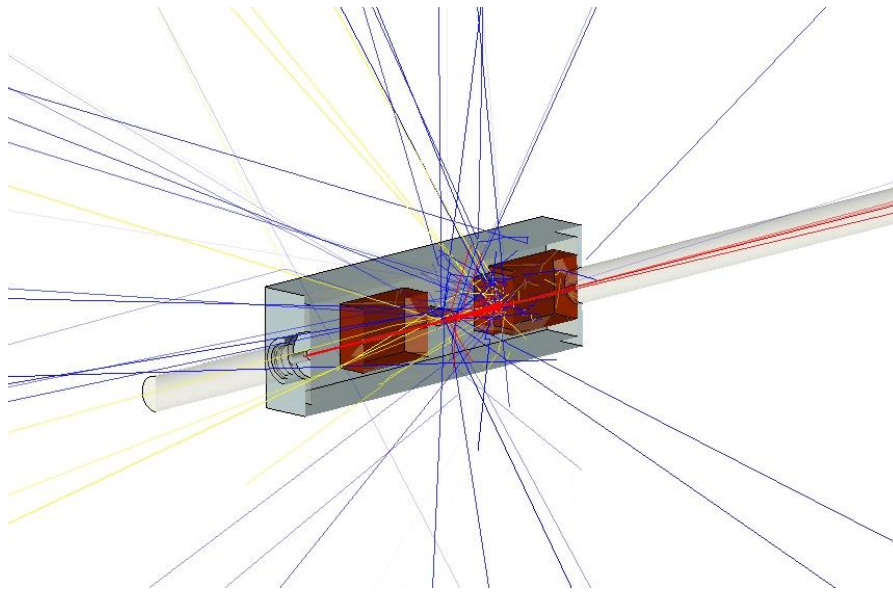


**Figure 5-52 – Overlap of the particles produced during the irradiation on the section of the degrader: tracks in the picture represent protons (red), electrons (green), photons, (yellow) and neutrons (blue). The plot was obtained using the SimpleGeo PipsiCAD 3D plugin.**

# ***Chapter 6***

## ***Conclusions***

Radiation Protection (RP), as defined by Prof. Carlo Polvani during his long teaching activity in the radiation protection course at the University “La Sapienza” in Rome, is a discipline with a strong biological, physical, technical and environmental content that has slowly grown in the past century and has then seen a fast development in the last 20 years. The main goal of Radiation Protection is to preserve the health and the welfare of the workers, the single individual of the population, the population as a whole and the environment, reducing hazards from ionizing radiations in human activities (Polvani, 1993). From a technical point of view, RP involves many aspects that, for historical reasons, are approached and studied separately without considering the mutual connections. Furthermore, in the past, a variety of analytical and semi-empirical models have been proposed, trying to generalize the available experimental results by fitting data or introducing correction factors of doubtful physical meaning. In particular, these methods fail to guarantee reliable results in case of “bad geometry” conditions, like mazes, ducts and wall penetrations. The availability of Monte Carlo codes makes it possible to revise the traditional approach to radiation protection problems. Currently, Monte Carlo codes are no longer available only to a limited number of specialists or dedicated only to applications in high energy physics research; on the contrary they have become applicable as routine tools in the study of particle transport down to energies of a few keV. Notwithstanding the availability of increasingly sophisticated codes and routines modelling complex 3D geometries, one should not lose sight of the need for a careful choice of the physics and transport parameters adopted, as well as of an accurate validation of the setup simulated through comparison with experimental measurements.

In this work the application of Monte Carlo simulation in the energy range of particle accelerators of medical interest was discussed: particular attention was devoted to radiation protection in the use of biomedical cyclotrons for the production of medical radionuclides and hadron therapy applications. The well-known FLUKA code, a fully integrated particle physics Monte Carlo simulation package developed and maintained under an INFN-CERN agreement, was used. The

choice and the optimization of physics and transport parameters were reported; the model developed was validated against experimental measurements and well-established reference data. Problems were studied with a unified approach to obtain a better optimization of the radiation protection. Practical examples of application of the validated models were discussed, showing the wide range of applications and physical quantities that can be studied (particles flow, dose, activation).

In Chapter 3 a MC model of the GE PETtrace cyclotron, installed at “S. Orsola-Malpighi” Hospital (Bologna, IT) and routinely used for the production of positron emitting radionuclides, was created and validated against experimental measurements of several quantities of radiological interest. A detailed FLUKA model of the cyclotron, capable of accelerating  $H^+$  and  $D^-$  ions up to an energy of 16.5 MeV and 8.4 MeV respectively, the GE target assembly comprised of a silver chamber filled with [ $^{18}\text{O}$ ]water, the cyclotron vault and ducts were created from original technical drawings of the accelerator and the nuclear medicine department. The production of  $^{18}\text{F}$  by the well-known reaction  $^{18}\text{O}(p,n)^{18}\text{F}$  was studied to find the set of physical and transport parameters that yielded the best result with the minimum cpu-time usage; results were compared with the recommended saturation activity for 1  $\mu\text{A}$  ( $A_2$ ) provided by IAEA database for medical radioisotopes production. Using the *NEW-DEFA* default and a proton transport threshold set at 1 MeV proved as the best combination giving an excellent agreement with the IAEA recommended value in the shortest simulation time.

Measurements of the neutron ambient dose equivalent  $H^*(10)$  were taken around the PETtrace to validate the model further: measurements were taken in 12 points located along 8 directions using a neutron rem-counter FHT-752 (Thermo Scientific) fitted with a  $\text{BF}_3$  proportional-counter and a PE-moderator, calibrated in  $H^*(10)$  and a set of 12 TLD dosimeters, CR39 (ENEA). The assessment of the neutron ambient dose equivalent resulted in excellent agreement with the experimental measurements: an average ratio  $H^*(10)_{\text{FLUKA}}/H^*(10)_{\text{experimental}}$  of  $0.99 \pm 0.14$  and  $1.55 \pm 0.15$  was found using the rem-counter and the TLDs respectively.

A basic beam transport line was modelled to study the radiation field produced in the irradiation of a cylindrical thick target of copper, iron, graphite, tantalum and aluminium to compare data obtained by Tesch in 1980's. The number of neutrons produced per primary incident proton was evaluated at energies characteristic of PET cyclotrons in addition to the ones above 50 MeV reported by Tesch to cover the entire energy range of biomedical cyclotrons. In the 50 – 250 MeV energy range the average ratio between Tesch data and FLUKA simulation was  $0.99 \pm 0.12$  for graphite,  $1.17 \pm 0.14$  for aluminum,  $1.15 \pm 0.14$  for iron,  $1.00 \pm 0.12$  for copper and  $0.94 \pm 0.10$  for tantalum. In the energy range of interest for proton therapy the overall agreement with Tesch was very good. Below 30 MeV the agreement was not as satisfactory (i.e.  $1.28 \pm 0.26$  for iron and  $2.0 \pm 0.4$  for aluminum at 19 MeV); Tesch

reported only limited data in this energy range likely due to the limited diffusion of PET cyclotrons during the 1970's and 1980's: a validated Monte Carlo model can fill this gap, providing accurate prediction of neutron yield in this low energy region as well.

Once the model had been validated it was applied to several experimental tests conducted at "S. Orsola-Mapighi" Hospital using the PETtrace cyclotron. The activity concentration of  $^{41}\text{Ar}$  within the cyclotron vault was assessed from both Monte Carlo simulation and an extensive measurement campaign. Marinelli beakers of  $1000\text{ cm}^3$  were placed inside the bunker, during a routine production of  $^{18}\text{F}$ , in a number of marked positions and then measured in high resolution gamma-ray spectrometry using a HPGe detector. A method using external cross sections with FLUKA data (external cross section method, ECSM) was developed and used in addition to the direct assessment performed with the standard FLUKA score. The overall average activity concentration of  $^{41}\text{Ar}$  produced in air, as resulted from experimental measurements, was  $0.86 \pm 0.15\text{ Bq/dm}^3 \cdot \mu\text{Ah}$ . Results of the simulations, over the whole air volume ( $\sim 120\text{ m}^3$ ), were  $2.18 \pm 0.11$  and  $2.19 \pm 0.07\text{ Bq/dm}^3 \cdot \mu\text{Ah}$  for the direct and the off-line assessment respectively. Sampling air within a bunker in irradiation conditions is a relatively complex task; all the main aspects were addressed, including significance of the sampling, timing between sampling and gamma ray spectrometry analysis, correction of the efficiency calibration accounting for sample's density. Individual measurement resulted affected by uncertainties of the order of 5 % at 1 sigma level; being the results quite similar in the different sampling positions, it was possible to evaluate an overall average, within a variability of less than 20 %. These results were considered satisfactory and useful, particularly to support the planning stage of new facilities and the choices regarding proper regulation of the ventilation system. The reasons for these differences should be investigated in low energy physical models used in current Monte Carlo programs, particularly when applied to target nuclei present at a very low concentration in a compound media. However, it has to be noted that analytical approaches to calculate  $^{41}\text{Ar}$  production in air require a relatively complex series of calculations, based on rough approximations of the real geometry, neutron spectra and fluence distribution. Their accuracy cannot be expected to be better than those obtained using Monte Carlo methods, based on a more accurate description of the real problem.

As a first, relevant result, it was confirmed that, as expected, production of  $^{41}\text{Ar}$  is the only significant air activation process. Nevertheless, we only obtain an agreement within a factor of 2 – 3 between simulations and experimental results. A similar level of discrepancy has been observed in other attempts to model activation in materials not directly interested by the primary beam

Finally, the development of a low-cost target for the direct cyclotron-production of  $^{99\text{m}}\text{Tc}$  via the  $^{100}\text{Mo}(p,2n)^{99\text{m}}\text{Tc}$  reaction was studied using MC simulation. Different

target setups (including material composition and thickness of the target) were simulated: production on  $^{nat/100}\text{Mo}$  foil and  $^{nat/100}\text{MoO}_3$  pellets was studied and compared. Given the impossibility of FLUKA to reproduce a correct production branching ratio between ground and metastable states of isotopes, a dedicated ECSM was developed. Considering all the targets, an overall average ratio experimental to FLUKA saturation yield of  $1.13 \pm 0.05$  was obtained for  $^{99m}\text{Tc}$ .

In Chapter 4 the Monte Carlo simulation was applied to the production of a number of established and emerging positron emitting radionuclides such as  $^{18}\text{F}$ ,  $^{13}\text{N}$ ,  $^{94}\text{Tc}$ ,  $^{44}\text{Sc}$ ,  $^{68}\text{Ga}$ ,  $^{86}\text{Y}$ ,  $^{89}\text{Zr}$ ,  $^{56}\text{Co}$ ,  $^{52}\text{Mn}$ ,  $^{61}\text{Cu}$  and  $^{55}\text{Co}$ , at TRIUMF (Vancouver, CA) TR13 cyclotron from liquid and solid targets. The collimation system and the target assembly of the TR13 cyclotron, for the liquid and the solid target, were modeled on the basis of the information taken from original technical drawings. Optimization of the parameters used in the modeling of the proton beam was performed through a sensitivity analysis and compared with current measurements on the baffle, collimator and target assembly. Saturation yield was assessed directly and with ECSM for the radionuclides reported above; results were compared with TR13 experimental productions and IAEA recommended values. Direct assessment provided an average ratio of saturation yield  $Y_{\text{exp}}/Y_{\text{FLUKA}}$  of  $0.7 \pm 0.4$  and  $1.1 \pm 1.3$  for liquid and solid targets respectively. There is reasonably good agreement between the simulated and the experimental data for liquid targets and a somewhat less consistent agreement for solid targets. Especially regarding liquid targets, the results obtained are very good if we consider that MC simulations do not take into account factors such as thermal and fluid-dynamic effects like density reduction, as well as loss of activity during delivery from the cyclotron in the transfer system. Saturation yields obtained with the ECSM resulted strongly dependent on the availability and the quality of cross section data: the cross section data have to fit certain requirements, including a large set of data points ideally spanning the energy range from cross-section threshold to 13 MeV with small uncertainties. Slightly better results were obtained with the very well-known reactions and the solid target materials

Chapter 5 was dedicated to the practical applications of the validated MC model to the planning and the decommissioning of cyclotron facilities. The design of the new PET facility of "Sacro Cuore-Don Calabria" Hospital (Negrar, IT) was completely done with MC simulation. Furthermore the calculations were included in the radiation protection technical report used for the licensing of the facility. A detailed MC model of the ACSI TR19 cyclotron, an external ion source cyclotron that accelerates negative hydrogen ions to 19 MeV, provided with two extraction ports each with a target selector and local shields composed of a proprietary mixture that allows a significant reduction of the dose field around the target selectors, was created. In a first stage the efficacy of the local shield was verified evaluating the attenuation factor: this step was fundamental since the composition and the density

of the local shield were not completely known. The cyclotron was simulated with and without the local shield. An average attenuation factor of  $146 \pm 8$  was found: the manufacturer reported an average attenuation factor of about 100. The design of the shielding was performed by assessing the neutron dose field. The reference dose equivalent  $H_{ref}(\theta, 100)$ , in the direction  $\theta$  at the reference distance of 100 cm from the target, was assessed from FLUKA simulations. An average effective thickness of  $132 \pm 22$  cm, including the additional HVL to shield scattering radiation, was calculated. To take into account a safety factor of 20% and the inaccuracy of the composition of the local shield, it was decided to add an additional HVL thus building a 200 cm thick concrete walls. Simulations allowed an accurate positioning of ducts through the vault walls: critical situations were studied and optimized, in keeping with mechanical requirements, to avoid transmission of radiations. The amount of  $^{41}\text{Ar}$  produced in 1h-1 $\mu\text{A}$  dual beam irradiation, without ventilation within the bunker, was  $0.045 \pm 0.026$  Bq/dm<sup>3</sup>\* $\mu\text{A}$ ; taking into account the ventilation rate and a conservative irradiation current the release of  $^{41}\text{Ar}$  in atmosphere was found to be under the limit of 1 Bq/g prescribed by the Italian national regulation. Finally, long-term activation of local shields and walls were studied to assess the order of magnitude of activity after 10 years in operation and to plan strategies for decommissioning.

Dose transmission through several types of plug-doors, in planning a new cyclotron facility, was studied. Critical points were identified and an optimal solution minimizing the transmission of neutron and gamma radiation was found.

The partial decommissioning of a PET facility and the replacement of a Scanditronix MC17 cyclotron with a new TR19 unit were evaluated using the validated MC model. The long-term activation of the vault walls was assessed the critical radionuclides identified, in terms of half-life and order of magnitude of the activity produced, for the planning of the decommissioning. The replacement of the MC17 cyclotron with a new TR19, using the previous layout of the cyclotron vault was evaluated, especially to assess the dose rate at the entrance of the maze.

Finally, a general and simplified model of the energy selection system (degrader) of a hadron therapy cyclotron was created, based on existing commercial devices. The model was used to assess the reference dose equivalent  $H_{ref}(\theta, 100)$ , for neutron and gamma radiation, for several outgoing proton energies. This reference data are particularly useful at the beginning of the planning of a new facility when civil engineers need a rough estimation of the cyclotron vault dimensions to design a more detailed layout of the site, including ducts and all the auxiliary systems such as the ventilation system.

In conclusion Monte Carlo simulation is currently feasible as a tool in the planning of new biomedical cyclotron installations, being a powerful tool both for

the optimization of radiation protection and in the study of feasibility and productivity of new radionuclides production methodologies. The availability of an experimentally validated Monte Carlo model makes it possible to revise the traditional approach to the assessment of radiation protection problems. The results obtained show how after an accurate validation of the model, in terms of physical and transport parameters in the energy range of medical application, Monte Carlo simulations predict with good accuracy the value of quantities of radiological interest. In particular, Monte Carlo simulations allow to reproduce more accurately, compared to analytical methods, the source term of radiation and to obtain reliable results in the case of “bad geometry” conditions, like mazes, ducts and wall penetrations. The Build-up effect is taken into account more accurately than in analytical methods and without any assumption on the radiation field. Most important, Monte Carlo simulation allows a unified approach to radiation protection problems considering simultaneously the interconnections between different aspects, contrary to traditional analytical methods.

# References

ACSI, 2014. *TR19 PET Cyclotron. Operating and Maintenance Manual Rev. 5.0*. Richmond, BC, Canada: Advanced Cyclotron System Inc. (ACSI).

Al-Abyad, M., Comsan, M. N. & Qaim, S. M., 2009. Excitation functions of protons-induced reactions on natFe and enriched <sup>57</sup>Fe with particular reference to the production of <sup>57</sup>Co. *Applied Radiation and Isotopes*, Volume 67, pp. 122-128.

Alpat, B. et al., 2012. Full Geant4 and FLUKA simulations of an e-LINAC for its use in particle detectors performance tests. Volume doi:10.1088/1748-0221/7/03/P03013.

Al-Saleh, F. S., AlMugren, K. S. & Azzam, A., 2007. Excitation function measurements and integral yields estimation for natZn(p,x) reactions at low energies. *Applied Radiation and Isotopes*, Volume 65, pp. 1101-1107.

Alsmiller, R. G., Mynatt, R. G., Barish, J. & Engle, W. W., 1969. High energy (<400 MeV) neutron transport using the method of discrete ordinates. *Nucl. Sci. Eng*, Volume 36, p. 251.

ANSI, 1999. *ANSI N42.14-1999. Calibration and Use of Germanium Spectrometers for the Measurement of Gamma-Ray Emission Rates of Radionuclides*. Washington: American National Standards Institute (ANSI).

Barbalat, O., 1994. *Applications of particle accelerators*. CERN/AC/93-04 (BLIT)/Rev, Geneve: EUROPEAN ORGANIZATION FOR NUCLEAR RESEARCH (CERN).

Battistoni, G., 2012. *Medical Applications of FLUKA*. [Online] Available at: [http://ssfm.fisica.unimi.it/Didattica/Slides di Corsi file/Metodo Monte Carlo e applicazioni in Fisica Medica-parte 2.pdf](http://ssfm.fisica.unimi.it/Didattica/Slides%20di%20Corsi%20file/Metodo%20Monte%20Carlo%20e%20applicazioni%20in%20Fisica%20Medica-parte%202.pdf)

Battistoni, G. et al., 2007. *The FLUKA code: Description and benchmarking*. Fermilab 6--8 September 2006, AIP Publishing, p. 896.

Beskrovnaia, L. et al., 2008. Verification of Monte Carlo transport codes FLUKA, GEANT4 and SHIELD for radiation protection purposes at relativistic heavy ion accelerators. *Nuclear Instruments and Methods in Physics Research B*, Volume 266, pp. 4058-4060.

Biju, K., Sunil, C. & Sakar, P. K., 2012. Scattering of neutrons in high energy proton accelerator enclosure and the production of  $^{41}\text{Ar}$  and  $^{14}\text{C}$  activity using FLUKA. *Indian Journal of Pure & Applied Physics*, Volume 50, pp. 435-468.

Biju, K., Sunil, C. & Sakar, P. K., 2013. Estimation of  $^{41}\text{Ar}$  production in 01-1.0-GeV proton accelerator vaults using FLUKA Monte Carlo code. *Radiation Protection Dosimetry*, 157(3), pp. 437-441.

Birattari, C. et al., 1987a. Biomedical applications of cyclotrons and review of commercially available models. *Journal of Medical Engineering & Technology*, 11(4), pp. 166-167.

Birattari, C., Bonardi, M., Ferrari, A. & Silari, M., 1985. Neutron activation of air by a biomedical cyclotron and an assessment of dose to neighbourhood populations. *Radiation Protection Dosimetry*, 14(4), pp. 311-319.

Birattari, C., Cantone, M. C., Ferrari, A. & Silari, M., 1989. Residual Activity at the Milan AVF Cyclotron. *Nuclear Instruments and Methods in Physics Research B*, Volume 43, pp. 119-126.

Birattari, C., Ferrari, A., Parnell, C. J. & Silari, M., 1987b. The environmental release of radioactive gases produced by neutron activation of air with the new Hammersmith cyclotron. *Radiation Protection Dosimetry*, 19(3), pp. 183-186.

Bohlen, T. T. et al., 2014. The FLUKA Code: Developments and Challenges for High Energy and Medical Applications. *Nuclear Data Sheets*, Volume 120, pp. 211-214.

Bonardi, M., 1987. *The contribution to nuclear data for biomedical radioisotope production*. Tokyo, Japan, International Atomic Energy Agency (IAEA), pp. 98-112.

Bronson, F. L., 2003. Validation of the accuracy of the LabSOCS software for mathematical efficiency calibration of Ge detectors for typical laboratory samples. *Journal of Radioanalytical and Nuclear Chemistry*, 255(1), pp. 137-141.

Brugger, M., Ferrari, A., Roesler, S. & Sala, P. R., 2007. *Calculation of radionuclide production cross sections with FLUKA and their application in the energy hadron collider studies*. Nice, France, s.n.

- Brugger, M., Ferrari, A., Roesler, S. & Ulrici, L., 2006. Validation of the FLUKA Monte Carlo code for predicting induced radioactivity at high-energy accelerators. *Nuclear Instruments and Methods in Physics Research A*, Volume 562, pp. 814-818.
- Brugger, M. et al., 2004. *Benchmark studies of induced radioactivity produced in LHC materials, part I: specific activities*. Madeira, Portugal, s.n.
- Buckley, K., 2006. *Production of a  $^{56}\text{Co}$  source for detector calibrations (TRI-DN-06-5)*, Vancouver, CA: TRIUMF.
- Buckley, K. et al., 2000. C-methane production in small volume, high pressure gas targets. *Radiochimica Acta*, Volume 88, pp. 201-205.
- Calandrino, R. et al., 2006. Decommissioning procedures for an 11 MeV Self-Shielded Medical Cyclotron after 16 Years of Working Time. *Health Physics*, 90(6), pp. 588-596.
- Carroll, L., 2002. *Decommissioning and Recommissioning Cyclotrons*. Turku, s.n.
- Carroll, L., Ramsey, F., Armbruster, J. & Montenero, M., 2001. *Recycling and Recommissioning a Used Biomedical Cyclotron*. Denton, s.n.
- Chao, J. H., Liu, W. S. & Chen, C. Y., 2007. Estimation of Argon-41 concentrations in the vicinity of a high-energy medical accelerator. *Radiation Measurements*, Volume 42, pp. 1538-1544.
- Chilton, A. B., 1974. *Working Paper on Neutron Skyshine for Accelerator Sources*, Urbana: s.n.
- Chu, W. T., 2005. Ernest Orlando Lawrence (1901-1958), Cyclotron and Medicine. *Zeitschrift Fur Medizinische Physik*, 16(2), pp. 109-110.
- Ciarmatori, A. et al., 2011. Some experimental studies on  $^{89}\text{Zr}$  production. *Radiochimica Acta*, Volume 99, pp. 1-4.
- Cicoria, G. et al., 2006. Development and operational tests of a solid target for the GE PET-trace cyclotron. *Q. J. Nuclear Medicine*, 50(Suppl. 1), pp. 3-4.
- D'Arenzio, M., Sandri, S. & Coniglio, A., 2014. *Radioprotezione Avanzata. Radionuclidi e acceleratori di elettroni fino a 10 MeV.*. Roma: CISU.
- De Bievre, P. & Taylor, P., 1993. IUPAC Recommended Isotopic Abundances. *Int. J. Mass. Spectrom. Ion Phys.*, Volume 123, p. 149.

DIN, 2003. *DIN 6871-1. Cyclotron systems for positron emission tomography - Part 1: Requirements for constructional radiation protection.*, Berlin: Deutsches Institut für Normung.

DIN, 2005. *DIN 6871-2. Cyclotron systems for positron emission tomography - Part 2: Radiation protection labyrinths and wall entrances*, Berlin: Deutsches Institut für Normung.

Dunn, W. L. & Shultis, J. K., 2012. *Exploring Monte Carlo Methods*. s.l.:Elsevier.

Embree, M., 2009. *Lecture 23: Interpolatory Quadrature. Lecture Notes by Prof. Mark Embree (Rice University)*. [Online]  
Available at: <http://www.eng.utah.edu/~cs6210/lecture23.pdf>

ENDF, 2014. *Evaluated Nuclear Data File (ENDF)*. [Online]  
Available at: <https://www-nds.iaea.org/exfor/endl.htm>

ENEA, 2013. *DOSIMETRO A CORPO INTERO PER NEUTRONI VELOCI (nv)*. [Online]  
Available at: <http://www.irp.enea.it/it/servizi/documenti/a5-dosimetro-neutroni-veloci>

European Commission, 1999. *Report EUR 19151. Evaluation of the Radiological and Economic Consequences of Decommissioning Particle Accelerators.*, Brussel: European Commission. Nuclear Safety and the Environment.

Fassò, A., Ferrari, A., Ranft, J. & Sala, P. R., 1995. *FLUKA: Performances and applications in the intermediate energy range*. Arlington, s.n.

Fassò, A. et al., 2003. *The physics models of FLUKA: status and recent developments*. La Jolla, California, s.n.

Fassò, A., Ferrari, A. & Sala, P. R., 2009. Radiation Transport calculations and Simulations. *Radiation Protection Dosimetry*, 137(1-2), pp. 118-133.

Ferrari, A., 2006. *Introduction and Applications of FLUKA*. [Online]  
Available at: <http://lins00.psi.ch/mcworkshop/papers/Fluka-PSI.pdf>

Ferrari, A., Fassò, A., Ranft, J. & Sala, P. R., 2011. *FLUKA2011 Manual*. s.l.:s.n.

Ferrari, A., Sala, P. R., Fassò, A. & Ranft, J., 2005. *FLUKA: a multi-particle transport code*, s.l.: s.n.

Ferreira, C. L. et al., 2007. 55Cobalt complexes with pendant carbohydrates as potential PET imaging agents. *Applied Radiation and Isotopes*, Volume 65, pp. 1303-1308.

FLUKA, 2010. FLUKA. [Online]  
Available at: <http://www.fluka.org>

Friesel, D. L. & Antaya, T. A., 2009. Medical Cyclotrons. *Reviews of Accelerator Science and Technology*, Volume 02, p. 133.

Gagnon, K. et al., 2011. Cyclotron production of  $^{99m}\text{Tc}$ : Experimental measurement of the  $^{100}\text{Mo}(p,x)^{99}\text{Mo}$ ,  $^{99m}\text{Tc}$ , and  $^{99g}\text{Tc}$  excitation functions from 8 to 18 MeV. *Nuclear Medicine and Biology*, Volume 38, pp. 907-916.

Gallerani, R. et al., 2008. Neutron production in the operation of a 16.5 MeV PETrace cyclotron. *Progress in Nuclear Energy*, Volume 50, pp. 939-943.

GE MEDICAL SYSTEMS, 2004. *PETtrace REFERENCE MANUAL - Rev 3*. Uppsala: GE Medical Systems.

Gorbatkov, D. V. & Kryuchkov, V. P., 1996. A comparison of computational data, obtained with a variety of well-known radiation transport codes (MCNP, ANISN, FLUKA, ROZ6H). *Nuclear Instruments and Methods in Physics Research A*, Volume 374, pp. 95-104.

Guimaraes, A. M. et al., 2012. Use of a TLD-based multisphere spectrometry system to measure the neutron spectra around a not-self-shielded PET cyclotron: Preliminary results. *Applied Radiation and Isotopes*, Volume 71, pp. 92-95.

Gutermuth, F., Wildermuth, H., Radon, T. & Fehrenbacher, G., 2005. Radiation impact caused by activation of air from the future GSI accelerator facility FAIR. *Radiation Protection Dosimetry*, 115(1-4), pp. 437-440.

Hanemaayer, V. et al., 2014. Solid targets for  $^{99m}\text{Tc}$  production on medical cyclotrons. *J Radioanal Nuc Chem*, Volume 1007-1011, p. 299.

Hoehr, C. et al., 2012. Radiometals from liquid targets:  $^{94m}\text{Tc}$  production using a standard water target on a 13 MeV cyclotron. *Applied Radiation and Isotopes*, pp. 2308-2312.

Hoehr, C. et al., 2013.  $^{44g}\text{Sc}$  production using a water target on a 13 MeV cyclotron. *Nuclear Medicine and Biology*, Volume doi: 10.1016/j.nucmedbio.2013.12.016.

Homann, S. G. & Aluzzi, F., 2013. *HOTSPOT Health Physics Codes Version 3.0 User's Guide*. LLNL-SM-636474, Livermore: National Atmospheric Release Advisory Center, Lawrence Livermore National Laboratory.

IAEA, 1988. *Technical Reports Series No. 283. Radiological Safety Aspects of the Operation of Proton Accelerators*, Vienna: International Atomic Energy Agency.

IAEA, 2001a. *Charged particle cross-section database for medical radioisotope production: diagnostic radioisotopes and monitor reactions. IAEA-TechDoc-1211*, Vienna: International Atomic Energy Agency.

IAEA, 2001b. *Technical Reports Series No. 403. Compendium of Neutron Spectra and Detector Response for Radiation Protection Purposes. Supplement to Technical Reports Series No. 318*, Vienna: International Atomic Energy Agency.

IAEA, 2004. *Status of the Decommissioning of Nuclear Facilities Around the World*, Vienna: International Atomic Energy Agency.

IAEA, 2006. *IAEA-DCRP/2006. Directory of Cyclotrons used for Radionuclide Production in Member States 2006 Update.*, Vienna: International Atomic Energy Agency.

IAEA, 2008. *Cyclotron Produced Radionuclides: Principles and Practice Technical. Technical Reports Series No. 465*, Vienna: International Atomic Energy Agency.

IAEA, 2009. *Cyclotron produced radio-nuclides: Physical Characteristics and production methods. IAEA Technical Report No. 468*, Vienna: International Atomic Energy Agency.

IAEA, 2011a. *Charged-particle cross section database for medical radioisotope production - Diagnostic radioisotopes and monitor reactions.* [Online] Available at: <https://www-nds.iaea.org/medical/>

IAEA, 2011b. *Cross section database for medical radioisotope production - Production of Therapeutic Radionuclides.* [Online] Available at: <https://www-nds.iaea.org/radionuclides>

IAEA, 2014. *Experimental Nuclear Reaction Data (EXFOR).* [Online] Available at: <https://www-nds.iaea.org/exfor/exfor.htm>

IAEA, 2014. *Radiation protection and safety of radiation sources: International Basic Safety Standards. IAEA SAFETY STANDARDS SERIES No. GSR Part 3.*, Vienna: International Atomic Energy Agency.

ICRP, 1996. Conversion Coefficients for use in Radiological Protection against External Radiation. ICRP Publication 74.. *Annals of the ICRP*, 26(3-4).

ICRP, 2007. *ICRP Publication 103. The 2007 recommendations of the International Commission on Radiological Protection.*, s.l.: J. VALENTIN.

ICRP, 2010. Conversion Coefficients for Radiological Protection Quantities for External Radiation Exposures. ICRP Publication 116. *Ann. ICRP*, 40(2-5).

IEC, 1995. *IEC Standard 61452. Nuclear instrumentation – measurement of gamma-ray emission rates of radionuclides – calibration and use of germanium spectrometers*, Geneva: International Electrotechnical Commission.

Infantino, A. et al., 2014a. Comparison of several assessments of neutron dose measurements around a biomedical cyclotron. *Eur J Nucl Med Mol Imaging*, 41(Suppl 2), p. S307.

Infantino, A. et al., 2011. Prediction of  $^{89}\text{Zr}$  production using the Monte Carlo code FLUKA. *Applied Radiations and Isotopes*, Volume 69, pp. 1134-1137.

Infantino, A. et al., 2015a. Accurate Monte Carlo modeling of cyclotrons for optimization of shielding and activation calculations in the biomedical field. *Radiation Physics and Chemistry*, doi:10.1016/j.radphyschem.2015.01.001(In Press).

Infantino, A. et al., 2014b. Monte-Carlo assessment of the saturation yield for liquid and solid targets at a medical cyclotron using FLUKA. *Eur J Nucl Med Mol Imaging*, 41(Suppl 2), p. S450.

Infantino, A. et al., 2015b. Assessment of the production of medical isotopes using the Monte Carlo code FLUKA: simulations against experimental measurements. *Nuclear instruments and methods in research B*, Volume Manuscript submitted for publication.

Jongen, Y., 2010. *Review on cyclotrons for cancer therapy*. Lanzhou, China, s.n., pp. 398-403.

Karamanis, D., 2003. Efficiency simulation of HPGe and Si(Li) detectors in gamma and X-ray spectroscopy. *Nuclear Instruments and Methods in Physics Research A*, Volume 505, pp. 282-285.

Knoll, G. F., 2000. *Radiation detection and measurement. 3rd Edition*. s.l.:Jhon Wiley & Sons, Inc..

Koning, A. J., Hilaire, S. & Duijvestijn, M. C., 2007. *TALYS-1.0*. Nice, EDP Sciences.

Krajewski, S. et al., 2013. Cyclotron production of  $^{44}\text{Sc}$  for clinical application. *Radiochimica Acta International journal for chemical aspects of nuclear science and technology*, 101(5), pp. 333-338.

Kreyszig, E., 2006. *Advanced Engineering Mathematics. 9th Edition*. Singapore: John Wiley & Sons, Inc..

Ladu, M., Pelliccioni, M., Picchi, P. & Verri, G., 1968. A contribution to the skyshine study. *Nucl. Instrum. Methods*, Volume 62, pp. 51-56.

Lauritzen, B. et al., 2003. Atmospheric dispersion of argon-41 from a nuclear research reactor: measurement and modelling of plume geometry and gamma radiation field.. *International Journal of Environment and Pollution*, 20(1-6), pp. 47-54.

Lawrence, E. O. & Livingston, M. S., 1932. The production of high speed light ions without the use of high voltages. *Physical Review*, Volume 40, pp. 19-35.

Laxdal, R. E., Altman, A. & Kuo, T., 1994. *Beam Measurement on a Small Commercial Cyclotron*. Geneva, CERN, pp. 545-547.

Lebeda, O. et al., 2012. Assessment of radionuclidic impurities in cyclotron produced  $^{99m}\text{Tc}$ . *Nuclear Medicine and Biology*, 39(8), pp. 1286-1291.

Lee, J., Watts, J. & Howell, L., 2001. Simulations of a thin sampling calorimeter with GEANT/FLUKA. *Nuclear Instruments and Methods in Physics Research A*, Volume 470, pp. 500-511.

Levkovskij, V. N., 1991. *Activation Cross Sections for the Nuclides of Medium Mass Region ( $A = 40-100$ ) with Medium Energy ( $E = 10-50$  MeV) Protons and Alpha Particles: Experiment and Systematics*. Moscow: Inter-Vesi.

Lucconi, G. et al., 2014. Development of a solid target for cyclotron production of  $^{99m}\text{Tc}$ . *Eur J Nucl Med Mol Imaging*, 41(Suppl 2), p. S347.

Lucconi, G., Cicoria, G., Pancaldi, D. & Marengo, M., 2013. Assessment of the feasibility of producing  $^{99m}\text{Tc}$  with a 16.5 MeV biomedical cyclotron using the TALYS nuclear reaction program and FLUKA code. *Clin Transl Imaging*, 1(Suppl 1), pp. S1-S38.

Mairani, A. et al., 2013. A Monte Carlo-based treatment planning tool for proton therapy. *PHYSICS IN MEDICINE AND BIOLOGY*, Volume 58, pp. 2471-2490.

McLane, V., 2004. *Memo CP-C/347. Cross sections measured on thick targets. Updated LEXFOR entry on thick target yields.*, Upton, NY, U.S.A.: Nation Nuclear Data Center. Brookhaven National Laboratory..

Milton, B. F., 1996. *Commercial Compact Cyclotrons in the 90's*. Cape Town, World Scientific Publishing Co..

Mladin, D. et al., 2013. Calculation of radioactive species transport in a TRIGA reactor.. *Nuclear Engineering and Design*, Volume 262, pp. 29-38.

- Monegato, G., 1998. *Fondamenti di Calcolo Numerico*. s.l.:CLUT.
- Morley, T. et al., 2012. The deposition of smooth metallic molybdenum from aqueous electrolytes containing. *Electrochemistry Communications*, Volume 15, pp. 78-80.
- Mosegaard, K. & Sambridge, M., 2002. Monte Carlo analysis of inverse problems. *Inverse Problems*, Volume 18, pp. R29-R54.
- NCRP, 1976. *NCRP Report No. 51. Radiation protection design guidelines for 0.1-100 MeV particle accelerator facilities*, Bethesda: National Council on Radiation Protection and Measurements.
- NCRP, 2003. *NCRP Report No. 144. Radiation Protection for Particle Accelerator Facilities*, Bethesda: National Council on Radiation Protection and Measurements.
- NCRP, 2004. *NCRP Report No. 147. Structural Shielding Design for Medical X-Ray Imaging Facilities*, Bethesda: National Council on Radiation Protection and Measurements.
- NCRP, 2005. *NCRP Report No. 151. Structural Shielding Design and Evaluation for Megavoltage X- and Gamma-Ray Radiotherapy Facilities.*, Bethesda: National Council on Radiation Protection and Measurements.
- NIST, 2014. *National Institute of Standards and Technology*. [Online] Available at: <http://www.nist.gov>
- OH, J. et al., 2011. Comparison of the FLUKA, MCNPX, and PHITS Codes in Yield Calculation of Comparison of the FLUKA, MCNPX, and PHITS Codes in Yield Calculation of. *Progress in Nuclear Science and Technology*, Volume 1, pp. 85-88.
- Omara, H. M. et al., 2009. Proton induced reactions on <sup>89</sup>Y with particular reference to the production of the medically interesting radionuclide <sup>89</sup>Zr. *Radiochimica Acta*, Volume 97, p. 467.
- Opelka, J. H. et al., 1979. *ANL/ES-82. Particle-accelerator decommissioning.*, Argonne: Argonne National Laboratory.
- Otsuka, N. & Takács, S., 2012. *Memo CP-D/631. Production thick target yield*, Vienna, Austria: Nuclear Data Section. International Atomic Energy Agency.
- Papash, A., 1993. *TR13 Cyclotron Extraction Studies (TRI-DN-93-5)*, Vancouver: TRIUMF.

Parodi, K., Ferrari, A., Sommerer, F. & Paganetti, H., 2007a. Clinical CT-based calculations of dose and positron emitter distributions in proton therapy using the FLUKA Monte Carlo code. *PHYSICS IN MEDICINE AND BIOLOGY*, Volume 52, pp. 3369-3387.

Parodi, K. et al., 2007b. PET/CT imaging for treatment verification after proton therapy: a study with plastic phantoms and metallic implants. *Med. Phys.*, 34(2), pp. 419-435.

Pelliccioni, M., 2000. Overview of fluence-to-effective dose and fluence-to-ambient dose equivalent conversion coefficients for high energy radiation calculated using the FLUKA code. *Radiation Protection Dosimetry*, 88(4), pp. 279-297.

Polvani, C., 1993. *Elementi di Radioprotezione*. Roma: ENEA.

Polz, S., 2014. *Personalized body counter calibration using anthropometric parameters*. Karlsruhe: KIT Scientific Publishing.

Qaim, S. M., 2004. Use of cyclotron in medicine. *Radiation Physics and Chemistry*, Volume 71, p. 917-926.

Qaim, S. M. et al., 2014. Evaluation of excitation functions of  $^{100}\text{Mo}(p,d+pn)^{99}\text{Mo}$  and  $^{100}\text{Mo}(p,2n)^{99m}\text{Tc}$  reactions: Estimation of long-lived Tc-impurity and its implication on the specific activity of cyclotron-produced  $^{99m}\text{Tc}$ . *Applied Radiation and Isotopes*, Volume 85, pp. 101-113.

Quarteroni, A., Sacco, R. & Salieri, F., 2000. *Numerical Mathematics*. New York: Springer.

Richards, V. N., Mebrahtu, E. & Lapi, S. E., 2013. Cyclotron Production of  $^{99m}\text{Tc}$  using  $^{100}\text{Mo}2\text{C}$  targets. *Nuclear Medicine and Biology*, 40(7), pp. 939-945.

Röcken, H. et al., 2010. *The Varian 250 MeV superconducting compact proton cyclotron: medical operation of the 2nd machine, production and commissioning status of machine No. 3 to 7*. Lanzhou, China, s.n., pp. 283-285.

Rockwell, T., 1956. *Reactor shielding design manual*. Princeton: D. Van Nostrand Company, Inc..

Ruth, T. J., 2009. The Production of Radionuclides for Radiotracers in Nuclear Medicine. *Reviews of Accelerator Science and Technology*, Volume 2, pp. 17-33.

Sandri, S., D'Arenzio, M. & Coniglio, A., 2008. *Radioprotezione di Base. Apparecchi radiologici con tensione di accelerazione inferiore a 400 kV.*. Roma: CISU.

- Schmor, P. W., 2010. *Review of cyclotrons used in the production of radioisotopes for biomedical applications*. Lanzhou, s.n., pp. 419-424.
- Severin, G. W. et al., 2012. Cyclotron produced  $^{44}\text{gSc}$  from natural calcium. *Applied Radiation and Isotopes*, pp. 1526-1530.
- Silari, M. et al., 2009. Intercomparison of radiation protection devices in high-energy stray neutron field. Part III: instrument response.. *Radiation Measurements*, Volume 44, pp. 673-691.
- Sommerer, F. et al., 2009. In-beam PET monitoring of mono-energetic  $^{16}\text{O}$  and  $^{12}\text{C}$  beams: experiments and FLUKA simulations for homogeneous targets. *PHYSICS IN MEDICINE AND BIOLOGY*, Volume 54, pp. 3979-3996.
- Stekl, I. et al., 2000. Monte-Carlo simulations of neutron shielding for the ATLAS forward region. *Nuclear Instruments and Methods in Physics Research A*, Volume 452, pp. 458-496.
- Strijckmans, K., 2001. The isochronous cyclotron: principles and recent developments. *Computerized Medical Imaging and Graphics*, Volume 25, pp. 69-78.
- Tanaka, S. & Furukawa, M., 1959. Excitation functions for (p,n) reactions with titanium, vanadium, chromium, iron and nickel up to 14 MeV. *Journal of the physical society of Japan*, Volume 14, p. 1269.
- Taylor, J. R., 1997. *An introduction to error analysis. The study of uncertainties in physical measurements. 2nd Edition*. Boulder, Colorado: University Science Books.
- Tesch, K., 1985. A Simple Estimation of the Lateral Shielding for Proton Accelerators in the Energy Range 50 to 1000 MeV. *Radiation Protection Dosimetry*, 11(3), pp. 165-172.
- Theis, C. et al., 2006. Interactive three dimensional visualization and creation of geometries for Monte Carlo calculations. *Nuclear Instruments and Methods in Physics Research A*, Volume 562, pp. 827-829.
- Thermo Scientific, 2013. *The Modular System for Radioactivity Measurements*. [Online]  
Available at: <http://www.thermoscientific.com/en/home.html>
- Topping, G. J. et al., 2013. Manganese-52 positron emission tomography tracer characterization and initial results in phantoms and in vivo. *Med. Phys.*, 40(4), p. doi: 10.1118/1.4793756.

Vallabhajosula, S., 2009. *Molecular Imaging. Radiopharmaceuticals for PET and SPECT*. s.l.:Springer.

Venkataraman, R. et al., 2005. Improved detector response characterization method in ISOCS and LabSOCS. *Journal of Radioanalytical and Nuclear Chemistry*, 264(1), pp. 213-219.

Vincke, H., Theis, C. & Roesler, S., 2011. Induced radioactivity in and around high-energy particle accelerators. *Radiation Protection Dosimetry*, 146(4), pp. 434-439.

Vlachoudis, V., 2009. *FLAIR: A Powerful But User Friendly Graphical Interface For FLUKA*. New York, Saratoga Springs.

WestGrid, 2013. *WestGrid*. [Online]  
Available at: <https://www.westgrid.ca/>

Wiegel, B. et al., 2009. Intercomparison of radiation protection devices in a high-energy stray neutron field, Part II: Bonner sphere spectrometry. *Radiation Measurements*, Volume 44, pp. 660-672.

Wyckoff, J. M. & Chilton, A. B., 1973. *Dose due to practical neutron energy distributions incident on concrete shielding walls*. Springfield, Virginia, Snyder, W.S., Ed., pp. 694-699.

X-5 Monte Carlo Team, 2003. *LA-UR-03-1987. MCNP - A General Monte Carlo N-Particle Transport Code, Version 5. Volume I: Overview and Theory*. Los Alamos: Los Alamos National Laboratory.

Zagni, F. et al., 2014. Monte Carlo modeling provides accurate calibration factors. *Applied Radiations and Isotopes*, Volume 94, pp. 158-165.

Ziegler, J. F., Ziegler, M. D. & Biersack, J. P., 2010. SRIM - The stopping and range of ions in matter (2010). *Nuclear Instruments and Methods in Physics Research Section B*, 268(11-12), pp. 1818-1823.

# ***Acknowledges***

First of all I want to acknowledge my advisor Prof. Ing. Domiziano Mostacci for his constant support and guidance in all these years of my university studies. His passion to the teaching and his total commitment to students inspired me, moreover he always gave me the possibility to make all the experiences allowing me to grow and to improve my competences, also (and especially) at an international level.

A special acknowledge goes to my co-advisor Dr. Mario Marengo. He handed down the passion for the radiation protection and he transformed a young student in a good (I hope) scientist. In all these years, he used his extraordinary teaching ability to introduce me into the medical physics field with his support and guidance but without forgetting my background in engineering. Nevertheless, as a real teacher, he also allowed me to grow by myself, to let me assume my responsibilities but to receive appreciations and encouragements when a good job was done. Of course, he introduce me also in the ancient tradition of the “Quality Control” and I will be always grateful to him.

A big “thank you” (but very big) goes to Davide and Gianfranco for their technical support and for their friendship in all these years. It was a pleasure to collaborate with both and you contributed a lot in my scientific growing.

I am very grateful to Dr. Conny Hoehr for giving me the opportunity to spend a short but very important and productive part of my PhD at TRIUMF centre in Vancouver. A special acknowledge goes also to Dr. Mike Trinczek for his support in and outside TRIUMF. I am very happy to have surprised with my work these two extraordinary people and I think that, a part from a scientific collaboration, a good friendship it is born.

Now, a special acknowledge goes to the group of people with which I have divided entire working days and really beautiful moments: Federico, Sara, Vittorio and Giulia. In these years we have created an extraordinary group in which everyone had a special competence but when mixed, we were able to produce very good works and results. The time spent together in and outside the lab, the time spent at the several European congresses of nuclear medicine will never come back again but

it will be always part of me wherever I will be in the future. I really hope to have the possibility, one day, to work again all together. Thank you from the deep of my heart for your friendship.

Last but not least, I want to acknowledge all my family for their support, not only moral but also economic thanks to their sacrifices, in all my university studies. Without them I would not be here today. A special acknowledge goes also to Sara.

To all the people reported above once again a very special *thank you!*

Angelo

April 29<sup>th</sup>, 2015  
Bologna, Italy